Title

Variety of Synapse Development in Drosophila Brain Studied by Genetics, Receptor Immunofluorescence, and Expansion Light Sheet Microscopy

Author

Kim, Alexander James

Publication Date

2024

Peer reviewed|Thesis/dissertation

UNIVERSITY OF CALIFORNIA

Los Angeles

Variety of Synapse Development in Drosophila Brain Studied by Genetics, Receptor Immunofluorescence, and Expansion Light Sheet Microscopy

A dissertation submitted in partial satisfaction of the requirements for the degree Doctor of Philosophy in Molecular Biology

by

Alexander James Kim

2024

ABSTRACT OF THE DISSERTATION

Variety of Synapse Development in Drosophila Brain Studied by Genetics, Receptor Immunofluorescence, and Expansion Light Sheet Microscopy

by

Alexander James Kim

Doctor of Philosophy in Molecular Biology

University of California, Los Angeles, 2024

Professor Stephen Lawrence Zipursky, Chair

During circuit assembly in the developing brain, neurons undergo dynamic expression of many neurotransmitter receptor (NR) subunits that are used to establish a series of postsynaptic domains. However, our understanding of the molecular logic that determines synapse composition between classes of inputs remains limited. The *Drosophila* central nervous system demonstrates particularly striking specificity of synapse types. Here, I report the use of new tools developed to study the localization of endogenously expressed NR subunits in sparsely distributed cells, thus offering a window into the process of synaptogenesis and the establishment of variously defined postsynaptic sites in the brain. I use a combination of genetic methods and expansion microscopy (ExM) to investigate NR localization in the fly brain at the scale of single synapses. In developmental studies, I also present evidence of temporally distinct dynamics of synapse formation that differ between NR type as well as cell type. Lastly, I explore methods to uncover

mechanisms that regulate NR localization in these cells. This work describes newly advanced methods that can be leveraged to probe the molecular architecture of synapses *in vivo* and suggests a complex picture of how synapse formation is coordinated through differential, synapse-specific processes during development.

The dissertation of Alexander James Kim is approved.

Orkun Akin

David E. Krantz

Gregory S. Payne

James A. Wohlschlegel

Stephen Lawrence Zipursky, Committee Chair

University of California, Los Angeles

2024

Contents

List of Figures

List of Tables

Acknowledgements

My time in the Zipursky Lab has been transformative. When I entered the Medical Scientist Training Program, I had envisioned myself working on a translational project that could one day change how we treat patients. I was fascinated by the potential of biology to be commandeered—to track and measure our health, to repair our tissues, to enhance or restore our functionality at the cellular level. Perhaps naively, I viewed biology as a thing that was ready to be harnessed at will and read like an open book. It wasn't long before my opinion changed.

On a quiet afternoon in medical school, I slipped out of class early and into the back of a research seminar being hosted by a member of the Zipursky Lab. I had decided to attend out of sheer curiosity. The speaker told us a story about a set of neurons that navigated their way through the brain during development and communicated with other cells using a pair of molecular signals and receptors. To reach this conclusion, the lab had conducted a series of experiments to demonstrate the process in which these neurons extended their axons out into a new layer and depended on the receptor-ligand interaction to control where they stopped. They had performed these experiments not in a dish, but within a live animal that was genetically engineered to perform all of the necessary manipulations in the particular neuron types they were studying. These *in* vivo experiments were done using a level of sophistication that I had never seen before. I was taken aback and inspired; I left the talk feeling nothing short of gleeful.

My search for a topic of graduate study had led me to explore many disparate fields, but I was ending up with more questions than answers. Over time, I developed a deeper appreciation for the complexity of biological systems and the challenges that lie at the forefront of discovery. Like I had experienced with physics, I was growing fond of the elegant experiments that were conceived to unravel biology's mysteries, one step at a time, despite how neatly things were

summarized in my textbooks. That fateful afternoon, followed by the conversations, group meetings, and ultimately the rotation I spent in the lab, cemented my feelings. I knew that I wanted to use the opportunity of graduate school to study a new field of basic science, one that I hoped would better equip me for medical challenges of the future. Working with *Drosophila*, I saw an opportunity to learn how to harness biology in ways that I had only dreamed of—and hopefully do some good science along the way.

The mentorship of Professor Zipursky, as well as my discussions with members of our laboratory and our collaborators, not only supported me in this research but also exposed me to the cutting edge of life sciences—from advances in genetics, molecular biology and immunohistochemistry, to transcriptomics, proteomics and connectomics. I would like to personally extend my gratitude to those I spent time with in the lab, including Drs. Saumya Jain, Yerbol Kurmangaliyev, Mark Dombrovski, Javier Valdés-Aleman, Fangming Xie, John Lee, Sarah Cheng, Qi Xiao, Sam LoCasio, and Shuwa Xu, as well as the more recent Drs. Juyoun Yoo, Ying Lin, and Bryce Bajar, and the postbaccalaureate researcher Vincent Xu. Of course, none of this work would have been possible without my close collaboration with Dr. Piero Sanfilippo, whose pioneering efforts to develop the genetic tools for tagging neurotransmitter receptors provided a foundation for this research. Piero also led the affinity purification and mass spectrometry work described in this dissertation in collaboration with the laboratory of Professor James A. Wohlschlegel. The collaboration with Yoshi Aso and Anu Bhukel at Janelia Research Campus additionally supported this research, and they provided me with key guidance in my application of expansion light sheet microscopy. In addition, I thank the students and technicians in the lab, including Parmis Mirshahidi, Pegah Mirshahidi, Catherine Lee, and Crystal Zhou, who

I worked with closely and who supported me in this research. I also thank Laura Schreiber and Dorian Gunning, who kept our lab running.

I thank the rest of my committee members, Professors Orkun Akin, David E. Krantz, and Gregory S. Payne for their support and guidance. I also thank the UCLA MSTP, including our current directors Professors David Dawson and Olujimi Ajijola, and former director Professor Carlos Portera-Cailliau, as well as my MSTP advisors, Professors Maureen Su and Leanne Jones, who have all had a hand in guiding me throughout this journey. The support from the MSTP and MBI offices have both been tremendous, and I thank Susie Esquivel, Staci Chikami, and Helen Houldsworth for their help.

I should also acknowledge the undergraduate training I received in the laboratory of Gerard Wong, whose background as a physicist personally inspired me to try my hand at biology, and the members of his lab who I worked with as graduate students, including Drs. Calvin Lee and Ernest Lee. The computational work I participated in at the Wong Lab conducting single-cell tracking of colonizing bacterial biofilms provided a foundation for my understanding of image analysis methods and informed my approach to segmenting expansion light sheet microscopy data.

My graduate training was sponsored by the UCLA Medical-Scientist Training Program (T32-GM008042) and the UCLA Molecular Biology Institute Whitcome Fellowship. In this dissertation, Chapter 2 is modified from published work: Sanfilippo P, Kim AJ, Bhukel A, Yoo J, Mirshahidi PS, … & Zipursky SL. Mapping of multiple neurotransmitter receptor subtypes and distinct protein complexes to the connectome. *Neuron*. 2024 Mar 20;112(6):942-958.e13. PMID: 38262414. Chapters 3, 4, and 5 were prepared by me for this dissertation to describe additional research that I conducted during my graduate studies that was not comprehensively included in our publication.

Last, I hope I can express my gratitude for the love and support from my friends and family throughout this journey, which has been among the most challenging and exciting experiences of my academic career. To my mother, Jacqueline Kim, for her unconditional support and her ability to always keep my head on straight. To my father, Choll Kim, who continues to inspire me as a physician and keeps my passion for medicine burning bright. To my partner, Tawny Tran, who has accompanied me as I reach this important milestone and has made my life fulfilling, creative, and full of love. To my longtime mentor and friend, Stan Schein, who was the first person to deeply inspire me as a scientist and has provided me with priceless wisdom and intellectual support over the years. To the many good friends who have kept me going along the way and made life interesting and novel, including Darren Vongphakdy and Allek Bien, who imparted their artistic sensibilities onto me and kept my horizons wide open by inviting me into their very different worlds. Nothing is achieved in a vacuum; I always had a place to turn in the face of something new.

Vita

Alexander James Kim

2017 Bachelor of Science in Biophysics, University of California, Los Angeles

SELECTED PUBLICATIONS

1. Sanfilippo P, Kim AJ, Bhukel A, Yoo J, Mirshahidi PS, Pandey V, Bevir H, Yuen A, Mirshahidi PS, Guo P, Li HS, Wohlschlegel JA, Aso Y, Zipursky SL. Mapping of multiple neurotransmitter receptor subtypes and distinct protein complexes to the connectome. *Neuron*. 2024 Mar 20;112(6):942-958.e13. PMID: 38262414.
2. Lee C.K., Kim A.J., Santos G.S., Lai P.Y., Lee S.Y., Qiao D.F., Anda J., Young T.D., Chen Y., Rowe A.R., Nealson K.H., Weiss P.S., Wong G.C.L. Evolution of Cell Size Homeostasis and Growth Rate Diversity during Initial Surface Colonization of Shewanella oneidensis. *ACS Nano*. 2016 Oct 25;10(10):9183-9192. PMID: 27571459.
3. Spokoyny I., Raman R., Ernstrom K., Kim A.J., Meyer B.C., Karanjia N.P.. Accuracy of First Recorded "Last Known Normal" Times of Stroke Code Patients. *J Stroke Cerebrovasc Dis*. 2015 Nov;24(11):2467-73. PMID: 26341734.

HONORS & AWARDS

2017 - 2025 NIH Medical Scientist Training Program Fellowship, David Geffen School of Medicine at UCLA

2021 - 2022	Whitcome Pre-Doctoral Fellowship in Molecular Biology, UCLA Molecular Biology Institute
2020 - 2021	Whitcome Pre-Doctoral Fellowship in Molecular Biology, UCLA Molecular Biology Institute
2019 - 2020	Anne Rosenthal Lothar Fellowship, David Geffen School of Medicine at UCLA
2017	Graduating with College Honors, UCLA Honors Program
2017	Graduating *summa cum laude*, UCLA College of Letters and Science
2017	Kaplan Award for Biological Physics, Center for Biological Physics at UCLA
2016	Marvin Hokom Undergraduate Research Award, UCLA Department of Bioengineering

Chapter 1: Introduction

In this chapter, I present the conceptual framework and key overarching questions for this dissertation, providing a brief perspective of several topics relevant to the work.

1.1 A connectomic view of the brain

An implicit feature of any multicellular organism is that multiple cell types exist. Differences in cell identities are largely assumed to exist via differences in gene transcription. However, this view does not fully explain how different identities are physically communicated among cells. In a system of even just two cell types, physically establishing identity at the points of contact is crucial if the organization or interaction between cells depends on their identities. The same issue also exists at the subcellular level, where the spatial relationships between cells can vary tremendously and can be multiplicitous. Even a simple planar distribution of cells will develop both divalent and trivalent cellular contacts, each of which must be specified. From a measure of gene expression, the monolithic state of the cell nucleus does not easily predict how these domains are defined. These same questions arise in the central nervous system but with extraordinary complexity.

The intricate architecture of the brain is one of biology's greatest puzzles. From *Drosophila* to humans, brain wiring involves millions to trillions of synapses and hundreds to thousands of neuron types. While our previous understanding of cell-type complexity and wiring specificity at the synapse level has been limited to a handful of well characterized circuits, recent advances in reconstruction-based connectomics derived from electron microscopy (EM) have proven our ability to reach a comprehensive, single-synapse level view of the brain. Some of our most advanced studies using EM have been conducted in *Drosophila* (Dorkenwald et al., 2023; Rivera-

Alba et al., 2011; Scheffer et al., 2020; Schlegel et al., 2023; Shinomiya et al., 2019; Takemura, Aso, et al., 2017; Takemura et al., 2013, 2015; Takemura, Nern, et al., 2017).

These studies revealed a highly stereotyped and cell-type-specific environment, in which synapses are established with precise subcellular localization between specific partner neurons. From the perspective of morphology and connectivity, the diversity of neuron types is immense, with upwards of 3,000 distinct cell types for the approximate 130,000 neurons and 53 million synapses established thus far from EM connectomic analysis in the adult *Drosophila* brain (Schlegel et al., 2023).

Several important lessons have emerged from EM studies. First, additional neuron types exist that can be recovered through EM reconstructions where prior studies using Golgi staining or genetic single-cell labeling methods failed (Takemura et al., 2013). Second, the connectivity between different neuron types is highly specific and poorly correlated with the extent of their surface contact (Takemura et al., 2015); thus, uncovering these circuits requires methods that can directly visualize the locations of synaptic densities or synaptic markers. Third, our understanding of circuit function and behavior crucially depends on a comprehensive understanding of the neuron types involved and the placement of synaptic connections. For instance, a pair of directionally selective motion detection circuits involving T4 and T5 neurons were identified in the fly using behavioral and optogenetic studies (Maisak et al., 2013). While two different motion detector models were initially proposed to underlie the function of these circuits, the actual connectivity suggested a more complex picture. EM studies uncovered at least seven distinct neuron types converging onto the dendritic arbors of T4 and T5 neurons along subdomains of their proximodistal dendritic axis (Shinomiya et al., 2019; Takemura et al., 2013; Takemura, Nern, et al., 2017). Considering these findings, a later model ultimately showed that both proposed detector

types could exist in the T4 and T5 circuits, enhancing their directional selectivity (Haag et al., 2016, 2017). Taken together, these studies highlight how connectomics can provide the necessary insight into synaptic architecture to properly study circuit function and identify the neuron types involved, which is crucial to understanding behavior. Furthermore, connectomics has uncovered the specificity and localization with which synaptic connections are made, raising important questions about the molecular mechanisms at play that define these many distinct cellular contacts.

However, EM studies have provided only a partial view into how brains are organized. Although connectomic reconstruction enables the unbiased identification of all neurons and synapses in a volume, it lacks the ability to characterize the rich molecular composition present at each synapse. Furthermore, EM studies are highly labor intensive and are thus limited by small sample sizes (typical publications report the reconstruction of part of a single brain). As such, the approach becomes unfeasible for investigations requiring multiple conditions, including developmental studies that would require the analysis of multiple separate brains at different time points, or larger phenotypic studies comparing wild type and mutant animals. Thus, EM provides us with a way to determine the cell type organization of adult circuitry, but not the molecular diversity present at different synapses, nor an understanding of how circuits arise during development.

1.2 Molecular diversity of synapses

Molecular complexity in neurobiology presents a formidable challenge. Neurons receive various types of synaptic inputs, requiring the precise organization of these connections with specific partners and the correct localization of synaptic components at each synapse. To orchestrate this process, neurons express a wide range of genes. Human brain transcriptomes

revealed that approximately 84% of genes are expressed in at least one brain region (Hawrylycz et al., 2012; Negi & Guda, 2017), while similar studies in mouse reported approximately 80% of genes showing brain expression (Lein et al., 2007).

At the synapse, correct molecular composition is crucial to brain activity. Among the genes involved, neurotransmitter receptors (NRs) serve the fundamental role of mediating synaptic transmission through one of several conserved classes of neurotransmitters. From simple invertebrates to humans, NR subunit families exist with numerous paralogs and isoforms (**Figure 1.1**) that can assemble into receptor complexes with distinct physiological properties, molecular composition, and pharmacology (Hansen et al., 2018; Olsen & Sieghart, 2009; Rosenthal & Yuan, 2021). As a result, synapses possess a range of NR subtypes that may instill different circuit functions or participate in connections between different synaptic partners, or both.

However, exactly how different synapse types are precisely assembled at the correct locations is not well understood. On one hand, specialized trafficking mechanisms that involve a series of adaptor and scaffold proteins as well as activity-dependent post-translational modifications are postulated to cluster NRs at the postsynaptic density (Radler et al., 2020). However, most studies fail to address how these mechanisms govern NR-subtype specificity or synaptic specificity between neuron types to establish proper circuit organization. On the other hand, a large number of synaptic adhesion molecules have been identified as 'wiring genes' that regulate synaptic specificity between partner neurons; however, many of these genes lack established evidence for molecular mechanisms or subcellular localization patterns (Cheng et al., 2019; Sanes & Zipursky, 2020; Südhof, 2018). Thus, the relationship between mechanisms that assemble synaptic machinery and wiring genes that instruct partner selectivity and circuit organization is not well understood.

In order to better understand the processes that govern synapse formation and circuit assembly, I sought to investigate the localization of NR subunits at different synapse types. This work lays the foundation to understanding molecular specificity at synapses and uncovering potential mechanisms that regulate synapse formation during development. Many NR subunits (as well as wiring genes) are expressed with diverse, cell-type-specific transcriptional dynamics (**Figure 1.2**)(Kurmangaliyev et al., 2020; Özel et al., 2021). Given the possibility that different processes could be regulating different synapses at distinct points in development, these localization studies would provide a framework that expands our understanding of circuit assembly to include a picture of how and when postsynaptic proteins actually localize to each of their respective domains.

1.3 Known mechanisms of neurotransmitter receptor localization

Extensive research has explored pathways governing neurotransmitter receptor localization at synapses. Classical studies on the neuromuscular junction (NMJ) provided many insights into these pathways. At the mammalian NMJ, the cytosolic adaptor protein Rapsyn is essential for clustering of acetylcholine receptors (AChRs) in muscle cells via a direct interaction between them (Apel et al., 1995). Innervating motor neurons provide multiple signals to postsynaptic muscle cells that regulate Rapsyn and the expression and clustering of AChRs. Agrin, a proteoglycan secreted at the developing motor neuron terminals, interacts with several receptors on the surface of muscle cells including the protein Muscle-specific kinase (MuSK), a receptor tyrosine kinase whose activation promotes Rapsyn-mediated clustering of AChRs (Apel et al., 1995; Gautam et al., 1996; Glass et al., 1996). Later studies demonstrated that Agrin directly interacts with the

coreceptor Low-density lipoprotein receptor-related protein 4 (Lrp4) to activate MuSK (W. Zhang et al., 2011). However, Rapsyn was demonstrated to not play a required role in interneuronal synapses and appears to be a specialized scaffold protein for the NMJ in mammals (Feng et al., 1998). (Interestingly, the *Drosophila* ortholog of Rapsyn, CG1909, was shown to have activity-dependent gene expression in the brain (Guan et al., 2005), although the function of CG1909 has not been characterized.) Taken together, these studies demonstrate that the mechanisms identified in NMJ studies cannot be directly extrapolated to the central nervous system (CNS), which may involve distinct pathways.

In the mammalian CNS, several scaffolding mechanisms that regulate neurotransmitter receptor localization have been identified. In excitatory synapses, the clustering of glutamate receptors, particularly ionotropic glutamate receptors (iGluRs), is facilitated by scaffold proteins such as PSD-95 and other members of the membrane-associated guanylate kinase (MAGUK) family. PSD-95 is crucial for organizing and stabilizing iGluRs at postsynaptic sites (X. Chen et al., 2015). Through its multiple interaction domains, PSD-95 interacts directly with iGluRs as well as indirectly through other synaptic proteins that organize the synapse (Sheng & Kim, 2011). For example, transmembrane AMPA receptor regulatory proteins (TARPs) such as Stargazin act as auxiliary subunits to regulate synaptic AMPA receptors and mediate interactions with PSD-95 (L. Chen et al., 2000; Kato et al., 2010).

At inhibitory mammalian synapses, localization of GABA receptors (GABAARs) is tightly regulated by proteins such as Gephyrin and Collybistin. Gephyrin, a multifunctional scaffold protein, plays a pivotal role in clustering and stabilizing GABAARs at postsynaptic sites (Moss & Smart, 2001). Through its various protein interaction domains, Gephyrin mediates the assembly of inhibitory postsynaptic densities, providing a structural framework for GABAAR clustering and

synaptic anchoring (Tyagarajan & Fritschy, 2014). Collybistin acts as a regulator of Gephyrin function by facilitating its recruitment and activation at inhibitory synapses (Harvey et al., 2004; Papadopoulos et al., 2007). In addition, the synaptic adhesion protein Neuroligin-2 is present at virtually all inhibitory synapses and interacts transsynaptically with presynaptic Neurexins and drives inhibitory postsynaptic assembly through interactions with Gephyrin and Collybistin (Poulopoulos et al., 2009; Varoqueaux et al., 2004). However, knockout studies in mouse demonstrated that Gephyrin is not universally required to form inhibitory synapses but rather has differing effects on differing GABAAR subtypes and differing circuits (Kneussel et al., 2001). Diverse processes of gephyrin and GABAAR localization have been observed during development, suggesting that inhibitory postsynaptic apparatus is organized in a heterogeneous manner throughout the brain (Viltono et al., 2008). In addition, *Nlgn2* knockout studies in mice also showed region-specific effects on inhibitory synapses and only partial, varying decreases in Gephyrin and GABAARs (Ali et al., 2020; Panzanelli et al., 2017). Thus, Gephyrin-independent pathways that assemble inhibitory synapses also exist and the effects of postsynaptic proteins may be differentially modulated for specific synapse types.

Overall, many synaptogenic regulators have been identified through prior studies that demonstrated the effects of various genes on the recruitment of synaptic machinery (including NRs). However, our understanding of how these processes instruct circuit-specific wiring remains limited when considering the studies described above. For one, many synaptic proteins exhibit a multiplicity of interactions and a redundancy in synapse forming pathways, obscuring their precise roles. In addition, our incomplete view of molecular composition from one set of synapses to another precludes a complete understanding of the specificity with which various proteins regulate different connections, though genetic analyses have demonstrated partial phenotypes limited to

particular brain areas or NR subtypes. Finally, our conceptual framework of synapse formation and regulatory molecules fails to adequately account for the subcellular precision with which synaptic connectivity is established (between only a subset of available synaptic partners). To summarize, we have yet to full elucidate the relationship between various synaptic molecules and the specificity of connections that they are involved in, and our knowledge at the gene level cannot address how these molecules target discretely localized synapses that are subcellularly regulated.

In this work, I elucidate the localization patterns of several NR subunits as well as other synaptic molecules at the protein level *in vivo*. I also uncover differential processes of synapse formation that vary between NR types and cell types and use a newly developed combination of approaches to probe the molecular composition of synapses in identified neurons. Finally, I explore several approaches designed to tackle undiscovered paradigms of synapse formation, which are poorly characterized in the *Drosophila* brain.

1.4 Expansion microscopy of synapses

Studying the subcellular localization of synaptic molecules poses major technical challenges given the resolution and cell-type identification required. Given the mounting evidence of complex, precisely organized circuits and immense transcriptional diversity across neuron types, a tractable approach that enables rapid visualization of synaptic connectivity and molecular localization in brain tissues becomes paramount. Expansion microscopy (ExM) has emerged as a promising technique, offering a novel way to reach effective super-resolution with immunofluorescence.

This innovative approach allows for a detailed investigation of synapses previously limited to EM, surpassing resolution limits through the physical expansion of hydrogel-embedded samples

that can be tuned to produce two- to 22-fold linear increases in size (F. Chen et al., 2015; Damstra et al., 2022; Lillvis et al., 2022; M'Saad et al., 2022; Sneve & Piatkevich, 2022; Tillberg et al., 2016). Furthermore, the gelled and expanded tissue results in an optically transparent sample that allows for straightforward acquisition of three-dimensional volumes with minimal signal degradation over imaging depth. Thus, neural circuits across large brain areas can be studied. The continued development and application of ExM techniques in neurobiology is crucial to advancing our understanding of brain wiring and synaptic organization at the molecular level.

As a model system, the *Drosophila* brain is well suited for these investigations due to several existing advantages: (i) The genetic tractability and extensive toolkit for studying individual cell types and conducting precise manipulations; (ii) The availability of detailed single-cell transcriptome data throughout brain development; (iii) EM reconstructions that provide synapse-level connectomes to unveil circuit organization. These resources offer unparalleled insight to comprehensively identify the expression of NRs and other genes for a given neuron and accurately map the locations and identities of its synaptic contacts, which can be probed *in vivo* in adult and developing animals.

1.5 Figures

Figure 1.1 Composition of chemical synapses

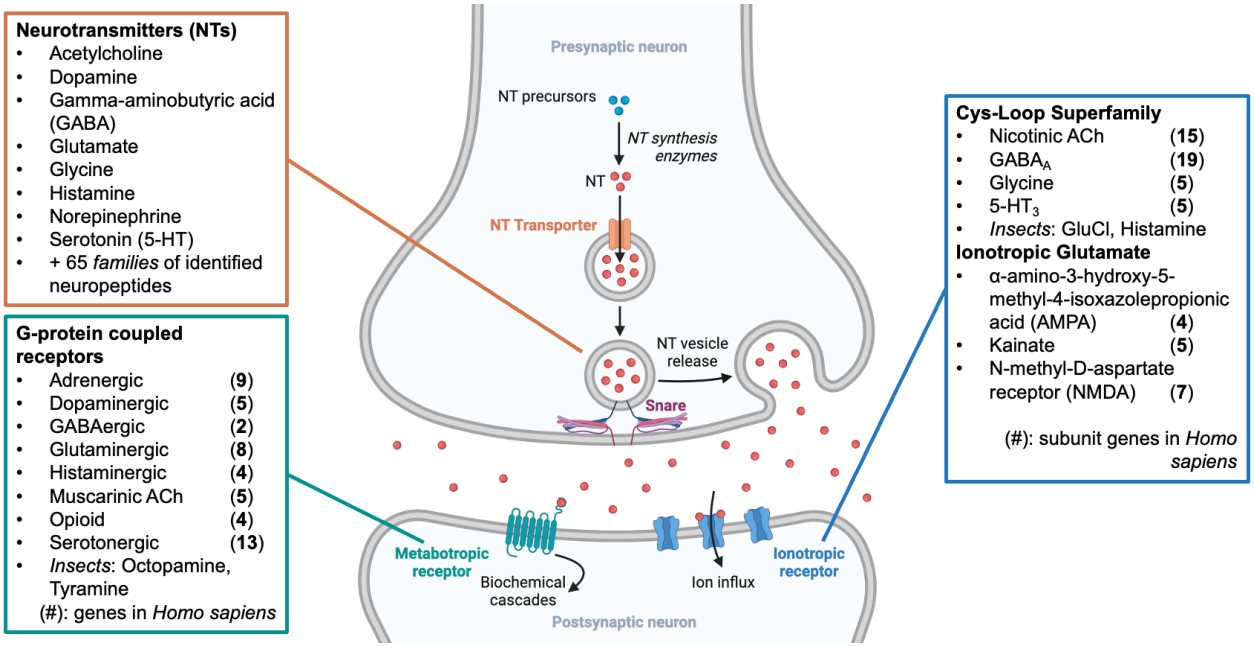

Chemical synapses between neurons utilize many classes of neurotransmitters (NTs), which each have conserved families of neurotransmitter receptors (NRs).

Upper left, Neurotransmitter types used in the mammalian brain (not comprehensive).

Lower left, numbers of metabotropic NRs encoded in the human genome for each major class of G-protein coupled receptors (GPCRs). The *Drosophila* genome encodes for additional GPCRs that respond to neurotransmitters used by invertebrates, such as octopamine and tyramine.

Right, numbers of ionotropic NRs encoded in the human genome, which fall into two superfamilies. Cys-loop receptors comprise the ionotropic receptor classes that respond to all NTs besides glutamate. The *Drosophila* genome encodes for additional cys-loop receptors specific to invertebrates that respond to glutamate and histamine and function as (inhibitory) ligand-gated chloride channels. Vertebrate ionotropic glutamate receptors (iGluRs) fall within three major

classes: α-amino-3-hydroxy-5-methyl-4-isoxazolepropionic acid (AMPA) receptors (AMPARs), kainate receptors, and N-methyl-D-aspartate receptor (NMDA) receptors (NMDARs). Numbers of genes do not account for alternatively spliced isoforms encoded in many NR gene loci. Additionally, GPCRs can dimerize or form higher-order oligomers; cys-loop receptors are requisite pentamers; iGluRs are requisite tetrameters—all classes can form heteromeric complexes. Thus, the variety of possible NR types is much greater than the number of genes. Schematic created with BioRender.com.

Figure 1.2 mRNA expression of neurotransmitter receptor genes in visual system neuron types

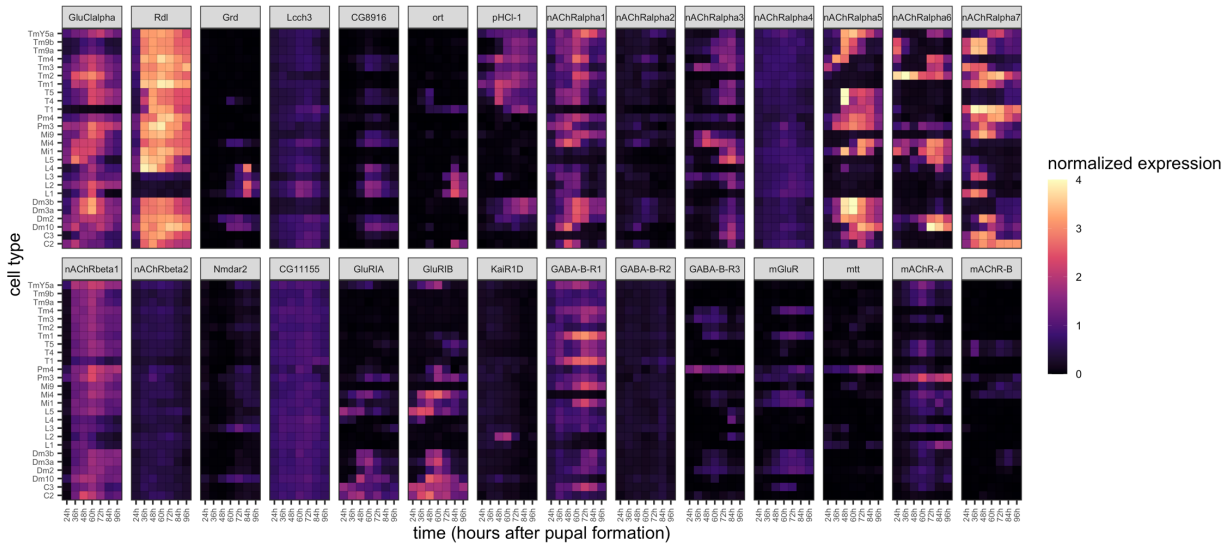

Normalized expression levels of mRNA from NR genes during pupal development. Sets of NR genes are expressed in cell-type specific combinations with widely ranging temporal dynamics. X-axis, Expression is plotted at 12-hour increments from 24 to 96 hours after pupal formation, corresponding to distinct sets of brains that were dissected and sequenced for each time point. Y-axis, Identified neuron-type clusters. Normalized expression values were averaged across all cells in a cluster for a given time point to reflect the mean expression of a neuron type at a given time during pupal development.

Source data from Kurmangaliyev et al., 2020.

Chapter 2: Mapping of multiple neurotransmitter receptor subtypes and distinct protein complexes to the connectome

2.1 Summary

Neurons express various combinations of neurotransmitter receptor (NR) subunits and receive inputs from multiple neuron types expressing different neurotransmitters. Localizing NR subunits to specific synaptic inputs has been challenging. Here, we use epitope-tagged endogenous NR subunits, expansion light-sheet microscopy, and EM connectomics to molecularly characterize synapses in Drosophila. We show that in directionally selective motion-sensitive neurons, different multiple NRs elaborated a highly stereotyped molecular topography with NR localized to specific domains receiving cell-type specific inputs. Developmental studies suggested that NRs or complexes of them with other membrane proteins determine patterns of synaptic inputs. In support of this model, we identify a transmembrane protein associated selectively with a subset of spatially restricted synapses and demonstrate its requirement for synapse formation through genetic analysis. We propose that mechanisms that regulate the precise spatial distribution of NRs provide a molecular cartography specifying the patterns of synaptic connections onto dendrites.

2.2 Introduction

Recent progress in electron microscopy (EM) has enabled the generation of single-synapse level connectomes of large brain volumes.[1–6] In *Drosophila*, EM reconstructions revealed extraordinary complexity and specificity of brain wiring. Hundreds of neuron types form specific

patterns of connections with multiple partners in highly reproducible ways.[2,7] Single-cell sequencing has uncovered distinct patterns of mRNAs in different neurons for proteins involved in the development and function of synapses.[8,9] This is particularly striking in the transcriptional expression patterns of neurotransmitter receptor (NR) subunits.

Most NRs fall into three families: pentameric cys-loop ionotropic receptors, tetrameric glutamate ionotropic receptors, and G protein-coupled metabotropic receptors. In this study, we focus on NRs of the cys-loop superfamily. Cys-loop receptors mediate responses to the major excitatory and inhibitory neurotransmitters, acetylcholine and GABA, respectively, in the *Drosophila* brain. These subunits come together in different combinations to form ligand-gated ion channels. The expression of distinct combinations of NR subunits gives rise to multiple molecularly distinct receptor complexes.[10–14] Different mammalian GABA receptors of this family have been shown to localize to different domains of pyramidal cells (e.g., axon initial segment vs soma).[15,16] Previous studies in *Drosophila* have also shown that targeted expression of cDNAs encoding tagged versions of the GABA receptor subunit Rdl and the nicotinic subunit nAChRα7 resulted in localization to different dendritic domains in motor neurons[17] and in T4/T5 neurons in the visual system.[18] Voltage and calcium imaging in visual circuits in the fly revealed characteristic patterns of activity in different neuronal compartments.[19] What underlies these subcellular specific activity patterns at the molecular level remains largely unknown. They likely include, in part, the subunit composition of NRs in the postsynaptic membrane and their spatial distribution in dendrites.

Localizing NRs at synapses in dendrites has been problematic for two reasons. First, it has been difficult to generate antibodies for multi-pass transmembrane proteins[20], which hinders specific immunohistochemical labeling of many NR subunits. To address this issue, we used

CRISPR-modification to introduce various epitope tags into the endogenous NR loci. These modified loci allowed us to label NR subunits with highly specific commercially available antibodies while preserving their endogenous expression patterns. We also engineered conditional alleles for the selective labeling of tagged NR subunits in single neurons through cell-type-specific expression of recombinases. Second, the density of the neuropil and diffraction-limited light microscopy preclude localizing receptors to synapses in identified neurons. And third, there are substantial technical challenges of EM localization of proteins.[21] To overcome these limitations, we take advantage of recent developments in Expansion Microscopy to localize protein in isotropically expanded tissue[22] using custom-built lattice light-sheet[23,24] and commercially available light-sheet microscopy (ExLLSM and ExLSM, respectively), to achieve effective super-resolution.

Here, we localize tagged NR subunits in specific neuron types throughout the brain in adult and developing neurons at the level of single cells and at single synapses between identified neuron types at super-resolution. We focus on the distribution of seven different subunits in directionally selective motion-sensing neurons and demonstrate that these NRs are localized to specific spatial domains along the proximodistal dendritic axis. Using affinity-purification-mass-spectrometry, we identify a transmembrane protein implicated in synaptic adhesion associated with an NR subunit selectively localized to one of these domains. Our findings raise the possibility that NR protein complexes selectively localized to specific dendritic domains provide molecular cues specifying patterns of synaptic inputs from different neuron types.

2.3 Results

2.3.1 NR subunits are expressed in different brain regions

There are around 60 genes encoding subunits of NRs in the *Drosophila* genome and about 100 in the mouse and human genomes.[25–27] We generated tagged alleles of 11 NR subunits of the cys-loop superfamily, which form pentameric ligand-gated ion channels. These include receptors responsive to acetylcholine and γ-aminobutyric acid (GABA), the major excitatory and inhibitory neurotransmitters in the fly (Figure 1A; Table S1). In addition, we tagged the invertebrate-specific single cys-loop NR subunit that forms glutamatergic receptors. Unlike the subunits of the tetrameric iGluR family (e.g., AMPARs) found in vertebrates and invertebrates, which typically mediate excitation, these receptors gate chloride entry and thus are inhibitory.

Endogenous tagging of NRs is preferable to transgenic expression systems for studying NR localization, as the endogenous proteins preserve their unique, cell-type specific patterns and developmental expression.[18,28] Overexpression of tagged proteins can lead to their accumulation in the cell body and, in extreme cases, may result in the loss of their natural subcellular localization (Figures S1A and S1B). It is crucial to use endogenous tagging to study protein localization during development, as the developmental dynamics of transcriptional and post-transcriptional cell-type specific regulation are key determinants of protein localization.[29]

To generate tagged alleles, the endogenous genomic loci encoding NR subunits were modified by directed knock-in of DNA sequences encoding epitope tags using CRISPR-targeted recombination[30,31] (Figure S1C). All tags were inserted into the cytoplasmic loop between the M3 and M4 transmembrane domains, which are shared amongst all cys-loop receptors (Figures 1A and S1D). Several studies have shown that NRs with insertions in this loop are functional and

localized to postsynaptic sites.[32–35] NR subunits form homomeric or heteromeric NRs, or both (Figure 1A), resulting in a large array of distinct NR types with unique functional properties.[11,12,36]

All tagged NRs localized to the neuropil (Figures 1B and S1E). Their expression patterns were similar to those seen with antibodies to the unmodified NR subunits (Figure S1F). Epitope-tagged proteins rescued lethality in cases where mutant alleles were not viable (see STAR Methods). Furthermore, all remaining homozygous tagged alleles were viable. Typically, the tagged NR subunits were broadly expressed throughout the brain, with some subunits highly enriched in specific neuropils. Each NR subunit exhibited a characteristic pattern of expression (Figures 1B and S1E-S1F; also see Figure S4A). Tagged proteins were expressed at levels similar to the untagged version as quantified by staining with different concentrations of antibody to the native proteins and normalizing to the intensity of staining to the pan-synaptic protein Brp (Figure S1G).

Due to the density of processes within neuropils, it is not possible to assign the expression of proteins detected by immunofluorescence to specific neuron types. To overcome this limitation, we generated inducible alleles and a new approach to tag NR subunits in identified cell types with single-cell resolution (Figures 1C, S1C and S4B). Reagents to label virtually any neuron in *Drosophila* in this way are available.[37,38] In this study, we explored the distribution of NR subunits in different neurons in the visual system and the mushroom body.

The mushroom body is the center for associative learning in insect brains, and its sensory inputs and output synapses are cholinergic[39,40] (Figure S3A). As expected from RNA-seq data[41], we observed the nAChRβ1 subunit in the dendrites of two different MBONs (Figures 1D and 1E). In contrast, the subcellular distribution of the GABAergic subunit Rdl in MBONs was highly cell-type-specific (Figures 1D, 1F and S3C-S3D). For instance, in MBON05, Rdl localized to both

axons and dendrites, while it was predominantly restricted to dendrites in MBON11 (Figures S3C and S3D). Thus, tagged NR subunits localize to specific neuronal domains, which may even differ between neurons with closely related functions. We next sought to address whether the tagged NR subunits were localized to synapses.

2.3.2 Tagged NR subunits localize to synapses

The resolution of light microscopy is not sufficient to localize NRs to synapses. To increase the effective resolution, we imaged expanded tissue[22] using a lattice light-sheet microscope[24] (ExLLSM). This method allows imaging of large volumes at an effective resolution of approximately 60 by 60 by 90 nm.[23] We assessed the localization of the tagged NRs by comparing images of synapses in the mushroom body with those previously obtained using stimulated emission depletion microscopy (STED) and EM.

Previous STED studies of the mushroom body (MB) calyx identified presynaptic sites characterized by Brp-stained donut-shaped structures with the Ca2+ channel Cacophony (Cac) at the center[42] (Figure 1G). Brains bearing an ALFA-tagged allele of Cac and stained for both the ALFA tag and Brp were imaged. We observed presynaptic structures in the MB calyx and in the medulla region of the optic lobe of similar dimensions to those previously described in the MB calyx in STED and EM studies (Figures 1G-1J and S2A). Tagged nAChRβ1 clustered in juxtaposition to these presynaptic sites (Figures 1I-1J and S2B). The synaptic structures identified by ExLLSM for other NR subunits in the calyx and medulla were also similar (Figures 1K-1M and S2C-S2E). All NR subunits were preferentially associated with Brp (see Figures S3M-S3P for quantification), consistent with their synaptic localization. In addition, tagged nAChR subunits localized in different types of synaptic structures similar to those described by EM[39,42,43] (Figures 1K, S3A-S3B and S3E-S3L).

In summary, endogenously tagged NRs visualized by ExLLSM were distributed in NR-type-specific patterns within the CNS and selectively localized to postsynaptic sites, which is consistent with previous studies using EM and STED.

2.3.3 NR subunit distribution matches the EM connectome

We next sought to determine whether the patterns of NRs correlated with the distribution of inputs from cholinergic, GABAergic, and glutamatergic neurons as determined by connectomic and gene expression studies. We focused on circuits in the fly visual system and, in particular, the medulla neuropil. The repetitive pattern allowed us to look at many different neurons of the same type in a single animal, and it is straightforward to generate sparsely labeled neurons of the same type. In the medulla neuropil, overlapping processes of many different neuron types form stereotyped circuits (Figure 2A). Each neuron type expresses different levels and combinations of transcripts encoding NR subunits[8] (Figure S4A).

The ten layers of the medulla comprise the highly branched processes and synapses of many neurons (>10,000 neurons, >100 neuron types, and ~2 million synapses).[7] Some receptors are broadly expressed, whereas others are preferentially enriched in specific layers (Figure 2B). For instance, the inhibitory GABA receptor subunit Rdl, which can form homomeric and heteromeric receptors[11,14], is expressed in most layers of the medulla. By contrast, the expression of Lcch3, another GABA receptor subunit that can form heteromeric receptors with Rdl[14], is more restricted (Figure 2B). Differential localization was also observed for different nAChR subunits (Figure 2B).

EM-level connectomes have established that many neuron types in the medulla receive inputs from multiple types of presynaptic neurons.[7,44] For instance, GluClα localized to domains of L5, which predominantly receive glutamatergic inputs in medulla layers M1 and M5 (Figure

2C). The number of puncta seen for GluClα in L5 neurons correlated well with EM data (Figure 2F). These neurons also receive cholinergic and GABAergic innervation to the same and different dendrites in discrete and reproducible patterns, and this is reflected in the distribution of Rdl and nAChRβ1 (Figures 2D-2F). Discrepancies between synapse numbers were observed in some cases with Rdl and different acetylcholine receptors. This may represent NRs that are extrasynaptic (e.g., small Rdl puncta, see Figure S2E) and different receptors for the same neurotransmitter at different synapses in the same neuron (e.g., multiple nAChRs). In general, however, there was a good correlation between the distribution of receptor puncta and synapses determined by EM across several neuron types (Figures 2G, S4C-S4F and S5F).

2.3.4 NR subunits are differentially localized along dendrites

The precise distribution of synaptic inputs from different neurons along the proximodistal axis of T4 dendrites is proposed to play a crucial role in motion detection. T4 dendrites receive inputs from GABAergic, cholinergic, and glutamatergic neurons from eight identified cell types in specific domains along the proximodistal axis[4,44] (Figure 3A). The synaptic inputs to T5 are different (Figure S5A; see below), with different neuron types also forming synapses within specific dendritic domains[4].

The distribution of NRs in T4 dendrites was consistent with the neurotransmitters used by the synaptic inputs. GluClα, as described above, was highly localized to the distal domains (Figures 3B and 3E). By contrast, Rdl was strongly enriched in the proximal region, with additional puncta sparsely scattered throughout the arbors (Figures 3C and 3E). T4 neurons also express two additional GABA NR subunits, Lcch3 and CG8916 (see Figure S4A). These two subunits were not localized proximally but exhibited a common distribution with enrichment in the distal region and then sparsely throughout the rest of the dendrite (Figures 3C and 3E). The proximal enrichment

of Rdl matches the innervation pattern by three different GABAergic neuron types (i.e. Mi4, C3, and CT1). By contrast, TmY15 synapses scattered along the length of T4 dendrites may signal through NRs containing Lcch3 and CG8916.

Different nAChR subunits also show different distributions in T4 dendrites. nAChRα5 localized to the middle domain of T4 dendrites, whereas both nAChRβ1 and nAChRα1 localized to the distal domain (Figures 3D and 3E). These patterns correlate with the cholinergic inputs from overlapping Mi1 and Tm3 neurons in the middle domain and to dendrodendritic synapses of overlapping T4 dendrites in the distal domain. These data suggest that the subunit composition of NRs to the same neurotransmitter is unique to specific synaptic inputs.

T5 dendrites receive inputs different from T4, and these also showed specificity along the proximodistal axis (Figures S5A-S5E). Rdl, nAChRα5, nAChRβ1, and nAChRα1 subunits were distributed similarly to T4 (Figures S5C-S5E). GluClα was not detected in T5 dendrites, consistent with the absence of glutamatergic inputs (Figures S5A and S5B). CG8916 and Lcch3 also lacked the enrichment to the tips observed for T4 dendrites (Figures S5C and S5E). There were twice the number of nAChRβ1 puncta in T5 as in T4 dendrites (Figure S5F). This is consistent with the additional cholinergic input T5 dendrites receive in the distal region by Tm9 neurons (Figures S5A and S5D). Three other Tm neuron types (Tm1, Tm2, and Tm4) provide inputs to the middle domain in a pattern similar to the distribution of nAChRα5 (Figures S5A and S5D).

The distribution of nAChRα1, nAChRβ1, and nAChRα5 partially overlap in the middle domain. To assess whether these nAChR subunits were in the same or different synapses, we tagged nAChRα1 or nAChRα5 in combination with nAChRβ1 in the same neuron with different epitopes (Figure S5G). nAChRα1 puncta largely co-localized with nAChRβ1, suggesting that these are found at the same synapses (Figures S5H and S5I). By contrast, nAChRα5 and nAChRβ1

did not co-localize, demonstrating that these are not at the same synapse (Figures S5H and S5I). This is consistent with findings showing that nAChRα5 subunits, which are closely related to the vertebrate α7 nAChR subunit known to form homomeric receptors[45,46], can also form homomeric receptors[12]. In contrast, there is evidence that nAChRα1 can only assemble into heteromeric receptors, which must include β nAChR subunits.[10] Thus, even within the same dendritic domain, different cholinergic neuron types may form synapses selectively onto postsynaptic sites expressing different receptors.

In summary, the distribution of NR subunits reflected the specific arrangement of various GABAergic, cholinergic, and glutamatergic inputs onto T4 or T5 dendrites with spatial specificity along their proximodistal axis. Different neuron types, which use the same neurotransmitter, may communicate through molecularly distinct receptors within the same or different dendritic domains.

2.3.5 Localization of NR subunits during development is cell-type specific

We next sought to explore how NRs become localized to synapses during development. NRs could localize directly to the discrete domains where synapses form. Alternatively, NRs could be initially uniformly distributed and subsequently stabilized at synapses, downregulated in incorrect locations, or both. Analysis of whole-animal tagged NR subunits for Rdl-smV5, nAChRβ1-smHA, and GluClα-smV5 showed progressive accumulation of NR subunits in the developing medulla neuropil (Figures S6A-S6D). To address whether this accumulation occurs similarly in different neurons, we turned to single-cell analysis in T4, T5, and L5 medulla neurons, where these NR subunits are expressed throughout pupal development (Figures 4 and S6A).

In sparsely labeled T4 and T5 neurons, Rdl accumulated as large puncta at the proximal region of dendrites at 48h APF, corresponding to the onset of dendrite extension (Figures 4A and

4B). As dendrites extend, Rdl remains enriched proximally with small fainter puncta distributed along their length. At 48 hrs, GluClα and nAChRβ1 puncta are also seen in incipient T4/T5 dendrites, but, over time, disappear from the proximal region of the dendrite and accumulate more distally (Figures 4C-4D and S6E-S6F). This is particularly striking for GluClα. It accumulates throughout T4 and T5 dendrites at 48 and 72 hrs APF, disappears from T5 dendrites (consistent with the lack of glutamatergic inputs to T5) between 72 hrs APF and eclosion, and is retained only in the distal domain of T4 dendrites in the adult (Figures 4C and 4D).

The accumulation of NR subunits in developing L5 neurons was different. In contrast to T4, Rdl puncta were observed throughout L5 terminals in the medulla from 48 hrs through 72 hrs APF but then disappeared from all but a highly restricted domain in medulla layers M1/M2 (Figure 4E). Also, in contrast to T4/T5 neurons, GluClα localized to terminals early, by 48 hrs APF, and this pattern remained into the adult (Figure 4F). To assess the timing of GluClα localization to developing synapses, we imaged GluClα-smV5 in developing L5 neurons with super-resolution using ExLSM. The analysis revealed progressive juxtaposition of GluClα puncta with Brp, as neurons develop from 48h APF to eclosion (Figures S6G-S6I); most GluClα puncta early in development do not cluster with Brp (see arrowheads, Figure S6G). Altogether, different NR subunits localize to dendrites with distinct developmental dynamics and can be cell-type-specific rather than an intrinsic property of a given NR.

2.3.6 A fly homolog of the synaptic adhesion protein ADAM22 forms a complex with GluClα

The exquisite localization of NR subunits to synapses in distinct dendritic domains raised the possibility that proteins associated with different NRs may regulate their localization, contribute to synaptic specificity, or both. As a first step to assessing this possibility, we focus on

GluClα. Using an affinity purification mass-spectrometry (AP-MS) workflow, proteins associated with epitope-tagged versions of GluClα were identified in extracts of fly brains. Two different tagged versions of GluClα and two complementary sets of controls were used (Figure 5A). Mind-meld (Mmd), a single-pass transmembrane protein, was specifically bound with both versions of GluClα (Table S2). Co-IP experiments confirmed that Mmd interacts with GluClα in homogenates of brain tissue but not with Rdl (Figure 5B).

As examined by confocal microscopy, there was a complete overlap in the distribution of Mmd and GluClα (Figure 5C). To assess the role of Mmd in the formation of synapses containing GluClα, we analyzed brains mutant for *mmd*. Strong loss of mmd resulted in a marked reduction in anti-GluClα staining (Figure 5C). Mmd is homologous to mammalian ADAM22, which has been shown to form a complex with AMPA receptors and acts as a synaptic adhesion molecule through its binding to LGI1[47] (Figure 5D). These data raise the possibility that in T4 neurons, GluClα and Mmd form a complex selectively in the distal domain of their dendrites, which, in turn, specifies the pattern of Mi9 inputs. We next sought to directly visualize GluClα and Mmd at these synapses.

2.3.7 Mi9 axons form synapses juxtaposing GluClα and Mmd in distal T4 dendrites

EM studies revealed that seven to nine Mi9 axon terminals, organized into retinotopic columns, are evenly distributed across the proximal, central, and distal domains of T4 dendrites (Figure 6A). Mi9 neurons synapse, however, only onto the distal-most domains[4] (Figure 6A). Other neuron types form synapses within different domains along the proximodistal axis of these dendrites.[4] Mi9 is the only glutamatergic input to T4 dendrites. Here, we applied ExLSM to

achieve sufficient resolution to visualize synapses between Mi9 and T4 dendrites and localize proteins within these synapses.

To detect synapses between Mi9 and T4, we coupled labeling of GluClα in single T4 dendrites with staining of the membranes of Mi9 axon terminals and presynaptic Brp within them (Figures 6A and 6B). Control experiments verified our ability to assign Brp to individual Mi9 terminals and separate them from Brp in other processes in the neuropil (see STAR Methods, Figures S7A and S7B). Consistent with EM studies, presynaptic sites in Mi9 terminals contacting the distal region of T4 dendrites were associated with GluClα expressed in these dendrites, while presynaptic sites of Mi9 terminals overlapping with the middle and proximal domains were not (Figures 6C and S7C-S7E). We next sought to determine whether Mmd also localized with GluClα at synapses between Mi9 and T4 dendrites.

We first confirmed via ExLSM the localization of Mmd and GluClα at synapses using both an antibody to the extracellular domain of Mmd and an antibody to an epitope tag inserted into its cytoplasmic domain (Figures 6D and 6E). To assess the localization of Mmd with GluClα in T4 neurons, we labeled single T4 neurons in which GluClα was selectively tagged with smV5 and co-stained with an anti-Mmd antibody. Each GluClα punctum co-localized with Mmd (Figure 6F). Mmd staining extended beyond anti-GluClα immunoreactivity. This was expected, given that each Mi9 presynaptic site contacts multiple postsynaptic elements from other T4 neurons, and only a single postsynaptic neuron was labeled with tagged GluClα at these synapses.[4] In summary, Mmd localized to the same synapses as GluClα in the distal domain of T4 dendrites juxtaposing Mi9 terminals.

2.3.8 Discussion

In this study, we described a strategy to study single synapses between identified cell types by combining genetic tools, EM-based connectomics, and protein localization through expansion microscopy. To devise probes for specific synapses, we developed tools to tag and map the distribution of endogenous NR subunits of receptors for the major neurotransmitters in *Drosophila* in single neurons and at single synapses between neurons. These studies highlighted the complexity of different NR subunit distributions in dendrites, the developmental dynamics of NR accumulation at different synapses, and their association with other proteins at subsets of synapses. These tagged receptors provide a resource for studies focusing on the subcellular localization of neuronal proteins, the assembly of synapses, and synaptic plasticity. As we discuss below, the unique features of wiring specificity of T4 and T5 dendrites suggest that in some developmental contexts, targeting NRs to discrete dendritic domains provides a spatial map of molecular determinants controlling synaptic specificity.

2.3.9 Mapping NR subunits to specific synapses in single neurons

Our approach to conditionally tag receptors by modifying genomic loci preserves their endogenous mRNA expression levels, patterns, and temporal dynamics. We chose to insert epitope tags into poorly conserved and unstructured regions of variable length within a large cytoplasmic loop found in all cys-loop receptors. The distribution of the tagged NRs accurately reflects the localization of endogenous receptors. Tagged NRs selectively localized at sites adjacent to presynaptic partners (i.e. Brp and Cac) when visualized by either ExLLSM or ExLSM, and the distribution of receptors matched the neurotransmitter specificity of the neurons providing synaptic inputs. The increasing availability of genomes for comparative sequence analysis and the development of structure prediction tools such as AlphaFold[48] facilitate the identification of sites

to successfully tag other classes of NRs and other synaptic proteins. The extensive synaptic connectivity maps in flies, reagents for manipulating specific cell types, and the array of endogenously tagged NR subunits reported here provide an opportunity to characterize the distribution of these receptors in many different circuits regulating a broad range of brain functions and behaviors.

For some NRs, receptor puncta and synaptic inputs identified at the EM level were concordant (i.e. GluClα). For other NRs (e.g. Rdl and nAChRs NR subunits), there was considerable variation between receptor puncta and EM. In some cases, for instance, more Rdl puncta were seen than predicted from EM. This may reflect extrasynaptic receptors or receptor populations within trafficking complexes en route to synapses. By contrast, there were fewer puncta for some nAChR subunits than predicted from EM, and this may reflect mutually exclusive expression of NR subunits in different populations of synapses receiving inputs from different cholinergic neuron types. This is likely to account for the discrepancy between cholinergic inputs inferred from the EM and puncta for single nAChR subunits in T4 and T5 dendrites. Matching different NR subunits to specific presynaptic inputs, as we showed for Mi9 and GluClα, provides a rigorous way to compare EM-based connectomics with light level analysis.

A lack of postsynaptic markers has hindered our understanding of the developmental dynamics of synapse formation in the fly brain. Tagged NR receptors have provided a key set of reagents for exploring this process. We demonstrate that the timing of the localization of different NR subunits to specific dendritic domains is specific to different neuron types. This may result from cell-autonomous mechanisms that direct receptors and associated factors, such as Mmd, to specific neuronal domains. Alternatively, the interaction with presynaptic neuron membrane proteins could influence the timing of clustering of NR subunits in the postsynaptic cell.

Mechanisms that regulate the trafficking of receptors to the plasma membrane could also gate synapse formation in time and space, for instance, by differential internalization of GluClα receptors in T4 and T5 dendrites. Our method of conditionally tagging receptors by modifying the endogenous locus maintains the endogenous mRNA expression levels, patterns, and temporal dynamics of these receptors. With the super-resolution provided by ExLSM, the tagged NR subunits we present are an invaluable resource for investigating the dynamics of synapse formation at fly central synapses.

Different receptors exhibit discrete localization patterns. For instance, the distribution of seven different tagged NR subunits for glutamate, GABA, and acetylcholine in the cys-loop superfamily in direction-sensitive T4 neurons was particularly striking. The stereotyped patterns of each class of receptor matched the pattern of the neurotransmitters used by their respective presynaptic inputs. Unexpectedly, different NRs to the same neurotransmitter are also localized to different domains, receiving input from different presynaptic partners. This was seen for both cholinergic (excitatory) and GABAergic (inhibitory) synapses. The differential distribution of NR subunits to different spatial domains may contribute to the unique computational features of T4 dendrites.[49] How these domains are established in neurons with diverse and often complex morphologies is not known. Perhaps the segregation of proteins to different domains may, at a mechanistic level, share features in common with the establishment of cell polarity domains in other cell types, including apical basal polarity in epithelial cells[50].

Cys-loop GABA receptors that differ in NR subunit composition are found in distinct domains in pyramidal cells of the mouse cortex.[16] It is likely that the complexity of receptor distributions in mammals also extends to different domains within the same dendrites as we have described here. In the mammalian brain, there is a great diversity of the cys-loop family of GABA

receptors (i.e. GABAAR), with 19 distinct genes encoding GABAAR subunits.[16] Thus, tagging approaches in the mouse similar to what we report here in the fly may provide a way to uncover the spatial distributions of NR subunits and combinations of them at different synapses. As these receptors have different physiological properties, their spatial distributions may contribute to understanding information processing in the dendrites of mammalian neurons.

2.3.10 NR subunit diversity and synaptic specificity

Our analysis of T4 neurons raised the intriguing possibility that in some developmental contexts, neurotransmitter receptors may serve as recognition molecules specifying the pattern of pre-synaptic inputs. In these dendrites, each presynaptic neuron type forms synapses within restricted domains along the proximodistal axis[44], and these patterns correspond to the distribution of different NR subunits. Mi9 neurons, for instance, only form synapses within the distal domains of T4 dendrites, while closely related Mi1 and Mi4 neurons form synapses in the middle and proximal regions, respectively. This specificity is particularly striking as the dendritic arbors of many T4s overlap extensively. Each input axon terminal contacts the entire range of dendritic domains and yet makes synapses only within restricted spatial domains (Figure 7). A simple model to account for this specificity is that targeting NR subunits to specific dendritic domains provides a spatial map of molecular signposts recognized by cell surface recognition proteins selectively expressed on the surface of different presynaptic terminal arbors. Alternatively, specific molecular determinants may be arranged along the proximodistal axis in discrete dendritic domains, and these may recruit both synaptic inputs and subsets of NR subunits to these sites. In either case, our studies suggest a close relationship between the targeting of NR subunits to different spatial domains and the specificity of synaptic inputs.

This model is consistent with studies in mammals. NRs have been shown to associate with other postsynaptic proteins that promote adhesion between pre, and postsynaptic membranes, and these complexes may be selectively localized.[51,52] Here, for instance, we report the identification of a transmembrane protein, Mmd, in the distal domains of T4 dendrites in close association with the GluClα receptor. A mammalian homolog of Mmd, Adam22, also co-localizes to synaptic glutamate receptors, albeit of a different class, and promotes adhesion between presynaptic and postsynaptic membranes[47,53,54] (Figure 5D). Alternatively, there is evidence that the extracellular domains of NR subunits can directly interact with proteins on the presynaptic membrane. For instance, the extracellular domain of the iGluR subunit GluA1 can interact with presynaptic neuronal pentraxin receptors, and this interaction can support the formation of synapses in a heterologous system.[55] Similarly, the N terminal of the α1 GABAAR subunit has been shown to interact with neurexin-2β and modulate GABAAR function.[56] Together, these observations raise the notion that, in some cases, the NR subunits are intimately involved in matching pre and postsynaptic membranes.

2.3.11 Perspective

The complexity of neural circuit structure has become increasingly clear with the completion of dense EM connectomes.[1–5] Extensive studies have argued that different domains along the proximo-distal axis of T4 dendrites play a crucial role in direction-specific motion processing.[49,57,58] The identification of different NRs and combinations of them within different domains provides an opportunity to understand computations at the molecular level.

How these specific molecular domains in dendrites form and their patterns of synaptic inputs emerge during development remains enigmatic. Localization of NR subunits to different domains at early stages of dendrite development raises the possibility that this molecular diversity

contributes to determining the spatial distribution of specific synapses in dendrites. The use of tagged NRs and cell type-specific manipulation with EM-based connectomics, ExLSM, genetics, and biochemical methods provides a way of understanding how NRs become localized to specific domains and linking these to the specificity of synaptic inputs.

2.4 Acknowledgments

We thank members of the Zipursky laboratory for their feedback on the manuscript. We thank M. DeSantis, D. Alchor of the Advanced Imaging Facility, and K. Close, C. Christoforou, Y. He, A. Hu, and P. Tillberg at the Janelia Research Campus for assistance and advice on the acquisition and analysis of ExLLSM and confocal microscopy data. We thank Gokul Upadhyayula for advice on ExLSM image analysis. We thank Nathan Hwangbo of the Statistical Consulting Center of the UCLA Department of Statistics for assistance with statistical analysis. Reagents kindly provided by A. Nern, H. Hama, R. Davis, L. Luo, and M. Silies, as well as the Bloomington Drosophila Stock Center, were critical for this work. Funding for this study in J.A.W laboratory was supported by the NIH (GM089778). This project was supported by an NIH BRAIN initiative grant (1RF1MH117823-01) in S.L.Z. laboratory, by the Howard Hughes Medical Institute in Y.A. laboratory, and by the Janelia Visiting Scientist Program. S.L.Z. is an investigator of the Howard Hughes Medical Institute.

2.5 Author Contributions (CRediT)

Conceptualization: P.S., S.L.Z.. Formal Analysis: Y.A., A.B., A.K., V.P., P.S., J.A.W.. Investigation: Y.A., H.B., A.B., P.G., A.K, Parmis, S.M., Pegah, S.M., V.P., P.S., J.Y., A.Y.. Methodology: Y.A., A.B., A.K., V.P., P.S., J.A.W.. Software: Y.A., A.K., V.P., P.S.. Supervision:

Y.A., H.-S.L., J.A.W, S.L.Z.. Visualization: Y.A., A.B., A.K., P.S.. Writing – original draft: P.S., S.L.Z. Writing – review & editing: A.K., P.S., S.L.Z.

2.6 Declaration of Interests

The authors declare no competing interests.

2.7 STAR Methods

2.7.1 Resource Availability

Lead contact

All requests for additional information and reagents should be directed to and will be fulfilled by the lead contact, S. Lawrence Zipursky (lzipursky@mednet.ucla.edu).

Materials availability

Flies generated in this study have been deposited to the Bloomington Drosophila Stock Center. Plasmids have either been deposited to Addgene or are available upon request.

Data and Code Availability

All data reported in this paper will be shared by the lead contact upon request. This paper does not report original code. Any additional information required to reanalyze the data reported in this paper is available from the lead contact upon request.

2.7.2 Experimental Model and Subject Details

2.7.2.1 Fly husbandry

Drosophila melanogaster was reared on cornmeal/molasses medium at 25°C in a humidity-controlled incubator. Females were dissected for experiments unless otherwise noted. White

prepupae were collected for developmental studies and designated as 0h after pupal formation (APF). Stocks used and generated in this study are listed in the key resources table. Genotypes used in each figure panel and related immunofluorescence staining conditions are reported in Table S3. Transgenic flies were generated by integrating DNA constructs into specific landing sites, while targeted alleles were created through CRISPR-mediated homologous recombination, as described below. This was carried out using a commercial injection service (BestGene, Inc.).

2.7.3 Method Details

2.7.3.1 Identification of NR subunit genes

NR subunit gene numbers were obtained from https://www.genenames.org (human), https://www.informatics.jax.org (mouse) or https://www.flybase.org (fly).[62–64] For each organism, Cys-loop NR subunits, iGluR subunits, and GPCR neurotransmitter receptor subunits were compiled. GPCRs responding to neuropeptides were omitted from the counts.

2.7.3.2 Selection of tag insertion sites

All tags were inserted within the unstructured intracellular loop between the third (M3) and fourth (M4) transmembrane domains. In addition, we chose insertion sites that were poorly conserved and favored ones with evidence of sequence insertion in other species. We generated sequence alignments with the Clustal Omega program in UniProt (https://www.uniprot.org/align).[65] Closely related (e.g., *D. yakuba*) and distantly related (e.g., *T. castaneum*) insect species were used for alignment. The insertion sites are indicated in Figure S1 and summarized in Table S1. Species abbreviations - DROME: *Drosophila melanogaster;* DROSE: *Drosophila sechellia;* DROSI: *Drosophila simulans;* DROYA: *Drosophila yakuba;* DROAN: *Drosophila ananassae;* DROPS: *Drosophila pseudoobscura;* DROPE: *Drosophila*

persimilis; DROWI: *Drosophila willistoni;* DROMO: *Drosophila mojavensis;* DROGR: *Drosophila grimshawi;* AEDAE: *Aedes aegypti;* ANOGA: *Anopheles gambiae;* CULSO: *Culicoides sonorensis;* TRICA: *Tribolium castaneum*.

2.7.3.3 Molecular biology

2.7.3.3.1 *Generation of conditional tag cassettes*

We generated a conditional tag cassette, pBS-KDRT-STOP-loxP-3XP3::dsRed-loxP-STOP-KDRT-smGFPTag, for the tags smGdP-10XV5, smGdP-10XHA, and smGdP-10XOllas. To generate the cassette, we used a combination of restriction enzyme-based cloning and HiFi DNA Assembly (NEB cat #E2621). First, we replaced the sequence between MluI and MfeI in KDRT-STOP-STOP-KDRT from pJFRC164 (Addgene plasmid #32141) with loxP-3XP3::DsRed-loxP from pHD-DsRed-attP-w+ (Addgene plasmid #80898). The 3xP3::DsRed marker allowed easy screening for successful genomic insertions, which are subsequently removed by germline expression of Cre recombinase. Next, we added a *Drosophila* codon-matched GS linker and the coding sequence for each tag downstream of KDRT. We cloned the sequence for each tag from the following plasmids: pJFRC206 (Addgene plasmid #63168) for smGdP-10XV5, pJFRC201 (Addgene plasmid #63166) for smGdP-10XHA, and pJFRC210 (Addgene plasmid #63170) for smGdP-10XOllas. To place the first KDRT sequence in frame, the cassette was preceded by the dinucleotide GG to encode a glycine with the first nucleotide of the KDRT sequence, and then the entire cassette was cloned into pBlueScriptII KS(-) (Agilent Cat# 212208) between PciI and XbaI. A second PciI site was inserted upstream of XbaI to facilitate cassette linearization in subsequent steps. All plasmids were sequence validated by Sanger sequencing. smGdPTag encodes a GFP protein with 10X epitope tags distributed amongst the C and N termini and one of the loops.[66] In addition to the inserted tags, the GFP sequence of smGdP contains amino

acid substitutions that render GFP non-fluorescent (GdP: fluorescence dead GFP[67]). For simplicity, we refer to smGdPTag throughout the study as smGFP-Tag or smTag.

We generated a conditional 1XALFA cassette by replacing smGdP-X from pBS-KDRT-STOP-loxP-3XP3::dsRed-loxP-STOP-KDRT-smGFP-Tag with Drosophila codon-optimized 1XALFA followed by a GS linker. ALFA-tag is a commercially developed epitope tag that forms a small and stable α-helix and is recognized by a high-affinity nanobody.[68] Detailed protocols are available upon request. The plasmids and sequences have been deposited in Addgene.

2.7.3.3.2 Generation of pU6-gRNA

We identified gRNA target sequences that cut within 1-11 nt of the selected insertion site with an efficiency score above 5, as defined by the CRISPR Efficiency Predictor (https://www.flyrnai.org/evaluateCrispr/). The gRNA sequence oligos were synthesized (Integrated DNA Technologies) with the forward oligo having a TTCG overhang at the 5' end and the reverse oligo having an AAAC overhang added to the 5' end for subsequent ligation into pU6. After annealing, the oligos were ligated into BbsI-linearized pU6b-sgRNA-short[69]. All pU6 vectors generated were verified by Sanger sequencing. The gRNA sequences used in this study are listed in Table S1. gRNA1, used for generating alleles using short homology arms[31] (see below), was cloned into pU6 as described for gene-specific gRNAs.

2.7.3.3.3 Generation of donor constructs

The generation of donor constructs involved two different methods for different sets of alleles. For the first set, long homology arms of approximately 1kb were used for homologous recombination of the conditional tag cassette. To improve cloning efficiency as well as donor integration by homologous recombination, we took advantage of a second method that employs shorter homology arms of around 100bp in combination with in vivo directed linearization of the

donor vector, as described.[31] This strategy was used to generate alleles of Grd, CG8916, and nAChRα3, as well as the 1XALFA tagged allele of GluClα.

For the generation of alleles using long homology arms, we employed HiFi DNA assembly (NEB Cat# E2621) to assemble the donor constructs. The long homology arms (~1kb) were PCR amplified and inserted into pHD-DsRed-attP-w+ (Addgene plasmid #80898), which was linearized with XhoI and EcoRI. The tag cassette was introduced by cloning in the PciI linearized conditional tag cassette of choice. For smGFP tags, we included a GS linker in the primer used to generate the 3' homology arm. In contrast, the 1XALFA tag contains the GS linker within the conditional cassette. All pHD-geneX donor plasmids were sequence validated. Single nucleotide polymorphisms (SNPs) were permitted in intronic regions and in coding regions only when leading to synonymous codon substitutions from the dm6 reference genome.

For the generation of alleles using short homology arms, we utilized HiFi DNA assembly (NEB Cat# E2621) with two steps. In the first step, we synthesized the donor homology arms into pUC57-Kan (Genewiz, Inc.), with each of the two ~125bp homology arms flanked on the outside by gRNA1 target and PAM sequences and DNA assembly-specific homology arms matched to the chosen PciI linearized conditional cassette. The two arms were separated by a random sequence linker flanked by restriction sites that were absent in the homology arms. We included a GS linker in the synthesized sequence for the generation of donors with smGFP tags, while the 1XALFA conditional cassette included the GS linker within the cassette. In the second stage, we linearized pUC57-Kan-geneX with restriction enzymes recognizing the sites within the linker and cloned in the PciI linearized fragment that encoded the required conditional cassette using HiFi DNA assembly (NEB Cat# E2621). All donor vectors were confirmed by Sanger sequencing. Plasmids and sequences are available upon request.

2.7.3.3.4 Generation of pJFRC-10XUAS-FRT-STOP-FRT-myrFP-2A-KDR::Pest

HIFI DNA assembly (NEB Cat# E2621) was used to generate either 10XUAS-FRT-STOP-FRT-myr::GFP-2A-KDR::PEST or 10XUAS-FRT-STOP-FRT-myr::tdTomato-2A-KDR::PEST. The GFP coding sequence of pJFRC177[70] (Addgene: 10XUAS-FRT-STOP-FRT-myrGFP, plasmid #32149) was replaced either by GFP-2A (cassette C: GS linker-FRT-STOP-FRT-GFP-2A-LexAVP16(Y. Chen et al., 2014a)or tdTomato-2A (UAS-DIPalpha-2A-tdTomato[72]), both followed by the coding sequence of KDR::PEST recombinase from pJFRC161[70] (Addgene: 20XUAS-IVS-KD::PEST plasmid #32140). Plasmids are available in Addgene.

2.7.3.3.5 Generation of pJFRC-13XlexAoP-10XUAS-FRT-STOP-FRT-myrFP-2A-KDR::Pest

A combination of HIFI DNA assembly (NEB) and restriction enzyme-based cloning was used to generate 13XLexAoP2-FRT-STOP-FRT-myr::GFP-2A-KDR::PEST through modification of pJFRC177 [70] (Addgene: 10XUAS-FRT-STOP-FRT-myrGFP, plasmid #32149). First, the 10XUAS sequence of pJFRC177 was replaced by 13XLexAoP2 from pJFRC19[38] (addgene:13XLexAoP2-IVS-myrGFP, plasmid #26224). Second, the GFP coding sequence of pJFRC177 was replaced either by GFP-2A (cassette C: GS linker-FRT-STOP-FRT-GFP-2A-LexAVP16[71]) followed by the coding sequence of KDR::PEST recombinase from pJFRC161[70] (Addgene: 20XUAS-IVS-KD::PEST plasmid #32140). Plasmids are available in Addgene.

2.7.3.3.6 Generation of pJFRC-5XUAS-GluClα-1XALFA and pJFRC-5XUAS-Rdl-1XALFA

We synthesized the coding sequence of GluClα-RM (protein isoform FBpp0307404 in FB2023_05) and Rdl-RA (protein isoform FBpp0076261 in FB2023_05). These sequences included a GS linker-1xALFA tag, which were placed at the same locations as in the respective conditionally tagged alleles (Table S1). The fragments were cloned into pJFRC5 (Addgene: 5XUAS-IVS-mCD8::GFP #26218), by replacement of the mCD8::GFP coding sequence.

Synthesis and cloning were carried out by Genewiz, Inc.. Plasmids and sequences are available upon request. Flies were generated by injecting plasmid into embryos for recombination into attP5 sites by BestGene, Inc..

2.7.3.4 Generation of tagged NR subunit alleles

For alleles generated using donor vectors with long homology arms, pHD-geneX donor plasmid, and pU6-geneX-gRNA were injected into flies expressing Cas9 in the germline by BestGene Inc. Successful integration of the donor cassette was identified through the expression of DsRed in the eyes and negative for expression of mini-white in the eye. The resulting flies were PCR-validated for correct insertion within the selected insertion site (Table S1). To generate the conditional tagged allele, we crossed flies to a line expressing Cre recombinase (RRID:BDSC_1092) to excise loxP-flanked DsRed from the STOP cassette within the targeted allele (Figure S1C). To generate the whole fly constitutively tagged allele, we crossed the conditional tagged allele to a line expressing KD recombinase in the germline (w; 3XUAS-KDR; nos-gal4::VP16; RRID:BDSC_1092 and RRID:BDSC_4937) to excise the KDRT flanked STOP cassette upstream of the tag within the targeted allele. Resulting conditional and whole fly constitutively tagged alleles were balanced. When the whole fly constitutively tagged allele was not homozygous viable, we backcrossed flies three times with w1118 to clean out any off-target CRISPR events that could underlie lethality. We were not able to outcross homozygous lethality for Rdl-KDRT-smV5, Rdl-KDRT-smHA, and GluClα-KDRT-smV5. To test if lethality was due to the insertion of the tag within the NR subunit locus or to off-target CRISPR-induced mutations, we tested viability over deficiency lines (Rdl Df: RRID:BDSC_8066, GluClα Df: RRID:BDSC_8964) or loss of function alleles for Rdl (Rdl^{1}, RRID:BDSC_1687). As these animals were viable, lethality in homozygous animals does not reflect disruption of receptor

function due to the tag. All tagged alleles were sequence validated to confirm the correct cassette excision. SNPs were allowed in intronic regions and in coding regions only when resulting in synonymous codon substitutions.

When generating alleles using short homology arms, pUC57-geneX donor plasmid, pU6-geneX-gRNA, and pU6-gRNA1 were injected into flies expressing Cas9 in the germline by BestGene Inc. Generation of flies was carried out as described above with the exception that flies were only screened for expression of DsRed in the eye. Conditionally tagged and whole fly tagged alleles of NR subunits were generated as described above.

2.7.3.5 Guidance for optimal sample processing and imaging of NR subunits in single neurons

The detection of endogenously tagged protein in single neurons requires optimal imaging and staining to achieve sufficient Signal-to-Noise Ratio (SNR) for the detection of receptor puncta in single neurons. In our experience, primary antibodies against V5 and HA provide the best SNR, making these epitopes preferable for tagging low-abundance proteins. Secondary antibodies often show significant lot-to-lot variability in SNR. Due to the lot-to-lot variation in polyclonal secondary antibodies, we recommend testing multiple antibodies to identify those with optimal SNR. We have summarized the antibodies used in this study and provided information on combinations that, in our experience, resulted in the best SNR (Table S4). It is also important to note that, as previously reported[73], immunostaining of many NR subunits is often unsuccessful using conventional 4% PFA fixation. To address this, we have developed a robust protocol employing acid-free glyoxal supplemented with sucrose (addaxS). This method enables robust detection of NR subunit puncta and ensures optimal preservation of neuronal morphology. We have also successfully used a previously published protocol for glyoxal fixation[74], which is

comparable to addaxS for the detection of receptor puncta, but provides decreased preservation of fine neuronal processes, such as the dendrites of T4 neurons.

Optimal imaging conditions are crucial for achieving the best SNR and the resolution necessary to resolve receptor puncta while minimizing bleaching. Mounting samples in DPX is optimal for imaging with high numerical aperture (NA) objectives due to its matched refractive index and sample clearing properties, which are essential for detecting receptor puncta with the necessary resolution. In our experience, Airyscan played a crucial role in enhancing SNR and imaging resolution, enabling robust detection of NR subunits puncta with reduced sample bleaching. In contrast, conventional confocal microscopy often proved inadequate for visualizing these puncta, and when detected, they frequently underwent rapid bleaching. We provide details of mounting and imaging settings to achieve optimal Airyscan imaging, which are key to achieving robust imaging of NR puncta in single neurons (e.g. use of high-precision coverslips, DPX mounting, etc.). Additionally, ExLSM also improves SNR over conventional confocal microscopy due to the substantial reduction in background signal."

2.7.3.6 Tagging of NR subunits in single neurons

Sparse labeling of cells was achieved as outlined in Figure S4B. To achieve sparse labeling of cells, we optimized the timing of heat shock to mediate Flp-out of the FRT-STOP-FRT (FSF) cassette from 10XUAS-FSF-myrFP-2A-KDR::Pest. To achieve sparse labeling of neurons found in each column or more than one per column, we used a less efficient variant of hsFlp (hsFlpG5::Pest(Opt); RRID:BDSC_77140). 0-24h APF pupae carrying hsFlp, 10XUAS-FSF-myrFP-2A-KDR::Pest, the cell type-specific GAL4 and the endogenous conditionally tagged allele of the NR subunit of interest (or more than one allele if more than one receptor was investigated, see Figures S5G-S5I), were heat-shocked at 37°C (Tm3:15 min, T4T5: 8-12 min, L5:

8 min) and subsequently reared at 25°C. The degree of labeled cells is very sensitive to small changes in time and temperature. The conditions for labeling were empirically established for every GAL4 driver. Brains for analysis were dissected from 1-5 day old flies. For developmental studies of NR subunit expression in T4/T5 and L5 neurons, the same procedure was followed as above, and brains were dissected at either 48h APF or 72h APF.

Expression of 5XUAS-GluClα-ALFA and 5XUAS-Rdl-ALFA in single T4 neurons (Figures S1A and S1B) was carried out using mosaic analysis with a repressible cell marker (MARCM).[75] 0-24h pupae were heat-shocked for 2 min at 37°C. ALFA-tagged constructs and myr::GFP were expressed in a restricted manner within single-cell clones under GAL4-UAS and were stained accordingly (see Table S3 for genotypes).

2.7.3.7 Immunostaining

For adult fly brains, 1-5 day old flies were decapitated, and the brain was dissected in ice cold Schneider Medium (SM) (Gibco, Cat# 21720001). Up to three brains were kept on ice in SM prior to fixation in a single well of a Terasaki plate (Thermo Scientific, Cat# 163118). All subsequent steps were carried out in Terasaki plates. Brains were fixed overnight at 4°C in glyoxal acid-free fixative (Addax Biosciences, Cat# VI25) supplemented with 5% (w/v) sucrose (addaxS) or in a fixative containing 3% glyoxal at pH 5.0 (3% glyoxal fixative)[74], as indicated in Table S3. When fixed with 3% glyoxal fixative, brains were fixed for 30 min at room temperature, followed by 30 min quenching in 0.1 M NH_4Cl. Fixation in acid-free glyoxal with 5% sucrose improves the preservation of fine neuronal morphology compared to 3% glyoxal fixative. Both fixatives improve immunostaining of NR subunits and Bruchpilot, compared to standard 4% PFA in PBS (some NR subunits, such as nAChRα7, cannot be visualized upon 4% PFA fixation). After fixation, brains were washed 3X and incubated for 2 hours at RT in PBSTX (PBS with 0.5% (v/v)

Triton X-100 (Sigma Aldrich Cat# T8787) with the addition of 10% normal goat serum (PBSTN) (Sigma-Aldrich Cat# G6767). Brains were incubated for 2-3 days at 4°C with primary antibody mix in PBSTN, subsequently washed 2X 2hrs with PBSTX, and further incubated 2-3 days overnight with secondary antibodies in PBSTN. The secondary antibody was washed out by incubating brains 2X for 2 hrs in PBSTX and subsequently mounted as described below.

The following primary antibodies and concentrations were used for samples imaged using confocal microscopy. Rabbit anti-nAChRα6[73] (1:1,000), rat anti-nAChRα7[76] (1:1,000), rabbit anti-Rdl[77] (1:100), rabbit anti-GluClα (raised against a peptide from *Musca domestica* GluCl[78], which is conserved in D. melanogaster, 1:500), rabbit anti-Mmd (1:500 Guo et al., manuscript under preparation), rabbit anti-Ollas (1:10,000; GenScript, Cat# A01658), rat anti-Ollas (L2, Novus Biologicals Cat# NBP1-06713, RRID:AB_1625979), rat anti-HA (3F10, Roche Cat# 11867423001, RRID:AB_390918), mouse IgG2a anti-V5 (SV5-Pk1, 1:500; abcam Cat# ab27671, RRID:AB_471093), chicken anti-V5 (1:500, abcam Cat# ab9113, RRID:AB_307022), mouse anti-V5-Tag:DyLight®550 (Bio-Rad Cat# MCA1360D550GA, RRID:AB_2687576), FluoTag X2 anti-ALFA::Atto488 (1:500; NanoTag Biotechnologies, Cat# N1502-At488), FluoTag X2 anti-ALFA::Alexa Fluor 568 (1:500; NanoTag Biotechnologies, Cat# N1502-AF568), FluoTag X4 anti-RFP::AZDye568 (1:500; NanoTag Biotechnologies, Cat# N0404-AF568), rabbit anti-DsRed (1:200, Takara Bio Cat# 632496, RRID:AB_10013483), guinea pig anti-RFP (1:1,000, Synaptic Systems, Cat# 390004, RRID:AB_2737052) and chicken anti-GFP (1:1000, abcam Cat# ab13970, RRID:AB_300798). Secondary antibodies were used at 1:500 for confocal microscopy. From abcam: Alexa Fluor 488 goat-anti-rat (Cat# ab150165, RRID:AB_2650997), Alexa Fluor 568 goat-anti-rat (Cat# ab175710, RRID:AB_2832918), and Alexa Fluor 488 goat-anti-rabbit (Cat# ab150081, RRID:AB_2734747). From Biotium: CF405S goat-anti-mouse IgG1 (Cat #

20380), CF633 goat-anti-rabbit (Cat# 20123-1, RRID:AB_10853138) and CF633 goat-anti-mouse (Cat# 20341). From Invitrogen: Alexa Fluor 488 goat-anti-mouse (Cat# A-11029, RRID:AB_2534088), Alexa Fluor 568 goat-anti-mouse IgG1 (Cat# A-21124, RRID:AB_2535766), Alexa Fluor 488 goat-anti-mouse IgG2a (Cat# A-21131, RRID:AB_2535771), Alexa Fluor 546 goat-anti-mouse IgG2a (Cat# A-21133, RRID:AB_2535772), Alexa Fluor 568 goat-anti-guinea pig (Cat# A-11075, RRID:AB_2534119), Alexa Fluor 488 goat-anti-rabbit (Cat# A-11034, RRID:AB_2576217), Alexa Fluor 568 goat-anti-rabbit (Cat# A-11036, RRID:AB_10563566), Alexa Fluor 647 goat-anti-rabbit (Cat# A-21244, RRID:AB_2535812), Alexa Fluor Plus 488 goat-anti-chicken (Cat# A32931, RRID:AB_2762843), and Alexa Fluor 488 goat-anti-chicken (Cat# A32931, RRID:AB_2762843). From NanoTag Biotechnologies: Atto 647N FluoTag X2 anti-mouse IgG1 (Cat# N2002-Atto647N) and AbberiorStar635P FluoTag X4 anti-rabbit (Cat# N2404-Ab635P). From Jackson ImmunoResearch Labs: Alexa Fluor 488 goat-anti-rat (Cat# 112-545-167, RRID:AB_2338362), Alexa Fluor 488 goat-anti-chicken (Cat# 103-545-155, RRID:AB_2337390) and Alexa Fluor 488 goat-anti-mouse (Cat# 115-545-166, RRID:AB_2338852).

2.7.3.8 Tagging of NR subunits in neurons of the mushroom body

The genotype used for tagging NR subunits in single neurons of the mushroom body is reported in Table S3. A 2 hr heat shock at 24-48 hrs APF was chosen to generate single neuron labeling. Dissection and immunohistochemistry of fly brains were carried out as previously described with 3% Glyoxal fixative instead of 2% PFA[37] using the antibodies listed in Table S3. Brains of 5-day-old female flies were dissected in Schneider's insect medium and fixed in 3% Glyoxal fixative (3% v/v glyoxal (Sigma-Aldrich, Cat# 128465), 5% v/v ethanol, 0.75% v/v acetic acid, pH 5.0) for 2 hr at room temperature (RT). The samples were quenched in 0.1M NH_4Cl for

30 min, followed by four washes in PBT (0.5% Triton X-100 in 1x-PBS), 10 min each. After washing in PBT, tissues were blocked in 5% normal goat serum (or normal donkey serum, depending on the secondary antibody) for 90 min. Subsequently, tissues were incubated in primary antibodies diluted in 5% serum in PBT for 2 days on a nutator at 4°C, washed four times in PBT for 30 min, then incubated in secondary antibodies diluted in 5% serum in PBT for 2 days on a nutator at 4°C. Tissues were washed thoroughly in PBT four times for 30 min or longer.

2.7.3.9 Sample mounting for confocal microscopy

Samples were mounted using either DPX mountant (EMS, Cat# 13510) as previously described[67] or Everbrite mounting medium (Biotium, Cat# 23001), as denoted in Table S3. DPX facilitates the imaging of neurons deep in the brain. The refractive index of DPX matches the refractive index of the immersion oil used with high NA objectives, facilitating higher resolution achievable using Airyscan.

2.7.3.10 Confocal microscopy

All confocal images were acquired on a Zeiss LSM880 with 405 nm, 488 nm, 561 nm, and 633 nm lasers. Images were acquired with a Plan-Apochromat 63x/1.4 Oil DIC M27 objective for single cell and whole brain imaging or a Plan-Apochromat 40xx/1.2 Imm Korr DIC M27 for whole optic lobe imaging (Figure S1).

Airyscan was used in conjunction with 63X objective imaging in RS mode to maximize signal capture and increase resolution compared to conventional confocal imaging. All samples were imaged using precision cover glasses with #1.5H thickness (Thorlabs, Cat# CG15CH2), and the Airyscan detector alignment was verified and adjusted prior to imaging each sample. Frame size and Z step were optimal to achieve maximal resolution. Images were processed using Zen Blue 2.3 with Airyscan processing set to auto-filter and 3D processing.

2.7.3.11 ExLLSM sample preparation and imaging

The samples for Expansion Microscopy (ExM) were dissected, fixed, and immunostained as stated for neurons of the mushroom body, and staining was done sequentially to avoid cross-reactivity. All samples were processed using a protein retention ExM protocol with minor modifications.[79,80] All solutions were prepared in milliQ-grade water unless otherwise stated: AcX stock (acryloyl-X, SE Invitrogen, A20770) at 10 mg/mL in anhydrous DMSO (Sigma-Aldrich, Cat # 276855); PLL solution (Ted Pella, Cat# 18026) with Photo-Flo detergent (EMS, Cat# 74257) added 1:500 (v/v); Acrylate stock at 4M, prepared by neutralizing 5.5 mL acrylic acid (99% purity; Sigma-Aldrich, Cat# 147230) with 10N NaOH using a water bath and fume hood, in a total volume of 20mL[81]; Acrylamide stock at 50% (w/v) (Sigma-Aldrich, Cat# A9099); and Bis-acrylamide stock at 1% (w/v) (Sigma-Aldrich, Cat# M7279). Monomer stock: 11.5 mL sodium acrylate stock, 2.5 mL acrylamide stock, 7.5 mL bis-acrylamide stock, 18 mL 5 M NaCl (Sigma-Aldrich, Cat# S5150), 5 mL 10xPBS (Gibco, Cat# 70011044), and 2.5 mL water for a total volume of 47 mL. 4HT stock: 4-hydroxy-TEMPO at 0.5% (w/v) (Sigma-Aldrich, Cat# 176141). TEMED stock: N,N,N′,N′-Tetramethylethylenediamine at 10% (v/v) (Sigma-Aldrich, Cat# T7024). APS stock: ammonium persulfate at 10% (w/v) (Sigma-Aldrich, Cat# A3678). ProK digestion buffer: 0.5% Triton X-100, 500 mM NaCl, 1 mM EDTA, and 50 mM Tris pH8. Appropriate caution was exercised when handling acrylamide, a known toxin.

Dissected, fixed, and immunostained samples were treated with AcX stock solution diluted 1:100 in 1xPBS overnight. Brains were then washed with 1xPBS. A gelation chamber was created by applying a Press-to-Seal silicone gasket (Invitrogen, Cat# P24740) to a glass slide, which was then coated with the PLL solution. AcX-treated brains were immobilized on the PLL surface, up to nine per gasket. Gelation solution was prepared just before gelation to prevent premature gel

polymerization on ice by adding 10 µL each of 4HT, TEMED, and APS stock solutions to 470 µL of monomer stock solution. Brains were washed with gelation solution, and then the gelation chamber was filled with ~200 µL of gelation solution and incubated on ice for 25 min. The gelation chamber was then sealed with a cover slip and placed in a 37°C incubator to gel and cure for 2 hr.

Gelation chambers were disassembled, and individual gels were trimmed close to each brain. Gels were trimmed to a right trapezoid shape to ease specimen orientation. Gels were incubated with proteinase K (NEB, Cat# P8107S) diluted 1:100 (v/v) in proK digestion buffer with shaking overnight at room temperature. Digested gels were stained in 500 ng/mL DAPI in PBS for 30 min, followed by four washes with water for 30min each, followed by equilibration overnight. Prepared ExM samples were stored in 1xPBS at 4°C for a week. The samples were expanded in MilliQ water for 3 hours for optimum expansion before imaging by LLSM. Samples expanded ~4.65x. All samples were scanned within 3-5 hr of expansion.

All ExM samples were imaged in objective scan mode as described[23] with minor modifications. For all imaging sessions, focus was maintained by periodic imaging of reference beads. The region of interest was identified by scanning the Brp channel with minimal exposure and acquired as a single tile of 1024x1024x501 voxels.

2.7.3.12 ExLSM sample preparation and imaging

2.7.3.12.1 Tissue staining and expansion for ExLSM

Tissue for ExLSM was expanded as described above with the following modifications. Fixation and staining of samples for ExLSM were performed with increased concentration of primary and secondary antibodies compared to samples prepared for confocal microscopy (see Table S3). Brains were incubated in gelation solution for 30 minutes at 4°C prior to transfer to the gelation chamber. Digested samples were washed in 1X PBS and stained with 1:1000 DAPI

(Sigma-Aldrich, Cat# D9542) in 1X PBS for 30 minutes at room temperature unless antibodies with 405-dye conjugate were used. Samples were expanded to ~4X in autoclaved Milli-Q water at room temperature before mounting onto PLL-coated coverslips that were subsequently bonded with Bondic UV-curing adhesive (Bondic starter kit, Bondic) onto a custom fabricated sample holder (Janelia Tech ID 2021-021) to be suspended vertically in the imaging chamber. Mounted samples were imaged in 1mM Tris Base (Fisher Scientific, Cat# BP152-500) in MilliQ water after a minimum of 2 hours of incubation at room temperature or overnight at 4°C. Unexpanded gels were stored at 4°C in 1X PBS + 0.02% sodium azide (Sigma-Aldrich, Cat# S8032) for up to 10 days before expansion and imaging.

2.7.3.12.2 Light-sheet imaging on Zeiss LS7

Images were acquired on a Zeiss LS7 microscope equipped with 405 nm, 488 nm, 561 nm, and 638 nm lasers. Illumination optics with a 10x/0.2 NA were used for excitation (Zeiss, Cat# 400900-9020-000). Detection was performed using a W Plan-Apochromat 20x/1.0 DIC M27 water immersion objective (Zeiss, Cat# 421452-9700-000). The LS7 optical zoom was set to 2.5x, resulting in a total magnification of 50x. CF405S and AF546 dyes were simultaneously excited by the 405 nm and 561 nm laser lines, and emission light was separated by a dichroic mirror SBS LP 510 with emission filters BP 420-470 (Zeiss, Cat# 404900-9312-000) and a modified BP 527/23 (Chroma, Cat# ET672/23m). Similarly, AF488 and SeTau647 dyes were simultaneously excited via 488 nm and 638 nm, and the emission was split through a dichroic SBS LP 560 with emission filters BP 505-545 and LP 660 (Zeiss, Cat# 404900-9318-000). As the final pair, AF568 and SeTau647 dyes were excited together via the 561 nm and 638 nm laser lines, and emission was filtered by a dichroic SBS LP 640 with emission filters BP 575-615 and LP 660 (Zeiss, Cat# 404900-9322-000). To eliminate laser transmission, a 405/488/561/640 laser blocking filter (Zeiss,

Cat# 404900-9101-000) was added to the emission path. Images were captured using dual PCO.edge 4.2 detection modules (Zeiss, Cat# 400100-9060-000) with a 50 msec exposure time. Filter and camera alignment were manually calibrated prior to each imaging session. Image volumes were acquired at optimal Z-step and light-sheet thickness, and the Pivot Scan feature was used to reduce illumination artifacts by sweeping the light-sheet in the xy-plane. The LS7 microscope was operated using ZEN Black 3.1 (v9.3.6.393).

2.7.3.13 Affinity purification and mass spectrometry

To define GluClα interactors, we used affinity purification and mass spectrometry (Figure 5A). To increase confidence of true interactor identification, we used two different tagged alleles of GluClα (GluClα-smV5 or GluClα-ALFA) and defined putative interactors as the factors that were identified in mass spectrometry of the immunoprecipitation (IP) with matched nanobody to that of the tag (ALFA or V5) (V5, ProteinTech, Cat# v5tma, ALFA selector, NanoTag Biotechnologies, Cat# N1515). As a negative control, we used the same nanobodies against the unmatched tagged allele (e.g., ALFA nanobody with GluClα-smV5 samples). Each set of conditions was done in biological triplicate (Figure 5A). We used stringent criteria to identify GluClα interactors where a putative interactor had to be significantly enriched in both experimental conditions over the negative controls (Figure 5A). In this way, we identified the GluClα interactor Mmd (Table S2).

Immunoprecipitation was performed on 2-10 day old flies of either GluClα-smV5 (w;; GluClα-smV5/+) or GluClα-ALFA (w;; GluClα-1XALFA/+) genotype, which were previously frozen in liquid nitrogen and stored at -80°C. For each pulldown, 10 ml of frozen flies were sieved using a Bel-Art mini-sieve (Bel-Art, Cat# F378451000). Heads were pulverized in liquid nitrogen using a liquid nitrogen chilled mortar and pestle (Fisher Scientific, Cat# FB961C & FB961M) and

further homogenized in 1.5 ml of lysis buffer (50 mM Tris HCl (pH 7.6), 150 mM NaCl, 10% glycerol, protease inhibitor (cOmplete mini, Roche, Cat# 11836153001) using a Potter-Elvehjem tissue grinder (Cole Parmer, Cat # EW-04468-14) with 10 strokes at 900 rpm on a Steadystir digital S56 (Fisher Scientific) in a 4°C room on ice, spaced 10s apart to avoid sample overheating. Homogenate was centrifuged at 1,000 xg for 10 min at 4°C to remove the soluble fraction. The insoluble fraction was resuspended in an equal volume of lysis buffer with 0.5% sodium deoxycholate (DOC, Sigma-Aldrich, Cat# BCCG2249) and rotated head-over-tail for 30 min at 4°C. The solubilized homogenate was centrifuged for 15 min at 16,000 xg at 4°C. The supernatant was transferred to either V5-Trap magnetic agarose or ALFA selector PE agarose magnetic beads and washed 2 times in 1 mL of lysis buffer according to the manufacturer protocol. The sample and beads were incubated with head-over-tail rotation for 1 hour at 4°C. Samples were washed with lysis buffer containing 0.5% DOC according to the manufacturer's instructions. Bound protein was eluted in 100 µl of 2X Laemmli buffer (Bio-Rad, Cat# 1610737) for 5 min at 95°C with 1,000 rpm shaking in a Thermomixer (Fisher Scientific, Cat# 05-400-205).

For proteomic characterization of affinity-purified tagged GluClα samples, eluates in 1X Laemmli buffer were diluted two-fold to reduce the SDS concentration. Samples were reduced and alkylated by the sequential addition of 5 mM tris(2-carboxyethyl)phosphine (Goldbio, Cat# TCEP1) and 10 mM iodoacetamide (Sigma-Aldrich, Cat# I1149). This was followed by protein clean-up using the single-pot, solid-phase-enhanced sample preparation (SP3) protocol.[82] Subsequently, the samples underwent proteolytic digestion with Lys-C (NEB, Cat# P8109S) and trypsin (Thermo Scientific, Cat# 90057) at 37°C overnight. The resulting peptides were desalted using SP3-based peptide clean-up and analyzed by LC-MS/MS. Briefly, peptides were separated by reversed-phase chromatography using 75 µm inner diameter fritted fused silica capillary

column (Molex, Cat# 1068150019) packed in-house to a length of 25 cm with bulk 1.9mM ReproSil-Pur beads with 120 Å pores (Dr. Maisch, Cat# R119.AQ.0001).[83] The increasing gradient of acetonitrile (Fisher Chemical, Cat# A955) was delivered by a Dionex Ultimate 3000 (Thermo Fisher Scientific) at a flow rate of 200nL/min. The MS/MS spectra were collected using data-dependent acquisition on Orbitrap Fusion Lumos Tribrid mass spectrometer (Thermo Fisher Scientific) with an MS1 resolution (r) of 120,000 followed by sequential MS2 scans at a resolution (r) of 15,000.

2.7.3.14 Co-immunoprecipitation and western blotting

The interaction between GluClα and Mmd was validated by repeating the above immunoprecipitation experiment using magnetic agarose beads with a nanobody recognizing GFP (GFP Selector, NanoTag, Cat# N0315), which interacts with protein harboring the V5 tag (smV5). We used w1118 and w; Rdl-smV5/+ flies as controls to assess the specificity of the interaction. IP was carried out as described above on 5 ml of flies, and the solubilized homogenate (input) and the eluted protein were run on a denaturing SDS-PAGE using SurePage Bis-Tris 4-20% gels (GenScript, Cat# M00657). Proteins were transferred onto a nitrocellulose membrane with semi-dry transfer (Invitrogen, Cat# PB3210), and membrane was blocked in TBST (10mM Tris-HCl, 0.9% w/v NaCl, 0.02% v/v Tween 20) with 5% skim-milk. Membranes were probed with mouse anti-V5 (SV5-Pk1, 1:500; Abcam Cat# ab27671, RRID:AB_471093), rabbit anti-Mmd (Guo et al., manuscript under preparation), and mouse anti-αTub (DSHB, Cat# 4A1). Anti-V5 was detected with StarBright Blue 520 goat anti-mouse (Bio-Rad, Cat# 12005867), anti-Mmd with StarBright Blue 700 goat anti-rabbit (Bio-Rad, Cat# 12004162), and anti-αTub with HRP conjugated goat-anti-mouse (Jackson ImmunoResearch Labs, Cat#115-036-003). HRP-conjugated antibodies were detected with a commercial chemiluminescence system (Millipore,

Cat# WBKLS), while fluorescent dye-conjugated antibodies were directly detected on an iBright 1500 imaging system (Invitrogen).

2.7.3.15 Secondary antibody labeling

In-house dye conjugation of Fab goat anti-rabbit IgG Fc SeTau647 antibody was performed by cross-linking Fab fragment goat anti-rabbit IgG Fc (Jackson ImmunoResearch, Cat# 111-007-008, RRID: AB_2632459) with amine-reactive SeTau-647-NHS (SETA BioMedicals, Cat# K9-4149) at a 1:10 ratio with addition of 0.1M sodium bicarbonate. The mixture was incubated at room temperature with shaking at 500 rpm for 1 hour. Labeled antibody was passed through a Zeba spin desalting column (Thermo Scientific, Cat# 89882). Desalinated labeled antibody was diluted in 40% glycerol at a concentration of 1-5mg/mL and stored at 4°C.

2.7.4 Quantification and Statistical Analysis

2.7.4.1 EM connectome analysis and visualization

Coordinates of synapses and neuron skeletons for the Fib25 EM dataset were obtained online (https://github.com/janelia-flyem/ConnectomeHackathon2015). Only synapses with a confidence level of 1 were considered in the analysis. For Tm3 neurons, only fully reconstructed neurons (Tm3-home-ant, Tm3-B-ant (rep), and Tm3-C-ant) that fully arborized within the volume in which synapses were annotated were used. For L5 neurons, six L5 neurons (A-F) located in the columns surrounding the central home column, as well as the L5 neuron in the home column, were analyzed. The distribution of synapses from inputs that made three or more synapses onto L5 dendrites in the medulla was computed in each layer. Layer boundaries were determined using L1 neurons as reference (these neurons arborize in M1 and M5 layers). The neurotransmitter identity

of each neuron input was obtained from scSeq data.[8] The visualization of skeletons and synapses was done using neuTube.[84]

To visualize T4 and T5 EM data and synaptic inputs, the coordinates of synapses and neuron skeletons for the Fib19 dataset[4] were obtained by downloading the data using neuprintr[85]. This was done for five representative reconstructions of T4 and T5 neurons.[4] Specifically, for T4 neurons, inputs to the medulla were considered, while for T5 neurons, inputs to the lobula dendrites were analyzed. For Figure 7, all 20 reference T4 dendrites were visualized alongside the Mi1 and Mi9 Home and the ones from columns A-F. Synapses between the home column Mi1 and Mi9 and T4 dendrites were identified. Partners are shown if they made 5 or more synapses, except for a second T4c neuron, which was omitted in Figure 7C for simplicity but formed a similar number of synapses with Mi1 home in its middle domain as seen with T4c-2. The visualization of skeletons and synapses was done using neuTube.[84]

2.7.4.2 Confocal image analysis

Airyscan processed images of L5, Tm3, T4, and T5 neurons were analyzed using Imaris 9.8. First, the membrane channel was extracted using the surface function to create a mask of the neuron. The receptor signal within the mask was analyzed using the spot function to identify puncta above background. All single neuron images shown are 3D projections of masked membrane and receptor signal. To determine the distribution of receptor puncta in T4/T5 dendrites, we restricted the analysis to c/d type T4 or T5 neurons where the direction of dendrite projection was on the long axis of the dendrite, as this facilitated the identification of the direction of dendritic processes. The proximo-distal axis of dendrites was normalized to 1, and the position of detected puncta was computed onto the normalized axis. All analyses were performed using R Statistical Software[86] (v4.2.2) using the ggplot2[87] package. All other images were processed using FIJI ImageJ.[88]

A Wilcoxon rank sum test with continuity correction was used to obtain significance values when comparing T4, T5, L5, and Tm3 comparison to synapse counts in EM data. Bonferroni correction was applied to p values when comparing L5 and Tm3 synapse counts to EM data in the three distinct dendritic compartments.

Images were assembled into figures using Adobe Illustrator.

2.7.4.3 Quantification of NR subunit expression

For quantification of NR subunit expression in Figure S1G, for each brain, we acquired 5 frames of a central portion of the medulla spanning all ten layers in each optic lobe. We used FIJI imageJ to obtain the signal levels and computed the mean of all 5 frames and both optic lobes for each brain. The ratio of signal using an antibody against the native protein normalized with the signal of the pan synaptic Brp is shown. Different antibody dilutions were used to rule out saturation of the antibody signal at the standard antibody concentration typically used.

2.7.4.4 ExLLSM image analysis

Analysis of ExLLSM images was carried out as previously described[23] with minor modifications. All the datasets acquired were deconvolved with the Richardson-Lucy algorithm using experimentally measured point spread functions (PSFs) for each color channel for ten iterations[24]. Only the central 360x480x480 voxels where LLSM provides optimal resolution were analyzed. After deconvolution, images were filtered to remove small puncta below 9 voxels by 3D Gaussian kernel with a sigma value of 1 and intensity threshold defined as the larger value between the mean plus two standard deviations and the value calculated with Otsu's method. We applied a lower size threshold (9 instead of 1008 voxels) to include putative non-synaptic receptor signal that may appear as small puncta for analysis. The 3D local maxima above the intensity threshold were detected using 3D spheric kernels of 2 voxel-radius by running 3DIJ2[89]. The images were

segmented using the detected local maxima as seeds to run 3D watershed. The descriptive parameters of segmented objects, such as the center of mass (COM) and number of voxels, were measured using 3D ImageJ Suite[90]. We defined colocalization between receptor and Brp objects if each segmented object of the receptor channel had at least one voxel that was within 1 voxel distance from Brp objects irrespective of the distance of the COMs. The Brp-colocalized receptor objects defined by this criterion appeared to be larger and closer to Brp compared to the "non-colocalized" receptor objects (Figures S3M-S3P). The scale shown for ExLLSM and ExLSM images is based on the expansion rate of 4.65, which was estimated by epifluorescence imaging of 16 brains before and after expansion. The expansion rate was larger than previously reported[23] when using PFA as fixative instead of Glyoxal-based fixatives.

2.7.4.5 ExLSM image analysis

ExLSM images were processed using Python (v3.9.13). Richardson-Lucy deconvolution was performed for 80 iterations on puncta channels stained for nc82 or smV5 and for 10 iterations on membrane channels stained for myr::GFP or myr::tdTomato. Experimental PSFs for deconvolution were acquired by imaging 200 nm fluorescent microspheres (Invitrogen, Cat# T7280), and an average PSF was extracted using the Experimental PSF Wizard in ZEN Blue (v3.4.91.00000). Deconvolved data was intensity normalized in the range of -1 to +40 standard deviations, and binary masks were generated by applying a Laplacian of Gaussian function and setting a positive threshold (0.01 for all myr::GFP and myr::tdTomato channels, 0.02 for all nc82 channels, and 0.1 for all smV5 channels). Puncta channels were then processed as follows. First, local intensity peaks were identified using a 3-voxel diameter window. To group multiple peaks located at the same synapse, nearest neighbors below a defined distance threshold were iteratively averaged, using an 8-voxel radius for Brp-smV5 or nc82 channels and a 4-voxel radius for GluClα-

smV5. The processed peaks were used to perform a marker-controlled watershed transform on the masked image[91], giving the final segmentation results.

Neuron masks were created through manual proofreading and labeling of the membrane channel masks in VVD Viewer (v1.5.10) (for selecting the desired neuron segments) and Napari (v0.4.17) (for manually painting the neuron labels). Nc82 signal within Mi9 axon terminals was extracted by calculating the uniformly weighted centers of mass (i.e. centroids) of each segmented object in the nc82 channel and selecting the objects whose centroids fell within the neuron mask.

All image panels displayed in Figure 6 and Figure S7 show 3D representations produced in VVD Viewer from analyzed data. Each panel shows a representative T4 dendrite from three different brain samples.

2.7.4.6 Analysis of mass spectrometry data

The data generated by LC-MS/MS were analyzed using the MaxQuant bioinformatic pipeline[92]. The Andromeda integrated in MaxQuant was employed as the peptide search engine, and the data were searched against the Drosophila melanogaster database (UniProt Reference UP000000803). A maximum of two missed cleavages was allowed. The maximum false discovery rate for peptide and protein was specified as 0.01. Label-free quantification (LFQ) was enabled with LFQ minimum ratio count of 1. The parent and peptide ion search tolerances were set to 20 and 4.5 ppm, respectively. The MaxQuant output files were subsequently processed for statistical analysis of differentially enriched proteins using Analytical R tools for mass spectrometry (artMS)[93].

2.7.4.7 Sc-RNAseq expression

Heatmaps of the expression of genes at 96h APF (Figure S4A) or during pupal development (Figure S6A) were obtained from previously published scSeq RNAseq data[8] (GSE156455).

2.8 References for Chapter 2

1. MICrONS Consortium, Bae, J.A., Baptiste, M., Bodor, A.L., Brittain, D., Buchanan, J., Bumbarger, D.J., Castro, M.A., Celii, B., Cobos, E., et al. (2023). Functional connectomics spanning multiple areas of mouse visual cortex. Biorxiv, 2021.07.28.454025. 10.1101/2021.07.28.454025.

2. Scheffer, L.K., Xu, C.S., Januszewski, M., Lu, Z., Takemura, S., Hayworth, K.J., Huang, G.B., Shinomiya, K., Maitlin-Shepard, J., Berg, S., et al. (2020). A connectome and analysis of the adult Drosophila central brain. eLife *9*, e57443. 10.7554/elife.57443.

3. Shapson-Coe, A., Januszewski, M., Berger, D.R., Pope, A., Wu, Y., Blakely, T., Schalek, R.L., Li, P.H., Wang, S., Maitin-Shepard, J., et al. (2021). A connectomic study of a petascale fragment of human cerebral cortex. bioRxiv, 2021.05.29.446289. 10.1101/2021.05.29.446289.

4. Shinomiya, K., Huang, G., Lu, Z., Parag, T., Xu, C.S., Aniceto, R., Ansari, N., Cheatham, N., Lauchie, S., Neace, E., et al. (2019). Comparisons between the ON- and OFF-edge motion pathways in the Drosophila brain. eLife *8*, e40025. 10.7554/elife.40025.

5. Takemura, S., Bharioke, A., Lu, Z., Nern, A., Vitaladevuni, S., Rivlin, P.K., Katz, W.T., Olbris, D.J., Plaza, S.M., Winston, P., et al. (2013). A visual motion detection circuit suggested by Drosophila connectomics. Nature *500*, 175–181. 10.1038/nature12450.

6. Winding, M., Pedigo, B.D., Barnes, C.L., Patsolic, H.G., Park, Y., Kazimiers, T., Fushiki, A., Andrade, I.V., Khandelwal, A., Valdes-Aleman, J., et al. (2023). The connectome of an insect brain. Science *379*, eadd9330–eadd9330. 10.1126/science.add9330.

7. Takemura, S., Xu, C.S., Lu, Z., Rivlin, P.K., Parag, T., Olbris, D.J., Plaza, S., Zhao, T., Katz, W.T., Umayam, L., et al. (2015). Synaptic circuits and their variations within different

columns in the visual system of Drosophila. Proc. Natl. Acad. Sci. *112*, 13711–13716. 10.1073/pnas.1509820112.

8. Kurmangaliyev, Y.Z., Yoo, J., Valdes-Aleman, J., Sanfilippo, P., and Zipursky, S.L. (2020). Transcriptional Programs of Circuit Assembly in the Drosophila Visual System. Neuron *108*, 1045-1057.e6. 10.1016/j.neuron.2020.10.006.

9. Özel, M.N., Simon, F., Jafari, S., Holguera, I., Chen, Y.-C., Benhra, N., El-Danaf, R.N., Kapuralin, K., Malin, J.A., Konstantinides, N., et al. (2021). Neuronal diversity and convergence in a visual system developmental atlas. Nature *589*, 88–95. 10.1038/s41586-020-2879-3.

10. Chamaon, K., Smalla, K., Thomas, U., and Gundelfinger, E.D. (2002). Nicotinic acetylcholine receptors of Drosophila: three subunits encoded by genomically linked genes can co-assemble into the same receptor complex. J. Neurochem. *80*, 149–157. 10.1046/j.0022-3042.2001.00685.x.

11. Gisselmann, G., Plonka, J., Pusch, H., and Hatt, H. (2004). Drosophila melanogaster GRD and LCCH3 subunits form heteromultimeric GABA-gated cation channels. Br. J. Pharmacol. *142*, 409–413. 10.1038/sj.bjp.0705818.

12. Lansdell, S.J., Collins, T., Goodchild, J., and Millar, N.S. (2012). The Drosophila nicotinic acetylcholine receptor subunits Dα5 and Dα7 form functional homomeric and heteromeric ion channels. BMC Neurosci. *13*, 73. 10.1186/1471-2202-13-73.

13. Schulz, R., Sawruk, E., Mülhardt, C., Bertrand, S., Baumann, A., Phannavong, B., Betz, H., Bertrand, D., Gundelfinger, E.D., and Schmitt, B. (1998). Dα3, a New Functional α Subunit of Nicotinic Acetylcholine Receptors from Drosophila. J. Neurochem. *71*, 853–862. 10.1046/j.1471-4159.1998.71020853.x.

14. Zhang, H.G., Lee, H.J., Rocheleau, T., ffrench-Constant, R.H., and Jackson, M.B. (1995). Subunit composition determines picrotoxin and bicuculline sensitivity of Drosophila gamma-aminobutyric acid receptors. Mol. Pharmacol. *48*, 835–840.

15. Panzanelli, P., Gunn, B.G., Schlatter, M.C., Benke, D., Tyagarajan, S.K., Scheiffele, P., Belelli, D., Lambert, J.J., Rudolph, U., and Fritschy, J. (2011). Distinct mechanisms regulate GABAA receptor and gephyrin clustering at perisomatic and axo-axonic synapses on CA1 pyramidal cells. J. Physiol. *589*, 4959–4980. 10.1113/jphysiol.2011.216028.

16. Contreras, A., Hines, D.J., and Hines, R.M. (2019). Molecular Specialization of GABAergic Synapses on the Soma and Axon in Cortical and Hippocampal Circuit Function and Dysfunction. Front. Mol. Neurosci. *12*, 154. 10.3389/fnmol.2019.00154.

17. Ryglewski, S., Vonhoff, F., Scheckel, K., and Duch, C. (2017). Intra-neuronal Competition for Synaptic Partners Conserves the Amount of Dendritic Building Material. Neuron *93*, 632-645.e6. 10.1016/j.neuron.2016.12.043.

18. Fendl, S., Vieira, R.M., and Borst, A. (2020). Conditional protein tagging methods reveal highly specific subcellular distribution of ion channels in motion-sensing neurons. eLife *9*, e62953. 10.7554/elife.62953.

19. Yang, H.H., St-Pierre, F., Sun, X., Ding, X., Lin, M.Z., and Clandinin, T.R. (2016). Subcellular Imaging of Voltage and Calcium Signals Reveals Neural Processing In Vivo. Cell *166*, 245–257. 10.1016/j.cell.2016.05.031.

20. Hamakubo, T., Kusano-Arai, O., and Iwanari, H. (2014). Generation of antibodies against membrane proteins. Biochim. Biophys. Acta (BBA) - Proteins Proteom. *1844*, 1920–1924. 10.1016/j.bbapap.2014.08.007.

21. Boassa, D. (2015). ELISA, Methods and Protocols. Methods Mol. Biol. *1318*, 173–180. 10.1007/978-1-4939-2742-5_17.

22. Chen, F., Tillberg, P.W., and Boyden, E.S. (2015). Expansion microscopy. Science *347*, 543–548. 10.1126/science.1260088.

23. Gao, R., Asano, S.M., Upadhyayula, S., Pisarev, I., Milkie, D.E., Liu, T.-L., Singh, V., Graves, A., Huynh, G.H., Zhao, Y., et al. (2019). Cortical column and whole-brain imaging with molecular contrast and nanoscale resolution. Science *363*, eaau8302. 10.1126/science.aau8302.

24. Chen, B.-C., Legant, W.R., Wang, K., Shao, L., Milkie, D.E., Davidson, M.W., Janetopoulos, C., Wu, X.S., III, J.A.H., Liu, Z., et al. (2014). Lattice light-sheet microscopy: Imaging molecules to embryos at high spatiotemporal resolution. Science *346*, 1257998. 10.1126/science.1257998.

25. Littleton, J.T., and Ganetzky, B. (2000). Ion Channels and Synaptic Organization Analysis of the Drosophila Genome. Neuron *26*, 35–43. 10.1016/s0896-6273(00)81135-6.

26. Kondo, S., Takahashi, T., Yamagata, N., Imanishi, Y., Katow, H., Hiramatsu, S., Lynn, K., Abe, A., Kumaraswamy, A., and Tanimoto, H. (2020). Neurochemical Organization of the Drosophila Brain Visualized by Endogenously Tagged Neurotransmitter Receptors. Cell Rep. *30*, 284-297.e5. 10.1016/j.celrep.2019.12.018.

27. Deng, B., Li, Q., Liu, X., Cao, Y., Li, B., Qian, Y., Xu, R., Mao, R., Zhou, E., Zhang, W., et al. (2019). Chemoconnectomics: Mapping Chemical Transmission in Drosophila. Neuron *101*, 876-893.e4. 10.1016/j.neuron.2019.01.045.

28. Mikuni, T., Nishiyama, J., Sun, Y., Kamasawa, N., and Yasuda, R. (2016). High-Throughput, High-Resolution Mapping of Protein Localization in Mammalian Brain by In Vivo Genome Editing. Cell *165*, 1803–1817. 10.1016/j.cell.2016.04.044.

29. Perez, J.D., Fusco, C.M., and Schuman, E.M. (2021). A Functional Dissection of the mRNA and Locally Synthesized Protein Population in Neuronal Dendrites and Axons. Annu. Rev. Genet. *55*, 1–25. 10.1146/annurev-genet-030321-054851.

30. Gratz, S.J., Harrison, M.M., Wildonger, J., and O'Connor-Giles, K.M. (2015). CRISPR, Methods and Protocols. Methods Mol. Biol. *1311*, 335–348. 10.1007/978-1-4939-2687-9_22.

31. Kanca, O., Zirin, J., Garcia-Marques, J., Knight, S.M., Yang-Zhou, D., Amador, G., Chung, H., Zuo, Z., Ma, L., He, Y., et al. (2019). An efficient CRISPR-based strategy to insert small and large fragments of DNA using short homology arms. eLife *8*, e51539. 10.7554/elife.51539.

32. Drenan, R.M., Nashmi, R., Imoukhuede, P., Just, H., McKinney, S., and Lester, H.A. (2008). Subcellular Trafficking, Pentameric Assembly, and Subunit Stoichiometry of Neuronal Nicotinic Acetylcholine Receptors Containing Fluorescently Labeled α6 and β3 Subunits. Mol. Pharmacol. *73*, 27–41. 10.1124/mol.107.039180.

33. Nashmi, R., Dickinson, M.E., McKinney, S., Jareb, M., Labarca, C., Fraser, S.E., and Lester, H.A. (2003). Assembly of α4β2 Nicotinic Acetylcholine Receptors Assessed with Functional Fluorescently Labeled Subunits: Effects of Localization, Trafficking, and Nicotine-Induced Upregulation in Clonal Mammalian Cells and in Cultured Midbrain Neurons. J. Neurosci. *23*, 11554–11567. 10.1523/jneurosci.23-37-11554.2003.

34. Raghu, S.V., Joesch, M., Sigrist, S.J., Borst, A., and Reiff, D.F. (2009). Synaptic Organization of Lobula Plate Tangential Cells in Drosophila: Dα7 Cholinergic Receptors. J. Neurogenet. *23*, 200–209. 10.1080/01677060802471684.

35. Slimko, E.M., and Lester, H.A. (2003). Codon optimization of Caenorhabditis elegans GluCl ion channel genes for mammalian cells dramatically improves expression levels. J Neurosci Meth *124*, 75–81. 10.1016/s0165-0270(02)00362-x.

36. Boorman, J.P., Beato, M., Groot-Kormelink, P.J., Broadbent, S.D., and Sivilotti, L.G. (2003). The Effects of β3 Subunit Incorporation on the Pharmacology and Single Channel Properties of Oocyte-expressed Human α3β4 Neuronal Nicotinic Receptors*. J. Biol. Chem. *278*, 44033–44040. 10.1074/jbc.m211719200.

37. Jenett, A., Rubin, G.M., Ngo, T.-T.B., Shepherd, D., Murphy, C., Dionne, H., Pfeiffer, B.D., Cavallaro, A., Hall, D., Jeter, J., et al. (2012). A GAL4-Driver Line Resource for Drosophila Neurobiology. Cell Rep. *2*, 991–1001. 10.1016/j.celrep.2012.09.011.

38. Pfeiffer, B.D., Ngo, T.-T.B., Hibbard, K.L., Murphy, C., Jenett, A., Truman, J.W., and Rubin, G.M. (2010). Refinement of Tools for Targeted Gene Expression in Drosophila. Genetics *186*, 735–755. 10.1534/genetics.110.119917.

39. Yasuyama, K., Meinertzhagen, I.A., and Schürmann, F. (2002). Synaptic organization of the mushroom body calyx in Drosophila melanogaster. J. Comp. Neurol. *445*, 211–226. 10.1002/cne.10155.

40. Barnstedt, O., Owald, D., Felsenberg, J., Brain, R., Moszynski, J.-P., Talbot, C.B., Perrat, P.N., and Waddell, S. (2016). Memory-Relevant Mushroom Body Output Synapses Are Cholinergic. Neuron *89*, 1237–1247. 10.1016/j.neuron.2016.02.015.

41. Aso, Y., Ray, R.P., Long, X., Bushey, D., Cichewicz, K., Ngo, T.-T., Sharp, B., Christoforou, C., Hu, A., Lemire, A.L., et al. (2019). Nitric oxide acts as a cotransmitter in a subset of dopaminergic neurons to diversify memory dynamics. eLife *8*, e49257. 10.7554/elife.49257.

42. Fulterer, A., Andlauer, T.F.M., Ender, A., Maglione, M., Eyring, K., Woitkuhn, J., Lehmann, M., Matkovic-Rachid, T., Geiger, J.R.P., Walter, A.M., et al. (2018). Active Zone Scaffold Protein Ratios Tune Functional Diversity across Brain Synapses. Cell Rep. *23*, 1259–1274. 10.1016/j.celrep.2018.03.126.

43. Takemura, S., Aso, Y., Hige, T., Wong, A., Lu, Z., Xu, C.S., Rivlin, P.K., Hess, H., Zhao, T., Parag, T., et al. (2017). A connectome of a learning and memory center in the adult Drosophila brain. eLife *6*, e26975. 10.7554/elife.26975.

44. Takemura, S., Nern, A., Chklovskii, D.B., Scheffer, L.K., Rubin, G.M., and Meinertzhagen, I.A. (2017). The comprehensive connectome of a neural substrate for 'ON' motion detection in Drosophila. eLife *6*, e24394. 10.7554/elife.24394.

45. Couturier, S., Bertrand, D., Matter, J.-M., Hernandez, M.-C., Bertrand, S., Millar, N., Valera, S., Barkas, T., and Ballivet, M. (1990). A neuronal nicotinic acetylcholine receptor subunit (α7) is developmentally regulated and forms a homo-oligomeric channel blocked by α-BTX. Neuron *5*, 847–856. 10.1016/0896-6273(90)90344-f.

46. Noviello, C.M., Gharpure, A., Mukhtasimova, N., Cabuco, R., Baxter, L., Borek, D., Sine, S.M., and Hibbs, R.E. (2021). Structure and gating mechanism of the α7 nicotinic acetylcholine receptor. Cell *184*, 2121-2134.e13. 10.1016/j.cell.2021.02.049.

47. Fukata, Y., Chen, X., Chiken, S., Hirano, Y., Yamagata, A., Inahashi, H., Sanbo, M., Sano, H., Goto, T., Hirabayashi, M., et al. (2021). LGI1–ADAM22–MAGUK configures

transsynaptic nanoalignment for synaptic transmission and epilepsy prevention. Proc. Natl. Acad. Sci. *118*, e2022580118. 10.1073/pnas.2022580118.

48. Jumper, J., Evans, R., Pritzel, A., Green, T., Figurnov, M., Ronneberger, O., Tunyasuvunakool, K., Bates, R., Žídek, A., Potapenko, A., et al. (2021). Highly accurate protein structure prediction with AlphaFold. Nature *596*, 583–589. 10.1038/s41586-021-03819-2.

49. Strother, J.A., Wu, S.-T., Wong, A.M., Nern, A., Rogers, E.M., Le, J.Q., Rubin, G.M., and Reiser, M.B. (2017). The Emergence of Directional Selectivity in the Visual Motion Pathway of Drosophila. Neuron *94*, 168-182.e10. 10.1016/j.neuron.2017.03.010.

50. Buckley, C.E., and Johnston, D.S. (2022). Apical–basal polarity and the control of epithelial form and function. Nat. Rev. Mol. Cell Biol. *23*, 559–577. 10.1038/s41580-022-00465-y.

51. Keable, R., Leshchyns'ka, I., and Sytnyk, V. (2020). Trafficking and Activity of Glutamate and GABA Receptors: Regulation by Cell Adhesion Molecules. Neurosci. *26*, 415–437. 10.1177/1073858420921117.

52. Südhof, T.C. (2021). The cell biology of synapse formation. J. Cell Biol. *220*, e202103052. 10.1083/jcb.202103052.

53. Lovero, K.L., Fukata, Y., Granger, A.J., Fukata, M., and Nicoll, R.A. (2015). The LGI1–ADAM22 protein complex directs synapse maturation through regulation of PSD-95 function. Proc. Natl. Acad. Sci. *112*, E4129–E4137. 10.1073/pnas.1511910112.

54. Yamagata, A., Miyazaki, Y., Yokoi, N., Shigematsu, H., Sato, Y., Goto-Ito, S., Maeda, A., Goto, T., Sanbo, M., Hirabayashi, M., et al. (2018). Structural basis of epilepsy-related ligand–receptor complex LGI1–ADAM22. Nat. Commun. *9*, 1546. 10.1038/s41467-018-03947-w.

55. Lee, S.-J., Wei, M., Zhang, C., Maxeiner, S., Pak, C., Botelho, S.C., Trotter, J., Sterky, F.H., and Südhof, T.C. (2016). Presynaptic Neuronal Pentraxin Receptor Organizes Excitatory and Inhibitory Synapses. J. Neurosci. *37*, 1062–1080. 10.1523/jneurosci.2768-16.2016.

56. Zhang, C., Atasoy, D., Araç, D., Yang, X., Fucillo, M.V., Robison, A.J., Ko, J., Brunger, A.T., and Südhof, T.C. (2010). Neurexins Physically and Functionally Interact with GABAA Receptors. Neuron *66*, 403–416. 10.1016/j.neuron.2010.04.008.

57. Groschner, L.N., Malis, J.G., Zuidinga, B., and Borst, A. (2022). A biophysical account of multiplication by a single neuron. Nature *603*, 119–123. 10.1038/s41586-022-04428-3.

58. Gruntman, E., Romani, S., and Reiser, M.B. (2018). Simple integration of fast excitation and offset, delayed inhibition computes directional selectivity in Drosophila. Nat. Neurosci. *21*, 250–257. 10.1038/s41593-017-0046-4.

59. Huang, Q.T., Sheng, C.W., Jones, A.K., Jiang, J., Tang, T., Han, Z.J., and Zhao, C.Q. (2021). Functional Characteristics of the Lepidopteran Ionotropic GABA Receptor 8916 Subunit Interacting with the LCCH3 or the RDL Subunit. J. Agric. Food Chem. *69*, 11582–11591. 10.1021/acs.jafc.1c00385.

60. Zheng, Z., Lauritzen, J.S., Perlman, E., Robinson, C.G., Nichols, M., Milkie, D., Torrens, O., Price, J., Fisher, C.B., Sharifi, N., et al. (2018). A Complete Electron Microscopy Volume of the Brain of Adult Drosophila melanogaster. Cell *174*, 730-743.e22. 10.1016/j.cell.2018.06.019.

61. Fischbach, K.-F., and Dittrich, A.P.M. (1989). The optic lobe of Drosophila melanogaster. I. A Golgi analysis of wild-type structure. Cell Tissue Res. *258*, 441–475. 10.1007/bf00218858.

62. Gramates, L.S., Agapite, J., Attrill, H., Calvi, B.R., Crosby, M.A., Santos, G. dos, Goodman, J.L., Goutte-Gattat, D., Jenkins, V.K., Kaufman, T., et al. (2022). FlyBase: a guided tour of highlighted features. Genetics *220*, iyac035. 10.1093/genetics/iyac035.

63. Blake, J.A., Baldarelli, R., Kadin, J.A., Richardson, J.E., Smith, C.L., Bult, C.J., Group, the M.G.D., Anagnostopoulos, A.V., Beal, J.S., Bello, S.M., et al. (2020). Mouse Genome Database (MGD): Knowledgebase for mouse–human comparative biology. Nucleic Acids Res. *49*, gkaa1083. 10.1093/nar/gkaa1083.

64. Seal, R.L., Braschi, B., Gray, K., Jones, T.E.M., Tweedie, S., Haim-Vilmovsky, L., and Bruford, E.A. (2022). Genenames.org: the HGNC resources in 2023. Nucleic Acids Res. *51*, D1003–D1009. 10.1093/nar/gkac888.

65. UniProt Consortium. (2022). UniProt: the Universal Protein Knowledgebase in 2023. Nucleic Acids Res. *51*, D523–D531. doi: 10.1093/nar/gkac1052.

66. Viswanathan, S., Williams, M.E., Bloss, E.B., Stasevich, T.J., Speer, C.M., Nern, A., Pfeiffer, B.D., Hooks, B.M., Li, W.-P., English, B.P., et al. (2015). High-performance probes for light and electron microscopy. Nat. Methods *12*, 568–576. 10.1038/nmeth.3365.

67. Nern, A., Pfeiffer, B.D., and Rubin, G.M. (2015). Optimized tools for multicolor stochastic labeling reveal diverse stereotyped cell arrangements in the fly visual system. Proc. Natl. Acad. Sci. *112*, E2967–E2976. 10.1073/pnas.1506763112.

68. Götzke, H., Kilisch, M., Martínez-Carranza, M., Sograte-Idrissi, S., Rajavel, A., Schlichthaerle, T., Engels, N., Jungmann, R., Stenmark, P., Opazo, F., et al. (2019). The ALFA-tag is a highly versatile tool for nanobody-based bioscience applications. Nat. Commun. *10*, 4403. 10.1038/s41467-019-12301-7.

69. Ren, X., Sun, J., Housden, B.E., Hu, Y., Roesel, C., Lin, S., Liu, L.-P., Yang, Z., Mao, D., Sun, L., et al. (2013). Optimized gene editing technology for Drosophila melanogaster using germ line-specific Cas9. Proc. Natl. Acad. Sci. *110*, 19012–19017. 10.1073/pnas.1318481110.

70. Nern, A., Pfeiffer, B.D., Svoboda, K., and Rubin, G.M. (2011). Multiple new site-specific recombinases for use in manipulating animal genomes. Proc. Natl. Acad. Sci. *108*, 14198–14203. 10.1073/pnas.1111704108.

71. Chen, Y., Akin, O., Nern, A., Tsui, C.Y.K., Pecot, M.Y., and Zipursky, S.L. (2014). Cell-type-Specific Labeling of Synapses In Vivo through Synaptic Tagging with Recombination. Neuron *81*, 280–293. 10.1016/j.neuron.2013.12.021.

72. Xu, S., Xiao, Q., Cosmanescu, F., Sergeeva, A.P., Yoo, J., Lin, Y., Katsamba, P.S., Ahlsen, G., Kaufman, J., Linaval, N.T., et al. (2018). Interactions between the Ig-Superfamily Proteins DIP-α and Dpr6/10 Regulate Assembly of Neural Circuits. Neuron *100*, 1369-1384.e6. 10.1016/j.neuron.2018.11.001.

73. Nakayama, M., Suzuki, E., Tsunoda, S., and Hama, C. (2016). The Matrix Proteins Hasp and Hig Exhibit Segregated Distribution within Synaptic Clefts and Play Distinct Roles in Synaptogenesis. J. Neurosci. *36*, 590–606. 10.1523/jneurosci.2300-15.2016.

74. Richter, K.N., Revelo, N.H., Seitz, K.J., Helm, M.S., Sarkar, D., Saleeb, R.S., D'Este, E., Eberle, J., Wagner, E., Vogl, C., et al. (2018). Glyoxal as an alternative fixative to formaldehyde in immunostaining and super-resolution microscopy. EMBO J. *37*, 139–159. 10.15252/embj.201695709.

75. Lee, T., and Luo, L. (1999). Mosaic Analysis with a Repressible Cell Marker for Studies of Gene Function in Neuronal Morphogenesis. Neuron *22*, 451–461. 10.1016/s0896-6273(00)80701-1.

76. Fayyazuddin, A., Zaheer, M.A., Hiesinger, P.R., and Bellen, H.J. (2006). The Nicotinic Acetylcholine Receptor Dα7 Is Required for an Escape Behavior inDrosophila. PLoS Biol. *4*, e63. 10.1371/journal.pbio.0040063.

77. Liu, X., Krause, W.C., and Davis, R.L. (2007). GABAA Receptor RDL Inhibits Drosophila Olfactory Associative Learning. Neuron *56*, 1090–1102. 10.1016/j.neuron.2007.10.036.

78. Kita, T., Ozoe, F., Azuma, M., and Ozoe, Y. (2013). Differential distribution of glutamate- and GABA-gated chloride channels in the housefly Musca domestica. J. Insect Physiol. *59*, 887–893. 10.1016/j.jinsphys.2013.06.005.

79. Asano, S.M., Gao, R., Wassie, A.T., Tillberg, P.W., Chen, F., and Boyden, E.S. (2018). Expansion Microscopy: Protocols for Imaging Proteins and RNA in Cells and Tissues. Curr. Protoc. Cell Biol. *80*, e56. 10.1002/cpcb.56.

80. Tillberg, P.W., Chen, F., Piatkevich, K.D., Zhao, Y., Yu, C.-C. (Jay), English, B.P., Gao, L., Martorell, A., Suk, H.-J., Yoshida, F., et al. (2016). Protein-retention expansion microscopy of cells and tissues labeled using standard fluorescent proteins and antibodies. Nat. Biotechnol. *34*, 987–992. 10.1038/nbt.3625.

81. Tillberg, P. (2021). Confocal Microscopy, Methods and Protocols. Methods Mol. Biol. *2304*, 147–156. 10.1007/978-1-0716-1402-0_7.

82. Hughes, C.S., Moggridge, S., Müller, T., Sorensen, P.H., Morin, G.B., and Krijgsveld, J. (2019). Single-pot, solid-phase-enhanced sample preparation for proteomics experiments. Nat. Protoc. *14*, 68–85. 10.1038/s41596-018-0082-x.

83. Jami-Alahmadi, Y., Pandey, V., Mayank, A.K., and Wohlschlegel, J.A. (2021). A Robust Method for Packing High Resolution C18 RP-nano-HPLC Columns. J. Vis. Exp. 10.3791/62380.

84. Feng, L., Zhao, T., and Kim, J. (2015). neuTube 1.0: A New Design for Efficient Neuron Reconstruction Software Based on the SWC Format 123. eNeuro *2*, ENEURO.0049-14.2014. 10.1523/eneuro.0049-14.2014.

85. Bates, A.S., Manton, J.D., Jagannathan, S.R., Costa, M., Schlegel, P., Rohlfing, T., and Jefferis, G.S. (2020). The natverse, a versatile toolbox for combining and analysing neuroanatomical data. eLife *9*, e53350. 10.7554/elife.53350.

86. R Core Team. (2022). R: A Language and Environment for Statistical Computing (Vienna, Austria: R Foundation for Statistical Computing).

87. Wickham, H. (2016). ggplot2: Elegant Graphics for Data Analysis (Springer-Verlag New York).

88. Schindelin, J., Arganda-Carreras, I., Frise, E., Kaynig, V., Longair, M., Pietzsch, T., Preibisch, S., Rueden, C., Saalfeld, S., Schmid, B., et al. (2012). Fiji: an open-source platform for biological-image analysis. Nat. Methods *9*, 676–682. 10.1038/nmeth.2019.

89. Haase, R., Royer, L.A., Steinbach, P., Schmidt, D., Dibrov, A., Schmidt, U., Weigert, M., Maghelli, N., Tomancak, P., Jug, F., et al. (2020). CLIJ: GPU-accelerated image processing for everyone. Nat. Methods *17*, 5–6. 10.1038/s41592-019-0650-1.

90. Ollion, J., Cochennec, J., Loll, F., Escudé, C., and Boudier, T. (2013). TANGO: a generic tool for high-throughput 3D image analysis for studying nuclear organization. Bioinformatics *29*, 1840–1841. 10.1093/bioinformatics/btt276.

91. Meyer, F., and Beucher, S. (1990). Morphological segmentation. J. Vis. Commun. Image Represent. *1*, 21–46. 10.1016/1047-3203(90)90014-m.

92. Cox, J., and Mann, M. (2008). MaxQuant enables high peptide identification rates, individualized p.p.b.-range mass accuracies and proteome-wide protein quantification. Nat. Biotechnol. *26*, 1367–1372. 10.1038/nbt.1511.

93. Jimenez-Morales, D., Rosa Campos, A., Von Dollen, J., Krogan, N. and Swaney, D. (2023). *artMS: Analytical R tools for Mass Spectrometry*. R package version 1.18.0, http://artms.org.

94. Molina-Obando, S., Vargas-Fique, J.F., Henning, M., Gür, B., Schladt, T.M., Akhtar, J., Berger, T.K., and Silies, M. (2019). ON selectivity in the Drosophila visual system is a multisynaptic process involving both glutamatergic and GABAergic inhibition. eLife 8, e49373. 10.7554/elife.49373.

95. Peng, J., Santiago, I.J., Ahn, C., Gur, B., Tsui, C.K., Su, Z., Xu, C., Karakhanyan, A., Silies, M., and Pecot, M.Y. (2018). Drosophila Fezf coordinates laminar-specific connectivity through cell-intrinsic and cell-extrinsic mechanisms. eLife 7, e33962. 10.7554/elife.33962.

2.9 Figures & Tables

Figure 2.1 Tagged NR subunits localize to synapses

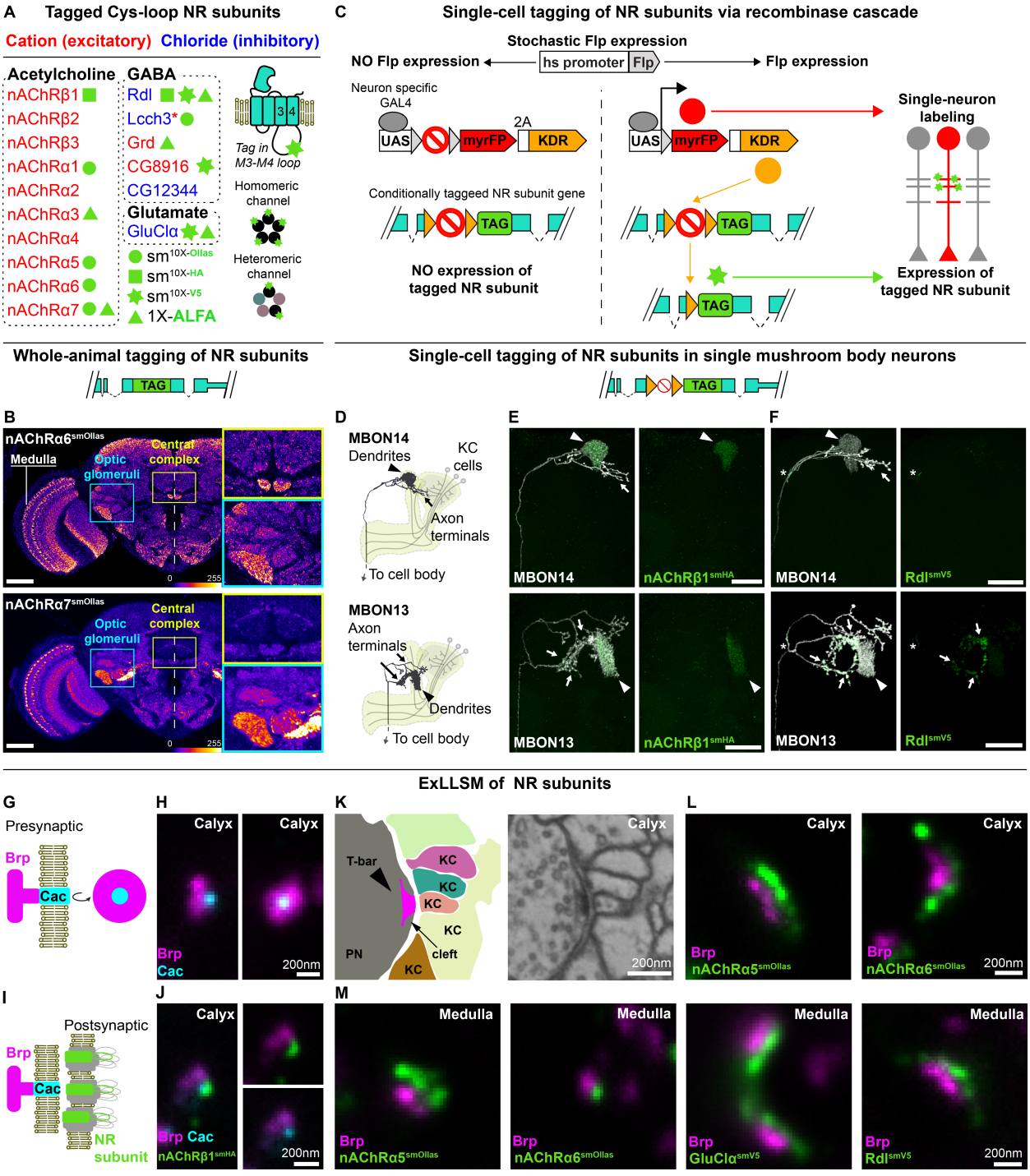

(Figure cross-referenced in Chapter 2 text as Figure 1.)

(A) Cys-loop superfamily NR subunits tagged in this study. For some NRs, two or three different tagged versions were made as indicated. Red asterisk, Lcch3, forms cationic channels with Grd and with CG8916 and chloride channels with Rdl.[11,14,59] The epitope tag was inserted into a poorly conserved region of the M3-M4 cytoplasmic loop in each NR subunit (Figures S1C and S1D). These proteins form homo- or heteropentameric channels.

(B) Whole animal tagging of NR subunits. For each conditionally tagged allele, a corresponding whole-animal tagged version was generated in which all cells expressing the receptor express a tagged version. Expression pattern of endogenously tagged alleles of nAChRα6 (top panel) and nAChRα7 (bottom panel). Dotted line, brain midline; yellow inset, neuropils of the central complex; cyan inset, optic glomeruli. Brp staining visualizes neuropils. Scale bars, 50 μm.

(C) Schematic for conditional tagging of NR subunits in sparsely distributed neurons. See Figure S4B for details. (D-F) Localization of NR subunits to domains of neurons with complex morphology in the central brain. MBONs have two main processes: one ending in a compact dendrite and another branched axonal process projecting to distinct brain areas. (D) Morphology of MBON14 or MBON13 – dendrites innervate select compartments of the mushroom body (yellow). Kenyon cells provide cholinergic inputs to MBON dendrites. Localization of nAChRβ1-smHA (E) or Rdl-smV5 (F) in MBON14 or MBON13. Arrowhead – dendrites; arrows – axonal projections; asterisk – putative axon initial segment. Scale bars, 25 μm.

(G) Schematic of synaptic active zone marked by Brp and the voltage-gated calcium channel Cacophony (Cac). In EM, cytoplasmic Brp protein localizes to a presynaptic T-bar structure associated with the presynaptic membrane (see panel K) and as a donut by STED and LLSM when immunostained for the Brp-directed antibody nc82.

(H) Brp with Cac at its center visualized using ExLLSM. The synapse shown is from the mushroom body calyx in the central brain. Lateral (left) and planar (right) views are shown.

(I) Schematic of NR subunits juxtaposing Brp and Cac.

(J) nAChRβ1 subunits cluster juxtaposed to an active zone in the calyx. Lateral views are shown.

(K) EM (right) and schematic (left) of multiple-contact synapse between projection neurons (PN) and Kenyon cells (KC) in the mushroom body (single synapse from EM data[60]).

(L) Immunostaining of PN-KC synapses, as indicated.

(M) Examples of active zones and different NR subunits (as indicated) paired at synapses in the medulla neuropil.

Scale bars in H, J, L, and M panels represent unexpanded tissue size (adjusted for 4.65X expansion factor; see STAR Methods). See also Figures S1-S3 and Table S1.

Figure 2.2 NR subunit distribution matches the EM connectome

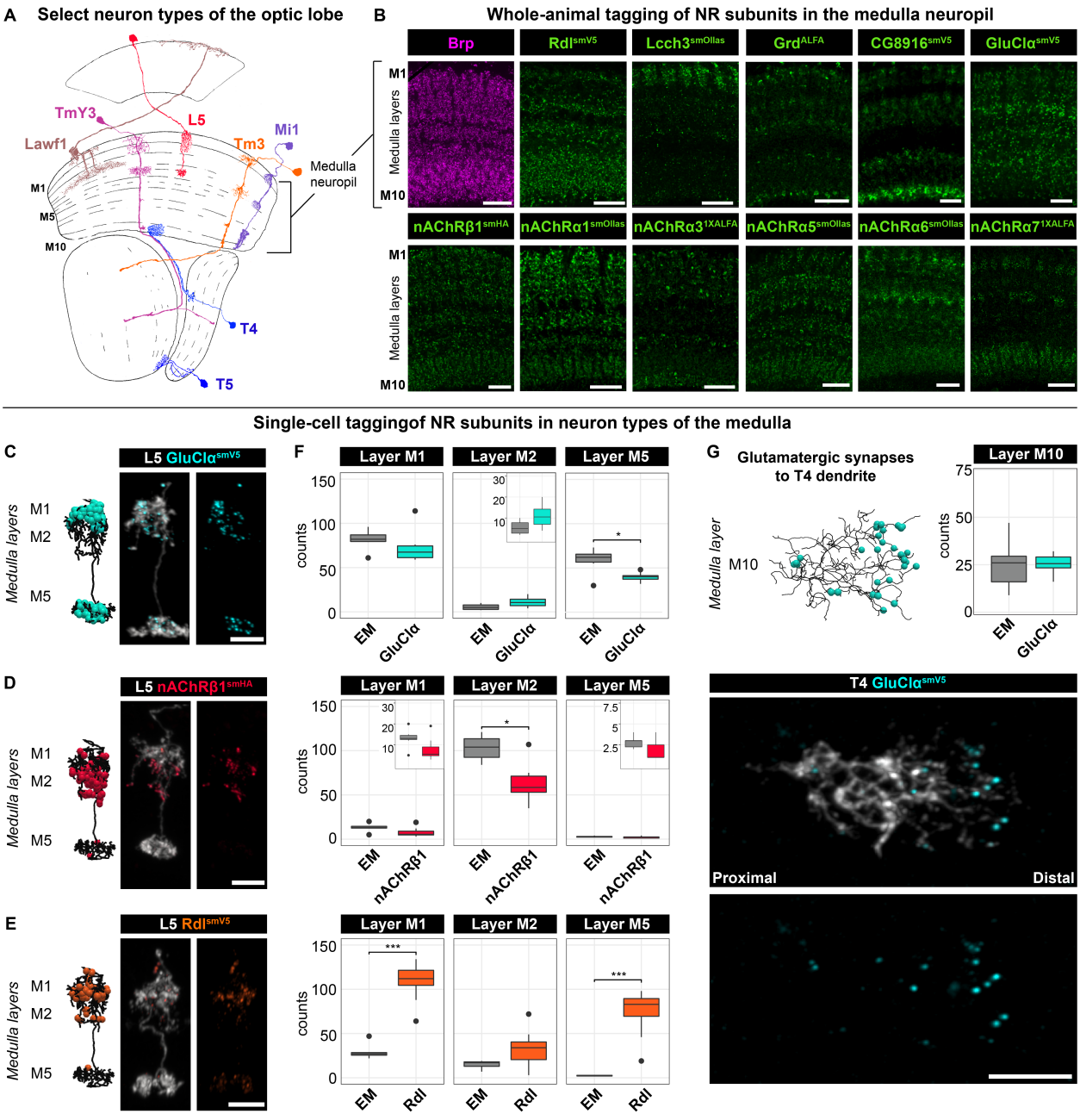

(Figure cross-referenced in Chapter 2 text as Figure 2.)

(A) Morphologies of a small selection of neuron types of the ~150 different types in the fly optic lobe (Adapted from ref.[61]). Three of ten medulla neuropil layers are labeled (M1, M5, and M10).

(B) NR subunit expression (green) across medulla layers (M1-M10). Presynaptic marker Brp (magenta) is detected with anti-Brp antibody throughout all medulla layers. NR subunits are detected with epitope-tag-specific antibodies (anti-V5, anti-Ollas, anti-HA, anti-ALFA). Scale bar, 10 μm.

(C-E) Localization of GluClα-smV5 (C), nAChRβ1-smHA (D), and Rdl-smV5 (E) in dendrites of L5 neurons. Left, EM-based reconstruction of L5 dendrites and annotated synapses for each neurotransmitter type[7]. Right two panels, neuron morphology (gray) and NR subunits (color-coded). Scale bars, 5 μm.

(F) Quantification of data shown in E-G and from the EM[7] (EM, n=7; Rdl, n=15; GluClα, n=12; and nAChRβ1, n=8). Bonferroni adjusted p-value (*), < 0.05, (***), < 0.001 from Wilcoxon rank-sum test. See text for a discussion of discrepancies between EM and tagged puncta.

(G) Distribution of GluClα-smV5 in T4 dendrites. Quantification is the same as in Figure S5F. Scale bars, 5 μm.

See also Figure S4.

Figure 2.3 NR subunits are differentially localized along dendrites

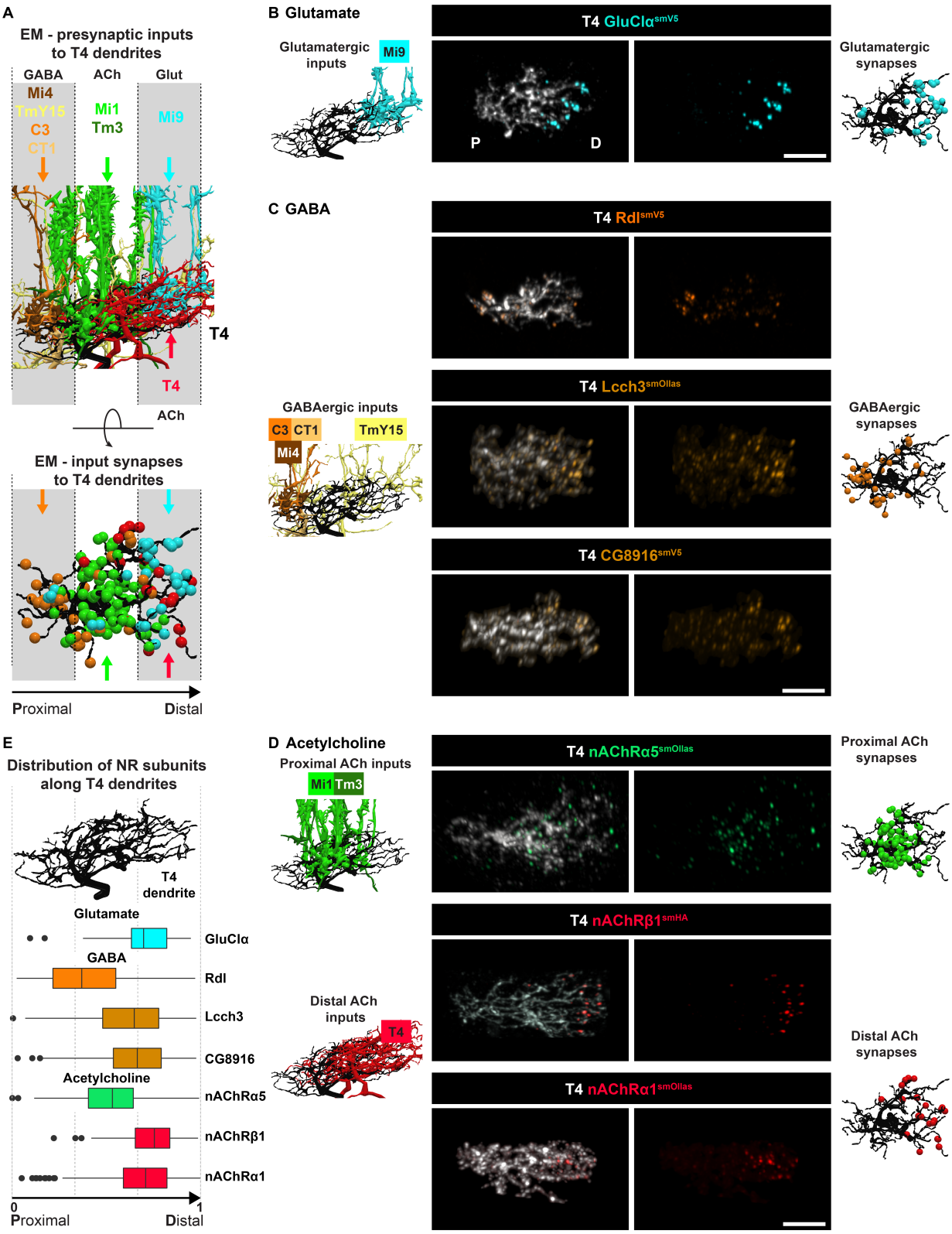

(Figure cross-referenced in Chapter 2 text as Figure 3.)

(A) Upper panel, EM reconstruction of different presynaptic inputs, as indicated, along the proximodistal axis of T4 dendrites. Dendrites span an average of three columns. Lower panel, annotated synapses for different neurotransmitter inputs are shown. Colored arrows in the lower panel show domains targeted by color-matched presynaptic inputs from the upper panel. TmY15 is an exception forming synapses across the length of T4 dendrites.

(B-D) Localization of tagged NR subunits in dendrites of single T4 neurons. Left-most column, EM reconstruction of glutamatergic, GABAergic, and cholinergic inputs. Central columns, NR subunit pattern observed by conditional tagging in single T4 dendrites. Right-most column, subset of EM-annotated synapses as shown in the lower part of panel A. Scale bars, 5 μm.

(E) Quantification of NR subunit expression along the normalized proximo-distal axis of T4 dendrites (see STAR Methods). Rdl, n = 6; CG8916, n=4; Lcch3, n=3; GluClα, n = 4; nAChRα1, n = 5; nAChRα5, n = 5; nAChRβ1, n = 10.

See also Figure S5.

Figure 2.4 Localization of NR subunits during development is cell-type specific

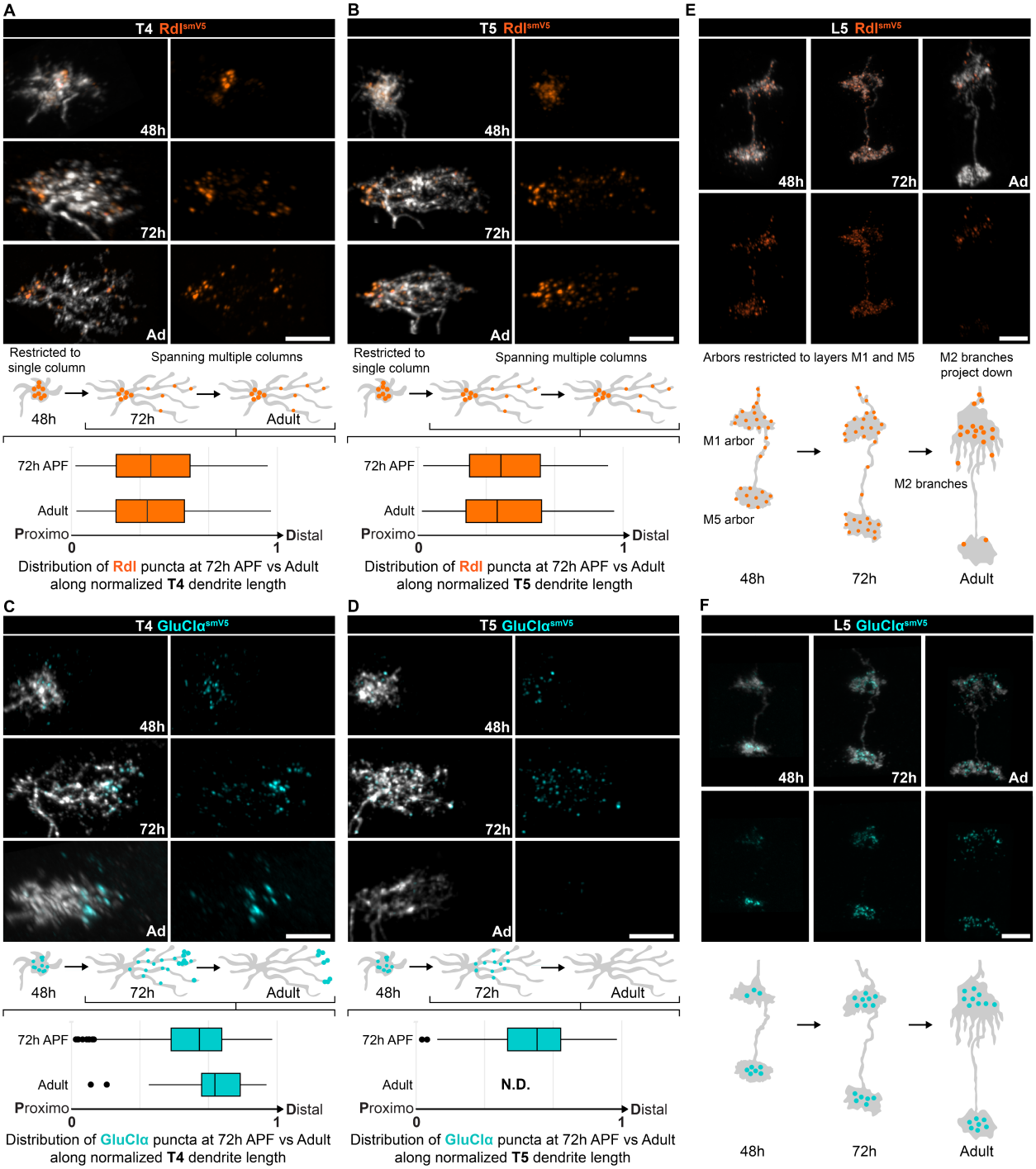

(Figure cross-referenced in Chapter 2 text as Figure 4.)

Time course of NR subunit accumulation during development of T4 (A, C), T5 (B, D) and L5 dendrites (E, F) of Rdl-smV5 (A-B, E) or GluClα-smV5 (C-D, F). Times shown are 48h and 72h

after pupal formation (APF) and adult (Ad). Schematic of dendrite development with NR distribution shown for these time points. For T4 and T5, quantification of puncta distribution along the normalized proximodistal axis at 72h APF and adult are shown below the schematics (T4: adult quantification data same as Figure 3E; Rdl 72h APF, n = 4; GluClα 72h APF, n= 6. T5: adult quantification data same as Figure S5E, Rdl 72h APF, n = 7; GluClα 72h APF n= 2). Scale bars, 5 μm.

See also Figure S6.

Figure 2.5 Mmd forms a complex with GluClα

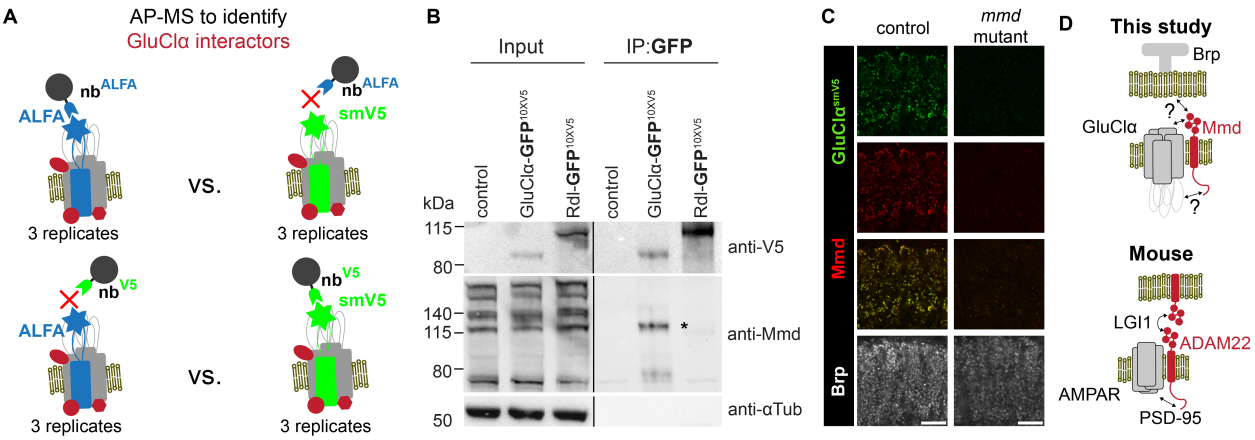

(Figure cross-referenced in Chapter 2 text as Figure 5.)

(A) Design of AP-MS experiment used to identify interactors of GluClα. Tagged proteins were purified as indicated from head homogenates and subjected to mass spectrometry. Under these conditions, a single protein, Mmd, co-purified with both tagged versions of GluClα but not in controls (see STAR Methods and Table S2). All samples represent three biological replicates.

(B) Mmd and GluClα form a complex. Immunoprecipitation experiment. Left panel, extracts from fly heads carrying smGFP-smV5-tagged GluClα and smGFP-smV5-tagged Rdl probed with anti-V5 and anti-Mmd antibodies. Right panel, a nanobody against GFP was used to pull down tagged GluClα or tagged Rdl and probed on blots as indicated. GluClα forms a complex with predominantly one form of Mmd. Asterisk, weak band co-precipitating with tagged Rdl.

(C) GluClα-smV5 staining is lost in an *mmd* mutant. Scale bar, 10 µm.

(D) Models. Bottom, synaptic complex comprising ADAM22, the mouse homolog of Mmd. ADAM22 on the postsynaptic membrane and ADAM22 or a related protein on the presynaptic membrane are bridged by interactions with a dimer of LGI1[54]; Top, localization of GluClα and Mmd at a synapse in Drosophila as shown in this study. Interactions of Mmd with other proteins are not known.

Figure 2.6 Mi9 axons form synapses juxtaposing GluClα and Mmd in distal T4 dendrites

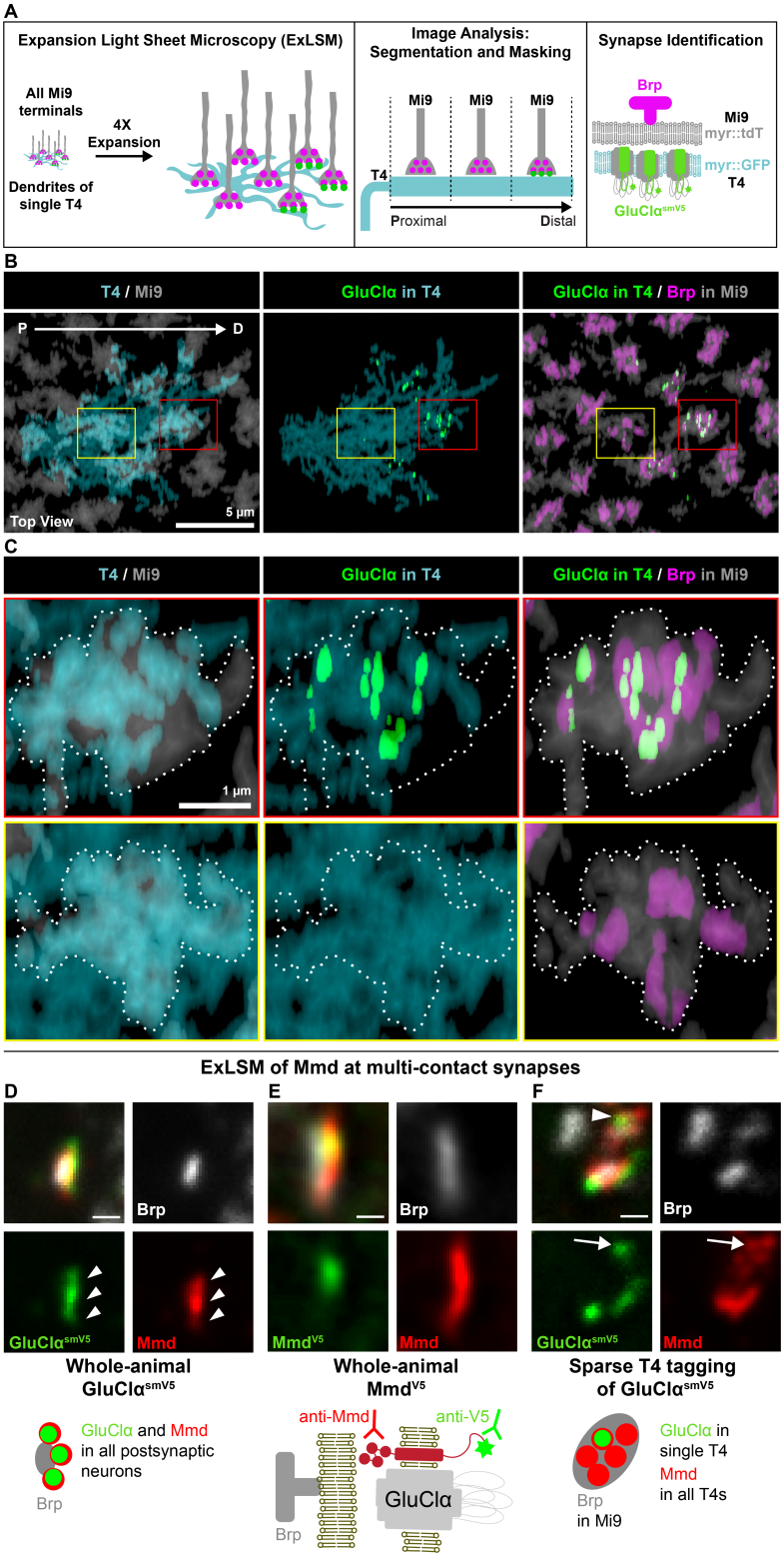

(Figure cross-referenced in Chapter 2 text as Figure 6.)

(A) Identification of synapses between identified neuron types using ExLSM. Synaptic partners, and pre- and postsynaptic proteins were visualized using four-channel light-sheet microscopy on expanded tissue (see STAR Methods). Colors correspond to expression in Panels B, and C. Arrow denotes proximo-distal axis along T4 dendrites.

(B-C) Mi9 forms synapses selectively in the distal domain of T4 dendrites. (B) T4 dendrites project across multiple columns. Mi9 axon terminals, one per column, contact all domains of T4 dendrites but only form synapses distally. (C) Upper row, synapses form between T4 and Mi9 in the distal domain (red box in B). Lower row, centrally located Mi9 terminals do not form synapses (yellow box in B).

(D) GluClα co-localizes with Mmd at multi-contact synapses. Arrowheads point to multiple postsynaptic sites at a single multi-contact synapse co-labeled with Mmd and GluClα.

(E) Mmd antibody recognizes an epitope in the Mmd ectodomain, and the V5 antibody labels a V5 tag in the cytoplasmic tail of Mmd knocked into the genomic locus.

(F) GluClα is tagged in a single T4 neuron. All other T4 synapses express Mmd but not tagged GluClα. Arrow points to a single postsynaptic site of a multiple-contact synapse co-labeled with Mmd and GluClα. Scale bars, 200 nm, represent unexpanded tissue size (adjusted for 4.65X expansion factor; see STAR Methods).

See also Figure S7.

Figure 2.7 Model: NR subunits as synaptic specificity determinants in dendrites

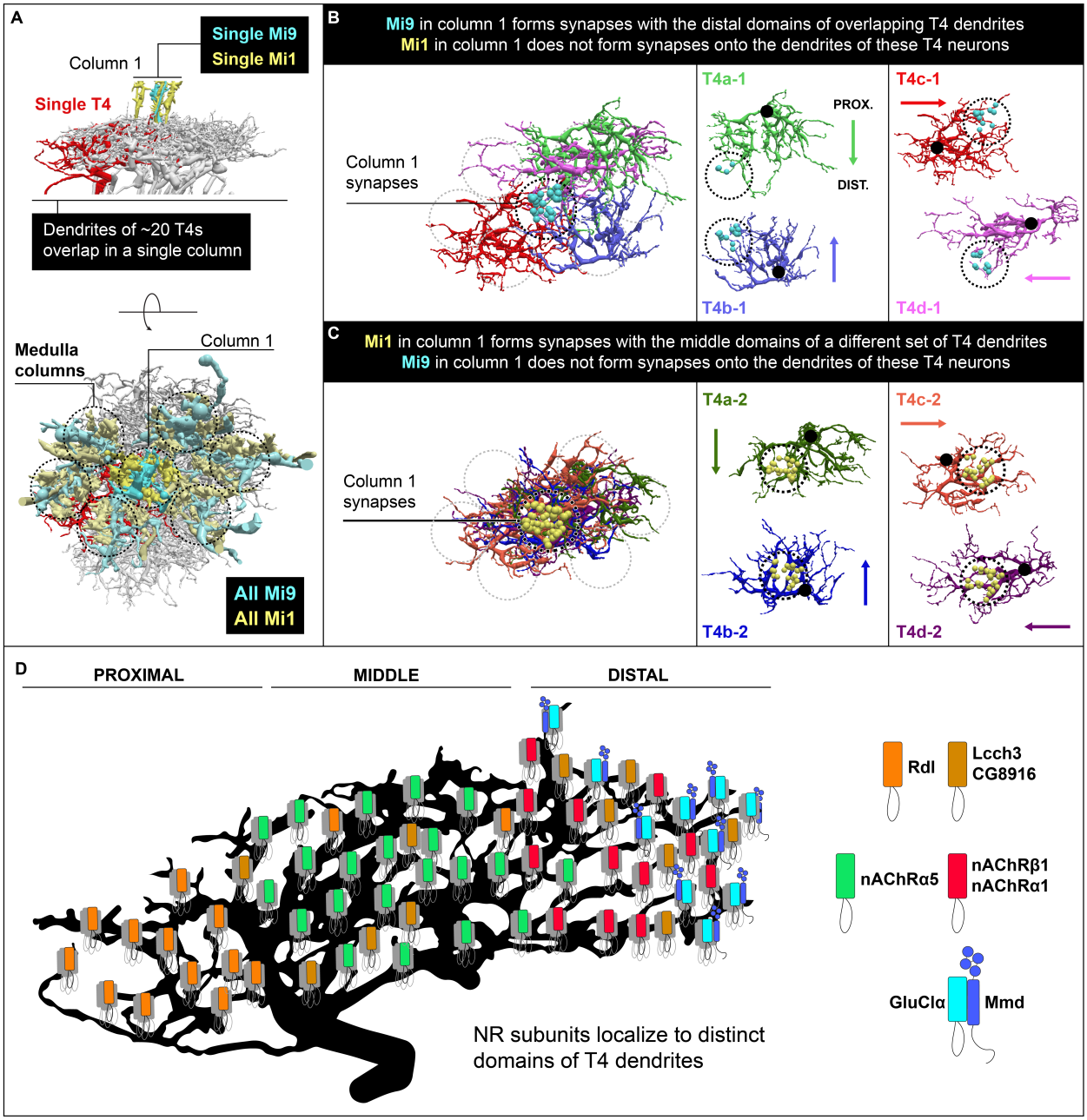

(Figure cross-referenced in Chapter 2 text as Figure 7.)

Neurons providing presynaptic inputs to T4 dendrites in each column in the medulla encounter the full range of spatial domains due to the staggered overlap of many T4 dendrites from adjacent columns. These inputs, however, discriminate between different T4 dendrites and selectively target specific dendritic domains. Based on this study, we propose that in some contexts, NRs or proteins

in complexes with them are sorted to specific dendritic spatial domains, and serve as determinants of synaptic specificity.

(A) Side and top views of 20 T4 dendrites contacting a single column. Upper panel (side view): The terminals of a single Mi9 and Mi1 in the central column (column 1) are depicted. Lower panel (top view): Dotted circular lines outline each medulla column. A single T4 dendrite is highlighted in red. Mi1 and Mi9 neurons in columns surrounding column 1 are shown in a slightly weaker shading than in column 1. The patterns of synaptic inputs to different T4s from Mi9 and Mi1 neurons in column 1 are shown in panels B and C. EM data in A-C from ref.[7].

(B-C) All T4 dendrites receive inputs from both Mi9 and Mi1 neurons. In each column, different subsets of T4 dendrites receive input from a single Mi9 (B) or a single Mi1 (C) neuron. We describe one column as an example (column 1). Each circle demarcated with dotted lines indicates a different column; each column contains a single Mi9 and a single Mi1 axon terminal. Cyan indicates synapses established selectively by Mi9 in the distal domains of T4 dendrites (B), and yellow indicates synapses formed by Mi1 in the same column selectively with the central domains of a different subset of T4 dendrites (C). Synapses formed by Mi9 and Mi1 in the surrounding adjacent medulla columns are not shown. The right panels show the individual T4 neurons with distal domains overlapping (B) and overlapping middle domains (C). Colored arrows matching the dendrite colors indicate the proximal (PROX.) to distal (DIST.) polarity of these dendrites. The large black dots indicate the base of the dendrite in the proximal domain.

(D) Summary illustrating the distribution of NR subunits across different domains of the T4 dendrites. The pattern of innervation of GABAergic, cholinergic, and glutamatergic input neurons matches the distribution of NR subunits (see Figure 3). NR subunits may serve as specificity determinants, allowing presynaptic neurons to distinguish between different T4 dendritic domains.

Alternatively, other spatial determinants, such as Mmd in T4, may recruit both NRs and presynaptic inputs to the same domain.

Figure 2.8 Tagged NR subunits localize to neuropils

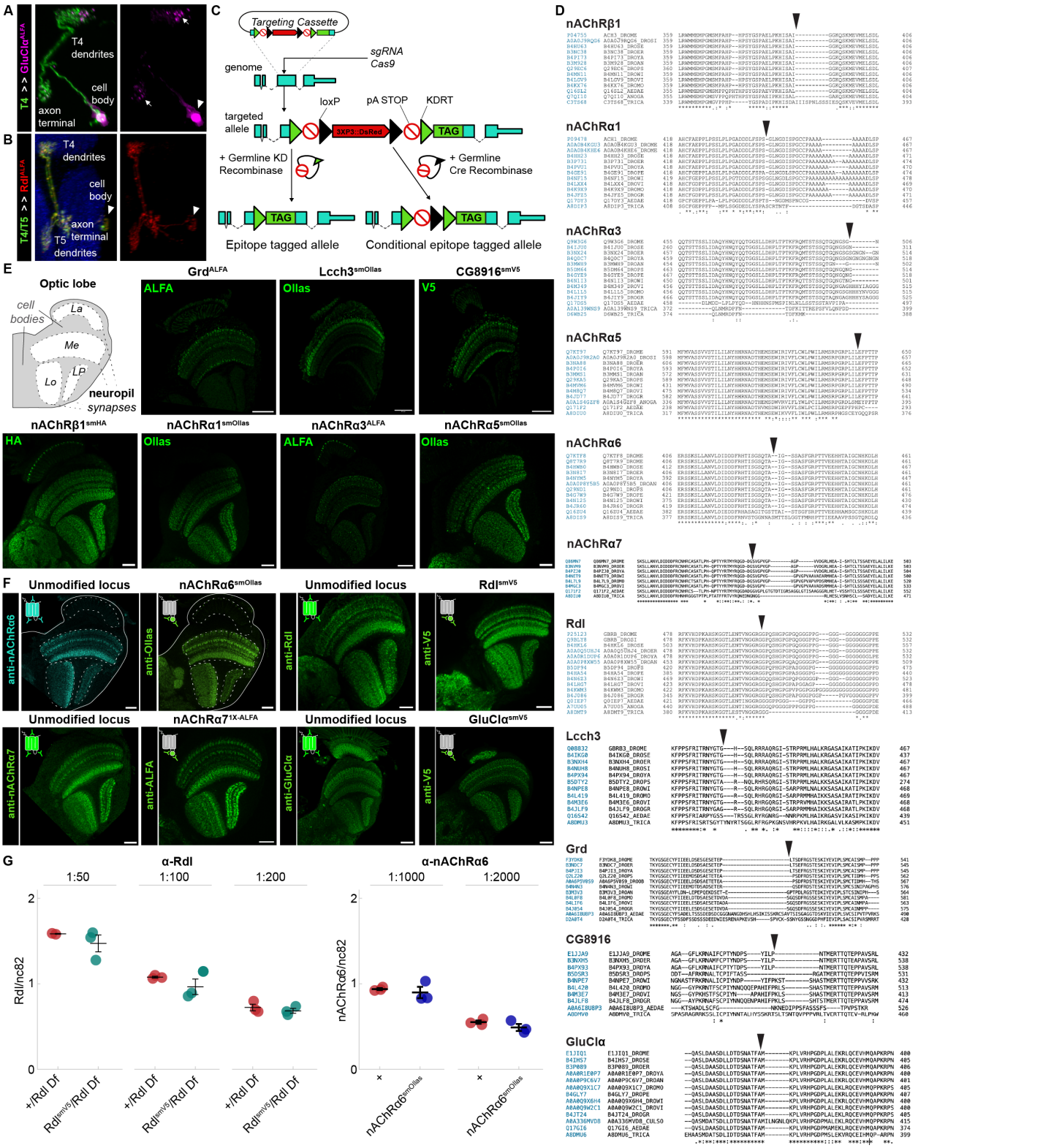

(Figure cross-referenced in Chapter 2 text as Figure S1.)

(A and B) MARCM analysis of GluClα-ALFA transgene expression in mutant GluClα T4 clones (A) or of a transgene of Rdl-ALFA in wild-type T4/T5 clones, driven by a T4/T5 GAL4 driver (B). (A) Arrowhead – accumulation of GluClα-ALFA in the cell body; arrows – GluClα puncta in dendrites and axon terminals. Cell body enrichment of GluClα is not observed with endogenously tagged GluClα (see Figures 2 and 3). (B) Rdl expression is detected throughout T4 and T5 neurons in contrast to the highly localized expression seen with endogenously tagged Rdl to T4 and T5 dendrites (see Figure 3).

(C) Generation of constitutive and conditional alleles of epitope-tagged NR subunits. A common knock-in construct for each NR subunit, as shown in A, was generated [S1, S2]. Constitutive and conditional tagged receptors were generated, as shown through passage of the knock-in through the germline carrying KD recombinase and Cre recombinase, respectively.

(D) Protein alignments of predicted NR subunit orthologs in multiple insect species (see STAR Methods for details). Regions of low conservation within the cytoplasmic loop between transmembrane domains 3 and 4 were selected for tag insertion. Insertion sites are denoted by arrowheads and listed in Table S1.

(E) Expression pattern of tagged NR subunits visualized using antibodies targeting the epitope tag (anti-V5, anti-Ollas, anti-HA, or anti-ALFA). Schematic of the Drosophila optic lobe (La, lamina; Me, medulla; Lo, lobula; LP, lobula plate). Scale bar, 25 μm.

(F) Expression pattern of endogenous and tagged neurotransmitter receptor subunits as indicated using antibodies against the native protein (left) and the epitope tag (right). Scale bar, 25 μm.

(G) Quantification of IHC signal from an antibody against the native receptor protein normalized to staining with nc82, which marks the neuropil. A region spanning all 10 medulla layers was

chosen in each optic lobe, and the mean of signal in five frames in each optic lobe region was computed. Data for each antibody are from three brains. Different antibody dilutions were used as indicated. Data are represented as mean ± SEM. The patterns of endogenous and tagged receptors visualized with the same antibody to the native proteins are similar.

Figure 2.9 Tagged NR subunits localize to synapses

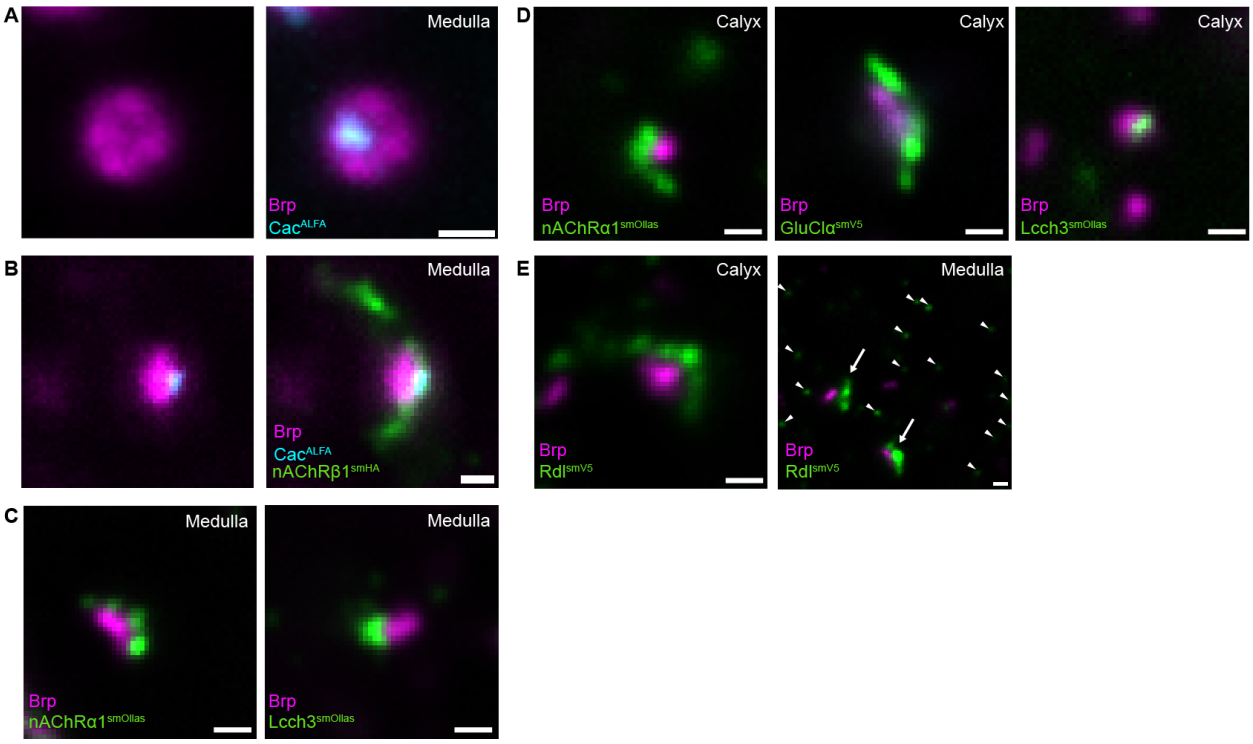

(Figure cross-referenced in Chapter 2 text as Figure S2.)

(A) Brp with Cac at its center in medulla neuropil visualized using ExLLSM, as shown for the calyx in Figure 1H. Planar view is shown.

(B) nAChRβ1 subunits cluster juxtaposed to an active zone in the medulla.

(C and D) Examples of active zones and different NR subunits paired at synapses in the medulla (C) or calyx (D) neuropils.

(E) Example of Rdl clustered at active zones (arrows) as well as isolated puncta of Rdl not associated with Brp in the medulla (arrowheads). Scale bars, 200 nm.

Figure 2.10 NR subunits localize at synapses of the mushroom body

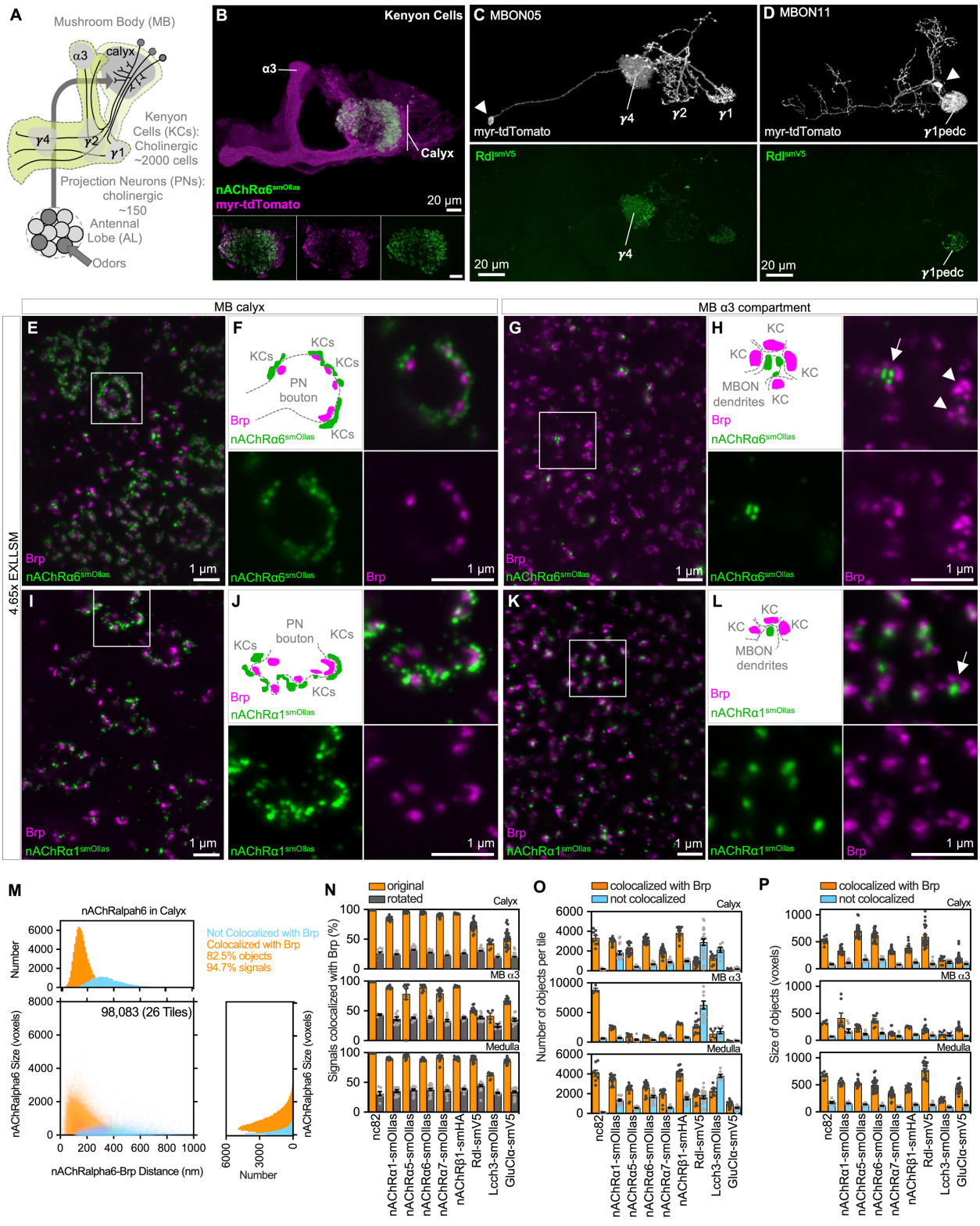

(Figure cross-referenced in Chapter 2 text as Figure S3.)

(A) A diagram of the MB circuit. Within the MB calyx, dendritic claw-like structures of multiple Kenyon cells (KCs) form synapses with the large axonal boutons of olfactory projection neurons (PN). In contrast, thin axons of KCs form converging synapses onto the dendrites of individual mushroom body output neurons (MBONs) in specific compartments of the MB lobes [S3].

(B) nAChRα6-smOllas in Kenyon cells. Inserts show magnified views of the calyx where olfactory PNs form diverging synapses with dendrites of KCs.

(C) Rdl-smV5 (bottom) and myr-tdTomato (top) in glutamatergic MBON05, which arborize dendrites in the g4 compartment and send axonal projections in the g1 and g2 compartments and outside the MB.

(D) Rdl-smV5 (bottom) and myr-tdTomato (top) in GABAergic MBON11 that arborize dendrites in the core of distal peduncle and g1 compartment (g1pedc) and send axonal projections to the α/b lobes and outside the MB.

(E) ExLLSM images of the constitutively tagged nAChRα6-smOllas and Brp labeled by nc82 antibody in the MB calyx. Projection of 6 frames is shown.

(F) Magnified view of the inset shown in E highlights a stereotypical microglomerulus where a large axonal bouton of a putative PN is surrounded by dendritic claws of KCs. Signal is organized in accordance with the characteristic arrangement of synaptic structures, as seen by EM.

(G) nAChRα6-smOllas and Brp in the α3 compartment of the MB lobe.

(H) A magnified view of G. The arrow indicates a putative “rosette synapse” where multiple KCs converge onto a single dendrite within the dendritic arbor of an MBON. The arrowheads indicate putative rosette synapses that do not stain for nAChRα6-smOllas.

(I-L) ExLLSM images of the constitutively tagged nAChRα1-smOllas and Brp in the calyx (I-J) and the α3 compartment (K-L).

(M) Colocalization analysis, as summarized in N-P, for nAChRα6-smOllas in the calyx. Top, distribution of distances between nAChRα6-smOllas and Brp for colocalized receptors (orange) and for receptors that are not colocalized with Brp (blue) (see STAR Methods). Bottom left, the size of nAChRα6-smOllas objects plotted against distance to the nearest Brp. Bottom right, the frequency distribution of the size of nAChRα6-smOllas objects. nAChRα6-smOllas objects were colocalized with Brp if they had at least a single voxel overlap or contact (see STAR Methods).

(N) The percentages of tagged-receptor signals (i.e. voxels above the threshold) in Brp- colocalized objects in the original (orange bars) and rotated (gray bars) images. Dots indicate the means of each 360x480x480 voxels tile. 8-24 tiles were analyzed for each condition. Bars represent mean ± SEM. The leftmost "nc82" bars are control experiments in which Brp was detected with nc82 primary antibody and two different secondary antibodies. All tagged-receptor signals were significantly enriched in Brp-colocalized objects compared to rotated images, except for Lcch3-smOllas in the MB α3 compartment. Sidak's multiple comparison test was used for the analysis.

(O) The numbers of tagged-receptor objects that colocalized with Brp (orange bars) or that did not colocalize (blue bars).

(P) The sizes of tagged-receptor objects that colocalized with Brp (orange bars) or that did not colocalize (blue bars). Brp-colocalized receptor objects are significantly larger than ones that did not colocalize with Brp, except for Lcch3-smOllas in the calyx and the MB α3 compartment and nAChRα7 in the MB α3 compartment. Sidak's multiple comparison test was used for this analysis. Scale bars in B and E-L panels represent unexpanded tissue size (adjusted for 4.65X expansion factor; see STAR Methods).

Figure 2.11 Tagged neurotransmitter receptor subunit distributions in Tm3 dendrites

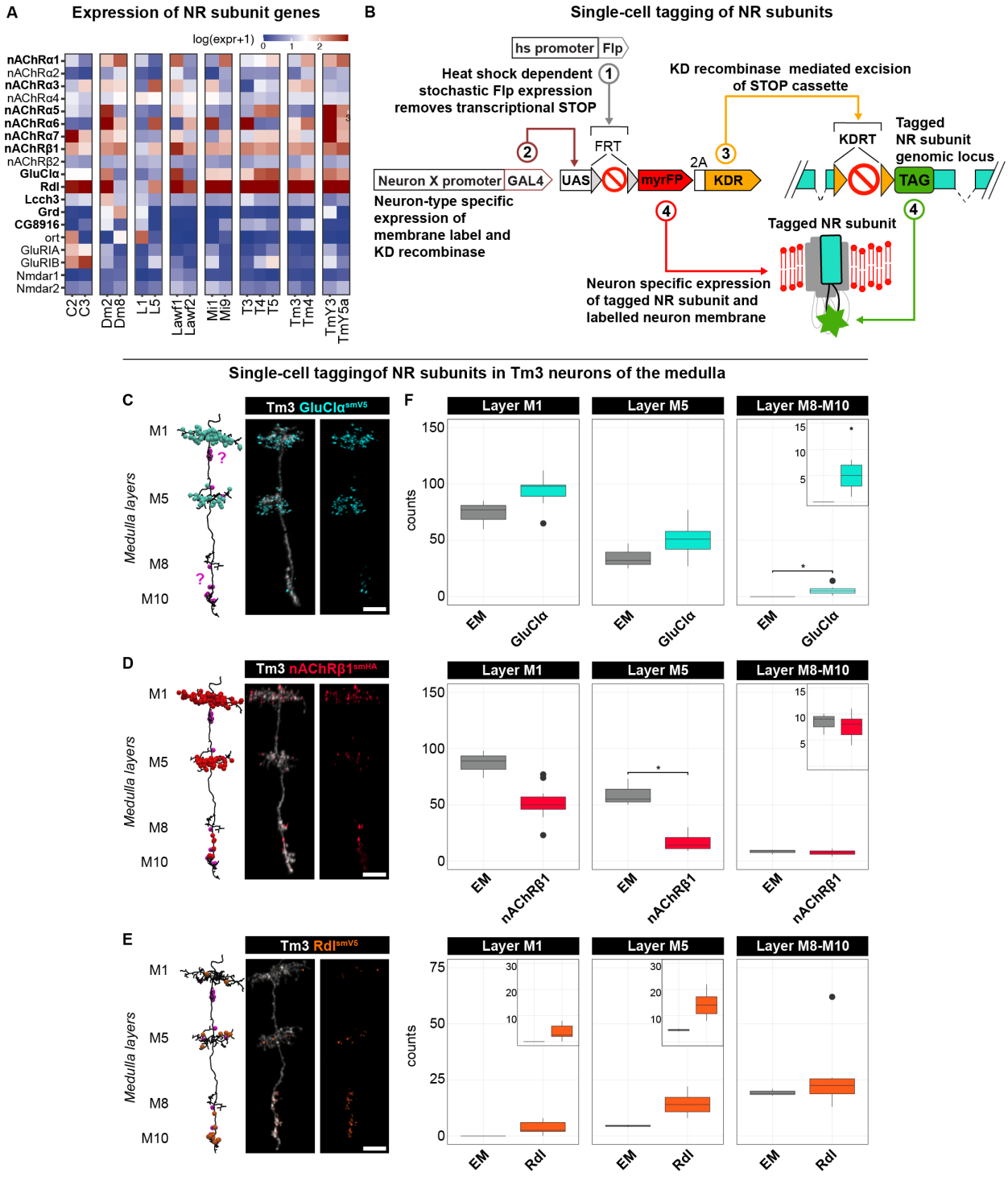

(Figure cross-referenced in Chapter 2 text as Figure S4.)

(A) NR subunit mRNA expression in optic lobe neurons from scRNA-seq at 96h after pupal formation [S4]. Bold type, tagged alleles generated in this study.

(B) Detailed step-by-step schematic illustrating the recombinase cascade that triggers the conditional tagging of NR subunits in sparsely distributed neurons.

(C-E) Localization of GluClα-smV5 (C), nAChRb1-smHA (D), and Rdl-smV5 (E) in Tm3 dendrites of the medulla. Left, morphology of reconstruction of the EM-based inputs to Tm3 neurons and annotated synapses for each neurotransmitter type; question mark on magenta synapses represents inputs from neurons of unknown neurotransmitter specificity [S5]. Right panels, neuron morphology (gray), and NR subunits in color as indicated. Scale bars, 5 μm.

(F) Quantification of data shown in A-C for several neurons (EM n=3, Rdl n=6, GluClα n=9, nAChRβ1 n=13) within each layer and of three neurons from the EM data. Bonferroni adjusted p-value (*) < 0.05 from the Wilcoxon rank-sum test.

Figure 2.12 Localization of NR subunits on T4 and T5 dendrites

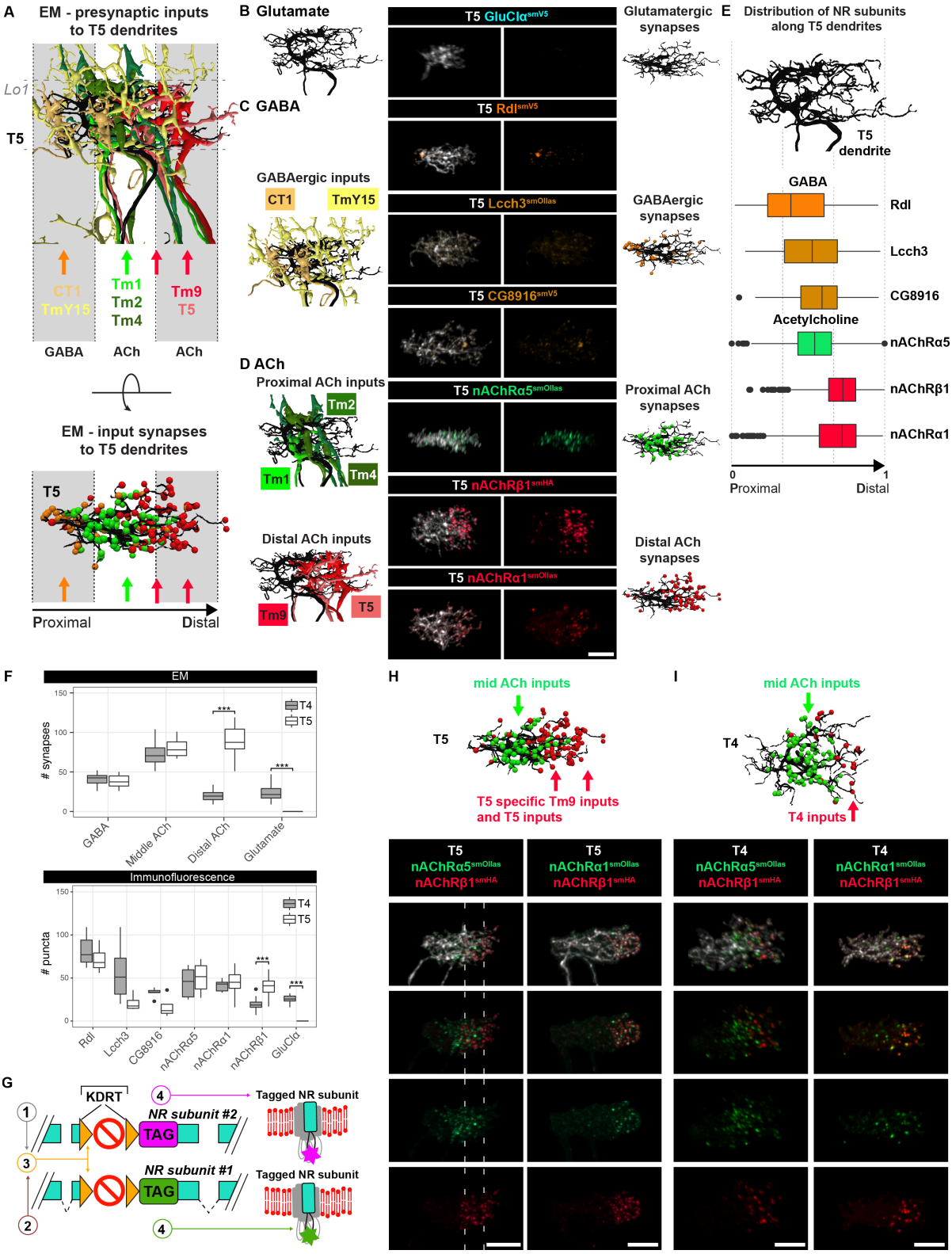

(Figure cross-referenced in Chapter 2 text as Figure S5.)

(A) Upper panel, EM reconstruction of different presynaptic inputs, as indicated, along the proximodistal axis of T5 dendrites. Dendrites span an average of three columns. Lower panel, annotated synapses for different neurotransmitter inputs are shown. Colored arrows show domains targeted by color-matched presynaptic inputs from the upper panel. TmY15 is an exception forming synapses across the length of T5 dendrites.

(B-D) Analysis of NR subunit localization in T5 dendrites as in Figures 3B-3D. Scale bars, 5 μm.

(E) Quantification of NR subunit expression along the normalized proximo-distal axis of T5 dendrites (Rdl, n = 7; Lcch3, n = 3; CG8916, n = 2; GluClα, n = 6; nAChRα1, n = 8; nAChRα5, n = 7; and nAChRβ1, n = 10).

(F) Quantification of inputs to T4 and T5 dendrites from EM reconstructions (upper panel) and this study (lower panel). Quantification of puncta from Figures 3B-3D and Figures S5B-S5D. T4 EM, n = 20. T4 immunofluorescence: Rdl, n = 11; CG8916, n = 6; Lcch3, n = 8; GluClα, n = 8; nAChRα1, n = 7; nAChRα5, n = 6; and nAChRβ1, n = 28. T5 EM, n = 20; T5 immunofluorescence: Rdl, n = 13; CG8916, n = 4; Lcch3, n = 4; GluClα, n = 6; nAChRα1, n = 12; nAChRα5, n = 8, and nAChRβ1, n = 19. Bonferroni adjusted p-value (***) < 0.001 from Wilcoxon rank-sum test for EM; p-value (***) < 0.001 from Wilcoxon rank-sum test for immunofluorescence.

(G) Genetic scheme for labeling two different NR subunits in the same neuron. The approach is analogous to the one described in Figure S4B (see steps 1-3), with the addition of an allele for the second subunit tagged with a different epitope.

(H and I) Double labeling of nAChRβ1-smHA with either nAChRα5-smOllas or nAChRα1-smOllas in single T5 dendrites (H) or T4 dendrites (I). (H) Within the overlapping region (vertical dashed lines), nAChRβ1-smHA and nAChRα5-smOllas puncta are separate, indicating that these are not at the same synapses. By contrast, nAChRβ1-smHA and nAChRα1-smOllas localization

domains within T5 dendrites have nearly complete overlap. Some puncta appear co-localized; however, at this level of resolution, it is not clear whether these NR subunits localize to the same synapses. (I) Double labeling of nAChRβ1-smHA with either nAChRα5-smOllas or nAChRα1-smOllas in single T4 dendrites. Scale bars, 5 μm.

Figure 2.13 Developmental dynamics of NR subunits expression

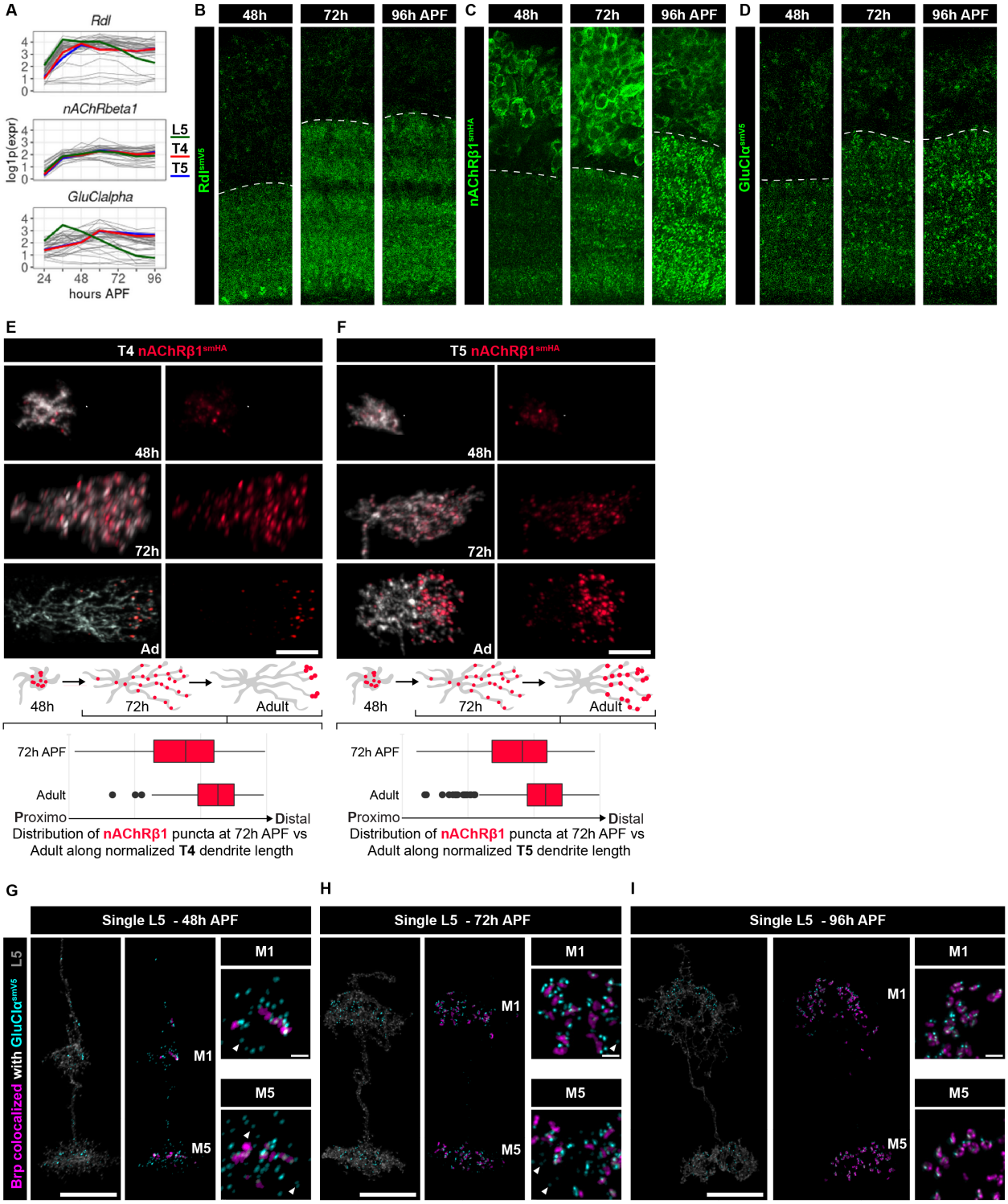

(Figure cross-referenced in Chapter 2 text as Figure S6.)

(A) Developmental expression dynamics of mRNAs of Rdl, nAChRβ1, and GluClα in distinct neuron types of the developing optic lobe as derived by scSeq data analysis [S4]. T4, T5, and L5 expression are colored as indicated.

(B-D) Immunofluorescence staining of NR subunits during development in the medulla neuropil of the optic lobe and neuronal cell bodies present in the above cortical layer. Dashed lines denote the boundary that separates the cell body layer located above the synapse-rich neuropil of the medulla. NR subunits probed in B-D, as indicated.

(E and F) Time course of nAChRβ1-smHA subunit accumulation during development of T4 (E) and T5 dendrites (F). Times shown are 48h APF, 72h APF, and adult (Ad). Schematic of dendrite development with NR subunits distribution along the normalized proximodistal axis at 72h APF and adult are shown. (T4: Adult same as in Figure 3E, nAChRβ1 72h APF n = 10: T5: Adult same as in Figure S5E, nAChRβ1 72h APF n=10).

(G-I) GluClα-smV5 localization at synapses in single L5 neurons at 48h (G), 72h (H), and 96h (I) APF in expanded tissue imaged by ExLSM. All presynaptic sites were labeled using an antibody against Brp; only colocalized Brp puncta juxtaposing GluClα-smV5 are shown. Insets show magnified images of dendritic domains in M1 or M5 layers. Arrowheads, examples of weak GluClα-smV5 puncta not juxtaposed to Brp. Scale bars for main neuron panels, 5 μm; scale bars for insets, 500 nm.

Figure 2.14 Strategy and validation of labeling of single synapses using ExLSM

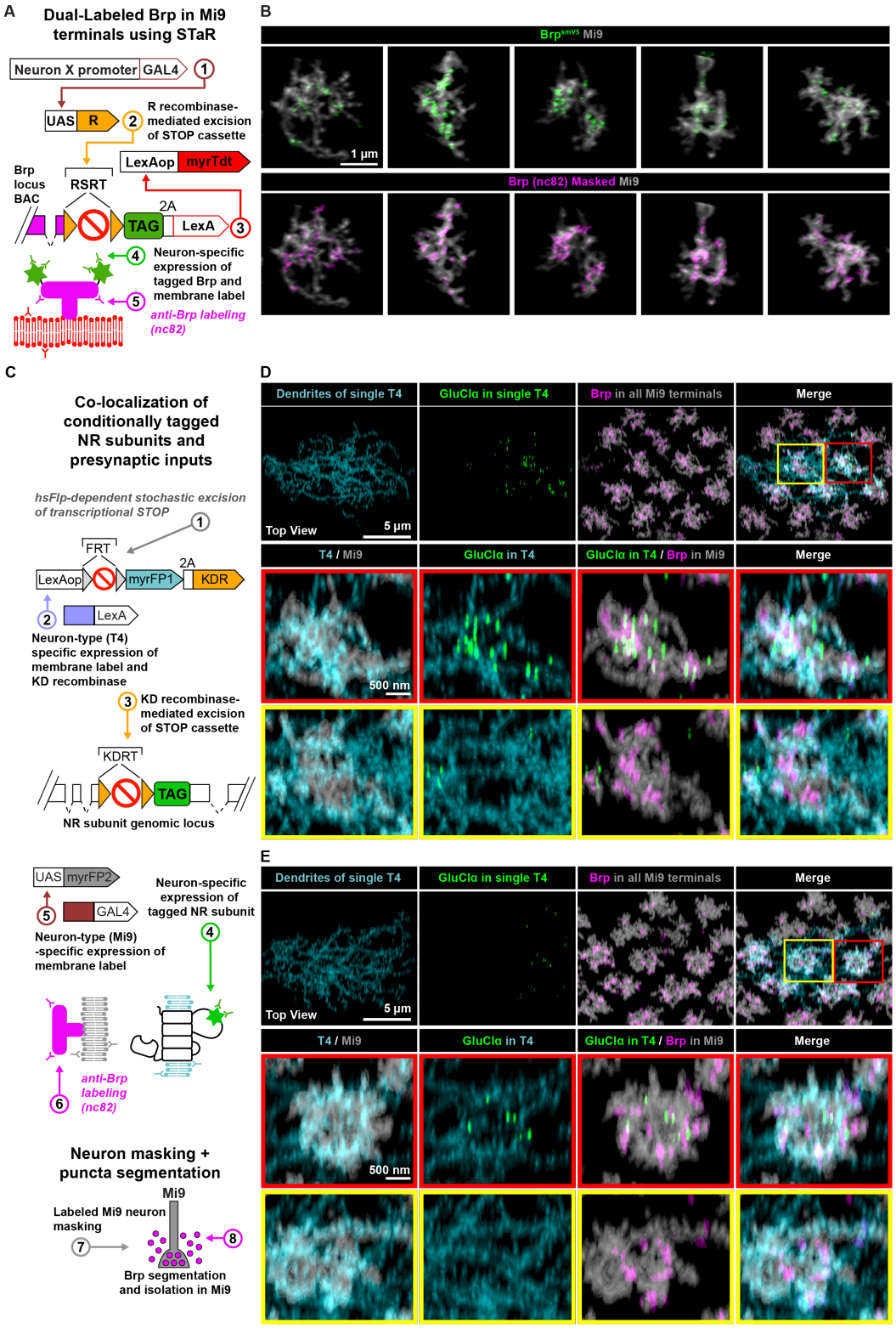

(Figure cross-referenced in Chapter 2 text as Figure S7.)

(A-B) (A) Brp-smV5 was selectively tagged in Mi9 neurons using synaptic tagging after recombination (STaR)[S6, S7], in combination with native Brp staining using the monoclonal anti-Brp antibody nc82. (B) Six examples of Mi9 axon terminals are shown with conditionally tagged Brp-smV5 and extracted nc82 signal in labeled Mi9 neurons. A separate analysis pipeline was developed for 4X-expansion light-sheet microscopy data acquired using a commercial light-sheet microscope (Zeiss LS7)(see STAR Methods).

(C-E) (C) Genetic strategy used to label GluClα in single T4 dendrites and Mi9 terminals. Presynaptic sites were labeled with Brp, and the signal was segmented and assigned to Mi9 terminals (see STAR Methods). (D-E) Representative examples from additional replicates in independent animals, as in Figures 6B-6C.

Table 2.1 List of tagged NR subunits and insertion sites

(Table cross-referenced in Chapter 2 text as Table S1.)

Gene	Reference protein isoform[a]	Insertion site[b]	Insertion location[c]	Tags[d]	gRNA-target(PAM)
nAChRβ1	FBpp0073155	I391	chr3L:4434861	smHA	CTTGGATTGCTTGCCGCCGA(TGG)
nAChRα1	FBpp0084003	S443	chr3R:24403383	smOllas	ATGTCTCCGTTGAGGCCCGA(CGG)
nAChRα3	FBpp0288426	G505	chrX:8285689	1XALFA	AGACGGGTCAGAATGGCAGC(GGG)
nAChRα5	FBpp0089367	L644	chr2L:14088048	smOllas	AGGGCGTGGTCGGGAACTCC(AGG)
nAChRα6	FBpp0079505	A404	chr2L:9797925	smOllas	TTACGCCGACGAGCCAATGG(CGG)
nAChRα7	FBpp0089248	G464	chrX:19330238	smOllas 1XALFA	GTGACGGCAGCGTGGGACCCG(TGG)
Rdl	FBpp0076261	R501	ch3L: 9151410	smV5 smHA 1XALFA	ACGGTGAATGGCGGACGCGG(TGG)
Lcch3	FBpp0089263	T427	chrX: 15928138	smOllas	ACGTCTAAGCTGGCTATGTC(CGG)
Grd	FBpp0074905	P504	chr3L:17838128	1XALFA	AGCCACTGACCTCGGACTTT(CGG)
CG8916	FBpp0290450	P517	chrX:15924237	smV5	CGTTTGGGTGGTTCTCTCCA(TGG)
GluClα	FBpp0307401	A375	chr3R:19765748	smV5	TAGCAATGCAACGTTCGCAA(TGG)

[a] Flybase protein isoform reference for amino acid insertion site.
[b] Targeted exon is common to all annotated protein isoforms (FlyBase r. FB2023_01).
[c] Coordinates based on dm6 *D. melanogaster* reference genome.
[d] smX – smGdP – spaghetti monster Green darkened Protein tagged with 10 copies of the indicate epitope tag.

Insertion sites relative to a reference protein isoform are reported alongside inserted tags and gRNA target sequences.

Table 2.2 Putative GluClα interactors as identified by AP-MS

(Table cross-referenced in Chapter 2 text as Table S2.)

Protein	GeneName	Comparison	log2FC	Pvalue	adj.pvalue	imputed	iLog2FC	iPvalue
E1JIQ1	GluClα	nbV5::GluClα-smV5 vs. nbV5::GluClα-1XALFA	#NUM!	–	0	yes	6.31E+00	3.79E-02
Q9VXL1	mmd	nbV5::GluClα-smV5 vs. nbV5::GluClα-1XALFA	#NUM!	–	0	yes	6.07E+00	3.52E-02
E1JIQ1	GluClα	nbALFA::GluClα-1XALFA vs. nbALFA::GluClα-smV5	7.89E+00	5.30E-05	1.17E-02	no	7.89E+00	1.17E-02
M9NH46	mmd	nbALFA::GluClα-1XALFA vs. nbALFA::GluClα-smV5	#NUM!	–	0	yes	3.15E+00	1.78E-02
Q9VXL1	Mmd	nbALFA::GluClα-1XALFA vs. nbALFA::GluClα-smV5	4.90E+00	4.24E-06	1.88E-03	no	4.90E+00	1.88E-03

The statistical analysis package ArtMS was used to identify proteins that were differentially enriched during pull-down experiments using a nanobody against either the ALFA or V5 tag. Pull-downs followed by LC-MS/MS were conducted on triplicate samples of brain homogenates from either GluClα-1XALFA or GluClα-smV5 (Figure 5A), and proteins were quantified using MS1-based label- free

quantitation. Listed are proteins that showed significant enrichment in the experimental samples when compared to the negative control (e.g., nb ALFA on GluClα-1XALFA vs. nb ALFA on GluClα-smV5) and were identified using both a nanobody against the ALFA tag and the V5 tag. Imputed indicates proteins that were identified solely in the experimental sample and not in the negative control. For proteins that were not identified in the negative control, the measured fold enrichment is undefined (#NUM!). In these cases, we imputed values in the negative control corresponding to the intensity of the least abundant proteins in that sample and then calculated the enrichment (iLog2FC) and p-values (iPvalue) after imputation.

Table 2.3 Table of genotypes and staining conditions for each figure panel

(Table cross-referenced in Chapter 2 text as Table S3.)

Figure panel	Subpanel	Genotype	Fixative	Mounting	Primary antibody	Secondary antibody
Figure 1						
1B	nAChRα6-smOllas	w; nAChRα6-KDRT-smGdP-10xOllas/+;	addaxS	DPX	1:20 nc82 (anti-Brp, mouse IgG1), 1:10,000 rabbit anti-Ollas	1:500 goat anti-mouse IgG1 CF405S (Biotium), 1:500 goat anti-rabbit AF488 (Abcam)
	nAChRα7-smOllas	w, nAChRα7-KDRT-smGdP-10xOllas/+;;	addaxS	DPX	1:20 nc82 (anti-Brp, mouse IgG1), 1:10,000 rabbit anti-Ollas	1:500 goat anti-mouse IgG1 CF405S (Biotium), 1:500 goat anti-rabbit AF488 (Abcam)

1E	MBON14 panel	w, P{w+, pBPhsFlp2PEST}attP3; P{w+, 10xUAS-FRT-STOP-FRT-myrTdt-2A-KDR.PEST}attP5/+; P{w+, R23C06-GAL4.DBD}attP2, PBac{w+, R40B08-p65.AD}VK00027/nAChRβ1-KDRT-stop-KDRT-smGdP-10xHA	3% glyoxal fixative	DPX	1:10 nc82 (anti-Brp, mouse IgG1), 1:1,000 guinea pig anti-RFP, 1:100 rat anti-HA	1:500 goat anti-mouse CF633 (Biotium), 1:500 goat-anti-guinea pig AF568 (Invitrogen), 1:250 goat-anti-rat AF488 (Jackson)

	MBON13 panel	w, P{w+, pBPhsFlp2PEST}attP3; P{w+, 10xUAS-FRT-STOP-FRT-myrTdt-2A-KDR.PEST}attP5/+; P{w+, R23C06-GAL4.DBD}attP2, PBac{w+, R40B08-p65.AD}VK00027/nAChRβ1-KDRT-stop-KDRT-smGdP-10xHA	3% glyoxal fixative	DPX	1:10 nc82 (anti-Brp, mouse IgG1), 1:1,000 guinea pig anti-RFP, 1:100 rat anti-HA	1:500 goat anti-mouse CF633 (Biotium), 1:500 goat-anti-guinea pig AF568 (Invitrogen), 1:250 goat-anti-rat AF488 (Jackson)

1F	MBON14 panel	w, P{w+, pBPhsFlp2PEST}attP3; P{w+, 10xUAS-FRT-STOP-FRT-myrTdt-2A-KDR.PEST}attP5/+; P{w+, R23C06-GAL4.DBD}attP2, PBac{w+, R40B08-p65.AD}VK00027/Rdl-KDRT-STOP-KDRT-smGdP-10xV5	3% glyoxal fixative	DPX	1:10 nc82 (anti-Brp, mouse IgG1), 1:1,000 guinea pig anti-RFP, 1:500 chicken anti-V5	1:500 goat anti-mouse CF633 (Biotium), 1:500 goat-anti-guinea pig AF568 (Invitrogen), 1:250 goat-anti-chicken AF488 (Jackson)

	MBON13 panel	w, P{w+, pBPhsFlp2PEST}attP3; P{w+, 10xUAS-FRT-STOP-FRT-myrTdt-2A-KDR.PEST}attP5/+; P{w+, R23C06-GAL4.DBD}attP2, PBac{w+, R40B08-p65.AD}VK00027/Rdl-KDRT-STOP-KDRT-smGdP-10xV5	3% glyoxal fixative	DPX	1:10 nc82 (anti-Brp, mouse IgG1), 1:1,000 guinea pig anti-RFP, 1:500 chicken anti-V5	1:500 goat anti-mouse CF633 (Biotium), 1:500 goat-anti-guinea pig AF568 (Invitrogen), 1:250 goat-anti-chicken AF488 (Jackson)

1H, 1J, S2A-S2B		w, Cac-1XALFA;;nAChRβ1-KDRT-smGdP-10xHA	3% glyoxal fixative	ExLLSM	1:10 nc82 (anti-BRP, mouse IgG1), 1:500 guinea pig fc::nb anti-ALFA, 1:100 rat anti-HA	1:500 goat anti-mouse atto647N, 1:500 goat-anti-guinea pig AF568 (Invitrogen), 1:250 goat-anti-rat AF488 (Jackson)
1L, 1M	nAChRα5-smGdP-10xOllas panel	w; nAChRα5-KDRT-smGdP-10xOllas/+;	3% glyoxal fixative	ExLLSM	1:10 nc82 (anti-Brp, mouse IgG1), 1:1,000 rat anti-Ollas	1:500 goat anti-mouse CF633 (Biotium), 1:250 goat-anti-rat AF488 (Jackson)

1L, 1M	nAChRα6-smGdP-10xOllas panel	w; nAChRα6-KDRT-smGdP-10xOllas/+;	3% glyoxal fixative	ExLLSM	1:10 nc82 (anti-Brp, mouse IgG1), 1:1,000 rat anti-Ollas	1:500 goat anti-mouse CF633 (Biotium), 1:250 goat-anti-rat AF488 (Jackson)
1M, S2D	GluClα-smGdP-10xV5 panel	w;; GluClα-KDRT-smGdP-10xV5/+	3% glyoxal fixative	ExLLSM	1:10 nc82 (anti-Brp, mouse IgG1), 1:500 chicken anti-V5	1:500 goat anti-mouse CF633 (Biotium), 1:250 goat-anti-chicken AF488 (Jackson)

1M, S2E	Rdl-smGdP-10xV5 panel	w;; Rdl-KDRT-smGdP-10xV5/+	3% glyoxal fixative	ExLLSM	1:10 nc82 (anti-Brp, mouse IgG1), 1:500 chicken anti-V5	1:500 goat anti-mouse CF633 (Biotium), 1:250 goat-anti-chicken AF488 (Jackson)
Figure 2						
2B	Brp	w, nAChRα7-KDRT-smGdP-10xOllas;;	addaxS	DPX	1:20 nc82 (anti-Brp, mouse IgG1), 1:10,000 rat anti-Ollas	1:500 FluoTag X2 anti-mouse IgG1 Atto647N (NanoTag), 1:500 goat anti-rat AF488 (Abcam)
2B, S1F	Rdl-smGdP-10xV5	w;;Rdl-KDRT-smGdP-10xV5/+	addaxS	DPX	1:500 mouse IgG2a anti-V5	1:500 goat anti-mouse AF488 (Invitrogen)

2B, S1E	Lcch3-smGdP-10xOllas	w, Lcch3-KDRT-smGdP-10xOllas/+;;	addaxS	DPX	1:10,000 rabbit anti-Ollas	1:500 goat anti-rabbit CF633 (Biotium)
2B, S1E	Grd-ALFA	w;;Grd-KDRT-1XALFA/+	addaxS	DPX	1:200 FluoTag X2 anti-ALFA::Atto488	
2B, S1E	CG8916-smGdP-10xV5	yw, CG8916-KDRT-smGdP-10xV5/w;;	addaxS	DPX	1:500 mouse IgG2a anti-V5	1:500 goat anti-mouse AF488 (Invitrogen)
2B, S1F	GluClα-smGdP-10xV5	w;;GluClα-KDRT-smGdP-10xV5/+	addaxS	DPX	1:500 mouse IgG2a anti-V5	1:500 goat anti-mouse AF488 (Invitrogen)
2B	nAChRβ1-smGdP-10xHA	w;;nAChRβ1-KDRT-smGdP-10xHA/+	addaxS	DPX	1:1,000 rat anti-HA; 1:200 rabbit anti-DsRed	1:500 goat anti-rat AF488 (Abcam); 1:500 nb anti-rabbit Atto565 (NanoTag)
2B, S1E	nAChRα1-smGdP-10xOllas	w;;nAChRα1-KDRT-smGdP-10xOllas/+	addaxS	DPX	1:10,000 rat anti-Ollas	1:500 goat anti-rat AF488 (Abcam)

2B, S1E	nAChRα3-ALFA	yw, nAChRα3-KDRT-1XALFA/w;;	addaxS	DPX	1:200 FluoTag X2 anti-ALFA::Atto488	
2B, S1E	nAChRα5-smGdP-10xOllas	w;nAChRα5-KDRT-smGdP-10xOllas/+;	addaxS	DPX	1:10,000 rat anti-Ollas	1:500 goat anti-rat AF488 (Abcam)
2B	nAChRα6-smGdP-10xOllas	w;nAChRα6-KDRT-smGdP-10xOllas/+;	addaxS	DPX	1:10,000 rat anti-Ollas	1:500 goat anti-rat AF488 (Abcam)
2B	nAChRα7-1XALFA	w, nAChRα7-KDRT-1XALFA/+;;	addaxS	DPX	1:200 FluoTag X2 anti-ALFA::Atto488	

2C, 2F	L5 GluClα-smGdP-10xV5	w, P{w+, hs-FLPG5.PEST.Opt)attP3/w; P{w+, 10xUAS-FRT-STOP-FRT-myrTdt-2A-KDR.PEST}attP5/+; P{w+, GMR64B07-Gal4}attP2/GluClα-KDRT-STOP-KDRT-smGdP-10xV5	addaxS	DPX	1:500 mouse IgG2a anti-V5, 1:500 rabbit anti-DsRed	1:500 goat anti-mouse AF488 (Invitrogen), 1:500 goat anti-rabbit AF568 (Invitrogen)

2D, 2F	L5 nAChRβ1-smGdP-10xHA	w, P{w+, hs-FLPG5.PEST.Opt)attP3/w; P{w+, 10xUAS-FRT-STOP-FRT-myrTdt-2A-KDR.PEST}attP5/+; P{w+, GMR64B07-Gal4}attP2/nAChRβ1-KDRT-STOP-KDRT-smGdP-10xHA	addaxS	DPX	1:1,000 rat anti-HA, 1:500 rabbit anti-DsRed	1:500 goat anti-rat AF488 (Abcam), 1:500 goat anti-rabbit AF568 (Invitrogen)

2E, 2F	L5 Rdl-smGdP-10xV5	w, P{w+, hs-FLPG5.PEST.Opt)attP3/w; P{w+, 10xUAS-FRT-STOP-FRT-myrTdt-2A-KDR.PEST}attP5/+; P{w+, GMR64B07-Gal4}attP2/Rdl-KDRT-STOP-KDRT-smGdP-10xV5	addaxS	DPX	1:500 mouse IgG2a anti-V5, 1:500 rabbit anti-DsRed	1:500 goat anti-mouse AF488 (Invitrogen), 1:500 goat anti-rabbit AF568 (Invitrogen)

2G	T4 GluClα-smGdP-10xV5	w, P{w+, hs-FLPG5.PEST.Opt)attP3/w; P{w+, GMR42F06-Gal4}attP40/+; P{w+, 13xLexAoP-FRT-STOP-FRT-myrGFP-2A-KDR.PEST}attP1/GluClα-KDRT-STOP-KDRT-smGdP-10xV5	addaxS	DPX	1:500 mouse IgG2a anti-V5:DL550, 1:1,000 chicken anti-GFP	1:500 goat anti-chicken AF488 (Invitrogen)
Figure 3						

3B, S5B		w, P{w+, hs-FLPG5.PEST.Opt)attP3/w; P{w+, 10xUAS-FRT-STOP-FRT-myrGFP-2A-KDR.PEST}attP40/+; P{w+, GMR42F06-Gal4}attP2/GluClα-KDRT-STOP-KDRT-smGdP-10xV5	addaxS	DPX	1:500 mouse IgG2a anti-V5:DL550, 1:1,000 chicken anti-GFP	1:500 goat anti-chicken AF488 (Invitrogen)

3C, S5C	Rdl panel	w, P{w+, hs-FLPG5.PEST.Opt)attP3/w; P{w+, 10xUAS-FRT-STOP-FRT-myrGFP-2A-KDR.PEST}attP40/+; P{w+, GMR42F06-Gal4}attP2/Rdl-KDRT-STOP-KDRT-smGdP-10xV5	addaxS	DPX	1:500 mouse IgG2a anti-V5:DL550, 1:1,000 chicken anti-GFP	1:500 goat anti-chicken AF488 (Invitrogen)

	Lcch3 panel	w, P{w+, hs-FLPG5.PEST.Opt)attP3/ Lcch3-KSK-smGdP-10xOllas; P{w+, 10xUAS-FRT-STOP-FRT-myrGFP-2A-KDR.PEST}attP5/+; P{w+, GMR42F06-Gal4}attP2/+	addaxS	DPX	1:10,000 rabbit anti-Ollas, 1:1,000 chicken anti-GFP	1:500 AbberiorStar635P Fluo Tag X4 anti-rabbit (NanoTag), 1:500 goat anti-chicken AF488 Plus (Invitrogen)

	CG8916 panel	w, P{w+, hs-FLPG5.PEST.Opt)attP3/ yw, CG8916-KSK-smGdP-10xV5; P{w+, 10xUAS-FRT-STOP-FRT-myrGFP-2A-KDR.PEST}attP5/+; P{w+, GMR42F06-Gal4}attP2/+	addaxS	DPX	1:500 mouse IgG2a anti-V5, 1:1,000 chicken anti-GFP	1:500 goat anti-mouse AF568 (Invitrogen), 1:500 goat anti-chicken AF488 Plus (Invitrogen)

3D, S5D	nAChRα5 panel	w, P{w+, hs-FLPG5.PEST.Opt)attP3/w; P{w+, 10xUAS-FRT-STOP-FRT-myrGFP-2A-KDR.PEST}attP40/nAChRα5-KDRT-STOP-KDRT-smGdP-10xOllas; P{w+, GMR42F06-Gal4}attP2/+	addaxS	DPX	1:10,000 rabbit anti-Ollas, 1:1,000 chicken anti-GFP	1:500 goat anti-rabbit AF568 (Abcam), 1:500 goat anti-chicken AF488 Plus (Invitrogen)

	nAChRβ1 panel	w, P{w+, hs-FLPG5.PEST.Opt)attP3/w; P{w+, 10xUAS-FRT-STOP-FRT-myrGFP-2A-KDR.PEST}attP40/+; P{w+, GMR42F06-Gal4}attP2/nAChRβ1-KDRT-STOP-KDRT-smGdP-10xHA	addaxS	DPX	1:1,000 rat anti-HA, 1:1,000 chicken anti-GFP	1:500 goat anti-rat AF568 (Abcam), 1:500 goat anti-chicken AF488 Plus (Invitrogen)

	nAChRα1 panel	w, P{w+, hs-FLPG5.PEST.Opt)attP3/ w; P{w+, 10xUAS-FRT-STOP-FRT-myrGFP-2A-KDR.PEST}attP40/+; P{w+, GMR42F06-Gal4}attP2/nAChRα1-KDRT-STOP-KDRT-smGdP-10xOllas	addaxS	DPX	1:10,000 rabbit anti-Ollas, 1:1,000 chicken anti-GFP	1:500 goat anti-rabbit AF568 (Abcam), 1:500 goat anti-chicken AF488 Plus (Invitrogen)
Figure 4						

4A, 4B		w, P{w+, hs-FLPG5.PEST.Opt)attP3/w; P{w+, 10xUAS-FRT-STOP-FRT-myrGFP-2A-KDR.PEST}attP40/+; P{w+, GMR42F06-Gal4}attP2/Rdl-KDRT-STOP-KDRT-smGdP-10xV5	addaxS	DPX	1:500 mouse IgG2a anti-V5:DL550, 1:1,000 chicken anti-GFP	1:500 goat anti-chicken AF488 (Invitrogen)

4C, 4D		w, P{w+, hs-FLPG5.PEST.Opt)attP3/w; P{w+, 10xUAS-FRT-STOP-FRT-myrGFP-2A-KDR.PEST}attP40/+; P{w+, GMR42F06-Gal4}attP2/GluClα-KDRT-STOP-KDRT-smGdP-10xV5	addaxS	DPX	1:500 mouse IgG2a anti-V5:DL550, 1:1,000 chicken anti-GFP	1:500 goat anti-chicken AF488 (Invitrogen)

4E		w, P{w+, hs-FLPG5.PEST.Opt)attP3/w; P{w+, 10xUAS-FRT-STOP-FRT-myrTdt-2A-KDR.PEST}attP5/+; P{w+, GMR64B07-Gal4}attP2/Rdl-KDRT-STOP-KDRT-smGdP-10xV5	addaxS	DPX	1:500 mouse IgG2a anti-V5, 1:500 rabbit anti-DsRed	1:500 goat anti-mouse AF488 (Invitrogen), 1:500 goat anti-rabbit AF568 (Invitrogen)

4F		w, P{w+, hs-FLPG5.PEST.Opt)attP3/w; P{w+, 10xUAS-FRT-STOP-FRT-myrTdt-2A-KDR.PEST}attP5/+; P{w+, GMR64B07-Gal4}attP2/GluClα-KDRT-STOP-KDRT-smGdP-10xV5	addaxS	DPX	1:500 mouse IgG2a anti-V5, 1:500 rabbit anti-DsRed	1:500 goat anti-mouse AF488 (Invitrogen), 1:500 goat anti-rabbit AF568 (Invitrogen)
Figure 5						

5C	control	w/Y;;GluClα-KDRT-smGdP-10xV5/+	addaxS	DPX	1:20 nc82 (anti-Brp, mouse IgG1), 1:500 mouse IgG2a anti-V5, 1:500 rabbit anti-Mmd	1:500 goat anti-mouse IgG1 AF568 (Invitrogen), 1:500 goat anti-mouse IgG2a AF488 (Invitrogen), 1:500 goat anti-rabbit AF647 (Invitrogen)
	mmd mutant	slrp[1]/Y;;GluClα-KDRT-smGdP-10xV5/+	addaxS	DPX	1:20 nc82 (anti-Brp, mouse IgG1), 1:500 mouse IgG2a anti-V5, 1:500 rabbit anti-Mmd	1:500 goat anti-mouse IgG1 AF568 (Invitrogen), 1:500 goat anti-mouse IgG2a AF488 (Invitrogen), 1:500 goat anti-rabbit AF647 (Invitrogen)

Figure 6						
6B-6C, S7D-S7E		w, P{w+, hs-FLPG5.PEST.Opt)attP3/ w, 10xUAS-myrTdt; P{w+, GMR42F06-LexA}attP40/P{w+, R48A07-p65.AD}attP40; GluClα-KDRT-STOP-KDRT-smGdP-10xV5, P{w+, 13xLexAoP-FRT-STOP-FRT-myrGFP-2A-KDR.PEST}attP1/P{w+, VT046779-DBD}attP2	addaxS	ExLSM	1:7.2 nc82 (anti-Brp, mouse IgG1), 1:500 chicken anti-GFP, 1:100 mouse IgG2a anti-V5, 1:100 rabbit anti-DsRed	1:100 goat anti-mouse IgG1 CF405S (Biotium), 1:100 goat anti-chicken IgY (H+L) AF488 (Invitrogen), 1:100 goat anti-mouse IgG2a AF546 (Invitrogen), 1:100 Fab goat anti-rabbit IgG Fc SeTau647 (labeled in-house, Jackson/SETA BioMedicals)

6D		w;; GluClα-KDRT-smGdP-10xV5/+	addaxS	ExLSM	1:7.2 nc82 (anti-Brp, mouse IgG1), 1:100 mouse IgG2a anti-V5, 1:100 rabbit anti-Mmd	1:100 goat anti-mouse IgG1 CF405S (Biotium), 1:100 goat anti-mouse IgG2a AF546 (Invitrogen), 1:100 goat anti-rabbit AF488 (Abcam)
6E		w, mmd[Tag:V5.FRT]/Y;;	addaxS	ExLSM	1:7.2 nc82 (anti-Brp, mouse IgG1), 1:100 mouse IgG2a anti-V5, 1:100 rabbit anti-Mmd	1:100 goat anti-mouse IgG1 CF405S (Biotium), 1:100 goat anti-mouse IgG2a AF546 (Invitrogen), 1:100 goat anti-rabbit AF488 (Abcam)

6F		w, P{w+, hs-FLPG5.PEST.Opt)attP3/w; P{w+, 10xUAS-FRT-STOP-FRT-myrGFP-2A-KDR.PEST}attP40/+; P{w+, GMR42F06-Gal4}attP2/GluClα-KDRT-STOP-KDRT-smGdP-10xV5	addaxS	ExLSM	1:7.2 nc82 (anti-Brp, mouse IgG1), 1:100 mouse IgG2a anti-V5, 1:100 rabbit anti-Mmd	1:100 goat anti-mouse IgG1 CF405S (Biotium), 1:100 goat anti-mouse IgG2a AF546 (Invitrogen), 1:100 goat anti-rabbit AF488 (Abcam)
Figure S1						

S1A	UAS-GluClα-ALFA	w; P{5XUAS-GluCla_ALFA}attP5/P{hs-FLPG5.PEST.Opt)attP40, P{10xUAS-myr::GFP}attP5; P{neoFRT}82B, P{tubP-GAL80}LL3/P{GMR42F06-Gal4}attP2, P{neoFRT}82B, GluClα-KDRT-STOP-KDRT-smGdP-10xV5	addaxS	DPX	1:2,000 chicken anti-GFP, 1:200 FluoTag X2 anti-ALFA::AF568	1:500 anti-chicken AF488 (Invitrogen)

S1B	UAS-Rdl-ALFA	w; P{5XUAS-Rdl_ALFA}attP5/P{hs-FLPG5.PEST.Opt)attP40, P{10xUAS-myr::GFP}attP5; P{neoFRT}82B, P{tubP-GAL80}LL3/P{GMR42F06-Gal4}attP2, P{neoFRT}82B	addaxS	DPX	1:2,000 chicken anti-GFP, 1:200 FluoTag X2 anti-ALFA::AF568, 1:20 nc82 (anti-Brp, mouse IgG1)	1:500 anti-chicken AF488 (Invitrogen), 1:500 mouse anti-mouse AF647 (Invitrogen)
S1E	nAChRβ1-smGdP-10xHA	w;;nAChRβ1-KDRT-smGdP-10xHA/+	addaxS	DPX	1:1,000 rat anti-HA	1:500 goat anti-rat AF488 (Abcam)
S1F	endogenous nAChRα6	w1118;;	3% glyoxal fixative	everbrite	1:1,000 rabbit anti-nAChRα6	1:500 goat anti-rabbit AF568 (Invitrogen)

S1F	nAChRα6-smGdP-10xOllas	w;nAChRα6-KDRT-smGdP-10xOllas/+;	3% glyoxal fixative	everbrite	1:10,000 rat anti-Ollas	1:500 goat anti-rat AF488 (Abcam)
S1F	endogenous nAChRα7	w1118;;	addaxS	DPX	1:1,000 rabbit anti-nAChRα7	1:500 goat anti-rabbit AF488 (Invitrogen)
S1F	nAChRα7-ALFA	w, nAChRα7-KDRT-1XALFA;;	addaxS	DPX	1:200 FluoTag X2 anti-ALFA::Atto488	
S1F	endogenous Rdl	w1118;;	3% glyoxal fixative	everbrite	1:100 rabbit anti-Rdl	1:500 goat anti-rabbit AF568 (Invitrogen)
S1F	endogenous GluClα	w1118;;	addaxS	DPX	1:500 rabbit anti-MdGluClα, 1:20 nc82 (anti-Brp, mouse IgG1)	1:500 goat anti-rabbit AF568 (Invitrogen), 1:500 goat anti-mouse AF647 (Invitrogen)

S1F	GluClα-smGdP-10xV5	w;;GluClα-KDRT-smGdP-10xV5/+	addaxS	DPX	1:500 mouse IgG2a anti-V5	1:500 goat anti-mouse AF488 (Invitrogen)
S1G	w1118	w;; Df(3L)ED4421, P{w[+mW.Scer\FRT.hs3]=3'.RS5+3.3'}ED4421/+	addaxS	DPX	different [] rabbit anti-Rdl, 1:20 nc82 (anti-Brp, mouse IgG1)	1:500 goat anti-rabbit AF488 (Abcam), 1:500 goat anti-mouse IgG1 CF405S (Biotium)
	Rdl-smGdP-10xV5	w;; Df(3L)ED4421, P{w[+mW.Scer\FRT.hs3]=3'.RS5+3.3'}ED4421/Rdl-KDRT-STOP-KDRT-smGdP-10xV5	addaxS	DPX	different [] rabbit anti-Rdl, 1:20 nc82 (anti-Brp, mouse IgG1)	1:500 goat anti-rabbit AF488 (Abcam), 1:500 goat anti-mouse IgG1 CF405S (Biotium)

	w1118	w;;	addaxS	DPX	different [] rabbit anti-nAChRα6, 1:20 nc82 (anti-Brp, mouse IgG1)	1:500 goat anti-rabbit AF488 (Abcam), 1:500 goat anti-mouse IgG1 CF405S (Biotium)
	nAChRα6-smGdP-10xOllas	w;nAChRα6-KDRT-smGdP-10xOllas;	addaxS	DPX	different [] rabbit anti-nAChRα6, 1:20 nc82 (anti-Brp, mouse IgG1)	1:500 goat anti-rabbit AF488 (Abcam), 1:500 goat anti-mouse IgG1 CF405S (Biotium)
Figure S2						
S2C-S2D	nAChRα1-smGdP-10xOllas	w;;nAChRα1-KDRT-smGdP-10xOllas/+	3% glyoxal fixative	ExLLSM	1:10 nc82 (anti-Brp, mouse IgG1), 1:1000 rat anti-Ollas	1:500 goat anti-mouse CF633 (Biotium), 1:250 goat-anti-rat AF488 (Jackson)

S2C-S2D	Lcch3-smGdP-10xOllas	w, Lcch3-KDRT-smGdP-10xOllas/+;;	3% glyoxal fixative	ExLLSM	1:10 nc82 (anti-Brp, mouse IgG1), 1:1000 rat anti-Ollas	1:500 goat anti-mouse CF633 (Biotium), 1:250 goat-anti-rat AF488 (Jackson)
Figure S3						

S3B		w, P{w+, pBPhsFlp2PEST}attP3; nAChRα6-KDRT-stop-KDRT-smGdP-10xOllas/P{R13F02-p65.AD}attP40; P{w+, R52H09-GAL4.DBD}attP2/P{w+, 10xUAS-FRT-STOP-FRT-myrTdt-2A-KDR.PEST}VK00033	3% glyoxal fixative	DPX	1:10 nc82 (anti-Brp, mouse IgG1), 1:1000 guinea pig anti-RFP, 1:1000 rat anti-Ollas	1:500 goat anti-mouse CF633 (Biotium), 1:500 goat-anti-guinea pig AF568 (Invitrogen), 1:250 goat-anti-rat AF488 (Jackson)

S3C		w, P{w+, pBPhsFlp2PEST}attP3; P{w+, 10xUAS-FRT-STOP-FRT-myrTdt-2A-KDR.PEST}attP5/P{R30E08-p65.AD}attP40; P{w+, R53C10-GAL4.DBD}attP2/Rdl-KDRT-STOP-KDRT-smGdP-10xV5	3% glyoxal fixative	DPX	1:10 nc82 (anti-Brp, mouse IgG1), 1:1000 guinea pig anti-RFP, 1:500 chicken anti-V5	1:500 goat anti-mouse CF633 (Biotium), 1:500 goat-anti-guinea pig AF568 (Invitrogen), 1:250 goat-anti-chicken AF488 (Jackson)

S3D		w, P{w+, pBPhsFlp2PEST}attP3; P{w+, 10xUAS-FRT-STOP-FRT-myrTdt-2A-KDR.PEST}attP5/+; P{w+, R13F04-GAL4.DBD}attP2, P{w+, R93D10-p65.AD}VK00027/Rdl-KDRT-STOP-KDRT-smGdP-10xV5	3% glyoxal fixative	DPX	1:10 nc82 (anti-Brp, mouse IgG1), 1:1000 guinea pig anti-RFP, 1:500 chicken anti-V5	1:500 goat anti-mouse CF633 (Biotium), 1:500 goat-anti-guinea pig AF568 (Invitrogen), 1:250 goat-anti-chicken AF488 (Jackson)
S3E-S3F, S3G-S3H, S3M-S3P	nAChRα6-smGdP-10xOllas	w;nAChRα6-KDRT-smGdP-10xOllas/+;	3% glyoxal fixative	ExLLSM	1:10 nc82 (anti-Brp, mouse IgG1), 1:1000 rat anti-Ollas	1:500 goat anti-mouse CF633 (Biotium), 1:250 goat-anti-rat AF488 (Jackson)

S3I-S3J, S3K-S3L, S3N-S3P	nAChRα1-smGdP-10xOllas	w;;nAChRα1-KDRT-smGdP-10xOllas/+	3% glyoxal fixative	ExLLSM	1:10 nc82 (anti-Brp, mouse IgG1), 1:1000 rat anti-Ollas	1:500 goat anti-mouse CF633 (Biotium), 1:250 goat-anti-rat AF488 (Jackson)
S3N-S3P	nc82	Canton-S	3% glyoxal fixative	ExLLSM	1:10 nc82 (anti-Brp, mouse IgG1)	1:500 goat anti-mouse CF633 (Biotium), 1:400 goat-anti-mouse AF488 (Jackson)
S3N-S3P	nAChRα5-smGdP-10xOllas	w;nAChRα5-KDRT-smGdP-10xOllas/+;	3% glyoxal fixative	ExLLSM	1:10 nc82 (anti-Brp, mouse IgG1), 1:1000 rat anti-Ollas	1:500 goat anti-mouse CF633 (Biotium), 1:250 goat-anti-rat AF488 (Jackson)

S3N-S3P	nAChRα7-smGdP-10xOllas	w, nAChRα7-KDRT-smGdP-10xOllas/+;;	3% glyoxal fixative	ExLLSM	1:10 nc82 (anti-Brp, mouse IgG1), 1:1000 rat anti-Ollas	1:500 goat anti-mouse CF633 (Biotium), 1:250 goat-anti-rat AF488 (Jackson)
S3N-S3P	nAChRβ1-smGdP-10xHA	w;;nAChRβ1-KDRT-smGdP-10xHA/+	3% glyoxal fixative	ExLLSM	1:10 nc82 (anti-Brp, mouse IgG1), 1:1000 rat anti-HA	1:500 goat anti-mouse CF633 (Biotium), 1:250 goat-anti-rat AF488 (Jackson)
S3N-S3P	Rdl-smGdP-10xV5	w;;Rdl-KDRT-smGdP-10xV5/+	3% glyoxal fixative	ExLLSM	1:10 nc82 (anti-Brp, mouse IgG1), 1:500 chicken anti-V5	1:500 goat anti-mouse CF633 (Biotium), 1:250 goat-anti-Ch AF488 (Jackson)

S3N-S3P	Lcch3-smGdP-10xOllas	w, Lcch3-KDRT-smGdP-10xOllas/+;;	3% glyoxal fixative	ExLLSM	1:10 nc82 (anti-Brp, mouse IgG1), 1:1000 rat anti-Ollas	1:500 goat anti-mouse CF633 (Biotium), 1:250 goat-anti-rat AF488 (Jackson)
S3N-S3P	GluClα-smGdP-10xV5	w;;GluClα-KDRT-smGdP-10xV5/+	3% glyoxal fixative	ExLLSM	1:10 nc82 (anti-Brp, mouse IgG1), 1:500 chicken anti-V5	1:500 goat anti-mouse CF633 (Biotium), 1:250 goat-anti-Ch AF488 (Jackson)
Figure S4						

S4C, S4F	Tm3 GluClα-smGdP-10xV5	w, P{w+, hs-FLPG5.PEST.Opt)attP3/w; P{w+, 10xUAS-FRT-STOP-FRT-myrTdt-2A-KDR.PEST}attP5/+; P{w+, GMR13E12-Gal4}attP2/GluClα-KDRT-STOP-KDRT-smGdP-10xV5	addaxS	DPX	1:200 rabbit anti-DsRed, 1:200 mouse IgG2a anti-V5	1:500 goat anti-rabbit AF568 (Invitrogen), 1:500 goat anti-mouse AF488 (Invitrogen)

S4D, S4F	Tm3 nAChRβ1-smGdP-10xHA	w, P{w+, hs-FLPG5.PEST.Opt)attP3/w; P{w+, 10xUAS-FRT-STOP-FRT-myrTdt-2A-KDR.PEST}attP5/+; P{w+, GMR13E12-Gal4}attP2/nAChRβ1-KDRT-STOP-KDRT-smGdP-10xHA	addaxS	DPX	1:200 rabbit anti-DsRed, 1:1,000 rat anti-HA	1:500 goat anti-rabbit AF568 (Invitrogen), 1:500 goat anti-rat AF488 (Abcam)

S4E, S4F	Tm3 Rdl-smGdP-10xV5	w, P{w+, hs-FLPG5.PEST.Opt)attP3/w; P{w+, 10xUAS-FRT-STOP-FRT-myrTdt-2A-KDR.PEST}attP5/+; P{w+, GMR13E12-Gal4}attP2/Rdl-KDRT-STOP-KDRT-smGdP-10xV5	addaxS	DPX	1:200 rabbit anti-DsRed, 1:200 mouse IgG2a anti-V5	1:500 goat anti-rabbit AF568 (Invitrogen), 1:500 goat anti-mouse AF488 (Invitrogen)
Figure S5						

S5H, S5I	nAChRα5-smGdP-10xOllas, nAChRβ1-smGdP-10xHA	w, P{w+, hs-FLPG5.PEST.Opt)attP3/w; {w+, 10xUAS-FRT-STOP-FRT-myrGFP-2A-KDR.PEST}attP40/nAChRα5-KSK-smGdP-10xOllas; P{w+, GMR42F06-Gal4}attP2/nAChRβ1-KDRT-STOP-KDRT-smGdP-10xHA	addaxS	DPX	1:10,000 rabbit anti-Ollas, 1:1,000 rat anti-HA, 1:1,000 chicken anti-GFP	1:500 goat anti-rabbit AF647 (Invitrogen), 1:500 goat anti-rat AF568 (Abcam), 1:500 goat anti-chicken AF488 Plus (Invitrogen)

	nAChRα1-smGdP-10xOllas, nAChRβ1-smGdP-10xHA	w, P{w+, hs-FLPG5.PEST.Opt)attP3/w; {w+, 10xUAS-FRT-STOP-FRT-myrGFP-2A-KDR.PEST}attP40/+; P{w+, GMR42F06-Gal4}attP2, nAChRβ1-KDRT-STOP-KDRT-smGdP-10xHA/nAChRα1-KDRT-STOP-KDRT-smGdP-10xOllas	addaxS	DPX	1:10,000 rabbit anti-Ollas, 1:1,000 rat anti-HA, 1:1,000 chicken anti-GFP	1:500 goat anti-rabbit AF647 (Invitrogen), 1:500 goat anti-rat AF568 (Abcam), 1:500 goat anti-chicken AF488 Plus (Invitrogen)
Figure S6						

S6B		w;;Rdl-KDRT-smGdP-10xV5/+	addaxS	DPX	1:500 mouse IgG2a anti-V5:DL550, 1:25 nc82 (anti-Brp, mouse IgG1)	1:500 goat anti-rat AF488 (Abcam) 1:500 FluoTag X2 anti-mouse IgG1 Atto647N (NanoTag)
S6C		w;;nAChRβ1-KDRT-smGdP-10xHA/+	addaxS	DPX	1:1,000 rat anti-HA, 1:20 nc82 (anti-Brp, mouse IgG1)	1:500 goat anti-rat AF488 (Abcam) 1:500 FluoTag X2 anti-mouse IgG1 Atto647N (NanoTag)
S6D		w;;GluClα-KDRT-smGdP-10xV5/+	addaxS	DPX	1:500 mouse IgG2a anti-V5:DL550, 1:25 nc82 (anti-Brp, mouse IgG1)	1:500 goat anti-rat AF488 (Abcam) 1:500 FluoTag X2 anti-mouse IgG1 Atto647N (NanoTag)

S6E-S6F		w, P{w+, hs-FLPG5.PEST.Opt)attP3/w; P{w+, 10xUAS-FRT-STOP-FRT-myrGFP-2A-KDR.PEST}attP40/+; P{w+, GMR42F06-Gal4}attP2/nAChRβ1-KDRT-STOP-KDRT-smGdP-10xHA	addaxS	DPX	1:1,000 rat anti-HA, 1:1,000 chicken anti-GFP	1:500 goat anti-rat AF568 (Abcam), 1:500 goat anti-chicken AF488 Plus (Invitrogen)

S6G-S6I	L5 GluClα-smGdP-10xV5 development	w, P{w+, hs-FLPG5.PEST.Opt)attP3/w; {w+, 10xUAS-FRT-STOP-FRT-myrTdt-2A-KDR.PEST}attP5/+; P{w+, GMR64B07-Gal4}attP2/GluClα-KDRT-STOP-KDRT-smGdP-10xV5	addaxS	ExLSM	1:7.2 nc82 (anti-Brp, mouse IgG1), 1:100 mouse IgG2a anti-V5, 1:100 rabbit anti-DsRed	1:100 goat anti-mouse IgG1 CF405S (Biotium), 1:100 goat anti-mouse IgG2a AF546 (Invitrogen), 1:100 Fab goat anti-rabbit IgG Fc SeTau647 (labeled in-house, Jackson/SETA BioMedicals)
Figure S7						

S7B		w; PBac{w+, brp-RSRT-STOP-RSRT-smGdP-10xV5-2A-LexA-VP16}VK00001, UAS-R, LexAoP-myrTdt/P{w+, R48A07-p65.AD}attP40; Sb/P{w+, VT046779-DBD}attP2	addaxS	ExLSM	1:100 mouse IgG2a anti-V5, 1:7.2 nc82 (anti-Brp, mouse IgG1), 1:100 rabbit anti-DsRed	1:100 goat anti-mouse IgG2a AF488 (Invitrogen), 1:100 goat anti-mouse IgG1 AF568 (Invitrogen), 1:100 Fab goat anti-rabbit IgG Fc SeTau647 (in-house Jackson/SETA BioMedicals)

Table 2.4 List of tags and antibodies used for their detection

(Table cross-referenced in Chapter 2 text as Table S4.)

Tag[a]	Abbreviation	Primary antibody	Secondary antibody	Comment[b]
spaghetti monster 10XV5	smV5	1:500 chicken anti-V5 (ExLLSM)	1:250 goat-anti-chicken AF488 (Jackson)	-
		1:100 mouse IgG2a anti-V5 (ExLSM)	1:100 goat anti-mouse IgG2a AF488 (Invitrogen) 1:100 goat anti-mouse IgG2a AF546 (Invitrogen)	-
		1:500 mouse IgG2a anti-V5 (confocal)	1:500 goat anti-mouse AF488 (Invitrogen) 1:500 goat anti-mouse IgG2a AF488 (Invitrogen)	good SNR
		1:500 mouse IgG2a anti-V5::DL550 (confocal)	-	best SNR
spaghetti monster 10XHA	smHA	1:100 rat anti-HA (ExLLSM)	1:250 goat-anti-rat AF488 (Jackson)	-
		1:1,000 rat anti-HA (confocal)	1:500 goat anti-rat AF488 (Abcam) 1:500 goat anti-rat AF568 (Abcam)	best SNR
spaghetti monster 10XOllas	smOllas	1:1,000 rat anti-Ollas (ExLLSM)	1:250 goat-anti-rat AF488 (Jackson)	-
		1:10,000 rat anti-Ollas (confocal)	1:500 goat anti-rat AF488 (Abcam)	good SNR
		1:10,000 rabbit anti-Ollas (confocal)	1:500 goat anti-rabbit AF488 (Abcam) 1:500 goat anti-rabbit AF568 (Abcam) 1:500 goat anti-rabbit AF647 (Invitrogen) 1:500 goat anti-rabbit CF633 (Biotium) 1:500 AbberiorStar635P Fluo Tag X4 anti-rabbit (NanoTag)*	AbberiorStar635 P Fluo Tag X4 anti-rabbit (NanoTag) – best SNR

1X ALFA	ALFA	1:500 guinea pig fc::nb anti-ALFA (ExLLSM)	1:500 goat-anti-guinea pig AF568 (Invitrogen)	-
		1:200 nb anti-ALFA::Atto488 (confocal)	-	weak signal

[a] Spaghetti monster is a variant of fluorescence dead GFP (GdP -Green darkened Protein) tagged with 10 copies of the indicated epitope tag.

[b] For single-cell receptor localization analysis, selecting antibody combinations that yield the highest signal-to-noise ratio (SNR) is critical, particularly for NR subunits with low expression levels. Since secondary antibodies can vary by lot, it is highly recommended to test different secondary antibodies to ensure optimal SNR for each experimental condition. Qualitative comment on the SNR achieved with different antibody combinations is provided. (-) Optimal antibody dilution and combinations used for ExLLSM and ExLSM.

Chapter 3: Localization of Endogenously Tagged Neurotransmitter Receptors

This chapter includes extended work with the endogenous tagging system for neurotransmitter receptor (NR) subunits not included in our publication (Chapter 2). Here, I describe early studies that identified the need to optimize our staining conditions for single-cell conditional tagging. I also provide extended results of developmental studies using the same genetic tools that supported our discovery of differential localization dynamics between cell types and between NR types. In studies on the connection between L1 and L5 neurons, I provide evidence of differential timing of synapse formation for the same synaptic partners between two separate dendritic domains. Finally, I discuss the limitations of using confocal imaging methods in our results and address some of the underlying questions raised from our quantitative analysis of NR localization compared to EM connectomic data.

3.1 Validation of the conditional NR tagging system

The NR tagging system developed in our lab provides a genetic toolkit to conditionally activate desired cell types that will express a modified NR subunit from the endogenous locus of the gene with an inserted epitope tag sequence. Sparse activation is accomplished through heat-shock-dependent, stochastic expression of Flp recombinase that mediates excision of an FRT-flanked stop cassette, allowing for subcellular localization studies of the tagged NR subunit in single cells (Figure 3.1A).

In the course of validating our novel NR tagging system, I conducted a series of preliminary experiments to evaluate the efficacy of single-neuron labeling with a particular focus on the GABA

receptor subunit Rdl. Through my analysis of connectomic data, I identified several neuron types with distinct patterns of presynaptic inputs from known GABAergic neurons (Figure 3.1B). Based on expression of Rdl (supported by transcriptomic data analysis) and the availability of genetic tools, I selected five postsynaptic neuron types in the optic lobe: Mi1, Mi4, Mi9, T1, and Tm3. I then used the conditionally tagging system to tag Rdl in these neuron types and carried out single-cell localization studies.

The studies revealed a consistent correlation between the localization of Rdl and the synaptic patterns predicted by the connectome. I also observed Rdl in regions lacking GABAergic inputs identified in the connectome, suggesting contributions from uncharacterized neurons. In Mi1 neurons labeled using a 19F01-GAL4, Rdl localized to dendritic processes in layers M1, M4, and M8, in accordance with connectomic data (Figure 3.1C). In Mi4 neurons labeled with 49B06-GAL4, Rdl localized throughout dendritic processes in M4 while being starkly absent from the processes in the M7 layer, with sparse puncta also concentrated in the terminals in M10, which also corresponded to connectomic data (Figure 3.1C). In Mi9 neurons (driver specified in Chapter 2), Rdl puncta were present in the M3-M4 processes as well as highly concentrated in the terminals in M10, also in accordance with connectomic data (Figure 3.1C). T1 neurons (labeled with a 31F10∩30F10 split GAL4) displayed a characteristic ‘cup’-shaped distribution of Rdl in the M2 dendritic processes, matching the synaptic inputs from EM (Figure 3.1C).

With the Tm3 driver 13E12-GAL4 and heat-shock-dependent activation, both Tm3a and Tm3b neurons were sparsely labeled as well as occasional Mi10 neurons. I restricted my analysis to Tm3a neuron types labeled with this driver. I used another driver, 12C11-GAL4, that exclusively labels Tm3b neurons to analyze those neurons. Morphologically, Tm3b neurons display a distinct branch that projects back from M10 up to layer M8 (Figure 3.1C). Both Tm3a

and Tm3b neurons demonstrated Rdl localization in M3 dendritic processes and M10 terminals, which corresponded to synaptic inputs identified in connectomic data (Figure 3.1C).

However, Tm3b neurons also displayed Rdl puncta in the M8 branch that I did not find in my connectome analysis (Figure 3.1C). This additional Rdl signal could reflect Rdl localizing at other unidentified synapses or localization to an extrasynaptic domain that would not be identified by connectomic EM studies. The unexpected Rdl signal was qualitatively similar in size and intensity to the puncta localized to identified input domains, suggesting synaptic localization. These findings underscore the capacity of NR localization data to complement, enrich and sometimes challenge our understanding derived from EM connectomic data.

This study initially validated the robust efficacy of our conditional NR tagging system across a range of optic lobe neurons, at least for the Rdl_KSK_smV5 allele. In these experiments with adult brains, I did not observe ectopic localization to cell bodies. Furthermore, all tested neurons displayed punctate signals in dendrites.

I also observed substantial nonspecific background in the conditionally tagged NR staining patterns, which had not been identified in earlier experiments with the constitutively tagged alleles that labeled NRs throughout the whole brain. The single-cell experiments revealed a need for higher sensitivity and lower background given the much weaker signal arising from the labeling of only a subset of NRs at a multi-contact synapse. Thus, we realized that evaluation of staining sensitivity in a single-cell context is imperative for proper optimization of molecular tagging techniques.

Having identified the need for more stringent labeling sensitivity, we sought to optimize our staining conditions for the tagged NR subunits. We found that the following changes provided the most significant benefits. (1) Lower (less concentrated) antibody dilutions in combination with

longer incubation periods significantly reduced punctate background signals without significantly reducing the real signals for the epitope tag. (2) Fixation using an acid-free glyoxal rather than conventional paraformaldehyde (PFA), preserved significantly more signal of both tagged NR subunits as well as natively stained synaptic markers such as nc82, while also reducing fragmentation of neuron membranes (see Chapter 2). (3) Imaging with Airyscan gave stronger signal to noise ratio but did not significantly improve resolution until moving to higher magnification, using a 63x oil objective instead of a 40x glycerol objective. (4) Finally, switching from a glycerol based mounting medium to a DPX mount further enhanced signal to noise ratio, resolution, and minimized signal quality degradation over imaging depth. For further discussion of these methods, see Chapter 2.

3.2 Localization of NR subunits throughout the optic lobe during development

In our initial studies of NR localization during development, we leveraged the constitutively tagged alleles to gain a picture of NR localization throughout the optic lobe across all cells. Developmental studies could be carried out using the same genetic tools by dissecting pupal brains at different stages throughout development. Here, we studied nAChRα1, nAChRβ1, nAChRα5, nAChRα6, and nAChRα7 in conjunction with Brp staining. (Brp staining marks the presynaptic active zone.) We dissected brains at 24-hour increments between 24-96 hrs APF (hours After Pupal Formation), following the approximate 100-hour time period of pupal development for animals raised at 25ºC.

At 24 hrs APF, nAChRα1 and nAChRα6 localized strongly to proximal medulla and lobula layers, with more distal layers accumulating signal throughout later development (**Figure 3.2**B,E).

In contrast, nAChRβ1 and nAChRα5 were largely restricted to cell bodies in the periphery of the brain (named the cortex) up through 72 hrs before becoming localized to neuropil by 96 hrs. (**Figure 3.2**C,D). Finally, nAChRα7 displayed strong signal in the lobula plate by 48 hrs and accumulated later in the medulla and lobula by 72 hrs (**Figure 3.2**F).

These studies provided early clues as to the differential localization dynamics of NR subunits during development. However, they could not provide insight into the identity of the cells in which they were being expressed or the patterns of subcellular localization within neuronal processes.

3.3 Developmental analysis of NR localization in single L5 neurons

To study subcellular localization during development, we turned to the conditional NR tagging system. Here, I provide extended results focused on the neuron type L5. Over the course of pupal development, L5 neurons progressively arborize sets of dendritic processes in the medulla neuropil at distinct stages. I set out to characterize the localization of various NR subunits during this period.

3.3.1 Background

The following description outlines the developmental stages of L5 neuron projection into the medulla neuropil that has been well characterized in previous studies (see Figure 3.3B for data adapted from Nern et al., 2008, which are summarized below). As early as 25 hrs APF, L5 neurites project into the medulla with nascent processes that arborize in layer M5. Around 48 hrs, an additional set of processes arborizes from a higher point in the neuron stalk, becoming the branches

in layer M1. Finally, by 90 hrs, the branches in layer M2 project down from the layer M1 processes, creating the final dendritic pattern of L5 neurons, with branches in layers M1, M2 and M5 (**Figure 3.3**A).

Analysis of transcriptomic data from our lab revealed highly dynamic gene expression of NR subunits during development, with some genes following distinct temporal patterns compared to the majority of other cell type clusters (**Figure 3.3**C). In L5 neurons, nAChRα1 and nAChRα5 had lower expression levels throughout development and GluClα expression declined much earlier (at the level of detected RNA) after 36 hrs APF compared to other cell types.

3.3.2 Results

To study the development and localization of GABAergic NR subunit Rdl and (inhibitory) glutamatergic NR subunit GluClα in L5 neurons, I dissected brains at 12-hour increments from 36 hrs to 84 hrs APF and used confocal microscopy to visualize the NR subunits. I performed these experiments in the same staining batch (but in different brains, of course) to guarantee identical staining conditions, leveraging the fact that we both Rdl and GluClα carried the same smV5 epitope tag. I analyzed and presented select timepoints (48 hrs, 72 hrs, and adult) from this data in our publication (see Chapter 2). Here, I provide a more complete description.

At 36 hrs, no Rdl puncta were localized to the nascent processes of L5 neurons in layer M5 (**Figure 3.4**Ai). By 48 hrs, the nascent processes in layer M1 had arborized, and Rdl puncta were diffusely distributed throughout the neuron (**Figure 3.4**Aii). This trend continued at later time points with increasing numbers of puncta at 60 hrs and 72 hrs before declining at 84 hrs (**Figure 3.4**Aiii-v). Finally, by the adult (roughly 120-144 hrs), Rdl puncta were refined to a restricted distribution within processes of layers M1 and M2 and lost elsewhere (**Figure 3.4**Avi), producing the mature distribution of GABAergic inputs seen in the connectome (see Chapter 2 and below).

The pattern of development for the (inhibitory) glutamatergic subunit GluClα was quite different (**Figure 3.4**B). At 36 hrs, sparse, large puncta of GluClα appeared in the nascent layer M5 processes of L5 neurons (**Figure 3.4**Bi). By 48 hrs, GluClα was more strongly expressed, restricted to processes in layers M1 and M5 with little in the main stalk (**Figure 3.4**Bii). However, at this timepoint and at 60 hrs, whereas GluClα in layer M1 was distributed in well-defined puncta, GluClα in layer M5 appeared in aggregates within the central core of these dendritic processes (**Figure 3.4**Biii). By 60 hrs, the picture was similar to that at 48 hrs but with greater amounts of GluClα detected in both domains (**Figure 3.4**Biv). By 72 hrs, puncta in layer M5 were distributed to well-defined puncta within the central branches (**Figure 3.4**Bv). The size of the dendritic processes and the numbers of puncta increased progressively at 84 hrs and into the adult (**Figure 3.4**Bvi).

I also performed a developmental analysis of the (excitatory) nicotinic acetylcholine receptor subunit nAChRβ1 in L5 neurons by dissecting brains at 72 hrs and 84 hrs. At 72 hrs, I observed nAChRβ1 entirely restricted to cell bodies of L5 neurons (**Figure 3.5**i), which agreed with my constitutively tagged nAChRβ1 experiments showing the same phenomenon throughout the optic lobe (see above). However, at 84 hrs, I also observed nAChRβ1 puncta densely localized to L5's nascent processes emerging in layer M2, with continued strong expression in the cell body (**Figure 3.5**ii). I observed additional sparse puncta throughout the main stalk between lamina and medulla neuropil (see correspondingly placed white arrow in **Figure 3.5**ii). An additional timepoint at 104 hrs in freshly eclosed animals confirmed that the tightly confined localization of nAChRβ1 to layer M2 remained stably intact, while signal in the cell body had disappeared (**Figure 3.5**iii).

3.3.3 Summary

During the development of L5 neurons, localization of receptor puncta occurs distinctly for each Rdl, GluClα and nAChRβ1. In the case of the (inhibitory) GABAergic NR subunit Rdl, receptor puncta diffusely and indiscriminately fill the dendritic processes before being later refined to a specific domain. In the case of the (inhibitory) glutamatergic subunit GluClα, receptor appears early and remains clustered in the center of nascent dendritic branches before distributing to defined puncta. As for the (excitatory) nicotinic acetylcholine receptor subunit nAChRβ1, protein is confined to the cell body until late in development and then localizes to well-defined puncta restricted to the nascent M2 branches that emerge around 90 hrs. In adult L5 neurons, all three of these NR subunits are ultimately localized to restricted dendritic domains. The following table summarizes my developmental findings in L5 neurons.

Table 3.1 Summary of Developmental NR Subunit Localization in L5 Neurons

Neurotransmitter Receptor Subunit	Time of Trafficking to Dendrites (hrs APF)	Time of Mature Localization	Comments
Rdl (GABA)	48 hrs	> 84 hrs (M1; M2)	Puncta are diffusely distributed throughout the neuron until being cleared elsewhere (lost in M5).
GluClα (Glut.)	36-48 hrs	48 hrs (M1) 72 hrs (M5)	Localizes directly to M1 and M5 domains. Distributes into puncta later in M5 than in M1.
nAChRβ1 (ACh)	84 hrs	84 hrs (M2)	Retained in cell body before localizing directly to puncta in M2 domain.

3.4 L1 Developmental Glutamatergic Input Localization

To further investigate synapse development in L5 neurons, I decided to study the localization of Brp to presynaptic active zones in L1 neurons, which provide the majority of glutamatergic inputs to L5 neurons in both layers M1 and M5. To label presynaptic sites in single L1 neurons, I used the genetic method STaR (Synaptic Tagging after Recombination), which is designed to conditionally expresses a smV5-tagged copy of Brp expressed at native levels similarly to our conditional NR tagging approach, except that the construct is expressed from a third locus inserted within a bacterial artificial chromosome rather than from the endogenous genomic locus (Y. Chen et al., 2014b).

At 48 hrs APF, I observed dense, aggregated Brp signal in the central bulk of layer M5 processes in L1 neurons, and a small number of Brp puncta in the layer M1 processes (**Figure 3.6**, left). By 72 hrs, Brp signal in both sets of L1 processes had increased, but Brp appeared more punctate in the layer M1 domain, while Brp in layer M5 branches was clustered in larger aggregates (**Figure 3.6**, middle). In adult brains, Brp appeared in well-defined puncta in both layer M1 and M5 processes of L1 neurons (**Figure 3.6**, right). Thus, presynaptic active zones in L1 neurons may begin developing in layer M1 by 48 hrs, whereas in layer M5 they develop after 72 hrs on a different, later time course.

Taken together with my developmental study of GluClα in L5 neurons, these findings revealed that both the presynaptic and postsynaptic components of glutamatergic synapses between L1 and L5 neurons are present in developing neurites by 48 hrs APF but that some may not localize to individual synaptic densities until later in development. In my confocal studies of GluClα in L5 neurons, I made a similar observation that the receptor was aggregated in layer M5 branches until 72 hrs (see above). There, I also observed significantly higher numbers of GluClα

puncta in L5 neurons than Brp puncta in L1 neurons at 48 hrs. These findings could suggest that GluClα localizes to L5 dendrites independently from the establishment of active zones in its presynaptic partner, and guides synapse formation through two distinct time courses between the layer M1 and layer M5 dendritic domains. Alternatively, additional glutamatergic inputs from Dm1 neurons that are restricted to layer M1 branches of L5 (see **Figure 3.7**A) may have a role in the earlier establishment of GluClα puncta in this layer, but the time course of Brp development in Dm1 neurons was not studied in this work.

The observations described here for synapse formation between L1 and L5 neurons are limited by our inability to directly address whether Brp and GluClα puncta colocalized to the same synaptic densities during development. In later studies using expansion microscopy (ExM), I followed the expression of GluClα in L5 neurons along with its colocalization to Brp during development, which revealed that the majority of GluClα puncta in layer M1 dendrites of L5 neurons were colocalized to Brp by 72 hrs, whereas many GluClα puncta that did not colocalize with Brp were still present in layer M5 dendrites until 96 hrs (see Chapter 4).

3.5 Limitations of Confocal Microscopy for studying L5 Connectivity

Analysis of connectomic data revealed that postsynaptic L5 neurons receive distinctly localized inputs from different presynaptic neuron types, even for different presynaptic neuron types using the same neurotransmitter. For glutamatergic inputs to L5 neurons, the primary inputs are from L1 neurons in medulla layers M1 and M5, with the second most inputs coming from Dm1 neurons, which innervate a thin band at the bottom of layer M1 (**Figure 3.7**A). Additionally, very sparse TmY5a inputs are annotated in layer M5 (**Figure 3.7**A).

For GABAergic inputs, extensive synapses from C2 neurons are found in layer M1 as well as distal to layer M1 in the stalk of L5 (**Figure 3.7**B). C3 neurons make additional inputs in a thin band at the base of layer M1 as well as scattered throughout the processes of layer M2 (**Figure 3.7**B). Finally, sparse inputs from Dm10 neurons appear throughout layer M1 (**Figure 3.7**B).

For cholinergic inputs, the primary presynaptic partner is the L2 neuron, which makes extensive inputs within a compact region of upper layer M2; Tm1 inputs are largely concentrated to the lower tips of L5 dendritic processes in layer M2, and Tm2 inputs are scattered between (**Figure 3.7**C). Finally, sparse inputs from neuron types Mi1, Mi15, and TmY3 as well as from neighboring L5 neurons are annotated in the connectome in layers M1 and M5 (**Figure 3.7**C). However, I observed no nAChRβ1 signal in layer M5 in my conditional NR tagging experiments (**Figure 3.7**F), suggesting that these synapses provisionally annotated in the connectome are in error. Additional NR tagging experiments failed to localize other nicotinic subunits in L5 neurons such as nAChRα3 and nAChRα6 that were suggested by transcriptomic data to be expressed in these cells (see **Figure 3.3**C).

However, as we discussed in our publication, the correspondence between NR signals and connectomic data was poor for some NR subunits, likely due to limitations of our tagging method observed with confocal microscopy (see Chapter 2). On the one hand, quantification of GluClα puncta in L5 neurons closely resembled glutamatergic synapse counts from EM. In support of this notion, the signal from conditionally tagged GluClα displayed the most uniform puncta, suggesting that these marked well-defined postsynaptic densities (**Figure 3.7**D). This correspondence was shared in additional analyses of GluClα within two other neuron types, T4 and Tm3, reported in our publication.

On the other hand, signals from Rdl and nAChRβ1 were more discrepant when compared to connectomic data. In L5 neurons as well as T4, T5, and Tm3 neurons reported in our publication, the counts of tagged Rdl puncta were significantly greater than synapse counts from EM. As for nAChRβ1, puncta counts from our immunohistochemical studies were significantly fewer than synapse counts from EM in these four neuron types. Across these studies, GluClα and Rdl were labeled with identical staining conditions against the smV5 tag, while nAChRβ1 was stained against smHA with otherwise identical staining conditions. In our analysis, the same quantification parameters were used across all samples to count NR puncta for each neuron type.

In L5 neurons, I observed two apparent distributions of Rdl puncta. A distribution of larger, brighter Rdl puncta appeared to resemble the distribution of GABAergic inputs identified by EM, even including a specific cluster of synapses at the base of the L5 stalk (above layer M1) characteristic for inputs from neuron C2 (**Figure 3.7**B,E). I also observed many smaller, dimmer puncta scattered all throughout L5 neurons (**Figure 3.7**E). As reported in our publication, counts of Rdl puncta were much higher than predicted by the connectome. I attempted to repeat a second tailored analysis to separate these two apparent populations of Rdl puncta, but failed to find parameters that effectively separated the two distributions. However, these results suggest that the observed Rdl puncta included both synaptic and extrasynaptic distributions of receptor, demonstrating the limitations of confocal microscopy and the need for more powerful imaging methods such as ExM that could determine whether only a subset of these Rdl puncta are present at synapses (via colocalization with Brp).

As for nAChRβ1 puncta in L5 neurons, I observed a distribution of small but bright puncta as well as some significantly larger and brighter puncta within layer M2 (**Figure 3.7**F). Quantification of for nAChRβ1 puncta in L5 neurons was lower than predicted by EM (see Chapter

2). In this case, the limitations of confocal microscopy could have potentially prevented us from resolving individual postsynaptic sites that were densely clustered together (see the concentration of L2 inputs onto L5 dendrites in **Figure 3.7**C).

Our confocal studies demonstrated clear patterns of differentially distributed NR subunits in various neuron types including L5. However, more powerful methods than conventional confocal microscopy are required in order to resolve individual puncta effectively and determine whether they are colocalized to Brp at synapses or not. This would address underlying questions that arose from both our adult and developmental studies. In the next chapter, I describe the advancement of ExM methods that enabled me to resolve individual synapses and clear colocalization of tagged NR subunits in juxtaposition to presynaptic active zones marked by Brp.

3.6 Figures

Figure 3.1 Validation of conditional tagging system comparing Rdl localization to EM-based GABAergic inputs

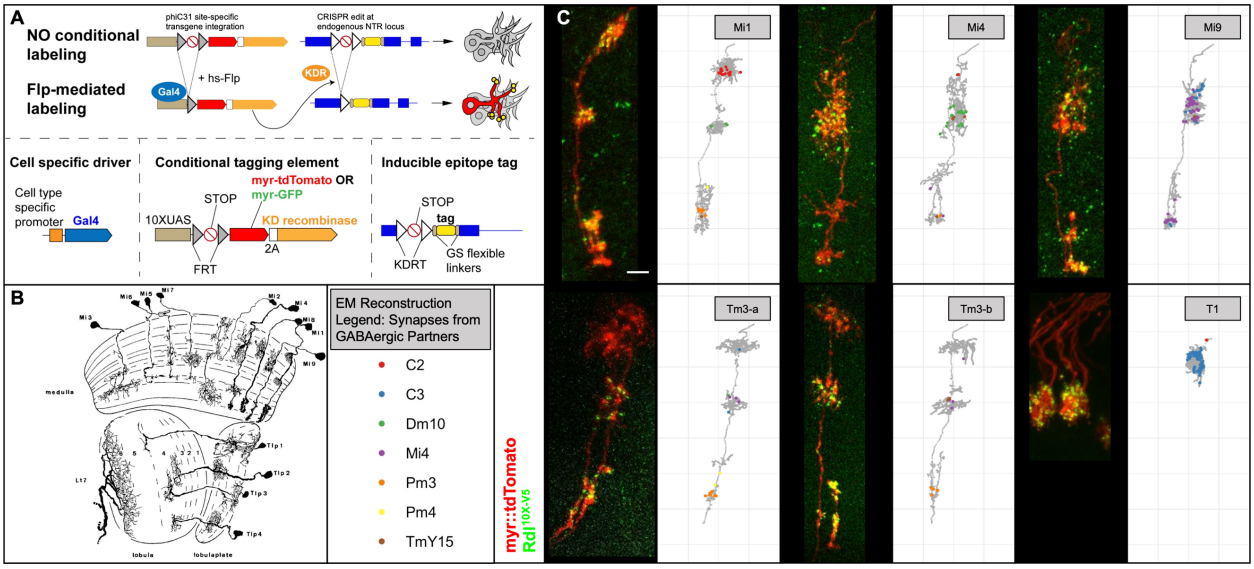

(A) Schematic of the conditional NR tagging system. Heat-shock-induced expression of Flp stochastically triggers a cascade of recombination mediated excisions. In the first step, Flp excises an FRT-flanked stop cassette to allow for cell-type-specific expression of KD recombinase and a membrane marker, in this case myr::tdTomato. Expressed KD recombinase then excises the KDRT-flanked stop cassette in the conditionally tagged NR allele, allowing for endogenous expression of in the activated cell.

(B) Diagram of various neuron types in the *Drosophila* optic lobe demonstrating stereotyped morphology with dendritic arborization restricted to specific neuropil layers. Adapted from Fischbach & Dittrich, 1989.

(C) Left subpanels, Immunofluorescence results obtained with the Rdl_KSK_smV5 allele demonstrating subcellular localization patterns within 6 neuron types, Mi1, Mi4, Mi9, Tm3-a and Tm3-b (two neuron subtypes), and T1. Tm3a and T1 subpanels show two adjacent cells. Scale

bar, 2 μm. Right subpanels, analyzed EM connectomic data plotting the skeleton of reconstructed neurons and locations of synaptic inputs from various GABAergic neuron types, colored as indicated. Source data from FIB-25 (Takemura et al., 2015).

Figure 3.2 NR development throughout the optic lobe

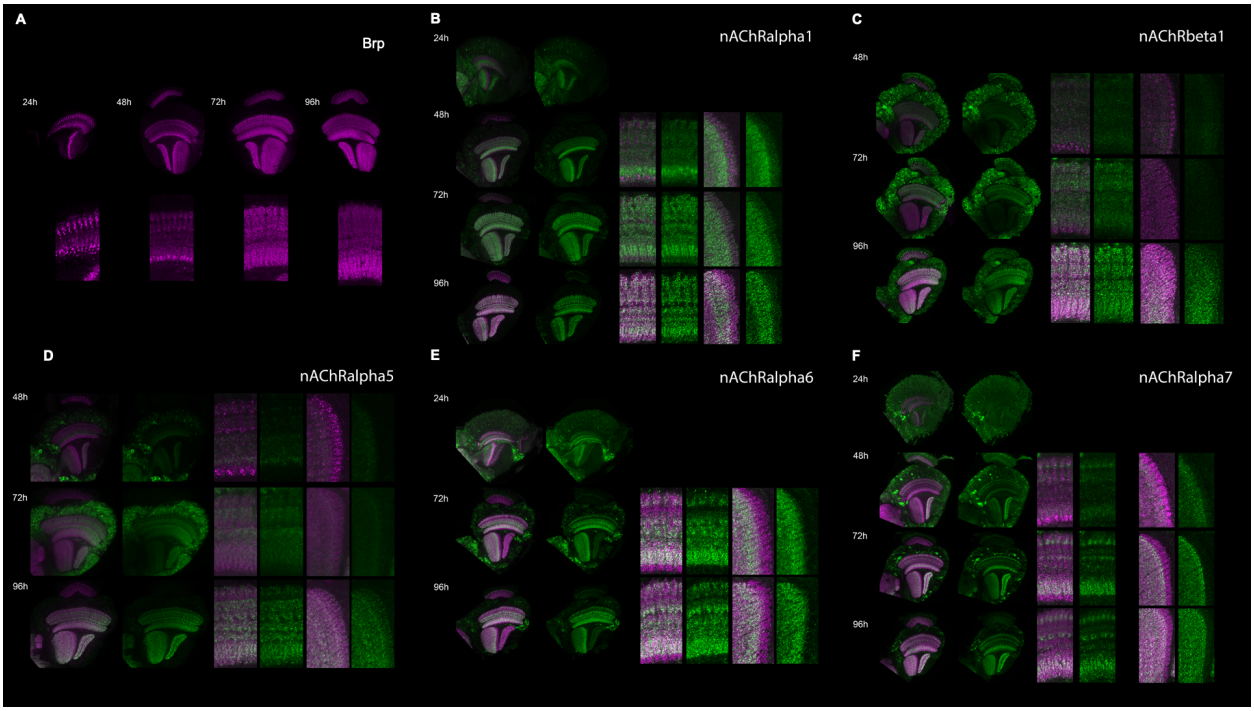

(A) Brp staining demonstrated in the optic lobe at 24-hour increments from 24 to 96 hours (h, hours after pupal formation).

(B-F) Developmental staining patterns of NR subunits (green), overlaying Brp (magenta), at indicated time points. See text for further description.

Figure 3.3 L5 dendritic development in the medulla neuropil and NR subunit gene expression

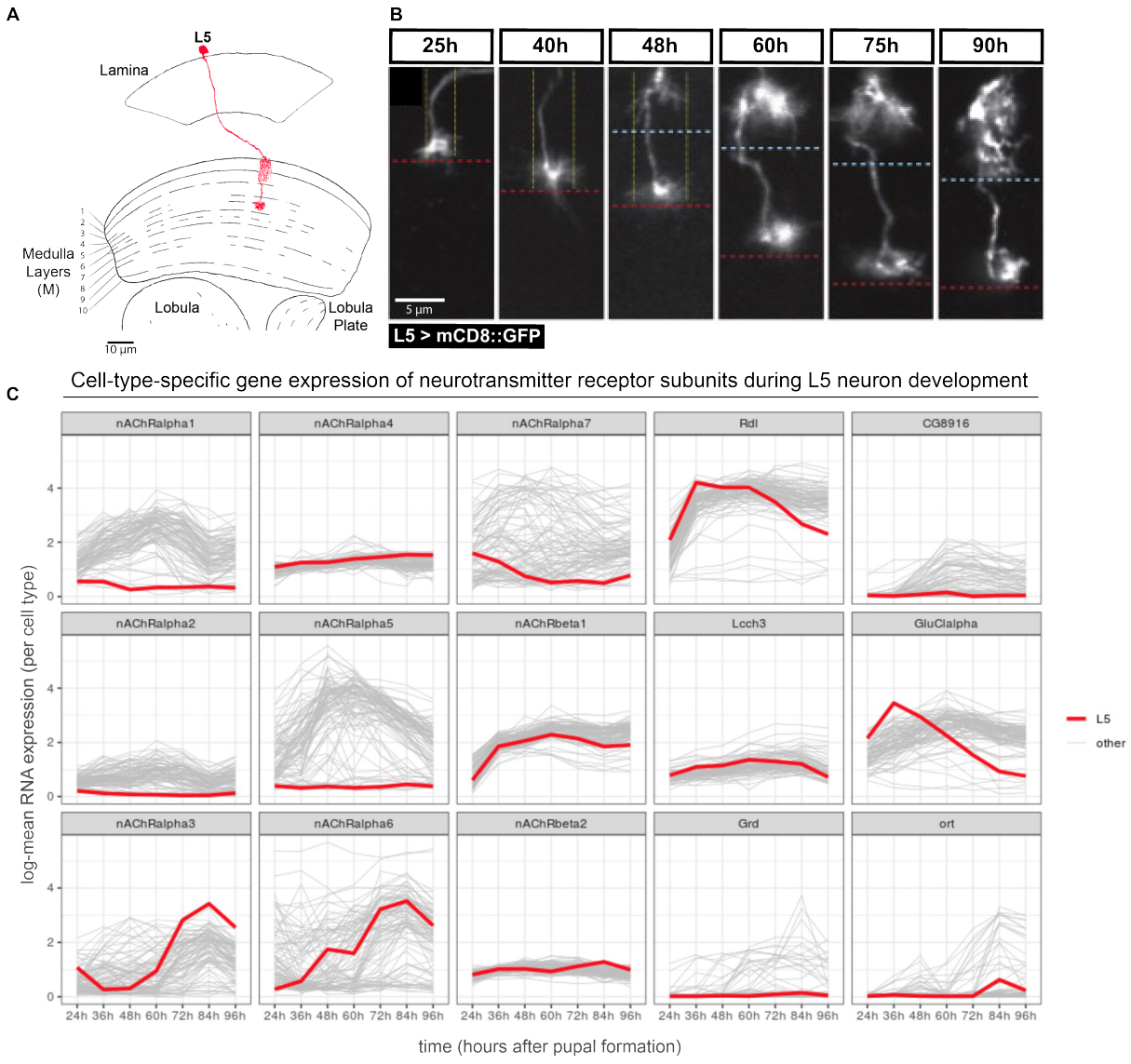

(A) Anatomical diagram of the L5 neuron sending projections to the lamina and medulla neuropils. Adapted from (Fischbach & Dittrich, 1989).

(B) Adapted from Nern et al., 2008. Representative images taken from multiple time points of the projection of L5 neuron processes in the medulla neuropil during pupal development (h, hours after pupal formation). Scale bar, 5µm. See text for further description.

(C) Cell-type-specific gene expression patterns of NR subunit genes during pupal development in L5 neurons (red) relative to other neuron types (each gray line indicates the plot for a different neuron type). Source data from Kurmangaliyev et al., 2020.

Figure 3.4 Developmental localization of Rdl and GluClα in L5 neurons

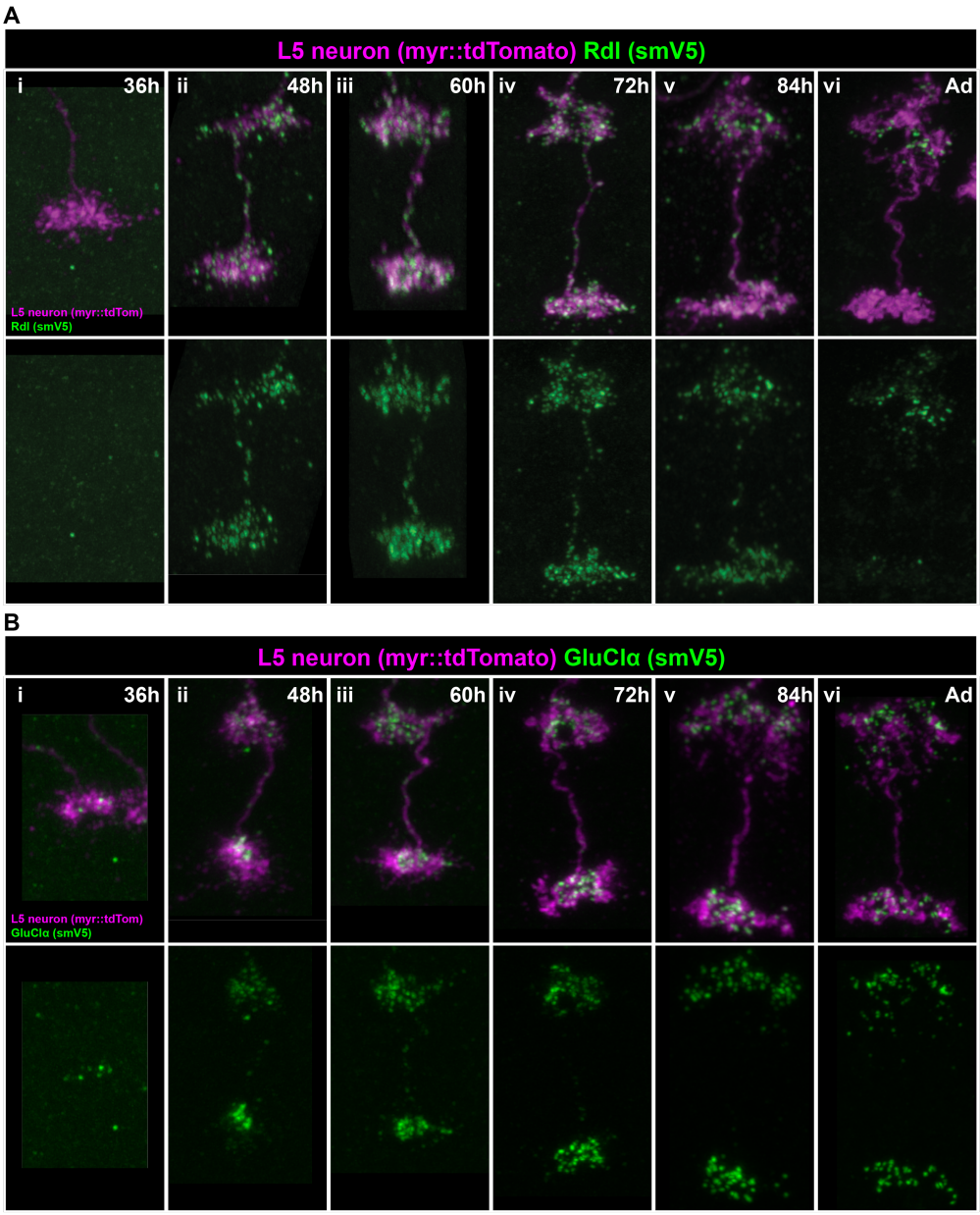

(A) Rdl expression in L5 neurons during pupal development. Times indicate hours after pupal formation. (B) GluClα expression in L5 neurons during pupal development. Times indicate hours after pupal formation. Scale bar, 5 μm; h, hours after pupal formation; Ad, adult. See text for further description.

Figure 3.5 Developmental localization of nAChRβ1 in L5 neurons

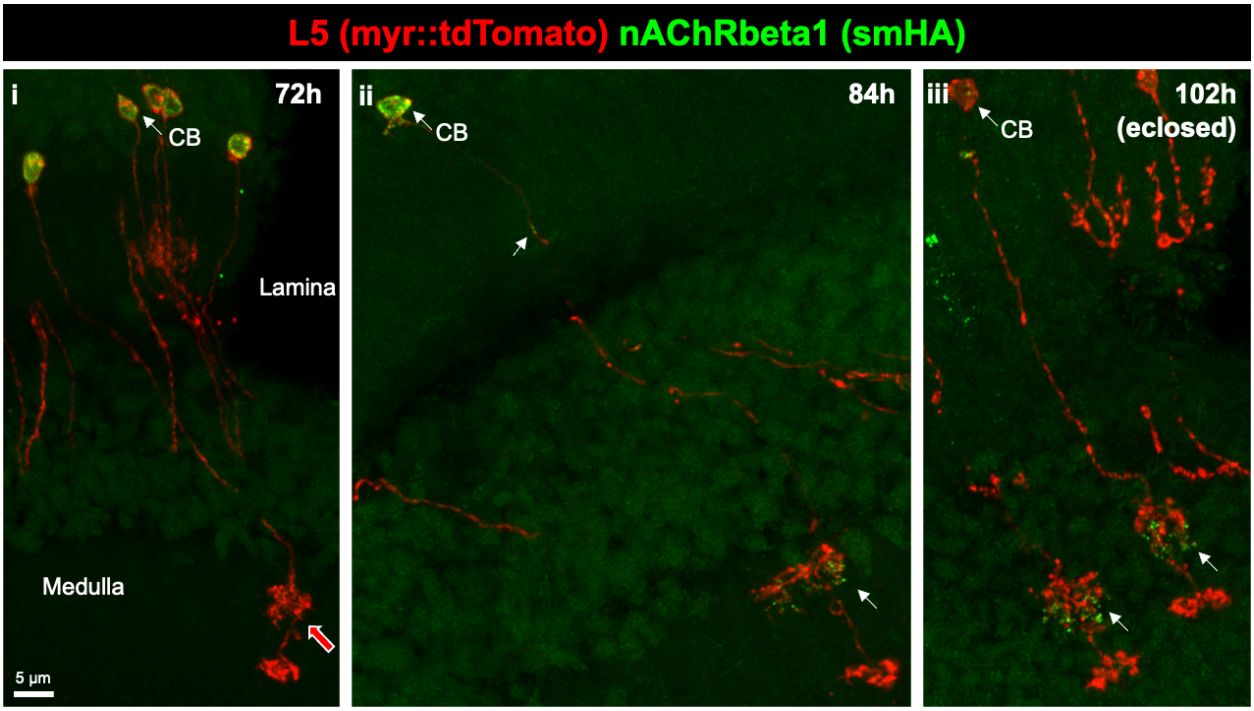

Localization nAChRbeta1 in L5 neurons at two pupal time points (i-ii) and newly eclosed animals (iii). Cell bodies (CB) are located distal to the lamina neuropil and send projections through the lamina to the medulla. nAChRbeta1 is restricted to the CB at 72 hrs. Some nAChRβ1 reaches terminals by 84hrs, but the receptor largely remains localized to the CB. By eclosion, there is little receptor in the CB with localization largely restricted to axon terminals. White arrows, nAChRβ1 at indicated subcellular locations. Red arrow, L5 dendrites devoid of receptor. Scale bar, 5 µm; h, hours after pupal formation.

Figure 3.6 Presynaptic development in L1 neurons

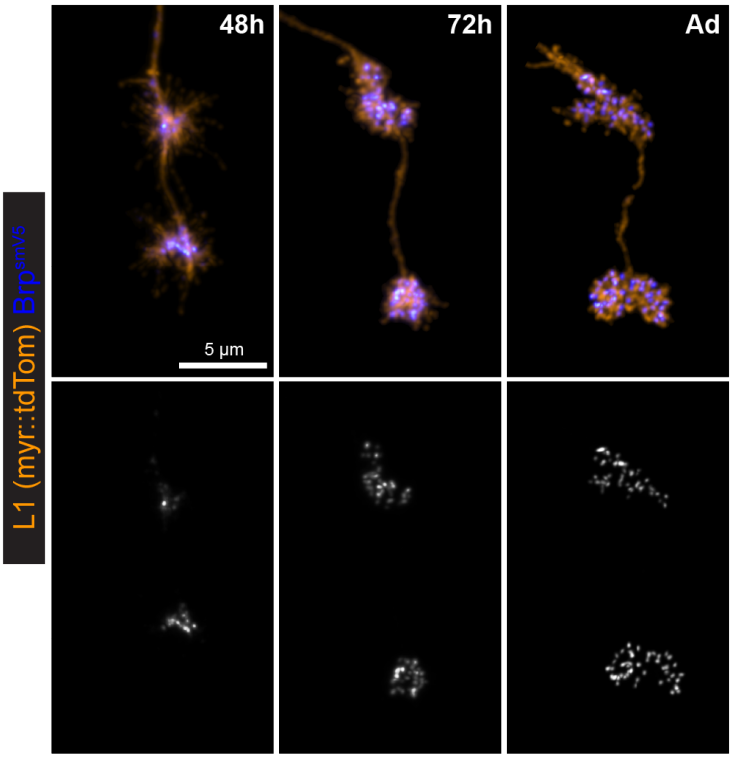

Synaptic tagging after recombination (STaR) of Brp sites in L1 neurons during development and in adult. At 48h, Brp is aggregated in puncta within the central arbors of L1 neurons in layers M1 and M5. By 72h, Brp puncta in layer M1 have spread out while Brp puncta in layer M5 remain aggregated. By young adults, Brp in L1 neurons is distributed into well-defined puncta spread throughout the branches in layers M1 and M5. Scale bar, 5 µm; h, hours after pupal formation; Ad, adult.

Figure 3.7 Organization of synaptic inputs and NR types in L5 neurons

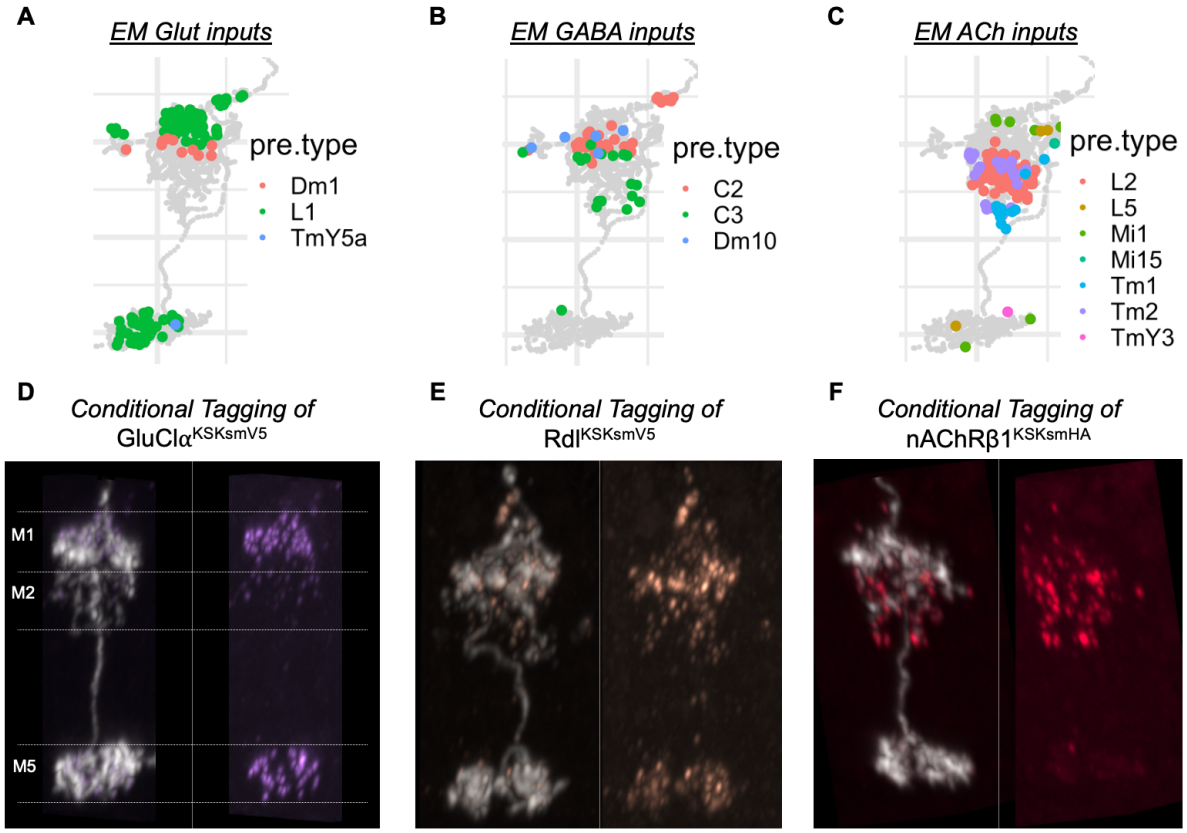

(A-C) Analyzed EM connectomic data plotting the skeleton of a reconstructed L5 neuron and locations of synaptic inputs from various neuron types, colored as indicated. Source data from FIB-25 (Takemura et al., 2015).

(A) Glutamatergic inputs from three presynaptic neuron types onto L5.

(B) GABAergic inputs from three presynaptic neuron types onto L5.

(C) Cholinergic inputs from seven presynaptic neuron types onto L5.

(D-F) Immunofluorescence results obtained with the indicated conditional tagging alleles for NR subunits in single L5 neurons.

(D) GluClα_KSK_smV5 (purple) conditionally tagged in L5 neurons labeled with a membrane marker (gray). Dashed lines represent the approximate boundaries of layers M1, M2, and M5.

(E) Rdl_KSK_smV5 (orange) conditionally tagged in L5 neurons labeled with a membrane marker (gray).

(F) nAChRβ1_KSK_smHA (red) conditionally tagged in L5 neurons labeled with a membrane marker (gray).

See text for further description.

Chapter 4: Expansion Microscopy of Synaptic Proteins

This chapter focuses on my efforts to utilize expansion microscopy (ExM) in studying molecular localization at synapses.

4.1 Background

Our studies using the newly generated epitope-tagged NR subunit alleles were limited by the constraints of confocal microscopy. Imaging single neurons revealed the subcellular distributions of various NR subunits, and developmental analyses demonstrated their progressive localization to respective synaptic domains. However, both results were inadequate in their ability to validate whether the observed staining patterns reflected synaptic puncta. While quantification for some NR subunit distributions, such as GluClα, correlated well with synapse counts derived from EM connectomics, other NR subunits showed discrepancies in their quantification across the multiple neuron types that we studied. These observations raised questions about whether detected NR puncta were localized to synapses or not and whether they were sufficiently resolved to reflect individual connections.

Of course, standard colocalization studies with known synaptic markers could directly address the question of synaptic localization. However, the sheer density of synapses in Drosophila neuropil precludes our ability to determine colocalization of ubiquitous synaptic markers such as Brp imaged by confocal microscopy. Furthermore, for some classes of synapses in *Drosophila* brain we lack specific postsynaptic markers. These limitations motivated us to develop ExM methods that would overcome the resolution barrier for colocalization analysis of our tagged NR subunits with synaptic markers.

A 4X expansion protocol developed for protein retention (Asano et al., 2018; Tillberg et al., 2016) was used with minor modifications (see Chapter 2) to prepare expanded tissue specimens for imaging with a light sheet microscope (ZeissLS7). With this approach, we could determine colocalization of tagged NR subunits with Brp, which we stained using the well-characterized monoclonal antibody nc82 that labels presynaptic active zones (Wagh et al., 2006).

Several unanswered questions could be studied using our ExM approach. In these studies, a primary goal was to determine whether epitope-tagged NR puncta were synaptically localized by conducting a colocalization analysis with Brp. In adult neurons, these studies would unveil whether NR subunits were distributed into both synaptic and extrasynaptic populations. Similarly, during development, the observation of trafficking NR puncta could be followed up to determine when and where they became localized to synapses. Other synaptic proteins could also be studied with available antibody reagents.

Finally, I advanced imaging and analysis methods to take advantage of the highly efficient acquisition of our LS7 light sheet microscope and the optically cleared conditions of the expanded samples to enable large volume datasets. Whether or not localization differed across brain regions or various synapse types could be determined throughout the whole brain. Furthermore, with our newly achieved resolution, the subsynaptic organization of molecules at different synapses could also be studied.

4.2 Localizing synaptic molecules with expansion microscopy

4.2.1 Signal retention of synaptic molecules with ExM

ExM protocols must maximize the retention of proteins (including antibodies of pre-stained samples) while simultaneously maximizing the ability of the gelled sample to expand isotropically without resistance. To allow for gel expansion, protocols rely on either protein digestion or protein denaturation. Our 4X protocol utilized a broad-spectrum digestion with Proteinase K (see Chapter 2). To minimize signal loss, proteins must first be maximally cross-linked into the gel during the anchoring step, which uses acryloyl-X, an amine-reactive molecule that allows acrylamide moieties to be covalently bonded to proteins such that they can be crosslinked into a polyacrylamide gel. Thus, retention of the desired protein fragments (in this case, the localized secondary antibodies carrying the conjugated fluorophores) must be maximally saturated with acrylamide moieties and sufficiently crosslinked, such that after proteinase K digestion the cleaved fragments carrying the fluorophore remain polymerized in the gel and are not washed out.

I evaluated the overall signal retention following each step of the expansion protocol and observed the greatest decline in signal following the digestion step (**Figure 4.1**). This suggests that a fraction of the protein content, including immunoreactive antibodies, is not retained in the gel by crosslinking (i.e. many fragments produced by proteinase K lack an anchoring point). Higher concentrations and longer incubation times of acryloyl-X did not increase the protein retention in our experiments or in others' (Damstra et al., 2022), but lower concentrations dramatically reduced protein retention. Previous studies also reported that decreased concentrations of proteinase K could improve signal retention but at the cost of incomplete expansion (Damstra et al., 2022). I

also observed subsequent decreases in signal over the following protocol steps, likely due to the dilution of fluorescent signal density as the sample is expanded.

These observations suggest that signal retention from protein immunohistochemistry using our ExM protocol is limited, in particular by the digestion step. Therefore, the potential impact of the ExM protocol on our observed staining patterns warrants several considerations. For instance, if the expansion process reduces signal intensity beyond a certain threshold, we would anticipate a reduced detection sensitivity for weaker staining. Furthermore, the ExM protocol could qualitatively change a staining pattern—immunoreactive protein complexes could, for example, be differentially amenable to acryloyl-X anchoring or differentially resistant to protease degradation. However, our ability to discern whether or a staining pattern is qualitatively altered by the ExM protocol is limited by our prior knowledge of its appearance under super resolution.

In our ExM samples, we observed staining patterns that appeared grossly similar to conventional confocal methods and in some cases actually appeared to have greater sensitivity, perhaps due to the reduced background from the clearing effect of the expansion process (see below). We also observed equivalent staining patterns with the synaptic marker nc82 relative to reported super-resolution results that used stimulated emission depletion (STED) microscopy (see Chapter 2), which can be performed on a conventional staining preparation. Thus, our comparable studies between confocal and ExM and the super-resolved appearance of nc82 staining in ExM versus STED gave us increased confidence in the reliability of our ExM-based observations.

4.3 Organization of Drosophila N-cadherin in adult synapses

4.3.1 N-cadherin localizes in juxtaposition with active zones

In a preliminary study, I investigated the localization of N-cadherin (CadN) in the adult brain given its reported role in synapse development (Nern et al., 2005; Prakash et al., 2005). With ExM, I observed CadN staining throughout the brain (**Figure 4.2**A). In brain regions including lamina, medulla, and mushroom body calyx neuropil, CadN puncta localized to virtually all synapses labeled by Brp, with additional CadN puncta present that did not colocalize with Brp (**Figure 4.2**B).

A study in cultured rat hippocampal neurons that super-resolved N-cadherin using structured illumination microscopy (SIM) demonstrated a comparable pattern of subsynaptic localization, with sparse puncta observed at the peripheries of synapses at baseline (**Figure 4.2**C)(Yam et al., 2013). See Section 4.3.3 for further discussion.

4.3.2 N-cadherin is associated with multiple synapse classes

To follow up on the observed colocalization of CadN with Brp, I carried out several additional experiments to co-stain these molecules in combination with constitutively tagged NR subunit alleles. Four subunits, nAChRβ1, nAChRα7, GluClα, and Rdl were studied in combination with Brp and CadN staining.

In different brain areas, the organization of Brp, CadN, and NR subunits appeared different. In lamina neuropil, nAChRβ1 and CadN were colocalized in sparse puncta in juxtaposition to Brp (**Figure 4.3**A). In the medulla, some Brp sites were observed with two CadN puncta similarly

juxtaposed to flanking sides of the Brp, however some of these synapses colocalized with a large, continuous cluster of nAChRβ1; additional Brp sites were observed with many colocalized CadN puncta and a few nAChRβ1 puncta (**Figure 4.3**B). In the mushroom body calyx, large glomerular structures were observed that likely reflect PN-to-KC synapses (see Chapter 2), where CadN and nAChRβ1 showed a checkered pattern (**Figure 4.3**C-D).

As for nAChRα7, it was observed in proximal medulla in continuous, laminar or paraboloid densities juxtaposing presynaptic Brp sites, with CadN puncta flanking the periphery of Brp in spaced intervals (**Figure 4.4**A). nAChRα7 is also strongly present in the lobula plate, where it is organized into continuous, ring-shaped densities surrounded by multiple Brp sites; CadN puncta are observed sparsely interspaced among the nAChRα7 signal around the periphery of Brp sites (**Figure 4.4**B). In the mushroom body calyx, I observed clusters of synapses likely reflecting the connection between projection neurons (PNs) and Kenyon cells (KCs) (see Chapter 2), with multiple Brp sites organized into glomerular-like structures surrounded by nAChRα7 that faced outwards; here, nAChRα7 was typically organized in direct juxtaposition to a Brp site and CadN puncta flanked the periphery of the Brp or nAChRα7 signal (**Figure 4.4**C).

Other NRs had distinct patterns of synaptic organization with CadN and Brp. In the lamina, GluClα was concentrated in large clusters that were not juxtaposing Brp, consistent with its reported glial localization in this neuropil (Li, 2011); GluClα was also seen juxtaposing Brp sites, and CadN puncta were distributed sparsely colocalized with either GluClα or Brp in both cases. (**Figure 4.5**A). In layer M10 medulla, GluClα was solely observed in larger structures that juxtaposed multiple Brp sites, with CadN puncta scattered in an overlapping pattern relative to GluClα (**Figure 4.5**B). These groups of synapses likely reflect the axon terminal boutons of individual Mi9 neurons, who form the only glutamatergic outputs in layer M10.

Rdl was also observed in several distinct arrangements with CadN and Brp. In lamina neuropil, Rdl was seen in various configurations densely accumulated or in sparse puncta that juxtaposed presynaptic Brp, with two or three CadN puncta typically flanking the sides (**Figure 4.6**A). Concordant with the presence of multiple GABAergic input classes demonstrated in connectomic data, several distinct patterns of Rdl synapses were observed in layer M10 proximal medulla neuropil. First, a synapse type was observed in which a single, claw-shaped Brp density was circumscribed by continuous Rdl, with CadN puncta sparsely, regularly interspersed along the ring, colocalized with Rdl (**Figure 4.6**B). Rdl was also observed organized into larger clusters of multiple synapses that either formed twisting groups facing different directions (**Figure 4.6**C), or formed a paraboloid surface with all the synapses facing outwards (**Figure 4.6**D); in both cases, CadN puncta were sparsely distributed flanking the Brp sites. Future work could investigate whether these different arrangements correlate to the synaptic architecture of different GABAergic terminals reconstructed in EM connectomic data.

4.3.3 Interpretation of N-cadherin ExM studies and limitations

In developing pupal optic lobe, the staining patterns of the anti-CadN monoclonal antibody reagent used in this study are well characterized (Chan et al., 2017; Hayashi & Carthew, 2004; C.-H. Lee et al., 2001; Nern et al., 2005, 2008; Prakash et al., 2005; Trush et al., 2019). Here, CadN concentrates in continuous surfaces of stereotyped geometries at the adherens junctions between contacting cells. However, in adult brains the appearance of anti-CadN staining is less reported (especially with super-resolution microscopy methods). One study reporting anti-CadN staining in adult medulla demonstrated a staining pattern of densely crowded puncta restricted to the neuropil, similar to Brp (Schnaitmann et al., 2018), which resembled our observations. The different appearance of CadN in adult neuropils compared to developing pupal brains could reflect different

functions and subcellular localizations, perhaps arising from different CadN isoforms. In some instances, for example, a shift in CadN isoform expression during pupal development has been demonstrated to mediate distinct steps of axon terminal targeting and termination in photoreceptor cells (Nern et al., 2005), supporting this notion.

Nonetheless, our preliminary observations of CadN staining are limited by several potential caveats of the ExM protocol. The highly punctate and relatively sparse staining pattern of CadN observed under ExM raised the possibility that the immunoreactivity could be degraded during the expansion process, for instance during the protein digestion step. In this scenario, the observed distribution of CadN could contain artifacts due to incomplete retention of the staining pattern. Given the lack of prior studies reporting CadN staining under ExM, we cannot make an easy comparison to validate our observations. Conventional imaging methods would fail to resolve CadN at adult synapses given their density in the neuropil. Thus, without comparable super-resolved immunofluorescence of CadN, we lack *a priori* knowledge of how to expect our ExM results to appear.

In vertebrates, N-cadherin is localized to the synaptic cleft (Yamagata et al., 1995). A previous study using SIM for super-resolution of synapses in cultured rat hippocampal neurons showed that N-cadherin was localized in a range of punctate to continuous distributions juxtaposing presynaptic active zones marked by Bassoon (see **Figure 4.2**C). The authors found that the distribution of N-cadherin was dynamic and shifted in observed frequency from peripherally to centrally localization at synapses following transient neuron depolarization (Yam et al., 2013). This phenomenon could account for the variety of configurations in which N-cadherin was observed. In my experiments, I rarely observed continuous densities of CadN in the synaptic cleft, but this discrepancy could be due to molecular differences (*Drosophila* N-cadherin has

significant variation in amino acid sequence compared to its mammalian counterpart, particularly in the extracellular domain, and could function differently), physiological differences (i.e. the state of invertebrate neurons *in vivo* versus the state of mammalian neurons *in vitro*), or technical differences (different antibody reagents, specimen preparations, and imaging modalities).

On the other hand, staining patterns could be readily validated for the well characterized organization of CadN in the developing pupal optic lobe. In preliminary experiments, I tested the ability of the ExM protocol to preserve a continuous (non-punctate) CadN staining pattern by dissecting and staining midpupal brains. In these experiments, I observed concentrated laminar patterns of CadN in pupal retina that resembled the stereotyped geometry of contacting R cell and cone cell adherens junctions (**Figure 4.7**). These findings demonstrated that a continuous pattern of CadN immunoreactivity could be preserved through the rigors of the ExM protocol. Thus, the sparse distribution of synaptically localized CadN puncta observed in adult brains is more likely to reflect an intact staining pattern rather than an artifact of ExM. Future work should conduct a time course analysis of CadN localization throughout pupal development. For studies in the retina, an isolated eye preparation co-stained with other markers (e.g., E-cadherin) would be best suited to validate the pattern of CadN at adherens junctions.

To summarize, several control studies should be utilized to validate newly observed staining patterns under ExM. Of primary importance, ExM should ideally be validated through comparison to other super-resolution methods such as STED or SIM that do not alter the histology. (This comparison was a key point of validation for Brp labeling with nc82 in Chapter 2.) Alternatively, the retina and lamina offer potential solutions where super-resolution may not be required to validate ExM staining patterns by comparison to standard confocal results, given that the lower density of these neuropils is more easily resolved. (This approach was demonstrated for

CadN staining.) Finally, the specificity of immunoreactivity under ExM can be validated through co-staining experiments using a second antibody reagent or a genetically tagged version of the target, depending on available reagents. (Co-staining a V5-tagged allele was a key point of validation for Mmd staining in Chapter 2). Together, these methods can support ExM observations for previously uncharacterized staining patterns.

4.3.4 N-cadherin staining reagents for ExM

These experiments utilized our standard ExM protocol with primary and secondary antibody dilutions equivalent to those described in Chapter 2. To stain for N-cadherin, I used the primary antibody rat anti-CadN (DN-Ex #8, Developmental Studies Hybridoma Bank), a monoclonal rat antibody generated against an extracellular fragment of CadN, diluted to 5 μg/mL. As a secondary antibody, I used goat anti-rat IgG::AF488 (Abcam, Cat# ab150165) or goat anti-rat IgG::AF546 (Invitrogen, Cat# A110811) diluted 1:100.

4.4 Synapse formation during development with ExM

Using the constitutively tagged alleles, I followed localization of NR types throughout the brain during brain development. Three tagged NR subunits, nAChRβ1, GluClα, and Rdl were co-stained with Brp and dissected at 48, 72, and 96 hrs APF.

In medulla neuropil, the process of localization over development was different in different layers. At 48 hrs, nAChRβ1 localization in the neuropil was limited and a small fraction of dim puncta were observed colocalize to Brp (**Figure 4.8**A, J). At 72 hrs, nAChRβ1 was observed colocalized to Brp in both layers M8 and M10 (**Figure 4.8**B, K). At 96 hrs, nAChRβ1 had further increased in localization to layer M10 but appeared unchanged in layer M8 (**Figure 4.8**AC, L).

GluClα developed differently in the medulla. At 48 hrs, large, bright clusters of GluClα appeared colocalized with Brp in layer M8, whereas in layer M10 GluClα was absent (**Figure 4.8**D, M). In layer M8, GluClα remained colocalized with Brp at 72 and 96 hrs (**Figure 4.8**E, F, Ni, Oi). In layer M10, at 72 hrs, GluClα was colocalized with Brp in glomerular structures (**Figure 4.8**E, Nii). At 96 hrs, GluClα in layer M10 was localized in larger, brighter clusters with Brp (**Figure 4.8**F, Oii). The glomerular structures of GluClα synapses observed in M10 likely reflect the footprint of individual axon terminals of glutamatergic Mi9 neurons (see Chapter 2).

Finally, Rdl showed a third, distinct process of development. At 48 hrs, Rdl was localized in large, bright clusters that colocalized with Brp in layer M10, as well as smaller clusters that colocalized with Brp in layer M8 (**Figure 4.8**G, P). Numerous smaller Rdl puncta were also present throughout the medulla that did not colocalize with Brp (**Figure 4.8**G, P). On one hand, in layer M10, Rdl localization to Brp appeared unchanged at 72 and 96 hrs (**Figure 4.8**H, I, Qii, Rii). On the other, in layer M8, Rdl localization progressively increased at 72 and 96 hrs, concentrated in larger clusters juxtaposing Brp (**Figure 4.8**H, I, Qi, Ri).

These studies provided evidence of differential localization processes throughout the developing brain across different regions, and for different NR types. In layer M10, the process of localization was concordant with corresponding developmental patterns in T4 dendrites. For instance, GluClα and nAChRβ1 localized late in T4 dendrites after 72 hrs, while Rdl localized early in T4 dendrites by 48 hrs (see Chapter 2). These time courses match the observed patterns in proximal medulla where T4 dendrites are the major postsynaptic processes innervating layer M10.

4.5 Single-neuron studies with ExM

4.5.1 Synaptic localization of nAChRβ1, GluClα, and Rdl in L5 neurons

NR localization studies in L5 neurons with confocal microscopy demonstrated several discrepancies in quantification when compared to EM synapse counts. Thus, I reinvestigated the localization of nAChRβ1, GluClα, and Rdl in L5 neurons in combination with anti-Brp staining using ExM.

In adult L5 neurons, nAChRβ1 was localized to M2 branches. Under ExM, smHA-tagged nAChRβ1 appeared in small, uniform puncta discretely distributed in the dendrites, as opposed to the larger conglomerates visualized in our confocal samples (**Figure 4.9**A). Co-stain with nc82 revealed that the individual nAChRβ1 puncta were juxtaposing Brp at presynaptic active zones (**Figure 4.9**B).

For GluClα and Rdl, I conducted developmental analyses by dissecting pupal brains at 48, 72, and 96 hrs APF. The figure for GluClα development in L5 neurons was added to our published manuscript after revisions, but it has been reproduced for this section. At 48 hrs, GluClα puncta were distributed in layer M1 and M5 dendrites, with only a small fraction colocalized to Brp (**Figure 4.10**A). At 72 hrs, GluClα had accumulated further in layers M1 and M5 and was no longer seen trafficking throughout the main neuron stalk (**Figure 4.10**B). Both layers M1 and M5 contained larger, brighter GluClα puncta that colocalized with Brp, and layer M5 contained additional smaller, dimmer GluClα puncta that were not colocalized with Brp (**Figure 4.10**B, white arrowheads). At 96 hrs, additional GluClα colocalizing to Brp had accumulated in layers M1 and M5, and the non-colocalized GluClα puncta in layer M5 had disappeared (**Figure 4.10**C).

As for Rdl, at 48 hrs, Rdl was seen distributed through the dendritic branches with no significant colocalization to Brp (**Figure 4.11**A). A few Rdl puncta annotated as colocalizing with Brp by my automated segmentation algorithm, but upon closer inspection these appeared to be erroneous. At 72 hrs, a large increase in Rdl puncta was seen distributed throughout dendritic branches, with a fraction colocalizing to Brp (**Figure 4.11**B). At 96 hrs, the overall amount of Rdl had decreased and none were seen in the main neuron stalk; a subset of brighter, larger Rdl puncta were colocalized to Brp in layers M1 and M2 (**Figure 4.11**C), reflecting the adult circuit determined by EM (see Chapter 2). This finding correlated with our observations under confocal microscopy that demonstrated two distributions of Rdl puncta, with the brighter, larger set distributed in the pattern of GABAergic inputs and additional smaller puncta seen throughout layers M1, M2, and M5.

4.6 Whole-brain studies with ExM

In preliminary experiments, I sought to optimize the imaging pipeline for whole-brain ExM studies. Example data and a description of the methods are described as follows. Constitutively tagged GluClα^{smV5} brains were co-stained with nc82 to label GluClα-bearing synapses and whole-mounted for ExM (**Figure 4.12**A). In these data, the magnification was reduced from 50x to 20x by adjusting the optical zoom of the ZeissLS7 microscope from 2.5 to 1.0 while using the same 20x objective (see Chapter 2). The whole-brain data using 20x magnification demonstrated clear individual synapses with similar resolution to images taken at 50x magnification reflecting the imaging parameters used for all other ExM data collected in this work (**Figure 4.12**B-C). Magnification at 20x produced a raw pixel scale of 0.235 μm/pixel (before adjusting for expansion).

Optimizing the signal resolution at this lower magnification required several additional adjustments to the parameters specified using the ZeissLS7 (see Chapter 2 for operating software details). First, the light-sheet thickness was minimized to a 1.4µm thickness, matching the thickness of images acquired at 50x magnification. The thinness of the light-sheet dropped off substantially along the x-axis away from the center of the field of view, leading to out of focus signal outside of the middle strip. To accommodate for this, the acquisition window was adjusted to a 256-pixel width in x, while maintaining the original 1920-pixel height in y. In order to acquire large volumes, image tile acquisitions were set up with a few dozen tiles in x (given the narrow width) and several tiles in y in order to capture the full area of the brain. A z-step of 300-400 nm was used. Analysis scripts to process the ExM data were adapted to process the tiled data.

4.7 Future Work

Quantification studies are vital for the complete analysis of ExM data. In order to accurately assess synapse counts, synaptic puncta must be correctly identified and separated through segmentation or centroid analysis. Characterization of synaptic markers in regard to puncta size, shape, colocalization, or other geometric properties requires three-dimensional segmentation. I developed a segmentation pipeline to process ExM data captured by the ZeissLS7 light sheet fluorescent microscope. However, these efforts were limited in their accuracy to quantify object counts.

Over-segmentation, for instance, would result in signals from a single synapse to be split into multiple objects and over counted as smaller volumes, whereas under-segmentation would result in multiple synaptic signals being grouped together and under counted as larger volumes. The sensitivity of segmentation pipelines to over- or under-segmentation is largely dependent on

the starting parameters, as well as the overall methods employed. Testing a range of parameters in my pipeline, I found that even in the ideal range some signals would be over-segmented while others would be under-segmented. Thus, there was likely no parameter set that could avoid both types of error. Even using optimized parameters, the pipeline would generate imperfect segmentation results.

Manual correction, or proof-reading of segmentation data, would be an ideal, albeit limiting, approach to ensure accurate segmentation results. By revising the segmented object labels to correct for over- or under-segmentation, the results can be improved to the threshold of human accuracy in signal interpretation. However, this approach is not easily done at scale, where acquired image volumes may contain millions of puncta.

Alternatively, object feature thresholds can be employed to filter out a higher-confidence subset of segmented puncta while ignoring those that are likely to be incorrect. For example, over-segmented objects should have significantly smaller volumes while under-segmented objects should have significantly larger volumes; the anticipated volume range can be used to exclude outliers from the final dataset. However, such methods may also introduce a bias toward segmentation results that fall within a desired range of features.

The observed signals of a synaptic marker under ExM can also be influenced by several factors. For instance, the conjugate dye of the secondary antibody has a significant impact on the appearance of the signal when approaching the diffraction limit—consider that the smallest resolvable signal, the point spread function (PSF), will have a larger diameter for a conjugate dye with a longer wavelength. Thus, the size of observed puncta or the thickness of toroidal or laminar signal densities are at least as great as the observed PSF diameter for that wavelength. As a result,

segmentation parameters must be adjusted for the conjugate dye used, and computed properties such as segmented object volume will be greater on average for longer wavelength dyes.

Future efforts must address the need for suitable analysis methods that can accurately extract measurements of synaptically localized signals. These methods must be equipped to recognize different staining patterns (punctate, toroidal, laminar, etc.) and accurately segment them into discrete synapses while avoiding over- or under-segmentation. In addition, the methods must be fairly robust, or easily adjusted, to account for different conjugate dyes, different light-sheet parameters, and different signal-to-noise ratios. Ideally, they would also be easily adapted for different expansion factors used in different ExM protocols or different magnification used during imaging. To assess these results, synapse counts from EM connectomics can serve as a comparison, as demonstrated for single-neuron confocal data in our publication (see Chapter 2).

4.8 Figures

Figure 4.1 Protein retention with a 4X expansion protocol.

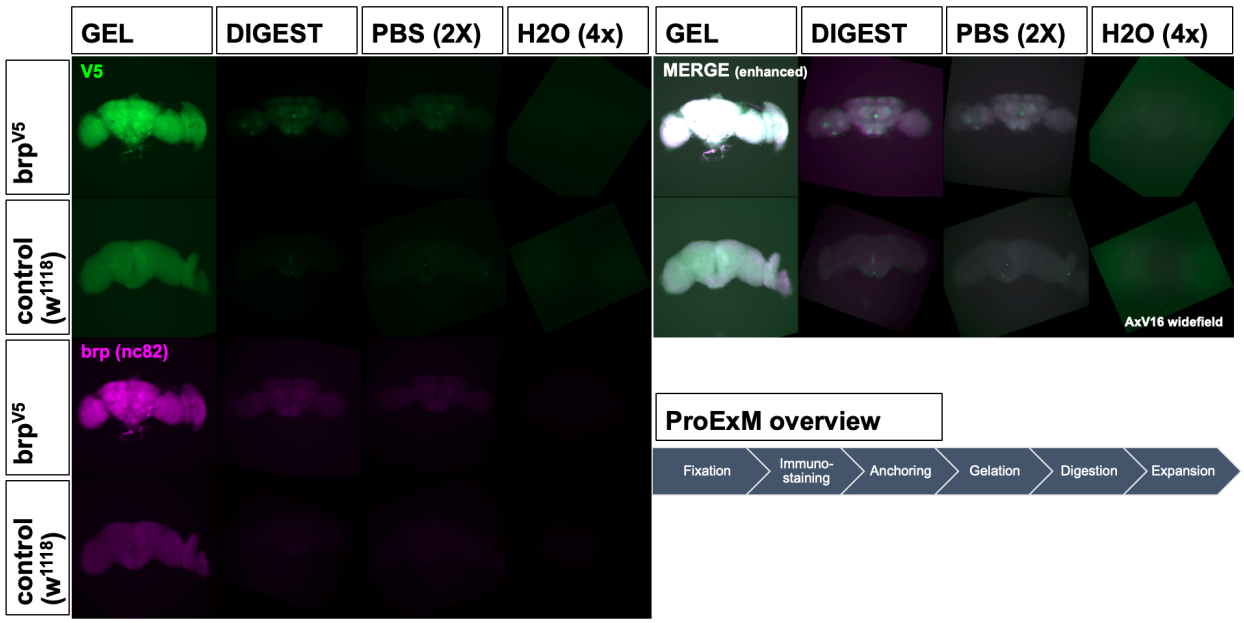

Normalized immunofluorescence signal from the same two brains following indicated steps of the expansion protocol. Upper row in each sub panel shows a brain with a tagged Brp_1XV5 allele, while lower row in each subpanel shows a negative control (w1118) brain. Lower right, overview of the sample preparation steps in the ExM protocol.

Figure 4.2 CadN staining throughout the brain under ExM

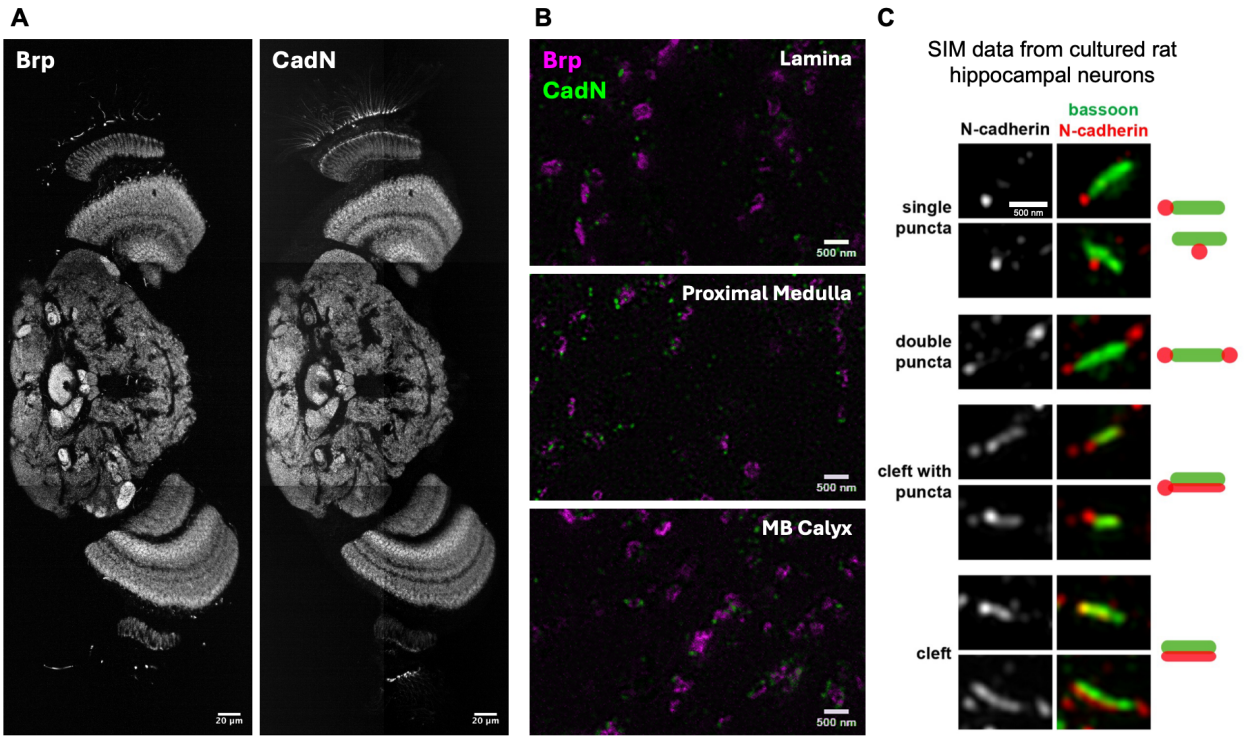

(A) Lower magnification view of a whole brain co-stained for Brp and N-Cadherin (CadN) following ExM preparation. Single z-slice view. Scale bar, 20 µm (adjusted for expansion).

(B) Higher magnification views in indicated neuropils showing overlay of Brp and CadN. Scale bars, 500 nm (adjusted for expansion).

(C) Adapted from Yam et al., 2013. N-cadherin staining in cultured rat hippocampal neurons co-stained for bassoon (a presynaptic active zone protein) and imaged using structured illumination microscopy (SIM) for super resolution. Similar to my studies in Drosophila, the authors observe a range of configurations in which N-cadherin is organized at synapses, which they attribute in part due to shifts from peripheral to central synaptic localization following activation. Scale bar, 500 nm.

Figure 4.3 CadN localizes to cholinergic synapses containing nAChRβ1

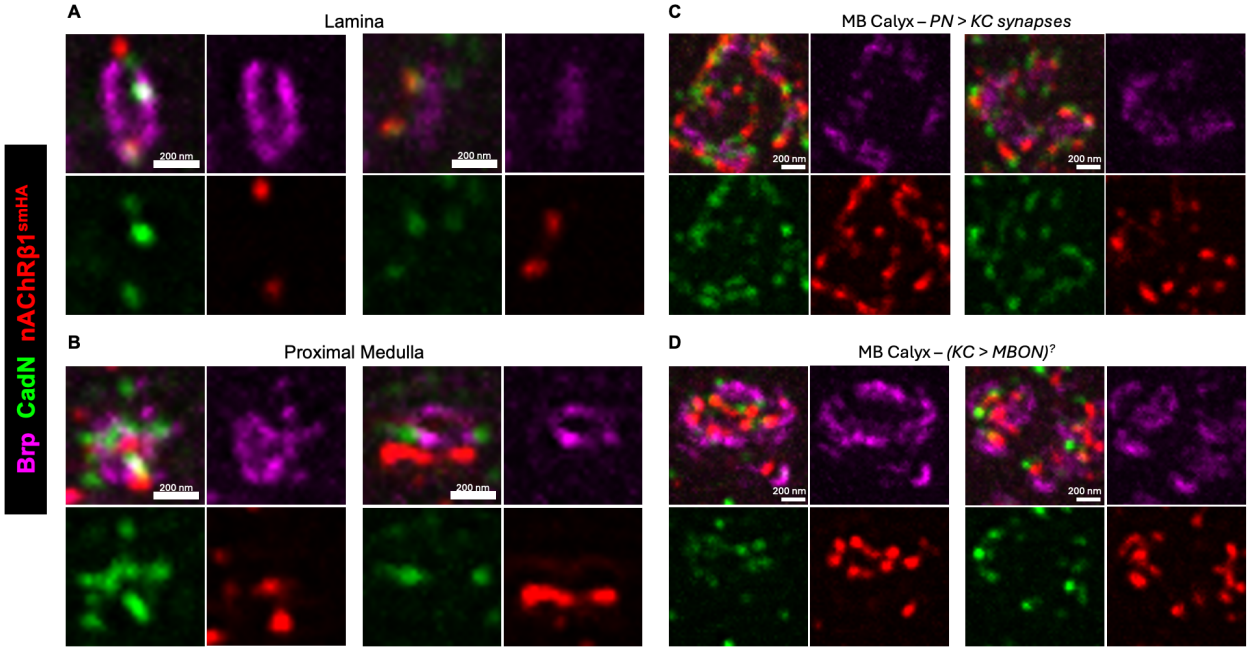

Representative images of various synapse types showing distinct molecular organization in triple-stained brains carrying the constitutively tagged nAChRβ1^{smHA} allele also labeled for Brp and CadN. Subpanels show overlay and isolated channels for each image. Z-projection view (5-11 z-slices). Scale bars, 200 nm (adjusted for expansion).

(A) Synapse types observed in lamina neuropil contain sparse nAChRβ1 with CadN flanking the ends of a presynaptic Brp site. nAChRβ1 and CadN occasionally overlap.

(B) Synapse types observed in proximal medulla neuropil (layer M10) that contain nAChRβ1. nAChRβ1 is seen colocalized to presynaptic Brp in either sparse puncta or a continuous laminar density. CadN is observed in puncta either densely clustered around or sparsely flanking the periphery of presynaptic Brp sites.

(C) Proposed synapse type between projection neurons (PNs) and Kenyon cells (KCs) observed in the mushroom body (MB) calyx (see Chapter 2). 'Glomerular' structures are observed with

multiple Brp sites and nAChRβ1 puncta typically faced outwards, with CadN puncta interspaced between the nAChRβ1 making a checkered appearance.

(D) Proposed synapse type between KCs and mushroom body output neurons (MBONs) observed in the MB calyx. This type of connection is reported in the MB α3 compartment (see Chapter 2), but we observe a similarly organized synaptic arrangement in the MB calyx, which may or may not reflect the same connecting neuron types.

Figure 4.4 CadN localizes to cholinergic synapses containing nAChRα7

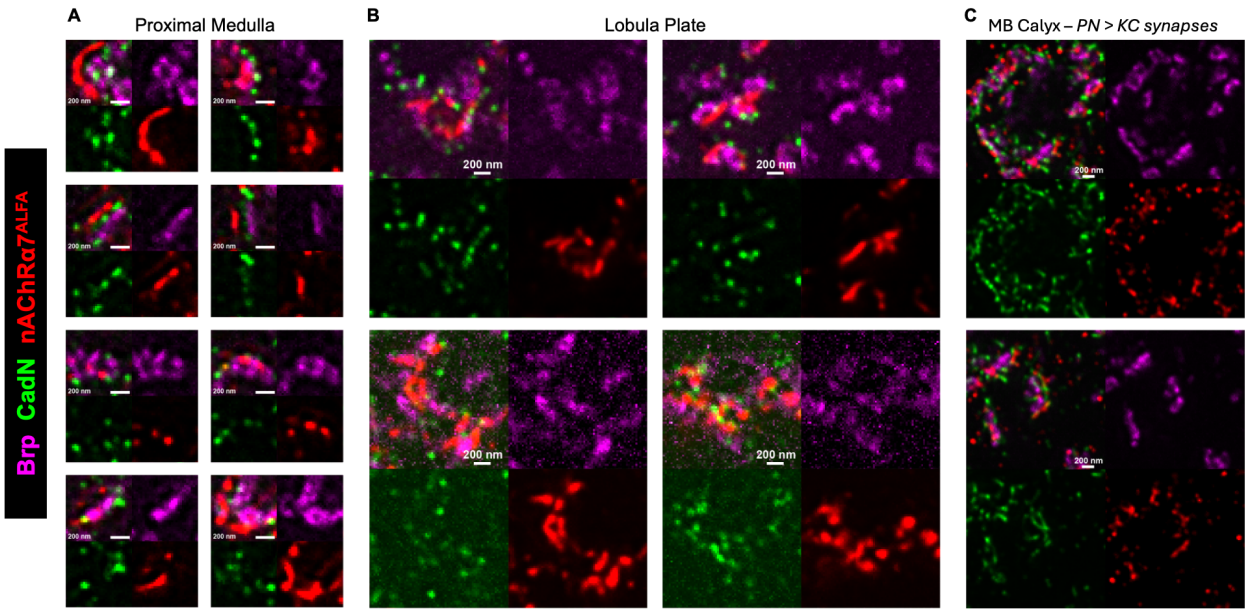

Representative images of various synapse types showing distinct molecular organization in triple-stained brains carrying the constitutively tagged nAChRα7_ALFA allele also labeled for Brp and CadN. Subpanels show overlay and isolated channels for each image. Z-projection view (5-11 z-slices). Scale bars, 200 nm (adjusted for expansion).

(A) Proximal medulla neuropil contains multiple synapse types with nAChRα7. Continuous, laminar or paraboloid densities of nAChRα7 are observed flanking a presynaptic Brp site, with CadN puncta flanking the periphery of Brp in spaced intervals. Some synapses are also observed in which single puncta of nAChRα7 are juxtaposing Brp and CadN puncta are similarly present.

(B) Lobula plate neuropil is rich with nAChRα7. Here, nAChRα7 is organized into continuous, ring-shaped densities surrounded by multiple Brp sites. CadN puncta are observed sparsely interspaced among the nAChRα7 signal around the periphery of Brp sites.

(C) The proposed synapses between projection neurons (PNs) and Kenyon cells (KCs) are observed in the mushroom body (MB) calyx (see Chapter 2). Similar to nAChRβ1, Multiple Brp sites are organized into 'glomerular' structures surrounded by nAChRα7 that typically faces

outwards. Here, the organization of nAChRα7 and CadN appears to generally involve nAChRα7 directly across from a juxtaposing Brp site and CadN puncta flanking the ends of the Brp or nAChRα7 signal. The checkered pattern, observed for nAChRβ1 and CadN, is not as visibly apparent here.

Figure 4.5 CadN localizes to glutamatergic synapses containing GluClα

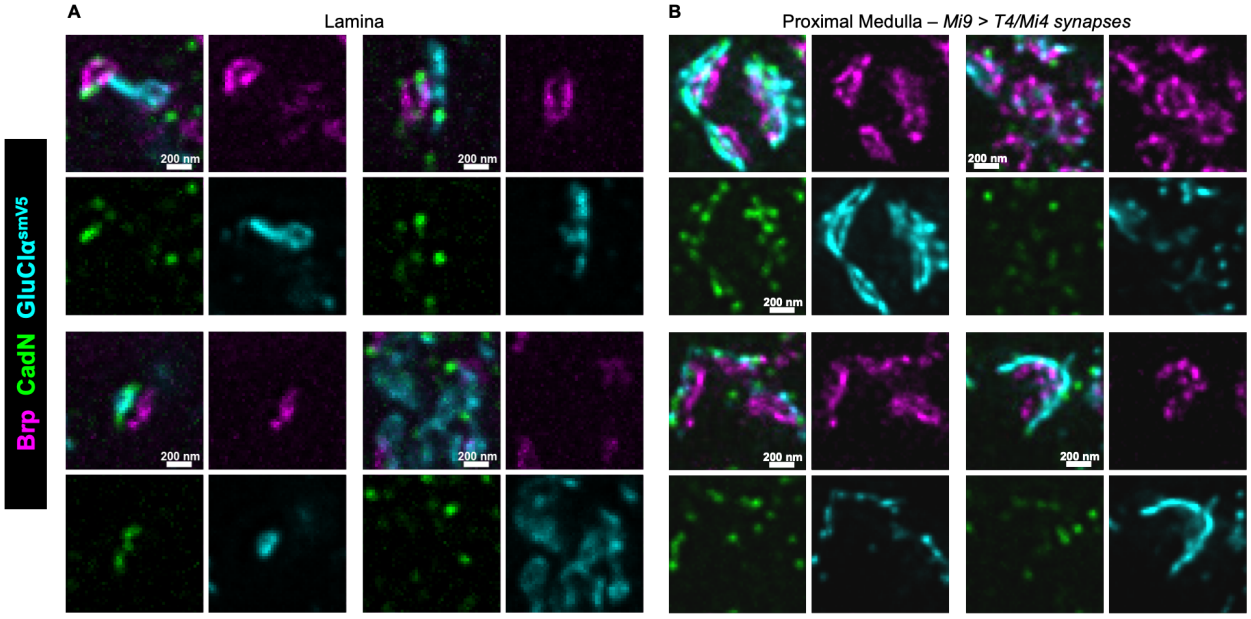

Representative images of the constitutively tagged GluClα^{smV5} allele co-stained for Brp and CadN. Subpanels show overlay and isolated channels for each image. Z-projection view (5-11 z-slices). Scale bars, 200 nm (adjusted for expansion).

(A) Lamina neuropil contains several distinct patterns of GluClα. In some instances, GluClα is organized into large densities that are in the vicinity of, but not juxtaposing, presynaptic Brp sites (upper left and lower right). In other cases, GluClα appears concentrated in direct juxtaposition to Brp sites, likely representing synaptic localization (upper right and lower left). CadN appears sparsely distributed in puncta that overlap both Brp and GluClα.

(B) Proximal medulla neuropil (layer M10) contains groups of GluClα-containing synapses that reflect the synaptic outputs of an Mi9 axon terminal bouton. Synapses captured in different angles reveal that GluClα is organized in a parabolic surface surrounding a cluster of presynaptic sites. CadN puncta are present at these synapses, primarily overlapping with GluClα signal.

Figure 4.6 CadN localizes to GABAergic synapses containing Rdl

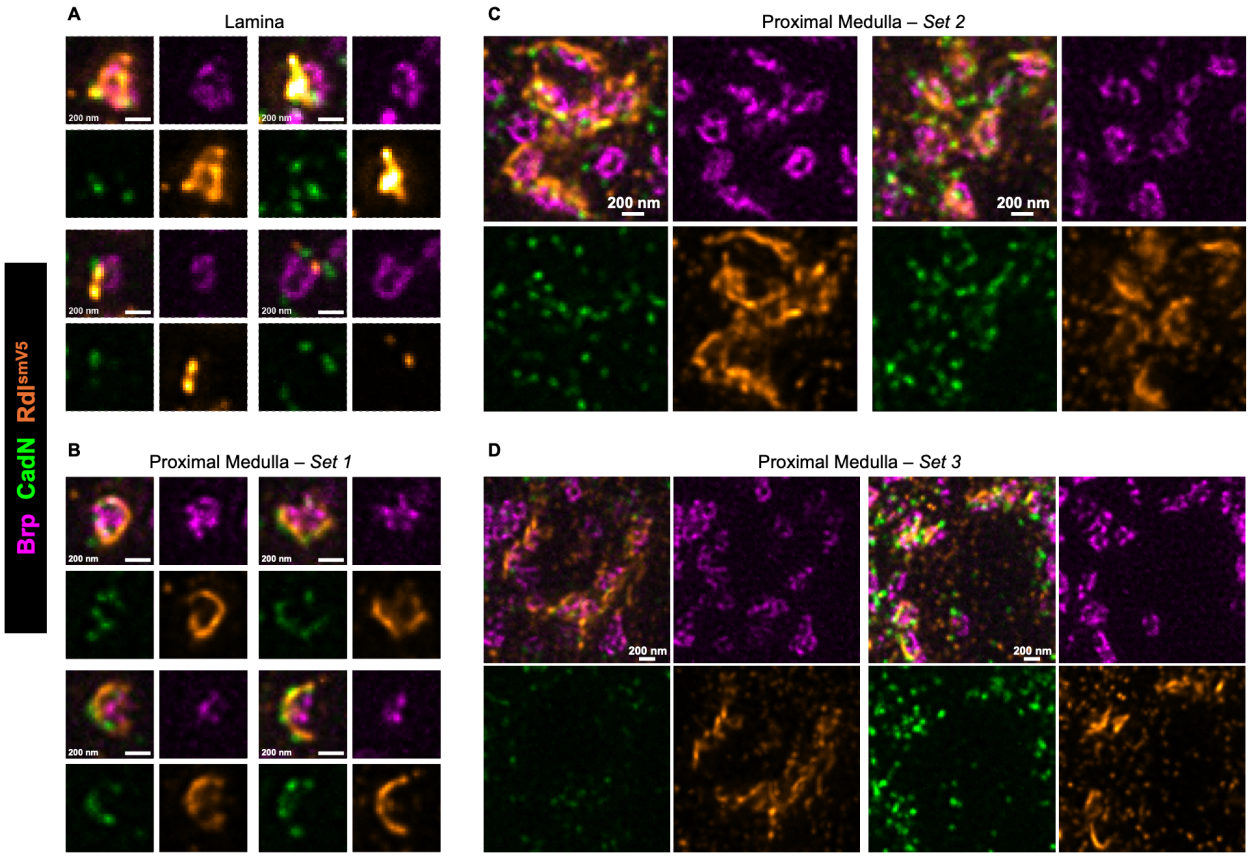

Representative images of the constitutively tagged Rdl^{smV5} allele co-stained for Brp and CadN. Subpanels show overlay and isolated channels for each image. Z-projection view (5-11 z-slices). Scale bars, 200 nm (adjusted for expansion).

(A) Representative images for several different types of Rdl-containing synapses observed in lamina neuropil. Rdl is densely accumulated in juxtaposition to a presynaptic Brp site (upper panels) or observed in more confined punctate densities (lower panels). CadN is frequently observed in two or three puncta that flank the sides of a Brp site.

(B) Representative images from one set of Rdl-containing synapses in the proximal medulla neuropil (layer M10). Captured from different orientations, Rdl forms a ring or parabolic surface

of continuous density around a single claw-shaped Brp site. CadN is regularly interspaced around the Brp site.

(C) Representative images of another set of Rdl-containing synapses observed in proximal medulla. Groups of Rdl-containing synapses are observed with Rdl organized in a dense, continuous fashion. The synapses are grouped in a twisting, contorting fashion with the direction of each synapse facing various directions. CadN puncta are sparsely distributed flanking the Brp sites.

(D) Representative images of a third set of Rdl-containing synapses in layer M10 medulla. Here, groups of Rdl-containing synapses are also observed, but the orientation of synapses are arranged in a continuous, outward-facing parabolic surface, likely reflecting the outputs of an unidentified axon terminal bouton (multiple types of GABAergic neurons form outputs in layer M10, so the identity of Rdl-containing synapses cannot be easily inferred). Rdl is densely accumulated in juxtaposition to Brp surrounding the footprint of the apparent bouton. CadN puncta are once again observed in puncta around the peripheries of Brp sites.

Figure 4.7 CadN staining in pupal retina under ExM

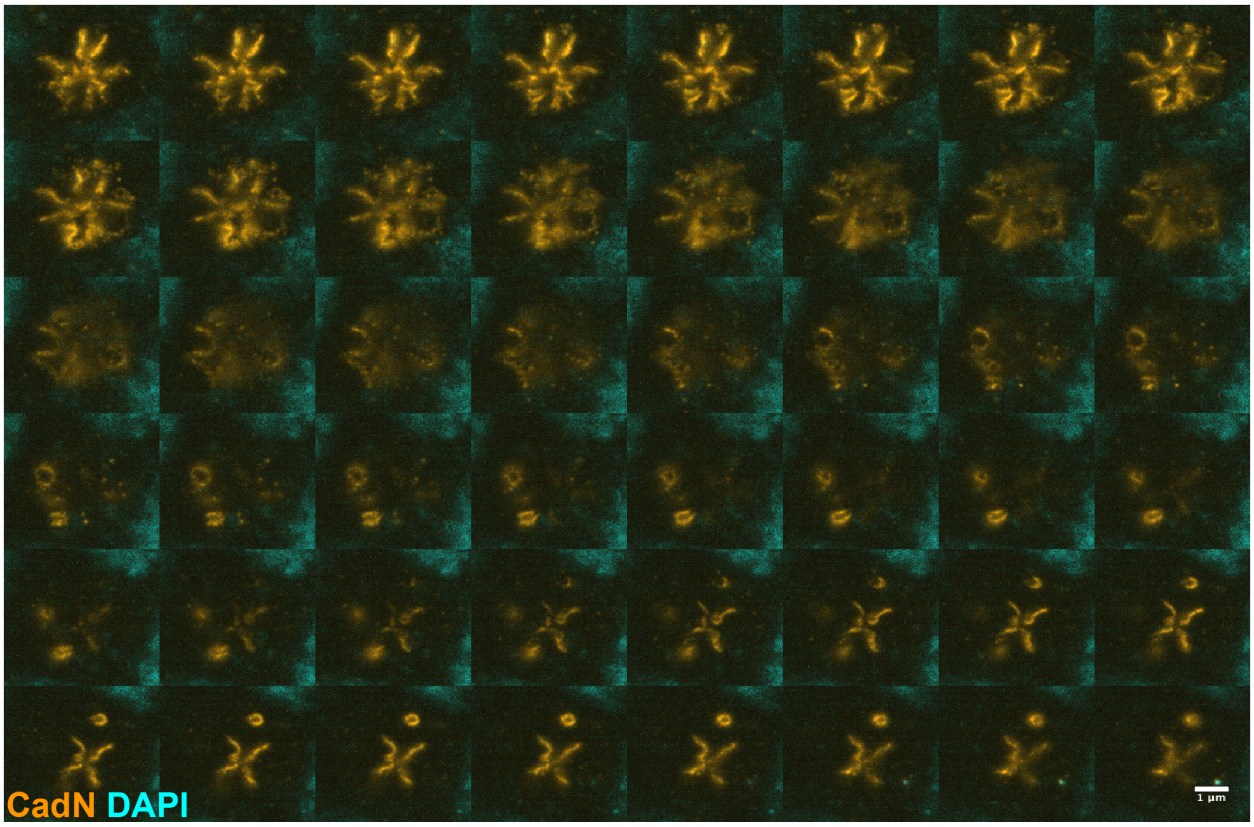

Z-stack montage through an ommatidium in mid-pupal retina, demonstrating CadN staining in a continuous pattern (rather than sparse puncta) of wild-type (w1118 genotype) animals. The observed patterns resemble the stereotyped geometry of R cell junctions (slices 1-16) and cone cell contacts (slices 37-48), where CadN staining is well characterized. Images shown are raw (not deconvolved) data, using whole-mount preparations. Each panel represents a single progressive z-slice. Scale bar, 1 µm and z-step, 0.049 µm (adjusted for expansion).

Figure 4.8 Developmental colocalization of NRs and Brp in medulla with ExM

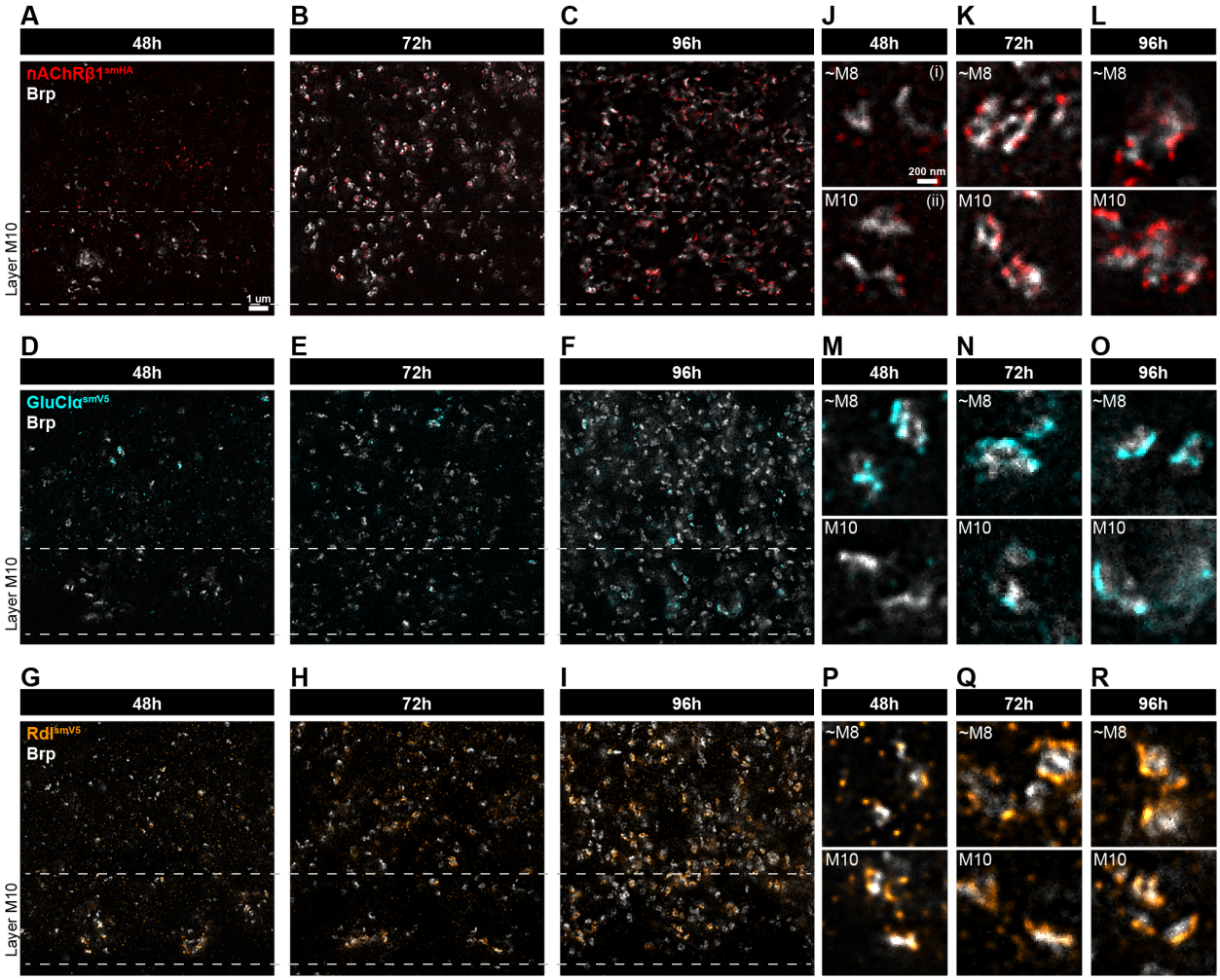

Developmental analysis using constitutively tagged NR alleles co-stained for Brp.

(A-I) Views of proximal medulla (approximately layer M8 to M10) of three different tagged NRs at three different pupal time points, as indicated. Single z-slice views. Scale bar, 1 µm.

(J-R) Upper subpanels, magnified insets of approximate layer M8 neuropil from each condition. Lower subpanels, magnified insets of layer M10 neuropil from each condition. Single z-slice views. Scale bar, 200 nm (adjusted for expansion); h, hours after pupal formation.

Figure 4.9 nAChRβ1 localization in L5 neuron with ExM

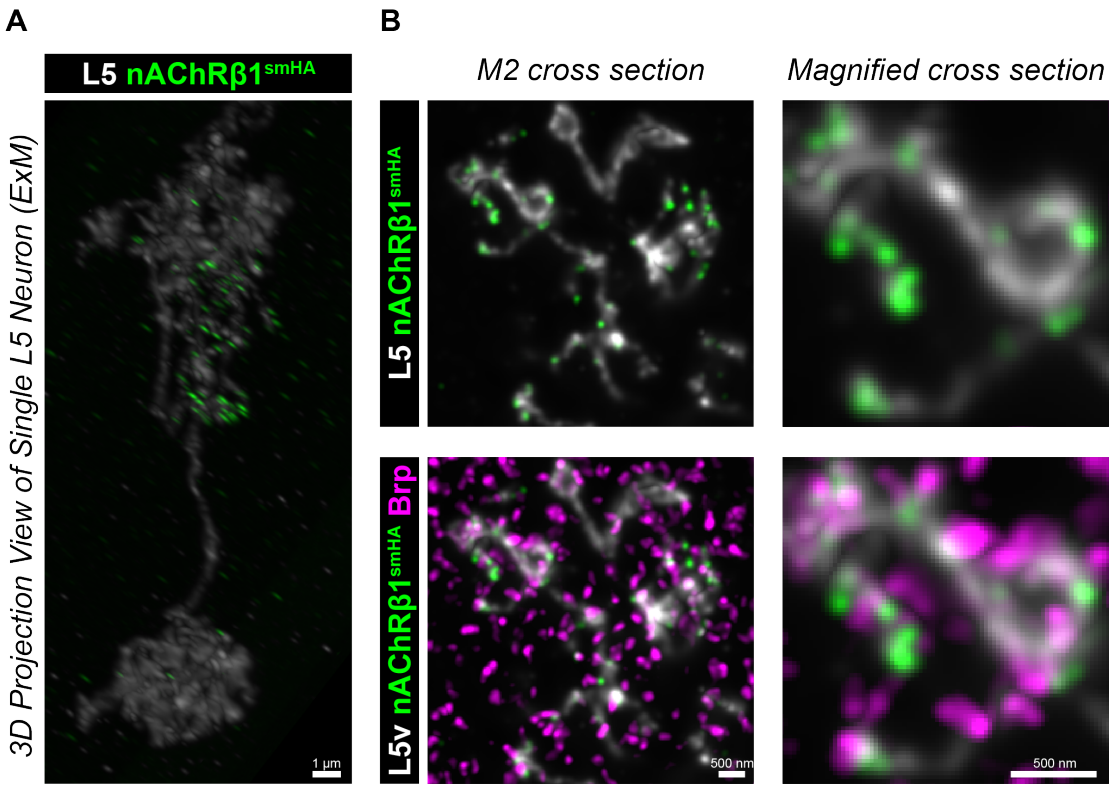

Conditionally tagging of nAChRβ1_KSK_smHA in adult L5 neurons.

(A) 3D projection view of a single L5 neuron with tagged nAChRβ1 localized in layer M2 dendrites. Scale bar, 1 µm (adjusted for expansion).

(B) Cross section (left subpanels) and magnified cross section (right subpanels) from the L5 neuron shown in A. Bottom row, Brp co-stain channel is overlaid, demonstrating that nAChRβ1 are juxtaposing presynaptic active zones. Single z-slice views. Scale bars, 500 nm (adjusted for expansion).

Figure 4.10 Formation of GluClα synapses in L5 neurons

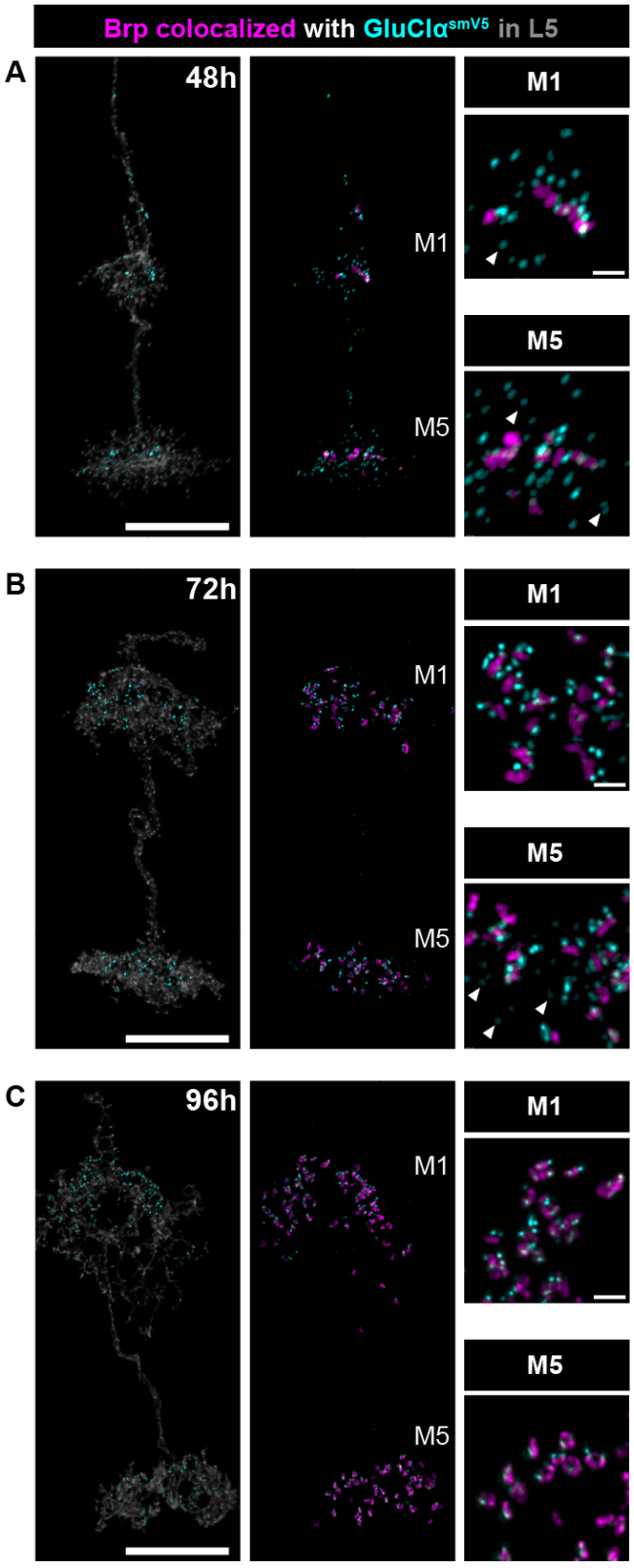

(A-C) Developmental time course of GluClα_KSK_smV5 conditionally tagged in L5 neurons at indicated pupal time points (h, hours after pupal formation). Brp puncta colocalized to GluClα puncta were computationally extracted following segmentation. White arrowheads, examples of dimmer GluClα puncta not juxtaposing Brp. GluClα is trafficked to layer M1 and M5 processes by 48 hrs, but few puncta are colocalized with Brp at this time. By 72 hrs, a majority of GluClα is colocalized with Brp in layer M1 and a mix of colocalized and non-colocalized puncta are present in layer M5. By 96 hrs, GluClα is refined almost exclusively to puncta juxtaposing Brp in layers M1 and M5. 3D projection views. Scale bars for main neuron panels, 5 μm; scale bars for insets, 500 nm (adjusted for expansion).

Figure 4.11 Formation of Rdl synapses in L5 neurons

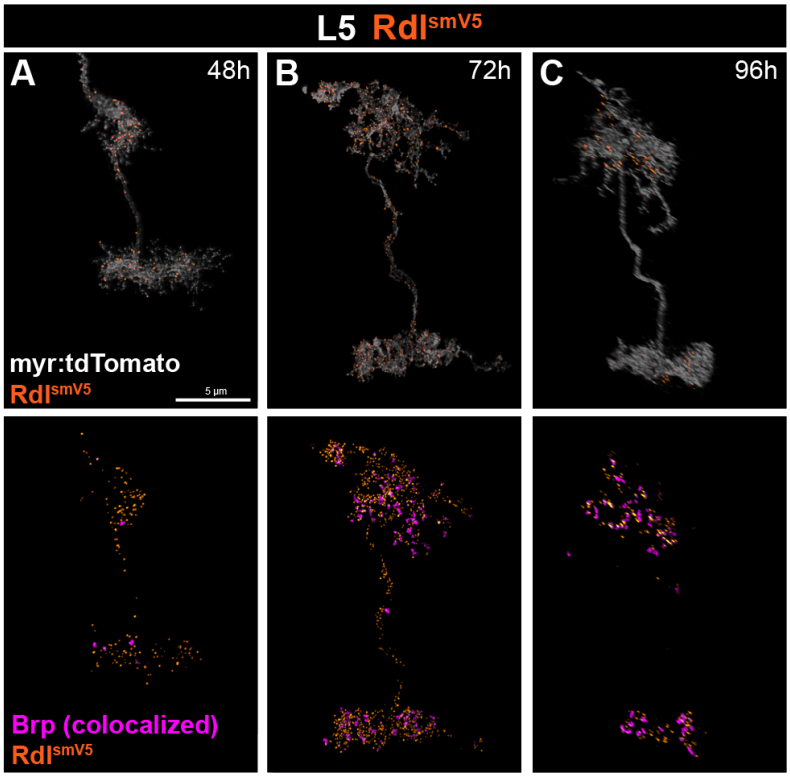

(A-C) Developmental time course of Rdl_KSK_smV5 conditionally tagged in L5 neurons at indicated pupal time points (h, hours after pupal formation). Brp puncta colocalized to Rdl puncta were computationally extracted following segmentation. Many Rdl puncta are visible throughout L5 neuron processes at 48h with virtually none colocalized to Brp. At 72h, the number of Rdl puncta have increased with a subset appearing colocalized to Brp. By 96h, larger and brighter Rdl puncta are observed strongly colocalized to Brp in the upper branches of L5 neurons; some Rdl puncta are still visible in the lower branches that are smaller and dimmer, in accordance with our observations under confocal microscopy (see Chapter 2). 3D projection views. Scale bar, 5 µm (adjusted for expansion).

Figure 4.12 Whole-Brain ExM Data

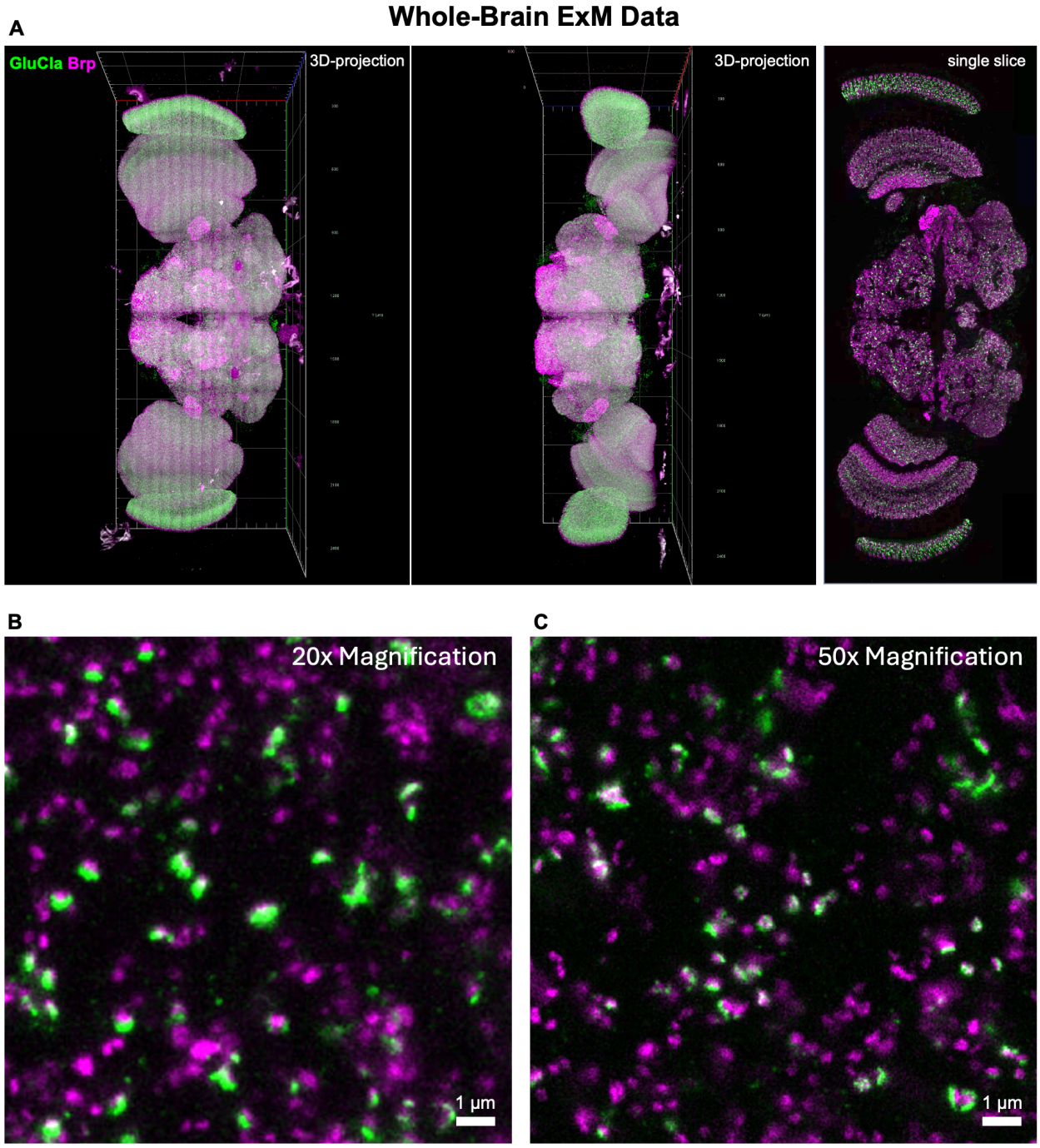

(A) Whole-brain ExM data acquired using constitutively tagged GluClα^{smV5} co-stained for Brp showing a tiled image mosaic capturing the entire brain volume in 108 tiles and 2000 z-slices. Left and middle panels depict a 3D projection of the data viewed through anterior-posterior and

dorsal-ventral axes, respectively. Right panel depicts a single-slice view of the tiled images, in an anterior view.

(B) Magnified view of the whole-brain data using 20x magnification, demonstrating individually resolved synaptic structures with GluClα juxtaposing Brp sites.

(C) For comparison, an image taken of the same brain (not an identical field of view) using the original ExM imaging parameters used in the rest of this work at 50x magnification.

Single z-slice views. Scale bar, 1 μm (adjusted for expansion).

Chapter 5: Investigating mechanisms of NR localization with chimeric receptors

In this section, I describe the use of genetic tools that produce chimeric NR subunits (in which the sequences of various domains are swapped) as a means to investigate mechanisms of differential subcellular localization of NRs. Here, I discuss the rationale to use this approach and report the results from an initial round of chimeras that investigated roles of the major extracellular and intracellular domains (ECD and ICD, respectively) of GluClα and Rdl, two inhibitory cys-loop receptor subunits.

5.1 Limitations in known mechanisms of NR localization

Our analysis of NR localization with our new conditional tagging system provided insights into the subcellular distributions of various NR types but left several unanswered questions about mechanisms. *What mechanisms instruct the specific localization of NR subunits to different synapses? What domains in NR subunits regulate this process and what other proteins do they interact with? How do mechanisms of synaptic specificity that require distinct subcellular localization relate to mechanisms of synapse assembly that recruit different synaptic machinery (i.e., different NRs) to different synapses?* To further address these questions, I devised a set of experiments to use chimeric receptors to investigate the processes driving differential localization of inhibitory synapses, which are poorly understood. This approach overcame the existing drawbacks of other possible experimental strategies.

One conceivable strategy to connect the establishment of differentially localized synapses to the recruitment of synaptic machinery would have been to study the role of postsynaptic scaffold

proteins. This approach could provide a direct link between synaptic specificity mechanisms and the organization of distinct NRs to their respective subcellular domains. However, the extent of our knowledge of postsynaptic scaffolds and our ability to extrapolate these findings are limited.

In *Drosophila,* only a few postsynaptic scaffold proteins have been identified to play a role in the brain, with none clearly established for inhibitory synapses. Although a natural first step would be to consider insights from other model organisms where this process is better understood, the ubiquity of identified scaffold proteins and their conservation across species is incomplete. In mammals, the protein Gephyrin (encoded by the GPHN gene) plays a vital role as a scaffold to organize $GABA_A$ and glycine receptors at inhibitory postsynaptic densities (see Chapter 1). The role of GPHN may be conserved across vertebrates, as it has also been shown to play a role in clustering glycine receptors in zebrafish (Ogino et al., 2019).

However, this role is not conserved in invertebrates, as different mechanisms are characterized as having a role in organizing GABA synapses in *C. elegans* (Tu et al., 2015), and the ortholog of GPHN in *Drosophila*, cinnamon (cin), has not been shown to participate in synapses and our analysis of transcriptomic data determined that it was not expressed in visual system neurons. One possible explanation for this is the fact that Gephyrin and its invertebrate orthologs share an unrelated enzymatic function in molybdenum cofactor biosynthesis (Wittle et al., 1999), which may have been conserved across eukaryotes while the role at inhibitory synapses was not. Furthermore, it is well documented that the role of Gephyrin in mammalian synapses appears to be compensated for by other mechanisms, as knockouts of Gephyrin and some of its essential interactors have only partial phenotypes, with significant subsets of synapses appearing unaffected (see Chapter 1).

Invertebrates carry an additional set of glutamate-gated chloride channels that function as inhibitory receptors (GluCl receptors), which are more closely related to ionotropic GABA receptor subunits than excitatory iGluRs. No scaffold proteins or localization mechanism have been well established for this class of receptors in any species. Thus, we have very little basis on which we can study inhibitory scaffold proteins in *Drosophila*. Instead, we must rely on approaches that can identify the domains within NRs that regulate localization or discover new interactions with possible scaffolding molecules.

5.2 Designing Rdl-GluClα chimeras to investigate roles of NR domains in localization

5.2.1 Experimental Rationale

To investigate how NRs are regulated to target different synaptic domains, I developed a set of genetic tools in which segments from two different NR subunits, Rdl (a GABA receptor subunit) and GluClα (a GluCl receptor subunit), were swapped. These studies were designed to identify the domains regulating localization to specific subcellular compartments, while avoiding the pitfalls of our limited understanding of inhibitory scaffold proteins in *Drosophila* and the challenges of identifying new genes that play a role.

Given that either intracellular interactions with proteins inside the cell, or extracellular interactions with transsynaptic, secreted, or neighboring molecules could be involved, I designed the first set of experiments to investigate the role of the largest domains in each of these compartments. I generated chimeric receptors in which I swapped sequences for the major intracellular domains (ICD) and extracellular domains (ECD) of Rdl and GluClα (**Figure 5.1**).

These constructs could be tested by examining their localization in a set of neurons where differential localization of GluClα and Rdl is well characterized. I selected the system of T4 and T5 neurons, which display differential subcellular localization of the two NR subunits to distinct neuropil. In previous experiments, we demonstrated that Rdl localizes to T4 dendrites in layer M10 of the medulla neuropil as well as T5 dendrites in layer Lo1 of the lobula neuropil. GluClα also localizes to T4 dendrites but not T5 dendrites, as well as the axon terminals of both T4 and T5 located in the four layers of the lobula plate neuropil. This pattern of localization is also reported in a recent study that tested similarly designed constructs expressing wild-type Rdl and GluClα in T4 and T5 neurons (Fendl et al., 2020).

The genetic scheme was designed to drive the expression of the chimeric receptors in T4 and T5 neurons using a cell-type-specific driver. The chimeric receptors would bear a high affinity epitope tag such that they could be labeled in the specific neurons expressing them while avoiding immunoreactivity with endogenous receptor, and the activated cells would also express a myristoylated GFP to label their cytosolic membrane (**Figure 5.2**).

By exchanging amino acid sequences in the chimeras, I could test whether the presence or absence of a given NR domain altered localization. If a particular NR domain was sufficient for a specific localization pattern, the chimeric receptor containing this sequence would display ectopic localization to the respective subcellular compartment. Oppositely, if a particular NR domain was necessary for proper localization, the chimeric receptor that lost this sequence would fail to localize to the corresponding subcellular compartment.

This approach is complicated by the fact that by substituting one sequence domain with another, the experimenter observes the combined effects of the chimeric sequence and loss of the original sequence. However, I elected to go with this approach given that alternative approaches

such as testing truncated domains posed a risk of failed expression given that they could disrupt pentameric assembly (see below).

5.2.2 Generation of genetic reagents

For these experiments, I generated fly lines bearing the engineered receptor transgenes under control of GAL4/UAS such that I could drive their expression in desired cell types (Jenett et al., 2012). I had Genewiz, Inc. generate plasmids and Bestgene, Inc. inject them into fly embryos, as described in our publication (see Chapter 2). Injected plasmids were integrated into the genome via site-specific transformation with φC31 integrase-mediated cassette exchange (Bateman et al., 2006).

To design the chimeric sequences, I first sought to compare the sequence homology between Rdl and GluClα. The coding sequence (CDS) for the Rdl-RA isoform transcript and the GluClα-RM isoform transcript were taken from Flybase (Gramates et al., 2022). Annotated amino acid sequences were aligned for sequence homology on Uniprot (Consortium et al., 2022)(**Figure 5.1**A). Despite these two receptors' sequence homology, they localize to drastically different places. (In retrospect, another exploration of this idea could have involved studying two different subunits of the *same* neurotransmitter class (as homologous as possible) that still localize to different places, such as the nicotinic receptor subunits nAChRβ1 and nAChRα5, although we did not uncover their differential localization in T4 and T5 dendrites until after the chimeras had been designed.)

The logic of the sequences for the engineered receptor transgene is as follows. To serve as controls, *nonchimeric* Rdl and GluClα sequences were synthesized (using the Rdl-RA and GluClα-RM isoform sequences) and cloned into plasmids. The sequences contained only the coding region and no endogenous untranslated regions (UTRs). For these constructs and all others that I

designed, I also included the DNA coding for the amino acid sequence constituting the high-affinity epitope tag ALFA (Götzke et al., 2019). The ALFA epitope tag was inserted in the same amino acid positions as the conditional tagging system used in our publication (see Chapter 2). When expressed in desired cell types, these tagged constructs could thus be visualized with immunofluorescence directed against the epitope tag in order to determine their localization.

To create the sequence for *chimeric* receptor transgenes, the major ECDs spanning from the N-terminus to the first transmembrane domain (M1), or the major ICDs spanning the cytosolic loop between the third and fourth transmembrane domains (M3 and M4), were swapped (**Figure 5.1**B). The internal boundaries of the swapped fragments were selected at positions where the amino-acid sequences for the two receptors were identical in the flanking transmembrane regions for a minimum of three consecutive amino acids. This approach ensured that in the vicinity of the swap ends, the chimeras contained no novel spans of amino-acid sequence.

5.3 Potential role of ECDs in GluClα and Rdl localization

5.3.1 Experimental Results

Expression of the chimeric constructs in T4 and T5 neurons led to several observed differences in localization, which suggested a possible role for the ECDs in regulating localization of GluClα and Rdl.

Control experiments validated the expected localization patterns of the wild-type Rdl and GluClα constructs. Rdl was expressed in thick, punctate distributions within medulla layer M10 and lobula layer Lo1, with no expression observed in the lobula plate neuropil (**Figure 5.2**B). In contrast, GluClα displayed a thinner band of expression in medulla layer M10 with no expression in lobula layer Lo1, with thick, punctate expression in all four layers of the lobula plate (**Figure**

5.2E). Ectopic expression of GluClα was also observed in cell bodies, likely an artifact overexpression. These patterns, aside from the ectopic cell body expression, agreed with the localization of Rdl and GluClα determined in prior studies (Fendl et al., 2020) as well as our work with the conditionally tagged Rdl allele (see Chapter 2).

When the Rdl_ICD$_{GluCl\alpha}$ chimera was expressed in T4 and T5 neurons, I observed a pattern virtually equivalent to Rdl. Rdl_ICD$_{GluCl\alpha}$ displayed thick bands of punctate expression within layers M10 and Lo1 and no lobula plate expression, with mild ectopic cell body expression (**Figure 5.2**C). These results suggest that introduction of the GluClα ICD sequence had no effect on driving localization, and that the presence of the original Rdl ICD sequence was not required for localization either.

The expression pattern of Rdl_ECD$_{GluCl\alpha}$ in T4 and T5 neurons was different. Overall, this chimera was not expressed at as high of a level compared to other constructs. I observed faint, diffuse signal in a thin band of layer M10 and a thick band of layer Lo1, as well as puncta throughout the layers of the lobula plate (**Figure 5.2**D). These results suggest that the GluClα ECD sequence is sufficient to drive localization to the axon terminal domain. However, the retained expression in lobula layer Lo1 suggests that the GluClα ECD is not sufficient (and the Rdl ECD is not required) for localization to T5 dendrites. Although the thinner band in layer M10 more closely resembled the pattern of GluClα than Rdl, the distinction between these two is uncertain.

The GluClα_ICD$_{Rdl\ also}$ chimera also failed to demonstrate robust expression in T4 and T5 neurons. Faint, diffuse signal was observed in a thin band in layer M10 and a thick band in layer Lo1, with punctate expression also present in layers of the lobula plate (**Figure 5.2**F). These results suggest that the Rdl ICD may be sufficient to drive localization to T5 dendrites in layer Lo1, but not sufficient to remove the localization to the axon terminals in the lobula plate, where the GluClα

ICD is also not required. Again, the thin band in layer M10 more closely resembled GluClα than Rdl but these results are not conclusive for the localization within T4 dendrites.

Finally, the localization pattern of GluClα_ECD$_{Rdl}$ was virtually equivalent to that of Rdl when expressed in T4 and T5 neurons. This chimera demonstrated strong expression in thick, punctate bands within layers M10 and Lo1, with no signal in the lobula plate (**Figure 5.2**G). These results suggest that the Rdl ECD is sufficient to drive localization to T5 dendrites in layer Lo1 and that the presence of the GluClα ECD is required for localization to axon terminals in the lobula plate.

5.3.2 Interpretations

Given the design of the plasmids, the control experiments with the wild-type constructs suggested that the 5' and 3' untranslated regions (UTRs) of the native transcripts are not necessary for localization of Rdl and GluClα. Thus, the localization likely depends on mechanisms occurring at the protein level.

The experiments with the receptor chimeras provided two symmetric sets of results (see **Table 5.1**). As observed in Rdl_ICD$_{GluClα}$ and GluClα_ECD$_{Rdl}$, constructs containing the ECD of Rdl rather than GluClα effectively phenocopied wild-type Rdl. The role of the GluClα ICD can be effectively ruled out, given that its presence or absence had zero effect on the localization of chimeric constructs. In contrast, as observed with Rdl_ECD$_{GluClα}$ and GluClα_ICD$_{Rdl}$, constructs that contained the ECD of GluClα rather than that of Rdl displayed localization to the lobula plate and a thinner band of expression in layer M10. However, the presence of the Rdl ICD rather than the GluClα ICD in these two constructs led to additional localization in layer Lo1. These results suggest that the GluClα ECD may have a clear role in localization at axon terminals.

In contrast, both the ECD and ICD sequences of Rdl demonstrated the ability to drive localization in T5 dendrites, albeit the Rdl ECD pattern more closely resembled Rdl expression than the faint, diffuse expression observed with the Rdl ICD pattern. The effects on localization to T4 dendrites are more difficult to interpret, given that both Rdl and GluClα localize to T4 dendrites, but the appearance of the staining pattern in M10 more closely reflected the appearance of whichever ECD was present in the construct. Given that Rdl and GluClα localize to different sub-dendritic domains within T4 dendrites, higher resolution single-cell experiments would make it possible to better determine the localization pattern in this compartment.

Table 5.1 Summary of Rdl-GluClα chimera results in T4/T5 neurons

Construct	Medulla Layer M1	Lobula Layer Lo1	Lobula Plate	Comments
UAS-Rdl	+	+	-	Rdl control
UAS-GluClα	+	-	+	GluClα control
UAS-Rdl_$ICD_{GluClα}$	+	+	-	Rdl unaffected
UAS-Rdl_$ECD_{GluClα}$	+	+	+*	*Rdl gained localization to axon terminals
UAS-GluClα_ICD_{Rdl}	+	+*	+	*GluClα gained localization to T5 dendrites
UAS-GluClα_ECD_{Rdl}	+	+*	-*	*GluClα gained localization to T5 dendrites and lost localization to axon terminals

5.4 Follow-up approaches to investigate NR localization with chimeras

Several key questions remained from the experiments testing Rdl-GluClα chimera expression in T4 and T5 neurons. First, the sub-dendritic localization of the expressed constructs could not be determined given that T4 and T5 dendrites significantly overlap with neighboring columns, making individual dendrites impossible to discern with confocal microscopy. Second, the background of endogenously expressed GluClα and Rdl presented a possibility that chimera localization could be altered by the association of the chimera with wild-type receptors forming heteromultimeric complex, rather than the intrinsic chimeric sequences driving localization. Third, the use of a transgenic vector to drive artificial expression in T4 and T5 neurons resulted in the chimeras being expressed later in development and at different levels than their endogenous counterparts. Finally, the total exchange of the ECD and ICD sequences in these chimeras could determine the overall roles of each domain in localization but was sufficient to identify the specific interactions responsible for regulating this process. In the following section, I describe several approaches that were devised to address these remaining questions and provide partial results for some experiments that were carried out successfully.

5.4.1 Single-cell localization with mosaic mutant analysis

To study localization of the expressed chimeras in sparsely labeled cells, and with a null background lacking endogenous NR subunit expression, I turned to Mosaic Analysis with a Repressible Cell Marker (MARCM)(T. Lee & Luo, 1999), which utilizes stochastic recombination of FRT-flanked chromosomal arms mediated by heat-shock induced FLP expression to generate sparsely distributed clones bearing two homozygous copies of the allele. With this approach, I

devised a set of MARCM experiments using GluClα_KSK_smV5, our conditional tagging allele, which acts as a knockout allele when the stop cassette is not excised. Thus, I could generate homozygous GluClα-null clones in mosaic animals and express the chimera construct as well as a GFP membrane marker using the T4/T5-specific GAL4 driver (**Figure 5.3**).

These experiments were challenged by several obstacles that prevented me from successfully carrying out the full set of conditions. First, I initially planned to carry out an equivalent experiment but in Rdl-null clones using the Rdl_KSK_smV5 allele. Recombination of FRT80B and the Rdl_KSK_smV5 allele on chromosomal arm 3L repeatedly failed. The first attempt to select for correct recombinants of FRT80B, Rdl_KSK_smV5 using neomycin selection failed, as the neomycin resistance gene in the FRT80B allele was evidently not effective. A titration experiment revealed that concentrations greater than 4 mg/mL were lethal to flies carrying the FRT80B allele and lower concentrations failed to select for neomycin resistance. A second attempt to directly validate recombinants with PCR amplification of the FRT80B locus also failed to capture positive hits in 30 candidates, despite an estimated recombination rate of 13%. In any case, considering that other GABA receptor subunits are also present in the genome, generating Rdl-null clones was not an optimal approach for eliminating interactions with endogenous subunits in the first place.

Furthermore, staining of the 1X-ALFA tag inserted in the constructs was severely challenged in the sparse single-cell conditions. Similar to my initial discoveries of the staining challenges for the conditional alleles, which were not appreciated in the whole-brain stains of the constitutive alleles, the ALFA staining in MARCM clones was at the limit of nonspecific background despite the fact that pan-T4/T5 expression showed very strong signals well above

background. I carried out extensive efforts to optimize the ALFA staining conditions, but ultimately these were unsuccessful.

However, using the GluClα MARCM fly lines that I successfully generated, I was able to test a limited number of conditions. First, my control experiments with the wild-type GluClα construct demonstrated that in both a wild-type background and a GluClα-null background, the artificially expressed GluClα construct correctly localized in T4 and T5 neurons (**Figure 5.4**A-C). Correct sub-dendritic localization of the GluClα construct at the distal tips of T4 dendrites was also observed (**Figure 5.4**C, right panel). These results confirmed that artificially expressed GluClα transcript lacking any endogenous UTRs is still capable of producing correctly localized protein.

Two chimeras were also tested in a GluClα-null background using MARCM. The Rdl_ECD$_{GluCl\alpha}$ chimera displayed strong puncta in the axon terminals, while weaker, diffuse signal was observed in T5 dendrites and no signal could be detected in T4 dendrites (**Figure 5.4**E). The redirected localization of the Rdl_ECD$_{GluCl\alpha}$ chimera to axon terminals, where GluClα is normally present, reinforced the notion that the GluClα ECD can instruct localization to this domain. By contrast, the GluClα ECD does not appear to be sufficient in dendritic localization, although these results are limited by the detection sensitivity of anti-ALFA staining in single neurons. The GluClα_ICD$_{Rdl}$ chimera produced a symmetric result, with localization observed in the axon terminals and weaker, diffuse signal that was inconsistently observed in T4 and T5 dendrites (**Figure 5.4**G). However, the significant background and overall weak signal of the ALFA-staining made these results difficult to interpret.

In the MARCM experiments I also struggled to get sparsely distributed clones. This obstacle was due to the dependence of the system to induce recombination in mitotically active

cells, which occurs earlier than the stage we typically used to heat shock for conditional labeling in T4/T5 neurons. I conducted several attempts to titrate the heat shock duration but found that any heat shock longer than two minutes, or earlier than the white pre-pupal stage, frequently generated clusters of cells, and any shorter or later heat shocks failed to produce clones. Thus, I could only successfully collect two to three isolated neurons across six brains on average.

5.4.2 Endogenous conditional chimera expression

To address the challenges described above regarding the artificial expression of NTR constructs and the suboptimal staining patterns using the ALFA tag, I designed a genetic scheme for conditional alleles that could be induced to express chimeric receptor subunits from the endogenous genomic locus (Figure 5.5), described in further detail below.

The approach relies on ΦC31 integrase-mediated cassette exchange, a technique well suited for making large substitutions in the genome (X. Zhang et al., 2014). In a two-step process, CRISPR-mediated homology-directed repair is first used to excise a desired section of the genome and substitute a universal gene trap cassette flanked by attP sites. Second, a custom cassette flanked by attB sites is used to replace the gene trap cassette with any desired sequence.

Pairs of single guide RNAs (sgRNA) can be developed to recognize the desired boundaries for a designed chimeric swap (for example the ECD or ICD coding regions), along with donor plasmids containing the gene trap cassette and respective homology arms. In the first step, the pair of sgRNAs and donor plasmid will be injected into embryos of Cas9-expressing, Ligase4-null flies to generate intermediary fly lines in which the coding region under investigation has been deleted and replaced with the gene trap cassette. The gene trap cassette contains a fluorescent eye marker to screen for successful insertion. Correct insertion location will be validated via PCR by

amplifying for expected fragments between the ends of the cassette and adjacent sequences in the genomic locus.

In the second step, a custom attB plasmid carrying the chimeric sequence will be injected into phiC31-integrase-expressing flies carrying the intermediary allele. To do this, the intermediary allele can be crossed to a germline-expressing phiC31 fly stock (e.g., Bloomington Drosophila Stock Center BDSC#34771), or a germline-expressed phiC31 plasmid can be co-injected with the custom attB plasmid (X. Zhang et al., 2014). Loss of the fluorescent eye marker will confirm successful insertion of the attB plasmid.

For example, to study the effect of the GluClα ECD on Rdl, an intermediary fly stock would first be generated in which the ECD coding sequence of Rdl is removed from the Rdl gene locus. With this intermediary Rdl_ΔECD fly stock, embryos can then be injected to insert any desired sequence in place of the deleted domain. To generate the Rdl_$ECD_{GluCl\alpha}$ chimera in the second step, the attB donor plasmid will be designed to contain the GluClα ECD coding sequence and injected into phiC31-integrase-expressing Rdl_ΔECD fly embryos. Using the same intermediary Rdl_ΔECD stock, other chimeric alleles could also be generated by designing additional attB plasmids to test various ECD modifications—for instance, a sub-ECD chimera could be generated by using an attB plasmid that reinserts the Rdl ECD coding sequence modified with a shorter span of swapped GluClα sequence. To test GluClα chimeras modified from the GluClα gene locus, a second intermediary GluClα_ΔECD fly line would need to be generated.

Visualizing the modified alleles will require a conditional epitope tag. In order to leverage our existing tools (see Chapter 2), the fly stocks carrying the conditional tagging allele can be used as a starting point to generate these reagents. DNAlig4-null flies expressing Cas9 (e.g., Bloomington Drosophila Stock Center BDSC#58492) can be balanced on the third chromosome

and then crossed to the conditional tagging allele fly stocks to generate Act5C-Cas9, w, DNAlig4; Rdl_KSK_smV5/TM6B flies. These fly stocks could then be injected create the Rdl_ΔECD_KSK_smV5 allele. If the domain under investigation is in the ICD of the M3-M4 loop where the epitope-tag is normally inserted, standard DNAlig4-null, Cas9-expressing flies can be used in the first step and the custom attB plasmid designed for the second step can be modified to include the conditional tagging cassette.

Although the endogenous conditional chimera alleles will allow for natively expressed single-cell studies, they will not rule out the possibility that the chimeric sequence enables complexing with endogenous NR subunits (in our example above, the GluClα ECD in chimeric Rdl_ECD$_{GluCl\alpha}$ could potentially facilitate heterocomplexing with endogenously expressed wild-type GluClα). Thus, the same technique of MARCM can be employed to generate sparse homozygous GluClα-null clones that express KD recombinase to activate expression of the conditionally tagged chimera. Additionally, MARCM could be designed to generate homozygous clones carrying two copies of the chimeric allele, such that all Rdl expression is replaced by Rdl_ECD$_{GluCl\alpha}$ expression in these cells.

Designing an experiment that removes the endogenous background expression of both Rdl and GluClα, or removes multiple other NR subunits that could heterocomplex with the chimera, would require more complex genetic approaches. However, the goal of future chimera studies would be to isolate smaller sequence fragments within the ECD or ICD that are sufficient to drive changes in localization. In this context, the possibility of the smaller chimeric sequence domains mediating heterocomplex interactions with other NR subunits may become less likely.

5.5 Figures

Figure 5.1 Design of Rdl-GluClα chimeric sequences

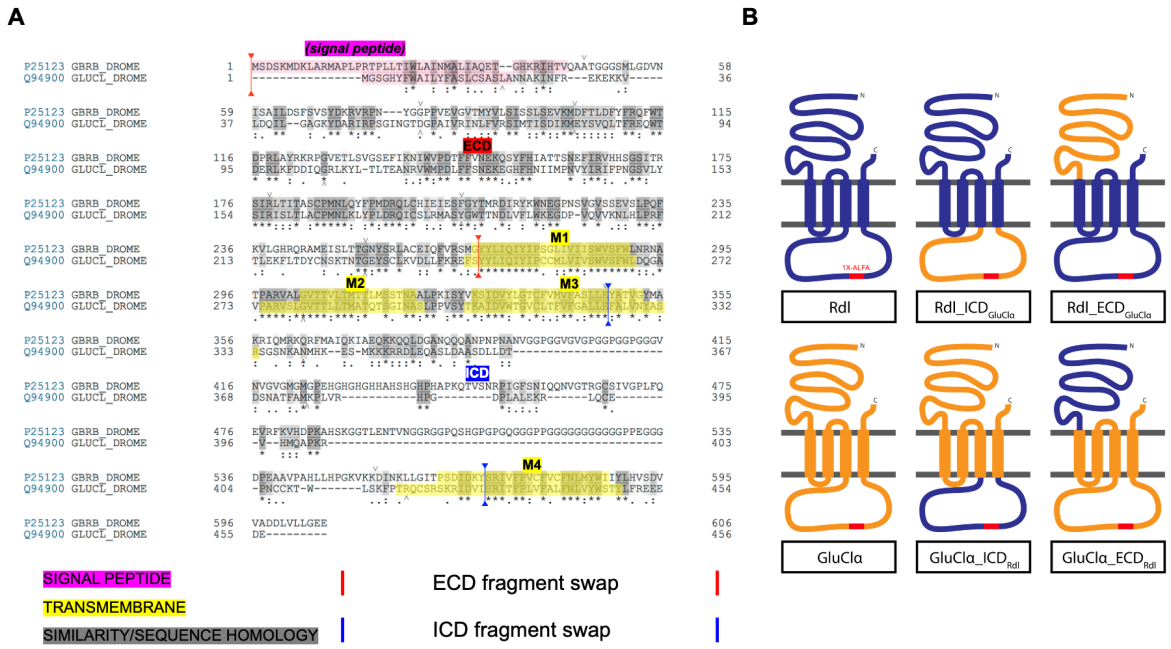

(A) Uniprot sequence alignment of Rdl-PA (upper row) and GluClα-PM (lower row) isoform amino acid sequences. Highlights mark annotated sequence domains: signal peptide sequence (pink/magenta), transmembrane domains M1 to M4 (yellow), and sequence similarity (gray, also marked by ., :, or * depending on sequence similarity). Red bars indicated the end points of the sequence swap for the ECD chimeras. Blue bars indicate the end points of the sequence swap for the ICD chimeras.

(B) Diagrams of the control and chimeric construct designed for Rdl (navy) and GluClα (orange). A 1XALFA tag was also inserted for labeling (red).

Figure 5.2 Expression of Rdl-GluClα chimeras in T4 and T5 neurons

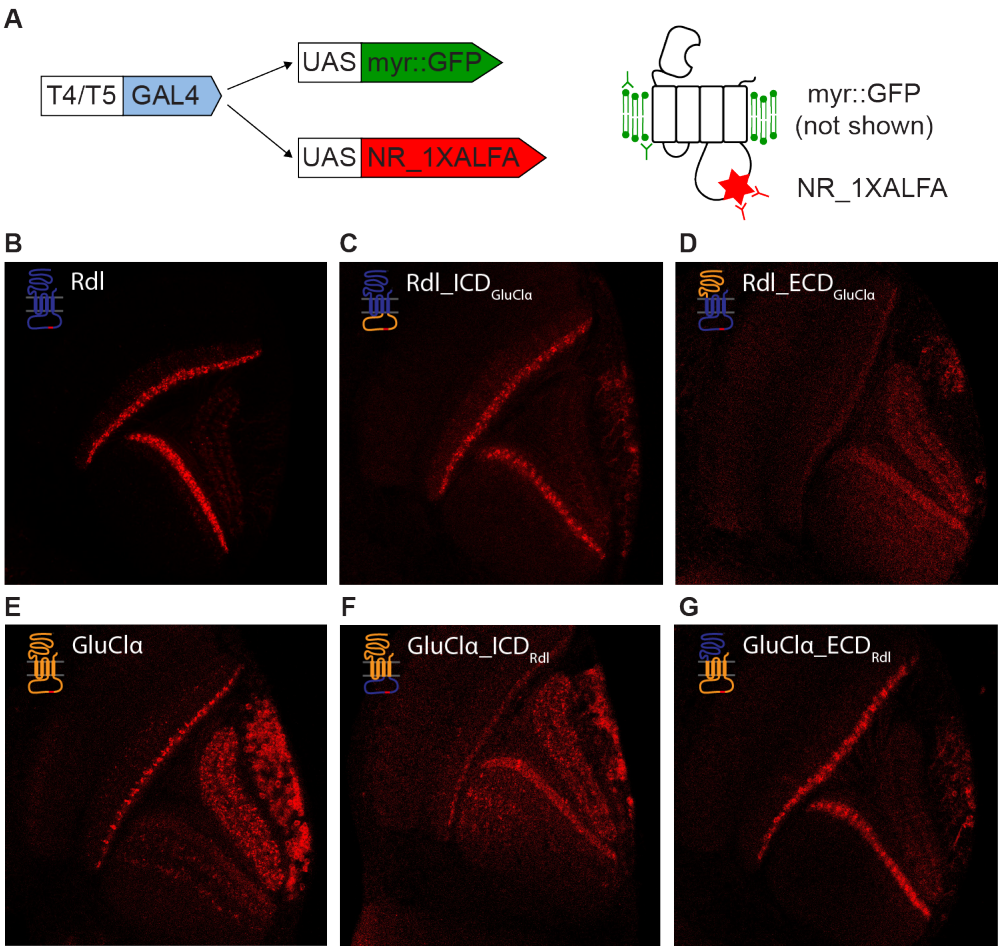

(A) Genetic schematic for this experiment. A T4/T5-specific GAL4 driver is used to artificially express a membrane marker (myr::GFP) and each desired construct (NR_1XALFA).

(B-G) Staining patterns for each control and chimeric receptor construct expressed in all T4 and T5 neurons viewed in Fischbach orientation. Schematics of each indicated construct are shown in the upper left.

Figure 5.3 Schematic for mosaic analysis of chimera expression in sparse cells

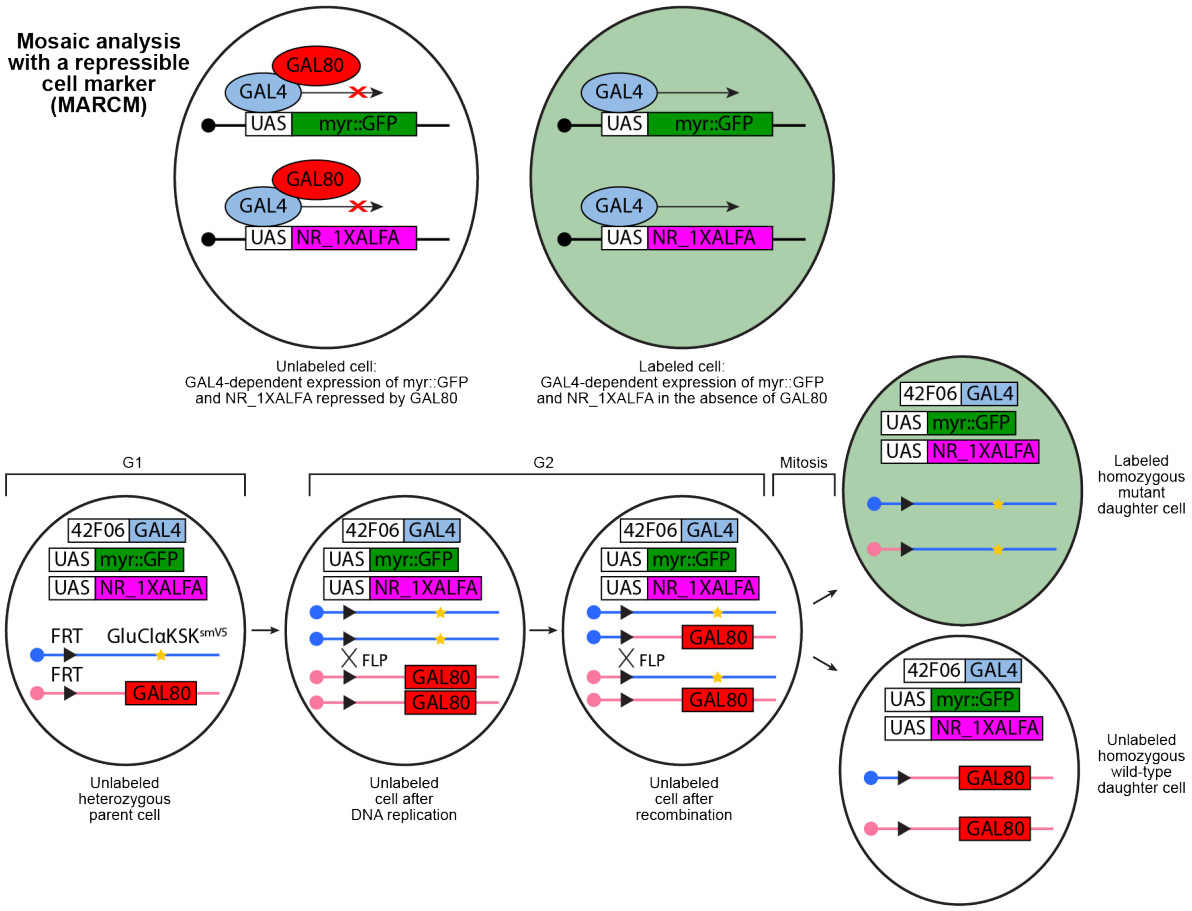

Genetic schematic of the MARCM experiments designed to express a receptor construct in sparse GluClα-null T4/T5 clones.

Figure 5.4 Localization of Rdl-GluClα chimeras in GluClα-null T4 and T5 mosaics

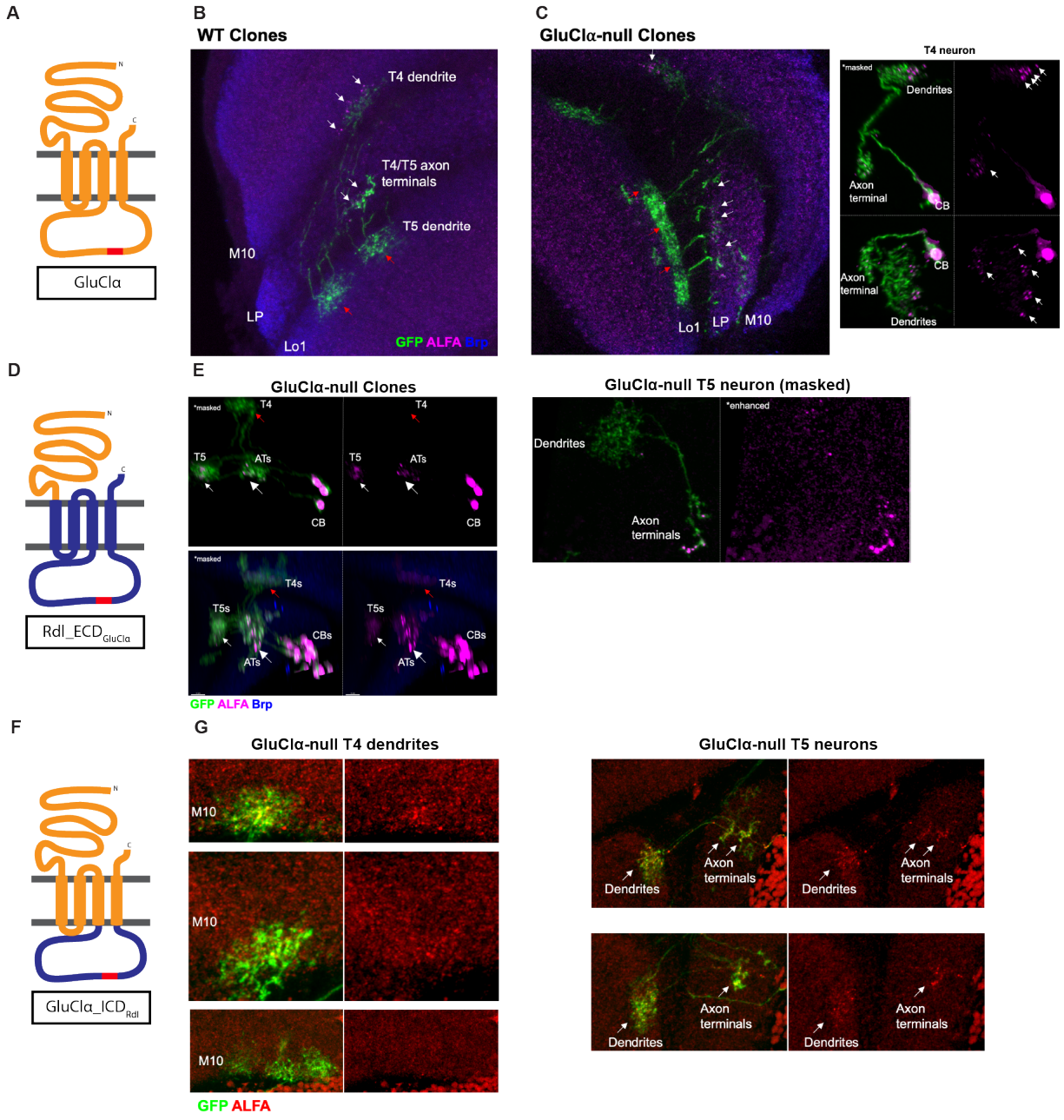

Results for the MARCM experiments. A, D, F show the schematics for each indicated construct.

(B) Expression of GluClα construct in several wild-type T4/T5 clones.

(C) Left, expression of Rdl_ECD$_{GluCl\alpha}$ construct in several GluClα-null T4/T5 clones. No detectable signal is observed in T4 dendrites (red arrow). Faint signal is observed in T5 dendrites, strong punctate signal is observed in axon terminals (ATs), and ectopic expression in

cell bodies (CBs) is also observed (white arrows). Right, single T5 neuron with masked signal in left subpanel and unmasked signal in right subpanel (Brp channel not shown).

(E) Left, expression of GluClα construct in several GluClα-null T4/T5 clones. Right, single masked T4 neuron (Brp channel not shown). These neurons show regular GluClα localization patterns in a GluClα-null background.

(G) Expression of GluClα_ICD_{Rdl} construct in T4 (left) and T5 (right) clones. Some punctate expression is observed (white arrows); however, significant background due to high exposure acquisition settings (due to weak signal) is also observed.

Figure 5.5 Schematic to generate endogenous conditional chimera alleles with RMCE

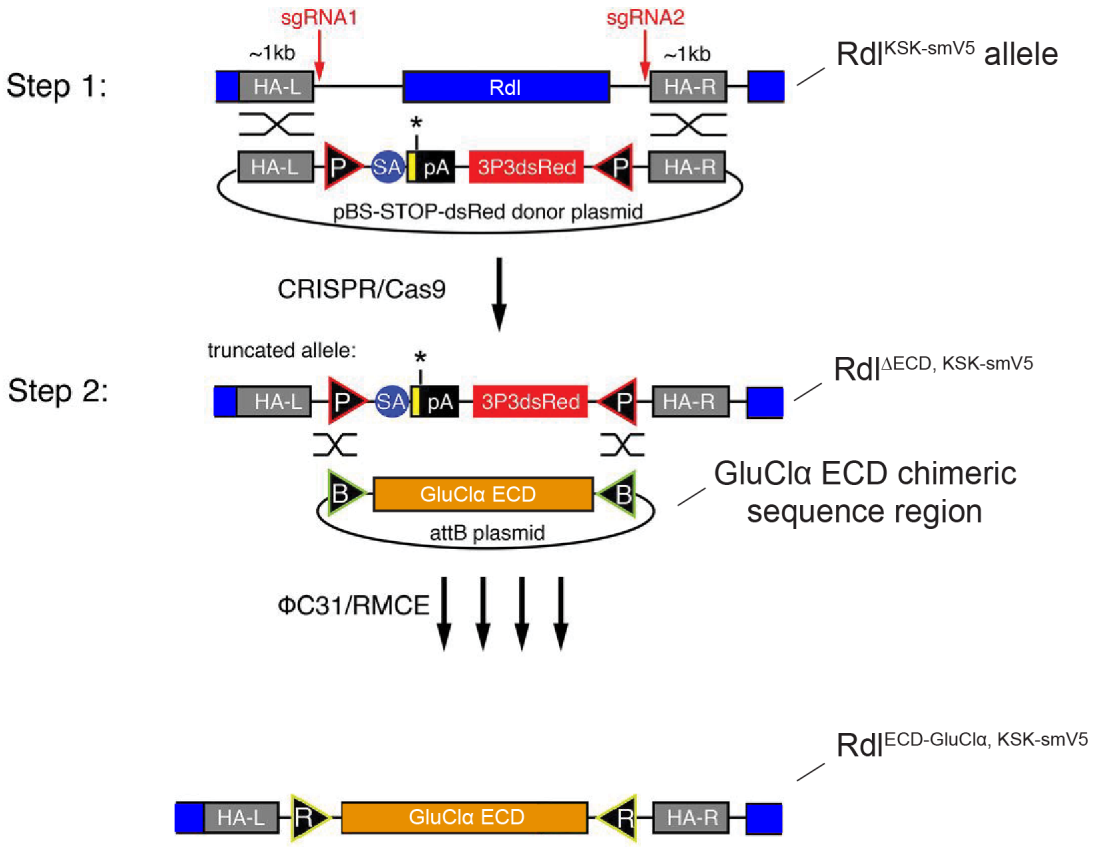

Genetic schematic to create endogenous conditional chimera alleles. See text for description.

Chapter 6: Conclusions

In this chapter I summarize the key findings and principal outcomes of this work and discuss their broader implications, the insights gained, and potential avenues for future exploration.

6.1 Molecular organization of the connectome

Brain connectomics has largely been restricted to morphological neuronal mapping and identification of synaptic connectivity patterns. While these studies are crucial to our understanding of the brain, they lack insight into the intricate molecular composition that dictates synaptic interactions and functionality.

The neurotransmitter identity of specific presynaptic cells can be readily determined by leveraging transcriptomic data, which reveals expression of genes for distinct neurotransmitter synthesis and transport machinery (Davis et al., 2020). However, postsynaptic composition cannot be determined by transcriptomics alone, given the multitude of NR subunits expressed in any given neuron and the diversity of synaptic inputs that neurons receive. Thus, protein localization studies are key to characterizing the particular NR subunits at each synapse.

Through the conditional tagging of NR subunits, we illuminated the precise molecular organization in part of the Drosophila connectome, underscoring the critical role of protein localization in defining synaptic specificity and circuit functionality. In T4 and T5 neurons, our studies revealed sub-dendritic organization of differentially localized NR subunits, including two distinct nicotinic receptor subunits whose spatial segregation correlated with synaptic inputs from different populations of presynaptic partners. In addition, EM studies revealed that T4 and T5 neurons receive contact from neurons along the entire span of their dendrites but only form synapses in the correct sub-dendritic domains (Shinomiya et al., 2019; Takemura, Nern, et al.,

2017). Thus, the localization of NR subunits to the specific postsynaptic domains may instruct synaptic specificity in these circuits.

6.2 Type-specific segregation of NR development in time and space

By use of our genomic tagging approach, our developmental studies revealed the endogenous expression patterns of NR subunits. In conditional tagging experiments that studied single neurons in developing pupal brains, we observed an unexpected diversity in NR expression and localization through development. For three different NR subunits I studied, the localization processes during development were distinct. Here are some examples: One NR subunit would accumulate early in development to the correct subcellular domains. Another would traffic indiscriminately throughout dendrites before being refined to the appropriate distribution late in development. Yet another NR subunit would be expressed but restricted in cell bodies until late in development, at which point it was swiftly localized to the appropriate domain.

These results suggest that different developmental processes regulate the localization and circuit maturation for different types of synapses. Our studies across multiple neuron types revealed that the same NR subunit could display distinct localization processes, exemplified in the contrasting patterns observed for Rdl and GluClα between T4 and L5 neurons. Additional studies that used the constitutively tagged NR subunit alleles demonstrated a broader trend across brain regions. In the medulla, different neuropil layers localized different NR subunits at different stages of development, which likely reflect different underlying neurons. Thus, circuit assembly processes vary between synapse types as well as cell types as evidenced by postsynaptic NR development.

The distinct patterns of NR localization during development provide evidence to suggest a potential strategy of circuit assembly where different synapse types are established in a spatiotemporally segregated manner. This strategy could avoid cross-interference of synaptogenic processes, given that many involved proteins are thought to play various roles across a wide range of synapses (see Chapter 1). Indeed, the use of common mechanisms of synapse formation is challenged by the requirement to establish many distinct circuits that are precisely arranged between neurons. Cell-type-specific wiring molecules have been proposed as key regulators of synaptic specificity, but to date we lack substantial evidence that explains how wiring genes actually mediate synaptogenic pathways as well as insight on their subcellular localization that would inform how they regulate connections in particular domains. Our studies implicate a potential role for NR subunits in this process given that they are expressed in cell-type-specific combinations and show precise coordination to differentially localized synapses during development.

One remaining conundrum lies in how NR subunits are differentially regulated between cell types to localize at different times. Whether localization processes are inherently cell autonomous or coordinated in groups (perhaps groups of processes targeting the same neuropil or sets of synaptic partners) has yet to be determined. Although this question was not directly addressed in our experiments, our developmental analyses revealed only a handful of localization processes that were repeated in more than one case. Thus, some shared principles may exist in how NRs can be regulated during development and effectively localized.

In our developmental studies, primarily one of two localization processes were observed. On the one hand, NR subunits could accumulate at the correct synaptic domains early in development, around 48 hrs APF, and continue to accumulate over time. This was the case for Rdl

in T4 neurons and GluClα in L5 neurons. On the other hand, NR subunits could be trafficked to dendrites and be distributed indiscriminately throughout all processes before becoming refined to the correct synaptic domains at a time point later than 72 hrs. This was the case for GluClα in T4 neurons, and Rdl in L5 as well as T1 neurons (data not shown). Interestingly, the shared timing of Rdl development in L5 and T1 neurons suggests that localization may be coordinated in shared neuropil, given that in both neuron types, Rdl localizes to dendritic branches arborized in the same layer, M2, of the medulla.

However, additional evidence in T4 and T5 neurons points to a case of cell autonomous programs for developmental localization. T4 and T5 are sister neurons that have similar transcription during development (Kurmangaliyev et al., 2020), similar morphology (Fischbach & Dittrich, 1989; Shinomiya et al., 2019), and similar (exactly inverse) functions (Haag et al., 2017; Maisak et al., 2013). However, dendrites of T4 and T5 project to entirely separate neuropils and receive inputs from different synaptic partners (Shinomiya et al., 2019). If localization were to be spatially regulated between neuropils, NR development might potentially be different between these neurons. However, developmental studies of GluClα in T4 and T5 revealed a common process. GluClα distributes broadly throughout T4 and T5 dendrites before accumulating in T4 dendrites and T4 and T5 axon terminals. Although GluClα is not required in T5 dendrites and is totally absent in adult lobula layer 1 neuropil (where they project), GluClα still shares the same developmental progression in both T4 and T5 dendrites. Furthermore, between two different domains in T4, the dendrites and axon terminals, which project to different neuropil, the developmental progression is also the same. These results would suggest that GluClα localization is regulated cell autonomously, with similar programs acting in both T4 and T5 neurons, across both the dendrites and axon terminals.

The differences observed between cell types may be attributable to the sequence of their morphological development. In T4 and T5 neurons, dendrites progressively extend from proximal to distal columns. Rdl localizes first at the proximal base while GluClα localizes later at the distal tips. In L5 neurons, the layer M5 branches develop first with the M1 branches following shortly after and the M2 branches projecting late in development. Similarly, GluClα localizes first in layers M1 and M5, while Rdl is refined later in M1 and M2 and nAChRβ1 localizes last strictly in M2. These observations suggest that NR localization during circuit assembly may somehow leverage the sequence of morphological development. Alternatively, NRs could be programmed to localize in the correct order and subsequently guide dendritic arborization.

Some aspects of the developmental timing of NRs may reflect broader trends in developing animal . For one, NR subunits appeared to either localize early by 48 hrs, or later than 72 hrs. These limited time windows fall around the major transitions of neural activity (PSINA) that occurs throughout the brain, beginning with a periodic stage at 55 hrs APF which transitions to a turbulent stage at approximately 70 hrs (Akin et al., 2019). Thus, NRs could be localizing in one of two general processes, occurring either before the onset of PSINA (and participate in it), or after the shift to the turbulent stage, which in this case would guide the refinement of NRs to late localization to synapses.

These developmental studies suggest a complex process of synapse formation during circuit assembly. Rather than occurring in a universal wave across the brain, synaptogenesis may occur in a stepwise fashion, allowing different circuits to ‘hook up’ in spatial and temporal isolation. This approach could enable synaptic specificity processes by sequentially connecting different partners, or they could allow for the widespread activity patterns present at 55 hrs APF onwards to sculpt the circuits established later in development.

6.3 Uncovering mechanisms of NR localization

The mechanisms determining NR subunit localization to specific synapses are only partially understood. In *Drosophila*, less is known about the interactions that regulate NR localization in the brain than in mammals, where many of the proteins that organize synapses have been identified. However, many of the *Drosophila* orthologs have not been shown to have an analogous role in invertebrates (see Chapter 5). This fact corresponds with our understanding of wiring molecules, many of which are comprised of different gene families between insects and vertebrates but utilize common principles (Cheng et al., 2019). For synaptic scaffold proteins and other players that recruit specific NR types, far fewer genes have been identified in *Drosophila* and thus the common principles that underlie these processes are less understood. This work demonstrates two approaches designed to identify regulators of NR localization.

NR chimera studies present a direct way to isolate cis-elements in the RNA or polypeptide sequence that instruct localization. In my studies with Rdl and GluClα chimeras, I successfully designed chimeric NR subunits that displayed altered localization to domains of T4 and T5 neurons characteristic of their opposing counterparts. These results suggested a role for the N-terminal extracellular domain in localizing the two NR subunits to the correct synapses. However, the approach was challenged by several caveats and technical limitations. Given the inherent background expression of native NR subunit genes, interpretation of the localization patterns depends on ruling out the effect of wild-type subunits in complex with the chimeras, which may in turn drive localization. Experiments with genetic mosaics were performed to investigate the localization of chimeric receptors in a null background of endogenous GluClα, given that knockout of this gene is lethal in the whole animal. Single-cell studies in mosaic clones revealed that endogenous UTR sequences were not required in the localization of GluClα, and also provided

evidence that the ECD of GluClα was sufficient to mis-localize chimeric Rdl subunits to the axon terminals of T4 and T5 neurons, where GluClα is normally present. Unfortunately, the limited efficacy of the epitope tag used in these chimeric constructs, ALFA, for immunofluorescence prevented further interpretation of the results. Additional constructs were designed using a more robust smV5 epitope tag but were ultimately not pursued in lieu of other research efforts. This dissertation proposes additional approaches to generate chimeric receptors at the endogenous genomic locus that could be used to replace native NR subunit expression.

Affinity purification using the tagged NR alleles also led to novel insights in the regulation of localization and synapse formation. AP-MS studies identified the adhesion protein Mmd as a specific interactor with GluClα. Following colocalization studies with ExM and analysis in mutants, Mmd was shown to be an essential component of GluClα-bearing synapses and required for the localization of GluClα in the neuropil. Thus, the combination of AP-MS with tagged alleles (providing a high affinity epitope for purification) and ExM to assess colocalization at synapses offers a powerful method to further characterize molecular composition of specific synapse types. Future approaches with AP-MS could leverage conditional, non-sparse tagging to identify the composition of synapses in specific cell types (for instance, T4 and T5 neurons), or leverage NR chimeras to identify interactors of particular receptor domains.

By utilizing the design of chimeric proteins and by leveraging proteomic insights from AP-MS studies, this work describes two different methods to investigate mechanisms of NR subunit localization through the identification of interactors and interaction domains. These approaches uncover potential avenues for how synapse formation can be regulated and provide a basis for powerful studies that could be carried out in the future.

6.4 ExM methods to study synapses

ExM is a demonstrated technique that can be applied to study synapses with unprecedented insight. Many iterations of this approach have been reported using different conditions that influence the factor of expansion (F. Chen et al., 2015; Damstra et al., 2022; Lillvis et al., 2022; M'Saad et al., 2022; Sneve & Piatkevich, 2022; Tillberg et al., 2016). These conditions can also affect the staining patterns. With each technique carrying its own advantages and setbacks, one key caveat to selecting an ExM approach is identifying a protocol that balances the ability to provide sufficient resolution for the biological question at hand with sufficient tractability and robustness so as to not bottleneck the experiment. . Ideally, this entails a short and simple expansion protocol, with little to no effect on the staining patterns of established immunohistochemical reagents, and minimal size requirements for image acquisition and analysis (which increase exponentially with expansion factor).

Here, I demonstrate the robustness of a 4X-expansion protocol and optimized workflow to image large volumes from whole-mounted *Drosophila* brain. Compared to recent studies that used an 8X expansion protocol, this approach produced similar results and avoided the use of a more cumbersome method with greater imaging requirements (Lillvis et al., 2022). The 4X protocol demonstrated clear evidence of sub-synaptic resolution and capability to perform segmentation analysis. Furthermore, this work demonstrated the viable use of a standard light sheet microscope as opposed to a bespoke lattice light sheet system, which are accessible to only a limited number of researchers.

The conditionally tagged alleles also demonstrated a significant advantage with ExM. Given that the cell identity or presynaptic vs. postsynaptic localization of a molecule cannot be determined by membrane staining alone, the conditional tagging approach can be leveraged to

anchor one marker to an identified cell type in which it is expressed, such that other molecules can be identified at that synapse via colocalization. This strategy was demonstrated for Brp and Mmd colocalization at GluClα-bearing synapses conditionally tagged in T4 neurons. Alternatively, application of more advanced ExM methods that achieve 16-20X expansion can also be used to determine molecular localization within reconstructed neurons where synaptic densities can be directly identified similar to EM (M'Saad et al., 2022; Tavakoli et al., 2024). However, this approach greatly increases the technical constraints to obtaining larger datasets (see below).

Analysis methods will also be critical in order to characterize ExM data quantitatively and uncover differences between synapse types (for a detailed discussion, see Chapter 4). Interestingly, my preliminary studies with N-cadherin revealed a range of configurations in which it was organized at synapses, similar to the variety observed for mammalian N-cadherin at synapses (Yam et al., 2013). Indeed, the observation of different synaptic structures raises one of two possibilities: Either the different structures reflect qualitatively distinct synapses, or the different structures reflect a dynamically organized synapse captured in different states. While histological studies cannot directly reveal dynamics, careful analysis could uncover evidence for these possibilities.

6.5 Future Directions and Recommendations

The combination of synaptic protein tagging with ExM presents a powerful method to probe the connectome at a molecular level. Generating additional tagged alleles for other NR subunits, adhesion molecules, and synaptic proteins is a desirable approach to provide precise tools in the investigation of subcellular localization within individual neurons. However, our ability to

generate protein tagging reagents is limited by the availability of insertion sites in the amino acid sequence that do not disrupt protein expression, localization, or function.

Where protein tagging is not feasible, generation of antibody reagents can be leveraged with ExM to study synaptic localization. Both existing and newly generated antibodies can be tested in combination with other synaptic markers to determine localization at various classes of synapses. Costain with Brp and tagged NR subunits can determine the synapse types where candidate proteins are localized, as demonstrated here for N-cadherin. Given that tagging efforts will have a limited success rate and require significant time to generate, these methods should be thoroughly examined, at a minimum testing available antibody reagents for known synaptic proteins.

Conditional tagging approaches can uncover the localization of new molecules at specific synapses of identified cell types. Importantly, our studies of the connection between Mi9 and T4 neurons demonstrated that localization to a synapse cannot be determined on the basis of membrane contact alone. Here the overlapping signals of labeled Mi9 and T4 membranes as well as stained Brp were observed throughout the entire span of T4 dendrites, despite the fact that synapses are only formed in the distal tips, evidenced by discrete localization of GluClα and what is known this circuit from EM. Thus, the use of conditional tagging and colocalization analysis may be vital to the determination of molecular composition at various synapses.

Tagged alleles can also be leveraged in future AP-MS studies to identify interactors for other NR subunits that may regulate their localization. As demonstrated in this work, the tagged alleles offer a high affinity epitope that can be used to purify and subsequently identify protein interactions. The specificity of pulldown is unbiased to each bait protein for alleles using the same

epitope tag. Follow up AP-MS studies can be used to identify additional interactors in the complex and the purified extracts can also be used to generate new antibody reagents to be tested by ExM.

Developmental studies will provide crucial insight into the process of synapse formation and involvement of various proteins. On the one hand, active zone assembly at the presynaptic terminus has been well characterized (Chou et al., 2020; Owald & Sigrist, 2009). On the other hand, however, the involvement of wiring genes is poorly understood. Many of the adhesion molecules thought to instruct wiring are expressed in cell-type-specific fashions (Davis et al., 2020; Kurmangaliyev et al., 2020). Given our new understanding of the various time courses of synapse formation across circuits, wiring genes that are expressed dynamically during development can be studied at various stages of pupal brains. These developmental analyses will be essential to our understanding of how wiring molecules act in the process of synapse formation. Furthermore, they will determine how wiring molecules are expressed and localized at the protein level, given that many have yet to be observed at the nascent synapses they are believed to regulate.

Additionally, one major untapped application of the conditional tagging system is its use in phenotypic assays. Indeed, this work only began to pursue mechanistic studies and we do not report any phenotypic evidence carried out in single neurons. Several preliminary attempts in our lab to study the role of various genes using null mutants or RNA interference via their effects on subcellular NR localization did not yield conclusive results. However, introduction of ExM now unlocks a more potent ability to observe phenotypic changes of synapses in genetic mutants.

The establishment of a tractable, high-throughput pipeline for ExM analysis can unlock novel datasets with powerful insight. These efforts require continued optimization of sample preparation, imaging, and analysis of whole-brain ExM samples. Consequently, pushing these boundaries will unlock one of the major advantages of ExM compared to EM. With a 7-day

protocol and a 2- to 3-hour imaging time for whole-brains described in this work, ExM can analyze dozens of brains within a span of two weeks. These studies could test a range of conditions, generating atlases of synaptic localization for various proteins, following developmental time courses, or conducting phenotypic screens to study the effects of various genes. Importantly, a whole-brain imaging approach would also provide an unbiased view across all brain regions to capture relevant observations in any circuit. The crucial balance of the expansion pipeline's robustness and its ability to garner biological insight will determine its efficacy in these studies, as the technical constraints become exponentially more cumbersome with higher expansion coefficients.

Whole brain studies demonstrated in this work used a 4X expansion protocol that provides synaptic labeling but cannot directly identify cell type identities or subcellular localization (including whether proteins were localized pre- or post-synaptically). As described above, newer ExM protocols have been developed that provide a deeper view of brain tissues that parallels EM. These 16-20X expansion protocols enable the reconstruction of unlabeled neurons and visualization of protein localization in pre- or post-synaptic processes. However, their ability to analyze larger brain volumes is highly limited. Compared to the 4X protocol used in this work, a single brain would require a 64- to 125- fold increase in imaging time and data size—amounting to a 16-day imaging session and a 64-TB dataset per brain. Hence, current microscopy methods make this approach unfeasible for whole-brain studies. In the future, more powerful systems and an optimized workflow could potentially be scaled to offer a pipeline for these studies. Nonetheless, this work demonstrates the use of an efficient 4X protocol, leveraged with powerful genetic tools, that provides valuable insights into the molecular basis of synapse formation and uses an approach that is tractable for academic research.

References for Chapters 1, 3-6

Akin, O., Bajar, B. T., Keles, M. F., Frye, M. A., & Zipursky, S. L. (2019). Cell-type-Specific Patterned Stimulus-Independent Neuronal Activity in the Drosophila Visual System during Synapse Formation. *Neuron*, *101*(5), 894-904.e5. https://doi.org/10.1016/j.neuron.2019.01.008

Ali, H., Marth, L., & Krueger-Burg, D. (2020). Neuroligin-2 as a central organizer of inhibitory synapses in health and disease. *Science Signaling*, *13*(663). https://doi.org/10.1126/scisignal.abd8379

Apel, E. D., Roberds, S. L., Campbell, K. P., & Merlie, J. P. (1995). Rapsyn may function as a link between the acetylcholine receptor and the agrin-binding dystrophin-associated glycoprotein complex. *Neuron*, *15*(1), 115–126. https://doi.org/10.1016/0896-6273(95)90069-1

Asano, S. M., Gao, R., Wassie, A. T., Tillberg, P. W., Chen, F., & Boyden, E. S. (2018). Expansion Microscopy: Protocols for Imaging Proteins and RNA in Cells and Tissues. *Current Protocols in Cell Biology*, *80*(1), e56. https://doi.org/10.1002/cpcb.56

Bateman, J. R., Lee, A. M., & Wu, C. (2006). Site-Specific Transformation of Drosophila via ϕC31 Integrase-Mediated Cassette Exchange. *Genetics*, *173*(2), 769–777. https://doi.org/10.1534/genetics.106.056945

Chan, E. H., Chavadimane Shivakumar, P., Clément, R., Laugier, E., & Lenne, P.-F. (2017). Patterned cortical tension mediated by N-cadherin controls cell geometric order in the Drosophila eye. *ELife*, *6*. https://doi.org/10.7554/eLife.22796

Chen, F., Tillberg, P. W., & Boyden, E. S. (2015). Expansion microscopy. *Science*, *347*(6221), 543–548. https://doi.org/10.1126/science.1260088

Chen, L., Chetkovich, D. M., Petralia, R. S., Sweeney, N. T., Kawasaki, Y., Wenthold, R. J., Bredt, D. S., & Nicoll, R. A. (2000). Stargazin regulates synaptic targeting of AMPA receptors by two distinct mechanisms. *Nature*, *408*(6815), 936–943. https://doi.org/10.1038/35050030

Chen, X., Levy, J. M., Hou, A., Winters, C., Azzam, R., Sousa, A. A., Leapman, R. D., Nicoll, R. A., & Reese, T. S. (2015). PSD-95 family MAGUKs are essential for anchoring AMPA and NMDA receptor complexes at the postsynaptic density. *Proceedings of the National Academy of Sciences*, *112*(50). https://doi.org/10.1073/pnas.1517045112

Chen, Y., Akin, O., Nern, A., Tsui, C. Y. K., Pecot, M. Y., & Zipursky, S. L. (2014a). Cell-type-specific labeling of synapses in vivo through synaptic tagging with recombination. *Neuron*, *81*(2), 280–293. https://doi.org/10.1016/j.neuron.2013.12.021

Chen, Y., Akin, O., Nern, A., Tsui, C. Y. K., Pecot, M. Y., & Zipursky, S. L. (2014b). Cell-type-Specific Labeling of Synapses In Vivo through Synaptic Tagging with Recombination. *Neuron*, *81*(2), 280–293. https://doi.org/10.1016/j.neuron.2013.12.021

Cheng, S., Park, Y., Kurleto, J. D., Jeon, M., Zinn, K., Thornton, J. W., & Özkan, E. (2019). Family of neural wiring receptors in bilaterians defined by phylogenetic, biochemical, and structural evidence. *Proceedings of the National Academy of Sciences*, *116*(20), 9837–9842. https://doi.org/10.1073/pnas.1818631116

Chou, V. T., Johnson, S. A., & Van Vactor, D. (2020). Synapse development and maturation at the drosophila neuromuscular junction. *Neural Development*, *15*(1), 11. https://doi.org/10.1186/s13064-020-00147-5

Consortium, T. U., Bateman, A., Martin, M.-J., Orchard, S., Magrane, M., Ahmad, S., Alpi, E., Bowler-Barnett, E. H., Britto, R., Bye-A-Jee, H., Cukura, A., Denny, P., Dogan, T.,

Ebenezer, T., Fan, J., Garmiri, P., Gonzales, L. J. da C., Hatton-Ellis, E., Hussein, A., … Zhang, J. (2022). UniProt: the Universal Protein Knowledgebase in 2023. *Nucleic Acids Research*, *51*(D1), D523–D531. https://doi.org/10.1093/nar/gkac1052

Damstra, H. G. J., Mohar, B., Eddison, M., Akhmanova, A., Kapitein, L. C., & Tillberg, P. W. (2022). Visualizing cellular and tissue ultrastructure using Ten-fold Robust Expansion Microscopy (TREx). *ELife*, *11*, e73775. https://doi.org/10.7554/elife.73775

Davis, F. P., Nern, A., Picard, S., Reiser, M. B., Rubin, G. M., Eddy, S. R., & Henry, G. L. (2020). A genetic, genomic, and computational resource for exploring neural circuit function. *ELife*, *9*. https://doi.org/10.7554/eLife.50901

Dorkenwald, S., Matsliah, A., Sterling, A. R., Schlegel, P., Yu, S., McKellar, C. E., Lin, A., Costa, M., Eichler, K., Yin, Y., Silversmith, W., Schneider-Mizell, C., Jordan, C. S., Brittain, D., Halageri, A., Kuehner, K., Ogedengbe, O., Morey, R., Gager, J., … Consortium, the F. (2023). Neuronal wiring diagram of an adult brain. *BioRxiv*, 2023.06.27.546656. https://doi.org/10.1101/2023.06.27.546656

Fendl, S., Vieira, R. M., & Borst, A. (2020). Conditional protein tagging methods reveal highly specific subcellular distribution of ion channels in motion-sensing neurons. *ELife*, *9*, e62953. https://doi.org/10.7554/elife.62953

Feng, G., Steinbach, J. H., & Sanes, J. R. (1998). Rapsyn Clusters Neuronal Acetylcholine Receptors But Is Inessential for Formation of an Interneuronal Cholinergic Synapse. *The Journal of Neuroscience*, *18*(11), 4166–4176. https://doi.org/10.1523/JNEUROSCI.18-11-04166.1998

Fischbach, K.-F., & Dittrich, A. P. M. (1989). The optic lobe of Drosophila melanogaster. I. A Golgi analysis of wild-type structure. *Cell and Tissue Research*, *258*(3), 441–475. https://doi.org/10.1007/bf00218858

Gautam, M., Noakes, P. G., Moscoso, L., Rupp, F., Scheller, R. H., Merlie, J. P., & Sanes, J. R. (1996). Defective Neuromuscular Synaptogenesis in Agrin-Deficient Mutant Mice. *Cell*, *85*(4), 525–535. https://doi.org/10.1016/S0092-8674(00)81253-2

Glass, D. J., Bowen, D. C., Stitt, T. N., Radziejewski, C., Bruno, J., Ryan, T. E., Gies, D. R., Shah, S., Mattsson, K., Burden, S. J., DiStefano, P. S., Valenzuela, D. M., DeChiara, T. M., & Yancopoulos, G. D. (1996). Agrin Acts via a MuSK Receptor Complex. *Cell*, *85*(4), 513–523. https://doi.org/10.1016/S0092-8674(00)81252-0

Götzke, H., Kilisch, M., Martínez-Carranza, M., Sograte-Idrissi, S., Rajavel, A., Schlichthaerle, T., Engels, N., Jungmann, R., Stenmark, P., Opazo, F., & Frey, S. (2019). The ALFA-tag is a highly versatile tool for nanobody-based bioscience applications. *Nature Communications*, *10*(1), 4403. https://doi.org/10.1038/s41467-019-12301-7

Gramates, L. S., Agapite, J., Attrill, H., Calvi, B. R., Crosby, M. A., Santos, G. dos, Goodman, J. L., Goutte-Gattat, D., Jenkins, V. K., Kaufman, T., Larkin, A., Matthews, B. B., Millburn, G., Strelets, V. B., Perrimon, N., Gelbart, S. R., Agapite, J., Broll, K., Crosby, L., … Lovato, T. (2022). FlyBase: a guided tour of highlighted features. *Genetics*, *220*(4), iyac035. https://doi.org/10.1093/genetics/iyac035

Guan, Z., Saraswati, S., Adolfsen, B., & Littleton, J. T. (2005). Genome-Wide Transcriptional Changes Associated with Enhanced Activity in the Drosophila Nervous System. *Neuron*, *48*(1), 91–107. https://doi.org/10.1016/j.neuron.2005.08.036

Haag, J., Arenz, A., Serbe, E., Gabbiani, F., & Borst, A. (2016). Complementary mechanisms create direction selectivity in the fly. *ELife*, *5*. https://doi.org/10.7554/eLife.17421

Haag, J., Mishra, A., & Borst, A. (2017). A common directional tuning mechanism of Drosophila motion-sensing neurons in the ON and in the OFF pathway. *ELife*, *6*. https://doi.org/10.7554/eLife.29044

Hansen, K. B., Yi, F., Perszyk, R. E., Furukawa, H., Wollmuth, L. P., Gibb, A. J., & Traynelis, S. F. (2018). Structure, function, and allosteric modulation of NMDA receptors. *Journal of General Physiology*, *150*(8), 1081–1105. https://doi.org/10.1085/jgp.201812032

Harvey, K., Duguid, I. C., Alldred, M. J., Beatty, S. E., Ward, H., Keep, N. H., Lingenfelter, S. E., Pearce, B. R., Lundgren, J., Owen, M. J., Smart, T. G., Lüscher, B., Rees, M. I., & Harvey, R. J. (2004). The GDP-GTP Exchange Factor Collybistin: An Essential Determinant of Neuronal Gephyrin Clustering. *The Journal of Neuroscience*, *24*(25), 5816–5826. https://doi.org/10.1523/jneurosci.1184-04.2004

Hawrylycz, M. J., Lein, E. S., Guillozet-Bongaarts, A. L., Shen, E. H., Ng, L., Miller, J. A., Lagemaat, L. N. van de, Smith, K. A., Ebbert, A., Riley, Z. L., Abajian, C., Beckmann, C. F., Bernard, A., Bertagnolli, D., Boe, A. F., Cartagena, P. M., Chakravarty, M. M., Chapin, M., Chong, J., … Jones, A. R. (2012). An anatomically comprehensive atlas of the adult human brain transcriptome. *Nature*, *489*(7416), 391–399. https://doi.org/10.1038/nature11405

Hayashi, T., & Carthew, R. W. (2004). Surface mechanics mediate pattern formation in the developing retina. *Nature*, *431*(7009), 647–652. https://doi.org/10.1038/nature02952

Jenett, A., Rubin, G. M., Ngo, T.-T. B., Shepherd, D., Murphy, C., Dionne, H., Pfeiffer, B. D., Cavallaro, A., Hall, D., Jeter, J., Iyer, N., Fetter, D., Hausenfluck, J. H., Peng, H., Trautman,

E. T., Svirskas, R. R., Myers, E. W., Iwinski, Z. R., Aso, Y., … Zugates, C. T. (2012). A GAL4-Driver Line Resource for Drosophila Neurobiology. *Cell Reports*, *2*(4), 991–1001. https://doi.org/10.1016/j.celrep.2012.09.011

Kato, A. S., Gill, M. B., Yu, H., Nisenbaum, E. S., & Bredt, D. S. (2010). TARPs differentially decorate AMPA receptors to specify neuropharmacology. *Trends in Neurosciences*, *33*(5), 241–248. https://doi.org/10.1016/j.tins.2010.02.004

Kneussel, M., Brandstätter, J. H., Gasnier, B., Feng, G., Sanes, J. R., & Betz, H. (2001). Gephyrin-Independent Clustering of Postsynaptic GABAA Receptor Subtypes. *Molecular and Cellular Neuroscience*, *17*(6), 973–982. https://doi.org/10.1006/mcne.2001.0983

Kurmangaliyev, Y. Z., Yoo, J., Valdes-Aleman, J., Sanfilippo, P., & Zipursky, S. L. (2020). Transcriptional Programs of Circuit Assembly in the Drosophila Visual System. *Neuron*, *108*(6), 1045-1057.e6. https://doi.org/10.1016/j.neuron.2020.10.006

Lee, C.-H., Herman, T., Clandinin, T. R., Lee, R., & Zipursky, S. L. (2001). N-Cadherin Regulates Target Specificity in the Drosophila Visual System. *Neuron*, *30*(2), 437–450. https://doi.org/10.1016/S0896-6273(01)00291-4

Lee, T., & Luo, L. (1999). Mosaic Analysis with a Repressible Cell Marker for Studies of Gene Function in Neuronal Morphogenesis. *Neuron*, *22*(3), 451–461. https://doi.org/10.1016/s0896-6273(00)80701-1

Lein, E. S., Hawrylycz, M. J., Ao, N., Ayres, M., Bensinger, A., Bernard, A., Boe, A. F., Boguski, M. S., Brockway, K. S., Byrnes, E. J., Chen, L., Chen, L., Chen, T.-M., Chin, M. C., Chong, J., Crook, B. E., Czaplinska, A., Dang, C. N., Datta, S., … Jones, A. R. (2007). Genome-wide atlas of gene expression in the adult mouse brain. *Nature*, *445*(7124), 168–176. https://doi.org/10.1038/nature05453

Li, H.-S. (2011). *A Glia-Mediated Feedback Mechanism for the Termination of Drosophila Visual Response: A Dissertation* [Doctoral Dissertation]. UMass Chan Medical School.

Lillvis, J. L., Otsuna, H., Ding, X., Pisarev, I., Kawase, T., Colonell, J., Rokicki, K., Goina, C., Gao, R., Hu, A., Wang, K., Bogovic, J., Milkie, D. E., Meienberg, L., Mensh, B. D., Boyden, E. S., Saalfeld, S., Tillberg, P. W., & Dickson, B. J. (2022). Rapid reconstruction of neural circuits using tissue expansion and light sheet microscopy. *ELife*, *11*. https://doi.org/10.7554/elife.81248

Maisak, M. S., Haag, J., Ammer, G., Serbe, E., Meier, M., Leonhardt, A., Schilling, T., Bahl, A., Rubin, G. M., Nern, A., Dickson, B. J., Reiff, D. F., Hopp, E., & Borst, A. (2013). A directional tuning map of Drosophila elementary motion detectors. *Nature*, *500*(7461), 212–216. https://doi.org/10.1038/nature12320

Moss, S. J., & Smart, T. G. (2001). Constructing inhibitory synapses. *Nature Reviews Neuroscience*, *2*(4), 240–250. https://doi.org/10.1038/35067500

M'Saad, O., Kasula, R., Kondratiuk, I., Kidd, P., Falahati, H., Gentile, J. E., Niescier, R. F., Watters, K., Sterner, R. C., Lee, S., Liu, X., Camilli, P. De, Rothman, J. E., Koleske, A. J., Biederer, T., & Bewersdorf, J. (2022). All-optical visualization of specific molecules in the ultrastructural context of brain tissue. *BioRxiv*, 2022.04.04.486901. https://doi.org/10.1101/2022.04.04.486901

Negi, S. K., & Guda, C. (2017). Global gene expression profiling of healthy human brain and its application in studying neurological disorders. *Scientific Reports*, *7*(1), 897. https://doi.org/10.1038/s41598-017-00952-9

Nern, A., Nguyen, L.-V. T., Herman, T., Prakash, S., Clandinin, T. R., & Zipursky, S. L. (2005). An isoform-specific allele of Drosophila N-cadherin disrupts a late step of R7 targeting.

Proceedings of the National Academy of Sciences, *102*(36), 12944–12949. https://doi.org/10.1073/pnas.0502888102

Nern, A., Zhu, Y., & Zipursky, S. L. (2008). Local N-Cadherin Interactions Mediate Distinct Steps in the Targeting of Lamina Neurons. *Neuron*, *58*(1), 34–41. https://doi.org/10.1016/j.neuron.2008.03.022

Ogino, K., Yamada, K., Nishioka, T., Oda, Y., Kaibuchi, K., & Hirata, H. (2019). Phosphorylation of Gephyrin in Zebrafish Mauthner Cells Governs Glycine Receptor Clustering and Behavioral Desensitization to Sound. *The Journal of Neuroscience*, *39*(45), 8988–8997. https://doi.org/10.1523/JNEUROSCI.1315-19.2019

Olsen, R. W., & Sieghart, W. (2009). GABAA receptors: Subtypes provide diversity of function and pharmacology. *Neuropharmacology*, *56*(1), 141–148. https://doi.org/10.1016/j.neuropharm.2008.07.045

Owald, D., & Sigrist, S. J. (2009). Assembling the presynaptic active zone. *Current Opinion in Neurobiology*, *19*(3), 311–318. https://doi.org/10.1016/j.conb.2009.03.003

Özel, M. N., Simon, F., Jafari, S., Holguera, I., Chen, Y.-C., Benhra, N., El-Danaf, R. N., Kapuralin, K., Malin, J. A., Konstantinides, N., & Desplan, C. (2021). Neuronal diversity and convergence in a visual system developmental atlas. *Nature*, *589*(7840), 88–95. https://doi.org/10.1038/s41586-020-2879-3

Panzanelli, P., Früh, S., & Fritschy, J.-M. (2017). Differential role of GABAA receptors and neuroligin 2 for perisomatic GABAergic synapse formation in the hippocampus. *Brain Structure and Function*, *222*(9), 4149–4161. https://doi.org/10.1007/s00429-017-1462-7

Papadopoulos, T., Korte, M., Eulenburg, V., Kubota, H., Retiounskaia, M., Harvey, R. J., Harvey, K., O'Sullivan, G. A., Laube, B., Hülsmann, S., Geiger, J. R. P., & Betz, H. (2007).

Impaired GABAergic transmission and altered hippocampal synaptic plasticity in collybistin-deficient mice. *The EMBO Journal*, *26*(17), 3888–3899. https://doi.org/10.1038/sj.emboj.7601819

Poulopoulos, A., Aramuni, G., Meyer, G., Soykan, T., Hoon, M., Papadopoulos, T., Zhang, M., Paarmann, I., Fuchs, C., Harvey, K., Jedlicka, P., Schwarzacher, S. W., Betz, H., Harvey, R. J., Brose, N., Zhang, W., & Varoqueaux, F. (2009). Neuroligin 2 Drives Postsynaptic Assembly at Perisomatic Inhibitory Synapses through Gephyrin and Collybistin. *Neuron*, *63*(5), 628–642. https://doi.org/10.1016/j.neuron.2009.08.023

Prakash, S., Caldwell, J. C., Eberl, D. F., & Clandinin, T. R. (2005). Drosophila N-cadherin mediates an attractive interaction between photoreceptor axons and their targets. *Nature Neuroscience*, *8*(4), 443–450. https://doi.org/10.1038/nn1415

Radler, M. R., Suber, A., & Spiliotis, E. T. (2020). Spatial control of membrane traffic in neuronal dendrites. *Molecular and Cellular Neuroscience*, *105*, 103492. https://doi.org/10.1016/j.mcn.2020.103492

Rivera-Alba, M., Vitaladevuni, S. N., Mishchenko, Y., Mischenko, Y., Lu, Z., Takemura, S.-Y., Scheffer, L., Meinertzhagen, I. A., Chklovskii, D. B., & Polavieja, G. G. de. (2011). Wiring Economy and Volume Exclusion Determine Neuronal Placement in the Drosophila Brain. *Current Biology*, *21*(23), 2000–2005. https://doi.org/10.1016/j.cub.2011.10.022

Rosenthal, J. S., & Yuan, Q. (2021). Constructing and Tuning Excitatory Cholinergic Synapses: The Multifaceted Functions of Nicotinic Acetylcholine Receptors in Drosophila Neural Development and Physiology. *Frontiers in Cellular Neuroscience*, *15*. https://doi.org/10.3389/fncel.2021.720560

Sanes, J. R., & Zipursky, S. L. (2020). Synaptic Specificity, Recognition Molecules, and Assembly of Neural Circuits. *Cell*, *181*(3), 536–556. https://doi.org/10.1016/j.cell.2020.04.008

Scheffer, L. K., Xu, C. S., Januszewski, M., Lu, Z., Takemura, S., Hayworth, K. J., Huang, G. B., Shinomiya, K., Maitlin-Shepard, J., Berg, S., Clements, J., Hubbard, P. M., Katz, W. T., Umayam, L., Zhao, T., Ackerman, D., Blakely, T., Bogovic, J., Dolafi, T., … Plaza, S. M. (2020). A connectome and analysis of the adult Drosophila central brain. *ELife*, *9*, e57443. https://doi.org/10.7554/elife.57443

Schlegel, P., Yin, Y., Bates, A. S., Dorkenwald, S., Eichler, K., Brooks, P., Han, D. S., Gkantia, M., Santos, M. dos, Munnelly, E. J., Badalamente, G., Capdevila, L. S., Sane, V. A., Pleijzier, M. W., Tamimi, I. F. M., Dunne, C. R., Salgarella, I., Javier, A., Fang, S., … Jefferis, G. S. X. E. (2023). Whole-brain annotation and multi-connectome cell typing quantifies circuit stereotypy in Drosophila. *BioRxiv*, 2023.06.27.546055. https://doi.org/10.1101/2023.06.27.546055

Schnaitmann, C., Haikala, V., Abraham, E., Oberhauser, V., Thestrup, T., Griesbeck, O., & Reiff, D. F. (2018). Color Processing in the Early Visual System of Drosophila. *Cell*, *172*(1–2), 318-330.e18. https://doi.org/10.1016/j.cell.2017.12.018

Sheng, M., & Kim, E. (2011). The Postsynaptic Organization of Synapses. *Cold Spring Harbor Perspectives in Biology*, *3*(12), a005678–a005678. https://doi.org/10.1101/cshperspect.a005678

Shinomiya, K., Huang, G., Lu, Z., Parag, T., Xu, C. S., Aniceto, R., Ansari, N., Cheatham, N., Lauchie, S., Neace, E., Ogundeyi, O., Ordish, C., Peel, D., Shinomiya, A., Smith, C., Takemura, S., Talebi, I., Rivlin, P. K., Nern, A., … Meinertzhagen, I. A. (2019).

Comparisons between the ON- and OFF-edge motion pathways in the Drosophila brain. *ELife*, *8*, e40025. https://doi.org/10.7554/elife.40025

Sneve, M. A., & Piatkevich, K. D. (2022). Towards a Comprehensive Optical Connectome at Single Synapse Resolution via Expansion Microscopy. *Frontiers in Synaptic Neuroscience*, *13*, 754814. https://doi.org/10.3389/fnsyn.2021.754814

Südhof, T. C. (2018). Towards an Understanding of Synapse Formation. *Neuron*, *100*(2), 276–293. https://doi.org/10.1016/j.neuron.2018.09.040

Takemura, S., Aso, Y., Hige, T., Wong, A., Lu, Z., Xu, C. S., Rivlin, P. K., Hess, H., Zhao, T., Parag, T., Berg, S., Huang, G., Katz, W., Olbris, D. J., Plaza, S., Umayam, L., Aniceto, R., Chang, L.-A., Lauchie, S., … Scheffer, L. K. (2017). A connectome of a learning and memory center in the adult Drosophila brain. *ELife*, *6*, e26975. https://doi.org/10.7554/eLife.26975

Takemura, S., Bharioke, A., Lu, Z., Nern, A., Vitaladevuni, S., Rivlin, P. K., Katz, W. T., Olbris, D. J., Plaza, S. M., Winston, P., Zhao, T., Horne, J. A., Fetter, R. D., Takemura, S., Blazek, K., Chang, L.-A., Ogundeyi, O., Saunders, M. A., Shapiro, V., … Chklovskii, D. B. (2013). A visual motion detection circuit suggested by Drosophila connectomics. *Nature*, *500*(7461), 175–181. https://doi.org/10.1038/nature12450

Takemura, S., Nern, A., Chklovskii, D. B., Scheffer, L. K., Rubin, G. M., & Meinertzhagen, I. A. (2017). The comprehensive connectome of a neural substrate for 'ON' motion detection in Drosophila. *ELife*, *6*, e24394. https://doi.org/10.7554/eLife.24394

Takemura, S., Xu, C. S., Lu, Z., Rivlin, P. K., Parag, T., Olbris, D. J., Plaza, S., Zhao, T., Katz, W. T., Umayam, L., Weaver, C., Hess, H. F., Horne, J. A., Nunez-Iglesias, J., Aniceto, R., Chang, L.-A., Lauchie, S., Nasca, A., Ogundeyi, O., … Scheffer, L. K. (2015). Synaptic

circuits and their variations within different columns in the visual system of Drosophila. *Proceedings of the National Academy of Sciences*, *112*(44), 13711–13716. https://doi.org/10.1073/pnas.1509820112

Tavakoli, M. R., Lyudchik, J., Januszewski, M., Vistunou, V., Agudelo, N., Vorlaufer, J., Sommer, C., Kreuzinger, C., Oliveira, B., Cenameri, A., Novarino, G., Jain, V., & Danzl, J. G. (2024). *Light-microscopy based dense connectomic reconstruction of mammalian brain tissue*. https://doi.org/10.1101/2024.03.01.582884

Tillberg, P. W., Chen, F., Piatkevich, K. D., Zhao, Y., Yu, C.-C. (Jay), English, B. P., Gao, L., Martorell, A., Suk, H.-J., Yoshida, F., DeGennaro, E. M., Roossien, D. H., Gong, G., Seneviratne, U., Tannenbaum, S. R., Desimone, R., Cai, D., & Boyden, E. S. (2016). Protein-retention expansion microscopy of cells and tissues labeled using standard fluorescent proteins and antibodies. *Nature Biotechnology*, *34*(9), 987–992. https://doi.org/10.1038/nbt.3625

Trush, O., Liu, C., Han, X., Nakai, Y., Takayama, R., Murakawa, H., Carrillo, J. A., Takechi, H., Hakeda-Suzuki, S., Suzuki, T., & Sato, M. (2019). N-Cadherin Orchestrates Self-Organization of Neurons within a Columnar Unit in the *Drosophila* Medulla. *The Journal of Neuroscience*, *39*(30), 5861–5880. https://doi.org/10.1523/JNEUROSCI.3107-18.2019

Tu, H., Pinan-Lucarré, B., Ji, T., Jospin, M., & Bessereau, J.-L. (2015). C. elegans Punctin Clusters GABAA Receptors via Neuroligin Binding and UNC-40/DCC Recruitment. *Neuron*, *86*(6), 1407–1419. https://doi.org/10.1016/j.neuron.2015.05.013

Tyagarajan, S. K., & Fritschy, J.-M. (2014). Gephyrin: a master regulator of neuronal function? *Nature Reviews Neuroscience*, *15*(3), 141–156. https://doi.org/10.1038/nrn3670

Varoqueaux, F., Jamain, S., & Brose, N. (2004). Neuroligin 2 is exclusively localized to inhibitory synapses. *European Journal of Cell Biology*, *83*(9), 449–456. https://doi.org/10.1078/0171-9335-00410

Viltono, L., Patrizi, A., Fritschy, J., & Sassoè-Pognetto, M. (2008). Synaptogenesis in the cerebellar cortex: Differential regulation of gephyrin and GABAA receptors at somatic and dendritic synapses of Purkinje cells. *Journal of Comparative Neurology*, *508*(4), 579–591. https://doi.org/10.1002/cne.21713

Wagh, D. A., Rasse, T. M., Asan, E., Hofbauer, A., Schwenkert, I., Dürrbeck, H., Buchner, S., Dabauvalle, M.-C., Schmidt, M., Qin, G., Wichmann, C., Kittel, R., Sigrist, S. J., & Buchner, E. (2006). Bruchpilot, a Protein with Homology to ELKS/CAST, Is Required for Structural Integrity and Function of Synaptic Active Zones in Drosophila. *Neuron*, *49*(6), 833–844. https://doi.org/10.1016/j.neuron.2006.02.008

Wittle, A. E., Kamdar, K. P., & Finnerty, V. (1999). The Drosophila cinnamon gene is functionally homologous to Arabidopsis cnx1 and has a similar expression pattern to the mammalian gephyrin gene. *Molecular and General Genetics MGG*, *261*(4–5), 672–680. https://doi.org/10.1007/s004380050010

Yam, P. T., Pincus, Z., Gupta, G. D., Bashkurov, M., Charron, F., Pelletier, L., & Colman, D. R. (2013). N-Cadherin Relocalizes from the Periphery to the Center of the Synapse after Transient Synaptic Stimulation in Hippocampal Neurons. *PLoS ONE*, *8*(11), e79679. https://doi.org/10.1371/journal.pone.0079679

Yamagata, M., Herman, J., & Sanes, J. (1995). Lamina-specific expression of adhesion molecules in developing chick optic tectum. *The Journal of Neuroscience*, *15*(6), 4556–4571. https://doi.org/10.1523/JNEUROSCI.15-06-04556.1995

Zhang, W., Coldefy, A.-S., Hubbard, S. R., & Burden, S. J. (2011). Agrin Binds to the N-terminal Region of Lrp4 Protein and Stimulates Association between Lrp4 and the First Immunoglobulin-like Domain in Muscle-specific Kinase (MuSK). *Journal of Biological Chemistry*, *286*(47), 40624–40630. https://doi.org/10.1074/jbc.M111.279307

Zhang, X., Koolhaas, W. H., & Schnorrer, F. (2014). A Versatile Two-Step CRISPR- and RMCE-Based Strategy for Efficient Genome Engineering in *Drosophila*. *G3 Genes|Genomes|Genetics*, *4*(12), 2409–2418. https://doi.org/10.1534/g3.114.013979